Single-Pass Generation and Detection of Ultrafast Multimode Squeezed Light

Tiphaine Kouadou

Thèse de Doctorat de
Sorbonne Université

présentée par

Tiphaine KOUADOU

le 26 mars 2021

pour obtenir le grade de Docteur de Sorbonne Université
sur le sujet:

Single-Pass Generation and Detection of Ultrafast Multimode Squeezed Light

Laboratoire Kastler Brossel
Physique quantique et applications

Membres du jury :

Pr. Alessandro ZAVATTA	Rapporteur
Dr. Virginia D'AURIA	Rapporteur
Pr. Valia VOLIOTIS	Membre du jury
Dr. Nadia BELABAS	Membre du jury
Dr. Valentina PARIGI	Membre invité
Pr. Nicolas TREPS	Directeur de thèse

Abstract

We present the generation of multimode continuous-variable entangled states featuring spatio-spectral correlations at a repetition rate of 156 MHz via a single-pass and non-collinear spontaneous parametric down conversion (SPDC) process in a bulk BBO crystal pumped by an optical frequency comb. The states are building blocks of highly entangled states called dual-rail cluster states and are useful for measurement-based quantum computation. It is a protocol for quantum information based on the successive measurement of the modes of a cluster state. We characterize the states generated in our experiment with a mode-selective homodyne detection where we shape the spectrum and spatial profile of a reference beam to unveil the multimode structure of the parametric light. This way, we measured squeezing in several spectral modes and and revealed non-classical correlations between spatio-spectral modes. Because of the configuration of the parametric process, the states generated are highly multimode both spatially and spectrally and they display a low level of squeezing par mode, i.e. just above the resolution of our homodyne detector. As squeezing is an important resource for measurement-based quantum computation, we decided to develop a new SPDC setup based on wavguides of periodically-poled KTP to replace the bulk BBO crystal. Thanks to the increased nonlinearity, light confinement inside the waveguide and the use of quasi-phase matching, the squeezing per mode of the generated states should be increased. In the meantime, we developed a wideband homodyne detector operating with pulsed light in order to perform pulse-by-pulse homodyne measurements.

Remerciements

Cette page est consacrée à remercier les personnes qui m'ont aidées de près ou de loin à préparer ma thèse dans de bonnes conditions. Tout d'abord mes encadrants Nicolas Treps et Valentina Parigi, je vous remercie de m'avoir intégrée à votre équipe, de m'avoir donné l'opportunité de gagner en autonomie, en confiance et de m'avoir permis de travailler sur des projets ambitieux et passionnant. Saïda Guellati, je suis reconnaissante de t'avoir eu comme marraine. Je te remercie pour nos discussions, pour tes conseils et pour tous ces petits moments d'attention que tu m'as accordés malgré ton emploi du temps chargé. Je remercie également mon tuteur scientifique, Michel Brune. Nous n'avons interagi qu'à quelques reprises au cours de ma thèse mais je te remercie pour le temps que tu m'as accordé et pour tes conseils.

Une des dures réalités d'une thèse effectuée en France est que les partenaires de recherche changent rapidement. Quand j'ai rejoint l'équipe en mars 2017, j'ai été chaleureusement accueillie par Luca La Volpe, Syamsundar De, Adrien Dufour, Pauline Boucher, Young-Sik Ra, Francesco Arzani et Mattia Walschaers. J'ai été très heureuse de commencer ma thèse auprès de vous. Et puis vous avez tous quitté l'équipe petit à petit. À l'exception de Mattia ! Qui est devenu chargé de recherche CNRS pendant ma thèse et dont j'ai eu la chance de partager le bureau. L'équipe SPOPA constituée de Luca, Syam (l'irremplaçable) et moi s'est réduite à juste moi. Par la suite, Matthieu Ansquer puis Francesca Sansavini ont rejoint le projet, le développement de l'expérience MUSiQS. Je suis heureuse d'avoir travaillé (galéré) avec vous. Commencer ce projet n'était pas facile, mais qui de nous se serait douté que le pire était à venir. Je suis reconnaissante d'avoir pu compter sur vous professionnellement et personnellement pendant cette année de pandémie. Vous êtes de bons doctorants et de bons amis, je vous souhaite le meilleur pour la suite. Et du courage.

Quiconque a interagi avec moi pendant ma thèse, n'ignore pas que mon projet incluait le développement d'un détecteur homodyne à grande bande passante. Inutile de passer par quatre chemins : le projet était Pénible. Très intéressant, certes, mais PÉNIBLE. Je remercie tous ceux qui m'ont encadrée, formée et aidée dans la poursuite de projet. Merci Bérengère Argence et Loïc Garcia, avec qui j'ai commencé, pour les journées et les soirées passées à l'atelier d'électronique à travailler sur les premières versions du détecteur. Et puis merci à vous Elie Gozlan et David Polizzi, qui avez

rejoint le projet par la suite et y avez consacré tant de temps. Je remercie Xavier Solinas, ingénieur électronicien au LOB, pour le temps qu'il nous a accordé, pour les nombreux conseils qu'il nous a donnés. Merci également à Pierre Cladé et à l'atelier d'électronique de Lhomond, Lionel et Toufik, merci beaucoup pour votre accueil (on ne peut jamais se tromper avec du café et des croissants) et pour le temps que vous nous avez accordé.

Je profite de cette page pour remercier aussi Antoine Heidmann, directeur du LKB, Carou Doré, Sébastien Colinot et Gaël Coupin de l'atelier mécanique ainsi que l'équipe administrative du LKB : Laetitia Morel, Romain Rybka, Nora Aissous, Stéphanie Dubois, Valérie Revelut (Valérie !) et Thierry Tardieu (qui résout TOUS les problèmes administratifs). J'ai apprécié les moments conviviaux que nous avons passé ensemble pendant la fête de la science, les pots du labo et les journées de prospectives. Je remercie aussi mes camarades du Friday Bar (qui avait lieu le Thursday), Adrien Cavaillès, Adrien Dufour, Valentin Métillon, Raphaël Saint-Jalm et Arthur Larrouy ainsi que mes co-organisateurs Léo Morel, Tom Darras, Tamara Bardon-Brun et Ferhat Loubat.

Finalement, je remercie les membres de mon jury de thèse, les rapporteurs de ma thèse Virginia D'Auria et Alessandro Zavatta, Nadia Belabas ainsi que la présidente du jury Valia Voliotis. Merci d'avoir accepté de faire parti de mon jury. Merci d'avoir lu ma thèse avec autant d'attention, merci pour vos corrections, commentaires et conseils ainsi pour vos questions lors de ma soutenance.

Contents

Introduction **1**

I Concepts of Multimode Quantum Optics **7**

1 Concepts of Classical and Modal Optics **9**
1.1 Modal Description of the Classical Field 9
1.2 Hermite-Gauss Mode Basis 11
1.2.1 Hermite-Gauss Function in the Spatial Domain 11
1.2.2 Hermite-Gauss Function in the Temporal Domain 13
1.3 Modes in a Rectangular Waveguide 14
1.3.1 Extension to 2D Field Amplitude 15
1.4 Pulsed Light 16
1.4.1 Pulsed Light in the Spectral Domain 19
1.4.2 Description of a Noisy Frequency Comb 20
1.4.3 Pulse Energy and Power 21

2 Description of Multimode Squeezed Light **23**
2.1 Electric Field Operator 23
2.2 Description of Light in the Phase Space 25
2.2.1 Coherent State 26
2.2.2 The Wave Function of Gaussian States 27
2.2.3 The Wigner Function 28
2.3 Representation of Squeezed Light 29
2.3.1 Single-mode Squeezing 30
2.3.2 Two-Mode Squeezed States 32
2.3.3 Multimode Squeezing 33
2.3.4 Description of Correlations with Covariance Matrices 34
2.3.5 Schmidt Decomposition 35
2.3.6 Bloch-Messiah Decomposition 37
2.3.7 Relation between Schmidt and Squeezed Modes 38

II Generation and Characterization of Ultrafast Multimode Squeezed Light 41

3 Spontaneous Parametric Down Conversion of Ultrafast Light 43
3.1 Birefringence . . . 44
3.2 Index Ellipsoid . . . 45
3.3 Sellmeier's Equations . . . 46
3.3.1 Influence of the Temperature . . . 48
3.4 Polarization in a Nonlinear Medium . . . 49
3.4.1 Electric Susceptibility . . . 49
3.4.2 Kleinman Symmetry . . . 51
3.5 Building the Parametric Process . . . 52
3.5.1 Coupled-Wave Equations . . . 54
3.5.2 Interaction Hamiltonian . . . 57
3.5.3 PDC Phase-Matchings . . . 59

4 Ultrafast Pulse Shaping for Mode Selectivity 63
4.1 Zero-dispersion Line . . . 64
4.2 Focal Length and Reflecting Telescope . . . 65
4.3 Spatial Light Modulator . . . 66
4.4 Blazed Grating . . . 66
4.4.1 Choose a Blazed Grating . . . 67
4.5 Shaping Performances . . . 68
4.6 Useful Phase Masks for Multimode Squeezing . . . 69
4.6.1 Masks for Homodyne Detection . . . 71
4.6.2 Correction of Dispersion . . . 71

5 Principle of Homodyne Detection for Ultrafast Light 75
5.1 Homodyne Signal . . . 75
5.2 Noise and Losses in Homodyne detection . . . 77
5.2.1 Non-Ideal Photodetection . . . 77
5.2.2 Electronic Noise . . . 80
5.2.3 Mode-Matching Losses . . . 81
5.3 Detector Performances . . . 82
5.3.1 Shot-Noise Clearance . . . 82
5.3.2 Common-Mode Rejection Ratio . . . 83
5.4 Noisy Squeezing Levels . . . 83
5.5 Examples of Homodyne Detections in the Multimode Regime . . . 85
5.5.1 Mode-Selective Homodyne Detection . . . 85
5.5.2 Multipixel Homodyne Detection . . . 85

6 Experimental Realisation of Multimode Squeezed Vacua **87**
6.1 Towards the Generation of Dual-Rail Cluster States 87
6.2 Laser Source 89
6.3 Bulk Non-Collinear Parametric Down Converter 89
6.3.1 Second Harmonic Generation 90
6.3.2 Type-I Parametric Down Conversion in Free Space 91
6.4 Guided Parametric Down Conversion 97
6.4.1 Numerical Analysis 98
6.4.2 Waveguide Chips 105
6.4.3 Waveguide Characterization 107
6.4.4 Reveal SPDC in PPKTP waveguides 108
6.4.5 Squeezing Measurements 109

III Development of a Homodyne Detector for Light Characterization **113**

7 Development of Fast Homodyne Detection **115**
7.1 Light Detection 116
7.1.1 P-N junction 116
7.1.2 PIN photodiode 118
7.2 Transimpedance amplifier 119
7.3 Voltage Amplification 123
7.3.1 Separate DC and AC Signals 124
7.3.2 Active High-Pass Filter 124
7.4 Development of a Printed Circuit Board with EAGLE 125
7.4.1 Multiple-layer Boards 126
7.4.2 Choosing the Size of Electronic Components 127
7.4.3 Characteristics of Conductive Tracks 127
7.4.4 Vias: Role and Characteristics 128
7.4.5 Filtering of the Power Supply 129
7.5 Analysis of the Detector Response 129
7.5.1 Noise Characterization with a Spectrum Analyzer 129
7.5.2 Detector Analysis with a Network Analyzer 131

8 Characterization of Homodyne Circuits **133**
8.1 Circuit Layouts 134
8.1.1 Dual-Output Detector with OPA847 134
8.1.2 Dual-Output Detector with OPA855 135
8.2 Detector Characterization in CW Light 135
8.2.1 Evaluation of the Saturation Threshold in CW Light 137

8.2.2 Shot-Noise Renormalization . . . 137
8.3 Detector Characterization with Pulsed Light . . . 142
8.3.1 Measurement of the Common-Mode Rejection Ratio . . . 142
8.3.2 Measurement of the Shot-Noise Clearance and Instabilities in the Pulsed Regime . . . 143
8.3.3 Analysis in the Temporal Domain . . . 144
8.3.4 Correction of the Amplifier Gain . . . 146
8.3.5 Latest Results . . . 150
8.3.6 Prospects . . . 150

Conclusion **153**

Appendices **155**

A Parasitic Oscillations in Homodyne Detection **157**
A.1 Oscillations in RLC-like circuits . . . 157
A.2 Temporal derivation . . . 158

B Notch Filters **161**

C Detailled LtSpice Schematics of Dual-Output Detectors **163**

D Eagle Schematics of the Dual-Output Detectors **167**

References **172**

Introduction

The quantum properties of light are known since 1900 when M. Planck published his work on black body radiation [Planck 00, Planck 01]. He suggested that radiations were emitted and absorbed in discrete quanta. In 1905, A. Einstein suggested in [Einstein 05, Arons 65] that the light energy was carried in discrete quantities to explain the experimental data from the photoelectric effect and introduced the photon as a constituent of light. He suggested that the energy in each quantum of light was equal to the frequency of the light multiplied by a constant, which would be later called the Planck's constant h. This was an important step in the development of quantum mechanics. In the years 1920, renowned physicists such as M. Born, W. Heisenberg, L. de Broglie or E. Schrödinger contributed to develop the theory of quantum mechanics. In a paper published in 1935, A. Einstein, B. Podolsky and N. Rosen introduced a counter-intuitive property of compound quantum systems, later known as entanglement [Einstein 35, Horodecki 09].

In 1960, T. Maiman implemented the first laser, which generated light pulses from a silver-coated slab of ruby pumped with an intense flash lamp [Maiman 60]. The laser exploits the process of stimulated emission introduced by A. Einstein in 1916 [Einstein 16, Einstein 17]. It emits light unidirectionally and has well defined spectral properties, which we call coherence. The properties of the laser beam encouraged the development of new experiments and the formulation of a quantum theory of light. Shortly after, the field of nonlinear optics emerged with the discovery of second-harmonic generation by P. Franken et al. in 1961 [Franken 61], while T. Siegman formulated a quantum mechanical description of parametric processes [Louisell 61]. The first experimental realisation of parametric down conversion was presented by D. Burnham and D. Weinberg [Burnham 70, Zel'Dovich 69]. This technique rapidly became the major source of photon pairs featuring non-classical correlations in numerous degrees of freedom including time [Hong 86], space [Heidmann 87] or polarization [Kwiat 95]. Parametric down conversion (PDC) allowed for the development of quantum optical applications starting from the implementation by C. Bennett and G. Brassard in 1984 of the first quantum protocol for secure communication using single photons for quantum key distribution [Bennett 84]. This was the emergence of quantum information. The first realization of the quantum squeezing of field quadratures, i.e. amplitude and

phase, was presented in [Slusher 85] in 1985. It found interest in the field of quantum metrology [Caves 81] and motivated the development of experiments aiming at increasing the level of quantum squeezing. Quantum squeezing also promoted the development of quantum information protocols in continuous variables, including quantum teleportation [Braunstein 98, Furusawa 98, Grosshans 01b]. Additionally, it motivated the implementation of the oscillator parametric oscillator (OPO) [Brosnan 79, Wu 87] and the characterization of various nonlinear materials such as Barium borate (BBO) [Chen 87], Potassium titanyl phosphate (KTP) [Porta 89] and lithium niobate (LN) [Byer 81]. In 2001, S. Tanzilli et al. [Tanzilli 01] presented the first demonstration of parametric down conversion inside nonlinear waveguides. They generated parametric photons with unprecedented brightness thanks to the confinement of light inside a waveguide of periodically poled LN. Waveguides also allow the development of compact schemes for fiber-based setups.

In the meantime, other research fields in physics, chemisty or biology required sources of pulsed light with high peak energy. Although the first generation of a short coherent pulse was performed in 1964 [Hargrove 64], several developments were needed to produce shorter pulses in a reproducible way and to achieve emission stability. The first experimental implementation of Kerr-Lens mode locking in 1991 in a titanium sapphire laser enabled the stable emission of 60-femtosecond pulses [Spence 91]. In the spectral domain, these sources, called frequency combs, presented a spectrum composed of regularly spaced frequency components of narrow linewidth. Nowadays, the improvement of stabilization techniques allows to produce sources which find applications in spectroscopy [Udem 99, Udem 02] and allowed the emergence of the field of ultrafast quantum optics. Researchers used pulsed sources to pump nonlinear processes, this included the implementation of synchronously pumped OPO [Powers 93, Esteban-Martin 09, Pinel 12], as well as the improvement of waveguide-based experiments [Mondain 19, Luo 20] in order to increase the level of squeezing generated in laboratory [Vahlbruch 16].

In 2000, M. A. Nielsen and I. L. Chuang did the first description of a quantum computer in [Nielsen 00]. Shortly after, H. J. Briegel and R. Raussendorf proposed a quantum-computing protocol based on the measurement of highly entanglement states called cluster states [Raussendorf 01, Raussendorf 03]. These cluster states are multipartite entangled states [Gerke 16], in which the nodes are modes of the field connected to eachother by entanglement links according to a specific graphical pattern such that the removal of one link following the measurement of one node does not destroy other links. In the following years, experimental realizations of cluster states of various shapes were published by our group [Roslund 14, Cai 17], the group of O. Pfister and the group of A. Furusawa, who proposed realizations of large clusters [Chen 14, Yokoyama 13]. In the meantime, one-way quantum computation with continuous-variable states was proposed in [Menicucci 06, Gu 09].

An other important element of the development of quantum optics experiments is the improvement of state-characterization techniques. From the years 1980, homodyne detection, proposed in the work published by H. P. Yuen [Yuen 83], was used for the measurement of quadrature squeezing [Mandel 82, Zavatta 02]. At the beginning, homodyne detectors were designed with a bandwidth above 10 MHz in order to get rid of the low-frequency noise, such as the $1/f$ noise [Yurke 85]. In more recent years, the development of ultrafast quantum optics encouraged the development of wideband detectors, such as A. Zavatta et al. in [Zavatta 02] or R. Kumar et al. in [Kumar 12], suited for the characterization of pulsed quantum sources. Today, the advances in quantum information impose to improve detectors and we approach the performance limits of electronic-based devices. As increasing the bandwidth is difficult, some groups proposed detectors operating in a restricted bandwidth around a high central frequency, they are called resonant detectors [Serikawa 18].

The work done during this thesis is motivated by all these advances and aims at the implementation of a measurement-based quantum computation system with optical pulses. It is a protocol based on the successive measurement of quantum states from a highly entangled network, the cluster state. We want to develop an experiment to generate large continuous-variable cluster states. Large clusters allow for the implementation of longer and more elaborate protocols. In this case, the difficulty of MBQC is on the one hand to produce such states and on the other hand to be able to maintain them stable over the duration of the protocol, i.e. protected from environmental perturbations. The advantage of the continuous-variable cluster state proposed by the group of A. Furusawa in [Yokoyama 13] is that it is not necessary to generate the whole state before starting the protocol. Our work is inspired by the one of A. Furusawa's group. The experiment relies on a spontaneous parametric down conversion process pumped with an optical frequency comb. The output states are multimode squeezed states of light. The long term goal of our experiment is to combine the multimode squeezed pulsed light with differing time delays on two beamsplitters to produce a dual-rail cluster state featuring time and frequency entanglement. Each mode of the cluster is an optical pulse emitted at 156 MHz, i.e. the laser repetition rate. During my thesis, we built an experiment of single-pass non-collinear SPDC using a bulk BBO crystal and pumped with pulsed light. In this configuration, the generated states are two-mode squeezed states featuring non-classical spatio-spectral correlations. They correspond to building blocks of a dual-rail cluster states, which emission rate is fixed by the repetition rate of our laser. Due to the single-pass and non-collinear configuration of our experiment, the generated states are highly multimode spectrally and spatially and display a low squeezing level per mode, i.e. just above the resolution of our homodyne detector. For that reason, we developed a SPDC setup using waveguides of periodically poled KTP to replace the bulk BBO crystal. The higher nonlinearity associated to light confinement

should allow us to produce states with a higher squeezing per mode. In the meantime, we also worked on the improvement of a wideband homodyne detector operating with pulsed light in order to perform measurements at the repetition rate of our laser (156 MHz). The outline of the manuscript is the following.

Outline of the manuscript

The chapter 1 deals with the classical description of light. We describe the modal structure of the electric field as well as the mode bases that we use to describe the structure of the states we produce in our experiments. In a final part, we give a mathematical description of our pulsed light source.

In chapter 2, we focus on the description of quantum light. We recall the operators associated to the discrete- and continuous-variable descriptions of quantum states of light. Then, we give the representation of squeezed states and introduce the basis changes that allow to unveil the modal structure of the states generated via parametric down conversion.

In chapter 3, we describe the properties of the nonlinear crystals and the different phase-matching configurations we use in our experiment. We also calculate the nonlinear polarization and the interaction hamiltonian associated to a parametric down conversion process.

The chapter 4 presents the necessary tools for the implementation of an ultrafast pulse shaper. It is used to shape the reference beam of a homodyne detection, called local oscillator, and allows to perform mode-selective homodyne detection.

In chapter 5, we recall the principle of homodyne detection. We describe a non-ideal detection and introduce the parameters that are used to assess the performances of a homodyne detector.

In chapter 6, we describe our experimental setup and present the generation of multimode squeezed states of light via a single-pass non-collinear PDC through a bulk BBO crystal. We also investigated the spatio-spectral correlations in the produced states and give the results. In a second part, we describe the design of a waveguide-based experiment using PPKTP crystals. We present the numerical simulations of the process and the implementation of the experiment.

The chapter 7 is about the design of a wideband homodyne detector. We describe the general structure of a detector and we present the development of a printed circuit

board.

Finally, in chapter 8, we present the characterization of some of the homodyne detectors we built in the laboratory as well as the prospects of improvement.

Part I

Concepts of Multimode Quantum Optics

Chapter 1

Concepts of Classical and Modal Optics

Contents

1.1 Modal Description of the Classical Field 9
1.2 Hermite-Gauss Mode Basis 11
1.2.1 Hermite-Gauss Function in the Spatial Domain 11
1.2.2 Hermite-Gauss Function in the Temporal Domain 13
1.3 Modes in a Rectangular Waveguide 14
1.3.1 Extension to 2D Field Amplitude 15
1.4 Pulsed Light 16
1.4.1 Pulsed Light in the Spectral Domain 19
1.4.2 Description of a Noisy Frequency Comb 20
1.4.3 Pulse Energy and Power 21

1.1 Modal Description of the Classical Field

Light propagation in vacuum is described by Maxwell's equations from which derives the wave equation. For simplicity, we will restrict ourselves to a plane-wave description of light. In this case, the electric field is a superposition of plane waves of frequencies close to a central frequency ω_0 and wavevectors close to a mean value $\|\vec{k}_0\|$ according to the narrow-band and paraxial approximations [Fabre 20]. Moreover, we assume that $\vec{k}_0$ is parallel to the z axis. Thus, the electric field $\mathbf{E}$ is a complex quantity defined by:

$$\mathbf{E}(\vec{r},t) = \sum_m \mathcal{E}_m \, \mathbf{f}_m(\vec{r},t) \, e^{-i(\omega_0 t + \vec{k}\cdot\vec{r})} + c.c. \tag{1.1}$$

$$\mathbf{E}(\vec{r},t) = \mathbf{E}^{(+)}(\vec{r},t) + \mathbf{E}^{(-)}(\vec{r},t) \tag{1.2}$$

Where $\mathbf{E}^{(+)}$ and $\mathbf{E}^{(-)}$ are complex conjugates. The bold and vector notations indicate vector quantities. The functions $\mathbf{f}_m$ are modes defined as normalized solutions of the Maxwell's equations, which means that they satisfy the following equations:

$$\frac{1}{V}\int_V d^3r\ \mathbf{f}^*_{m'}(\vec{r},t)\,\mathbf{f}_m(\vec{r},t) = \delta_{m',m} \tag{1.3}$$

Where V is the volume of the physical system in which light propagates. The modes evolve in space and time and to simplify we separate their spatial and temporal features as we consider a context in which these parameters are not intertwined. First, we write $\mathbf{f}_m$ as the product of a propagation part $\mathrm{f}_T(z,t)$ and a transverse envelop $\mathrm{f}_\ell(x,y,z)$ varying slowly with time:

$$\mathbf{f}_m(\vec{r},t) = \vec{\epsilon}_m\ \mathrm{f}_\ell(x,y,z) \times \mathrm{f}_T(z,t) \tag{1.4}$$

Where f_T and f_ℓ are scalar functions and $\vec{\epsilon}_m$ is the direction of the field polarization. In the paraxial approximation, the spatial envelop of the modes vary slowly in the transverse place (x,y) so the mode function $\mathrm{f}_\ell(x,y,z)$ at any position z can be deduced from its value at $z=0$ according to the Huygens-Fresnel integral accounting for diffraction. This allows us to simplify the equation 1.4 and write the mode functions as the factorization of a temporal mode function f_T and a spatial one f_ℓ:

$$\mathbf{f}_m(\vec{r},t) = \vec{\epsilon}_m\ \mathrm{f}_\ell(x,y,z) \times \mathrm{f}_T(\tau) \tag{1.5}$$

Where $\tau = t - \frac{z}{c}$. In the following, we assume to be at $z=0$, such that $\tau = t$. Via Fourier transform, it is possible to access modes in the conjugate space, such as spectral modes $\mathrm{f}_T(\omega)$ and spatial wavevector modes $\mathrm{f}_\ell(\vec{k})$.

$$\mathrm{f}_T(\omega) = \frac{1}{\sqrt{2\pi}}\int dt\,\mathrm{f}_T(t)\,e^{-i\omega t} \tag{1.6}$$

$$\mathrm{f}_\ell(\vec{k}) = \frac{1}{\sqrt{2\pi}}\int d\vec{r}\,\mathrm{f}_\ell(\vec{r})\,e^{-i\vec{k}\cdot\vec{r}} \tag{1.7}$$

Temporal-spectral modes are particularly useful in the description of pulsed light (section 1.4).
The complex amplitudes $\mathcal{E}_m$ of eq. 1.1 are composed by a real and an imaginary part $\mathcal{E}_{mq}$ and $\mathcal{E}_{mp}$ that are in quadrature.

$$\mathcal{E}_m = \mathcal{E}_{mq} + i\,\mathcal{E}_{mp} \tag{1.8}$$

In the following section, we focus on the mathematical description of the field amplitude.

1.2 Hermite-Gauss Mode Basis

1.2.1 Hermite-Gauss Function in the Spatial Domain

In the previous section, we described the electric field as the product of two parts: a propagation one, along the $\vec{z}$ direction and a transverse profile describing the field amplitude in the (x,y) plane at a given z. The most common spatial profile of laser sources can be described with a Gaussian function. At $z = z_0$ and ignoring the y direction:

$$g(x) = \frac{1}{w(z_0)\sqrt{\pi}}\, e^{-\frac{(x-x_0)^2}{w(z_0)^2}} \tag{1.9}$$

$$= \frac{1}{\sigma(z_0)\sqrt{2\pi}}\, e^{-\frac{(x-x_0)^2}{2\sigma(z_0)^2}} \tag{1.10}$$

Where the factor before the exponential is a normalization constant, x_0 is the coordinate of the beam center corresponding to the point of maximal intensity, $w(z_0)$ is the beam width and $\sigma(z_0)$ is the standard deviation. All these quantities vary with the propagation distance and are linked by the following equations, where we also define the Full Width at Half Maximum (FWHM):

$$w(z) = \sqrt{2}\,\sigma(z) \tag{1.11}$$

$$\text{FWHM} = w(z)\,\sqrt{2\,\ln 2} \tag{1.12}$$

$$= 2\sigma(z)\,\sqrt{\ln 2} \tag{1.13}$$

Gaussian beams are defined with a *waist* w_0 which indicates the narrowest cross-section of the beam. Away from its waist, the evolution of the beam width along the direction of propagation is given by:

$$w(z) = w_0 \sqrt{1 + \left(\frac{z}{z_R}\right)^2} \tag{1.14}$$

Where,

$$z_R = \frac{\pi w_0^2}{\lambda} \tag{1.15}$$

Along the Rayleigh length z_R, the beam width evolves from w_0 to $w(z_R) = \sqrt{2}\,w_0$. It is the distance over which the beam divergence θ is close to zero. It is defined by:

$$\tan(\theta) = \frac{w(z)}{z_R} \tag{1.16}$$

Moreover, away from the waist position, Gaussian beams acquire a Gouy phase shift $\phi(z)$ defined as follows:

$$\phi(z) = \arctan\left(\frac{z}{z_R}\right) \tag{1.17}$$

Gaussian functions are useful to describe the spatial profile of the modes in optical cavities, the TEM_{mn} mode basis [Siegman 86]. In particular, playing with the length L of an optical cavity allows to reveal different TEM_{mn} modes, which are modeled by bi-dimensional Hermite-Gauss (HG) functions $H_{mn}(x, y)$. These functions are composed of a normalized Gaussian function, weighted by a *Hermite polynomial* H_m, with m being the mode index. Here, we consider the Hermite polynomials commonly used by physicists:

$$H_m(x) = (-1)^m \, e^{x^2} \, \frac{d^m}{dx^m} e^{-x^2} \tag{1.18}$$

From this general expression, we derive the first polynomials:

$$H_0(x) = 1 \tag{1.19}$$
$$H_1(x) = 2x \tag{1.20}$$
$$H_2(x) = 4x^2 - 2 \tag{1.21}$$
$$H_3(x) = 8x^3 - 12x \tag{1.22}$$

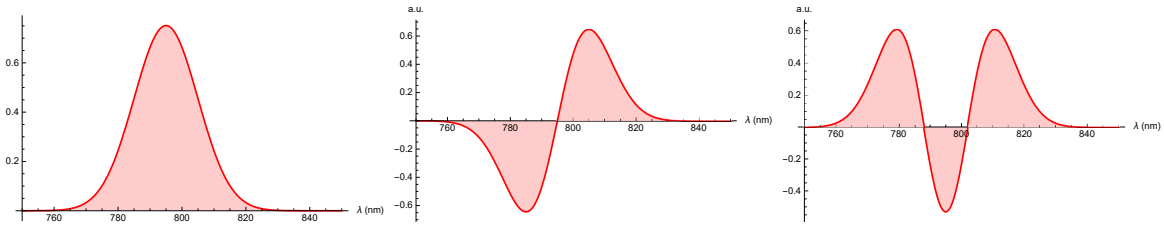

Figure 1.1 – 1D Hermite-Gauss functions HG_0, HG_1 and HG_2.

Bi-dimensional HG functions are weighted by bi-dimensional Hermite polynomials H_{mn}, which are separable functions of the polynomials in both directions $H_{mn}(x, y) = H_m(x) \times H_n(y)$ (fig.1.2). Using equation 1.9 we have:

$$HG_{mn}(x, y, z) = \sqrt{\frac{\pi}{2^{m+n+1} m!\, n!}} \, H_m\left(\frac{\sqrt{2}\,(x - x_0)}{w(z)}\right) \, H_n\left(\frac{\sqrt{2}\,(y - y_0)}{w(z)}\right) \times$$
$$g(x - x_0)\, g(y - y_0)\, e^{i\,\phi_m(z)}\, e^{i\,\phi_n(z)} \tag{1.23}$$

Where $\phi_m(z)$ and $\phi_n(z)$ are the Gouy phase for the mn^{th} HG mode.

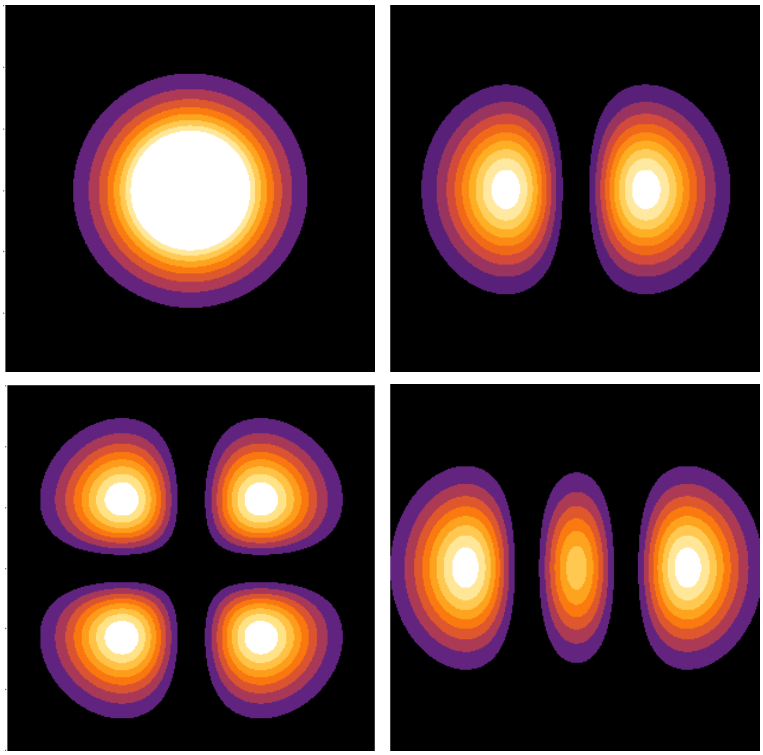

Figure 1.2 – 2D Hermite-Gauss function in arbitrary units. From top left to bottom right: HG_{00}, HG_{10}, HG_{11} and HG_{20}.

1.2.2 Hermite-Gauss Function in the Temporal Domain

In this manuscript, we will work with one dimensional HG functions to describe the spectral modes associated to a parametric process (see section 2.3.5). In the temporal and spectral domains, the Hermite-Gaussian basis can be used to describe the light in terms of its temporal/spectral modes. The general expression of the HG functions is given below (fig. 1.3).

$$HG_m(t) = \frac{1}{\sqrt{\pi 2^{m+1} m!}} H_m\left(\frac{t-t_0}{\sigma_t}\right) e^{-\frac{(t-t_0)^2}{2\sigma_t^2}} \tag{1.24}$$

Where $\sigma_t = \frac{\Delta t}{2\sqrt{\ln 2}}$ is linked to the mode duration Δt. The temporal description of light is discussed more thoroughly in section 1.4.

The expression of the HG function in the spectral domain is linked to the temporal one by a Fourier transform, from which we define the spectrum $\Delta\omega = 2\,\sigma_\omega\sqrt{\ln 2}$ and central angular frequency ω_0.

$$HG_m(\omega) = \frac{1}{\sqrt{\pi 2^{m+1} m!}} H_m\left(\frac{\omega-\omega_0}{\sigma_\omega}\right) e^{-\frac{(\omega-\omega_0)^2}{2\sigma_\omega^2}} \tag{1.25}$$

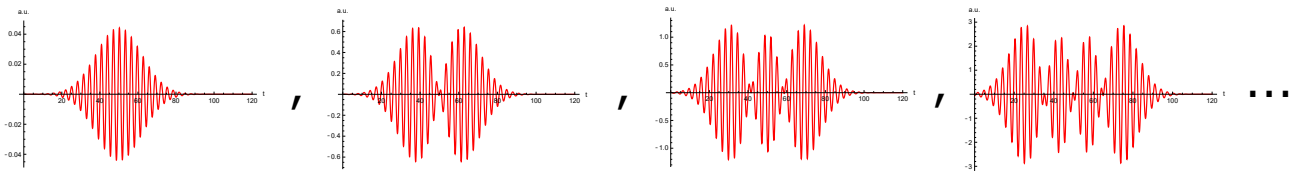

Figure 1.3 – Plot of the temporal-mode basis is arbitrary units. From left to right, HG_0, HG_1, HG_2 and HG_3.

1.3 Modes in a Rectangular Waveguide

In chapter 6, we will consider nonlinear processes inside waveguides. In free space, all frequencies or longitudinal modes can propagate. In an optical cavity, the number of frequency which can resonate in it depends on the dimensions of the cavity. Thus, by reducing the propagation volume in one or two dimensions, it is possible to restrict the number of wavelengths which can still propagate. Here, we consider the propagation of a field inside a rectangular waveguide of cross-section $\Delta x \times \Delta y = a \times b$. Light is thus confined in two dimensions of space x and y, and propagates along the z direction. In this section, we calculate the modes of a rectangular waveguide. First, let us consider a case where the light is confined in the x direction only. Thus, we will describe an electric field $E(x)$. Along the x direction, the boundary conditions are:

$$E(0) = E(a) = 0 \tag{1.26}$$

As light propagates along z only, the electric field can be defined in this section as the product of a propagation factor and an envelope $\mathcal{E}$, which does not depend on the propagation distance z. $\mathcal{E}(x)$ is the function we want to estimate.

$$E(x, z, t) = \mathcal{E}(x)\, e^{-i(\omega t - k_z z)} \tag{1.27}$$

As any wave, guided light satisfies the wave equation:

$$\nabla^2 E + \frac{n_{med}^2}{c^2} \frac{\partial^2 E}{\partial t^2} = 0 \tag{1.28}$$

Where n_{med} is the refractive index of the medium. One solution usually considered for the wave equation is a sinusoidal function, such that the field (eq. 1.27) reads:

$$E(x, z, t) = \sin(k_x x)\, e^{-i(\omega t - k_z z)} \tag{1.29}$$

Applying the boundary conditions 1.26 to this solution, we infer the wavenumbers which can propagate in the waveguide:

$$k_x a = n\pi \tag{1.30}$$

Where $n \in \mathbb{N}$ refers to the mode number.

From the wave equation we find:

$$k_x^2 E + k_z^2 E - \frac{n_{med}^2 \omega^2}{c^2} E = 0 \tag{1.31}$$

$$k_x^2 + k_z^2 - \frac{n_{med}^2 \omega^2}{c^2} = 0 \tag{1.32}$$

The dispersion relation related to light propagation inside a waveguide can be inferred as well as the wavevector k_z associated to the guided modes.

$$\omega = \frac{c}{n_{med}} \sqrt{k_x^2 + k_z^2} \tag{1.33}$$

$$k_z = \sqrt{\frac{n_{med}^2 \omega^2}{c^2} - \left(\frac{n\pi}{a}\right)^2} \tag{1.34}$$

1.3.1 Extension to 2D Field Amplitude

The same derivation can be done for the vertical direction y. It gives the following equations:

$$E(y,t) = \sin(k_y y)\, e^{-i(\omega t - k_z z)} \tag{1.35}$$

$$k_y b = m\pi \tag{1.36}$$

Then, the equation 1.32 becomes:

$$k_x^2 + k_y^2 + k_z^2 - \frac{n_{med}^2 \omega^2}{c^2} = 0 \tag{1.37}$$

And gives the following dispersion relations:

$$\omega = \frac{c}{n_{med}} \sqrt{k_x^2 + k_y^2 + k_z^2} \tag{1.38}$$

$$k_z = \sqrt{\frac{n_{med}^2 \omega^2}{c^2} - \left(\frac{n\pi}{a}\right)^2 - \left(\frac{m\pi}{b}\right)^2} \tag{1.39}$$

which can be linked to an effective refractive index $n_{\text{eff}}(\omega) = \frac{c}{\omega} k_z$ perceived by the light inside the waveguide.

As it was done previously, we consider no coupling between the vertical and horizontal directions, so that the guided mode amplitude is considered as the product of a vertical and a horizontal mode:

$$E(r,t) = \sin(k_x x) \times \sin(k_y y) \exp\left[-i\left(\omega t - z\sqrt{\frac{n_{med}^2\,\omega^2}{c^2} - \left(\frac{n\pi}{a}\right)^2 - \left(\frac{m\pi}{b}\right)^2}\right)\right] \tag{1.40}$$

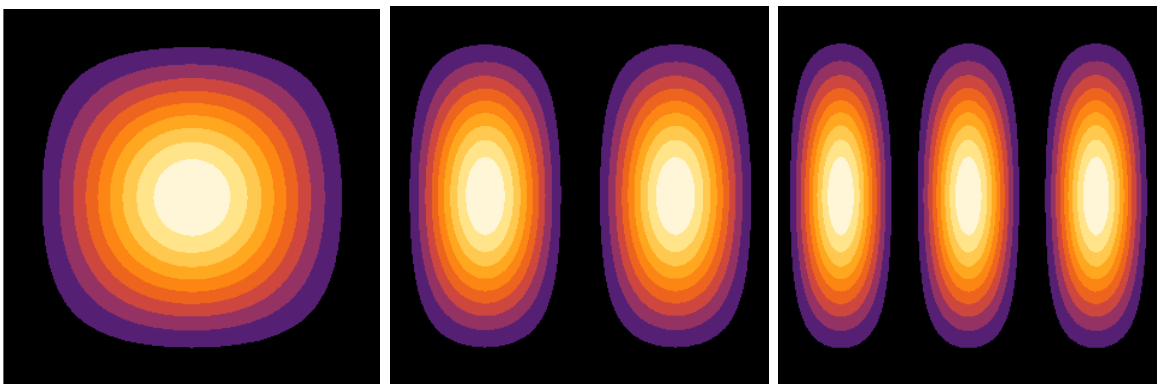

Figure 1.4 – Modes TE_{11}, TE_{21} and TE_{31} of a rectangular waveguide in arbitrary units.

The spatial mode basis of a rectangular waveguide is different from the basis of an optical cavity. In a rectangular waveguide, the spatial mode basis is described by *Transverse Electric* TE or *Transverse Magnetic* TM mode basis. In section 1.2, we presented the TEM modes basis of an optical cavity although we will describe in chapter 6 nonlinear processes occurring inside rectangular waveguides. The goal was to compare both mode basis, whose fundamental modes are similar, to highlight that it is possible to efficiently couple light in the fundamental TE_{00} mode of a rectangular waveguide with an incoming TEM_{00} mode. This section presents a simplified description of the modes of a rectangular waveguide, especially for the refractive index of the waveguides. A more complete description can be found in [Roman-Rodriguez 20]. Finally, we described a TE field and will not give a mathematical description of the magnetic field, which circulates in the (x, z) plane.

1.4 Pulsed Light

John L. Hall and Theodor W. Hänsch received a Nobel prize in 2005 for the development of frequency combs based mode-locked laser [Hänsch 06]. They can be made very stable and provide a wide spectrum of regularly spaced narrow frequency bands, referred

to as *teeth* (fig. 1.5), which makes them an essential tool in metrology, e.g., for clock stabilization and the estimation of fundamental constants [Fortier 19]. In the temporal domain, mode-locked lasers can deliver intense ultrashort pulses, up to the femtosecond regime [Udem 99], a characteristic used to study transient processes of Physics and Chemistry. Optical frequency combs with less stringent requirements than in the case of metrological applications can be used for pulsed-based protocols in quantum information [Dufour 18, Roslund 14, Brecht 15, Wasilewski 06, Polycarpou 12, Karpiński 17]. Frequency-comb characteristics depend on the properties and dispersion of the laser cavity. The pulse-emission rate is called *repetition rate* f_r and the frequency of the m^{th} tooth of the comb is defined by:

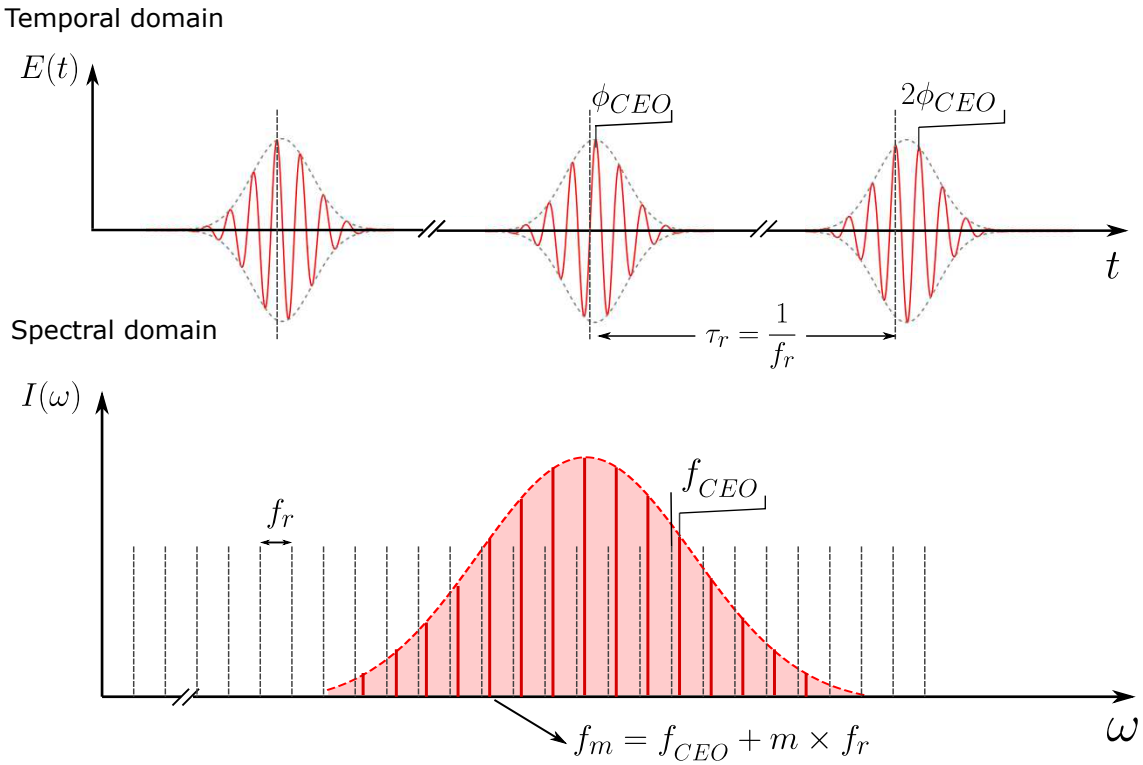

Figure 1.5 – Temporal and spectral representation of a mode-locked laser. Top graph shows the carrier-envelope representation of pulses, the carrier being the red curve and the envelope being the purple dashed curve.

$$f_m = f_{CEO} + m \times f_r \tag{1.41}$$

Where f_{CEO} describes a frequency-independent shift of the spectrum. In the temporal domain, it corresponds to an offset between the carrier and the envelope of the pulses as shown in figure 1.5. It is linked to what is called the *carrier-envelope* phase

ϕ_{CEO}. It is a constant phase, which shifts all the teeth of the comb by a quantity f_{CEO}. Dispersion inside the laser cavity leads to a relative fluctuation of the group and phase velocities. It is at the origin of a dephasing between the carrier and the envelope, which accumulates from pulse to pulse but does not affect the temporal shape. It can be defined as:

$$\phi_{CEO} = \left(\frac{1}{v_g} - \frac{1}{v_\phi}\right) \omega_0 \, L_{cav} \tag{1.42}$$

where $\omega_0 = 2\pi f_0$ is the carrier frequency. It is the central frequency of the frequency comb. v_g and v_ϕ are the group and phase velocities respectively. The phase velocity is given by the dispersion relation:

$$v_\phi = \frac{\omega}{k} \tag{1.43}$$

In a mode-locked laser, it corresponds to the velocity of the frequency components. The group velocity is the one associated to the propagation of the overall envelope of the pulse through space. It is obtained from the dispersion relation as:

$$v_g = \frac{d\omega}{dk} \tag{1.44}$$

In a regular laser cavity, several frequency modes co-exist and resonate in the cavity. Mode-locking is a technique used to generate pulsed laser light through the phase synchronization of laser cavity modes [Haus 20]. In this case, the period τ_r is the sum of a time $\Delta\tau \ll \tau_r$ during which high intensity light is emitted - this is the pulse duration - and a *dark* time $\tau_r - \Delta\tau$, during which light of least intensity is emitted. It is also defined as the time necessary for a pulse to travel inside the cavity:

$$\tau_r = \frac{L_{cav}}{c_{n_{med}}} \tag{1.45}$$

Where L_{cav} is the length of the laser-cavity and $c_{n_{med}} = \frac{c}{n_{med}}$ is the speed of light in the cavity. The pulse duration is linked to the width of the light spectrum Δf. In the model of Gaussian pulses, it reads:

$$\Delta\tau = \frac{0.441}{\Delta f} = \frac{2\pi \times 0.441}{\Delta\omega} \tag{1.46}$$

Where $\omega = 2\pi f$ is the angular frequency. This relation stands for Fourier limited - noiseless - pulses [Sorokin 00].

Theoretically, the train of pulse is described as a convolution between a temporal Dirac comb $C_\tau(t)$ and the field of one pulse $E_{pulse}(\vec{r}, t)$. For a transverse mode m, the field reads:

$$E(\vec{r},t) = E_{pulse}(\vec{r},t) \ * \ C_\tau(t) \tag{1.47}$$

$$= \left(\mathcal{E}_m \, \mathrm{f}_m(\vec{r},t) \, e^{-i(\omega_0 t - \vec{k}\cdot\vec{r})}\right) \ * \ \left(\sum_n \delta(t - n\tau_r)\right) \tag{1.48}$$

$$= \sum_n \mathcal{E}_m \, \mathrm{f}_m(\vec{r}, t - n\tau_r) \, e^{-i(\omega_0 \, (t - n\tau_r) - \vec{k}\cdot\vec{r})} \tag{1.49}$$

Where $f_m(\vec{r}, t - n\tau_r)$ contains information about the pulse duration. A Fourier transform of 1.49 gives the spectrum of the frequency comb, i.e. a Dirac comb in frequency $C_\nu(f)$ weighted by an envelope:

$$E(\vec{r},f) = E_{pulse}(\vec{r},f) \ \times \ C_\nu(f) \tag{1.50}$$

$$E(\vec{r},f) = E_{pulse}(\vec{r},f) \ \times \ \left(\sum_n \delta(f - n f_r)\right) \tag{1.51}$$

1.4.1 Pulsed Light in the Spectral Domain

The electric field of an optical pulse $E(\omega)$ can be described by an amplitude $\mathcal{E}(\omega)$ and a phase $\varphi(\omega)$ such that:

$$E(\omega) = \mathcal{E}(\omega) \, e^{\varphi(\omega)} \tag{1.52}$$

Where we consider one mode of the field only, with the spectral amplitude being $\mathcal{E}(\omega) = \mathcal{E} \, \mathrm{f}(\omega)$, where $\mathcal{E}$ is the field amplitude defined in eq. 1.8 and $\mathrm{f}(\omega)$ is the normalized mode function. The spectral phase $\varphi(\omega)$ can be decomposed in a Taylor expansion to reveal its constituents:

$$\varphi(\omega) = \varphi(\omega_0) + (\omega - \omega_0) \left.\frac{d\varphi}{d\omega}\right|_{\omega_0} + \frac{1}{2}(\omega - \omega_0)^2 \left.\frac{d^2\varphi}{d\omega^2}\right|_{\omega_0} + \frac{1}{6}(\omega - \omega_0)^3 \left.\frac{d^3\varphi}{d\omega^3}\right|_{\omega_0} + \mathcal{O}[(\omega - \omega_0)^4] \tag{1.53}$$

$$= \phi_0(\omega_0) + (\omega - \omega_0)\phi_1(\omega_0) + \frac{1}{2}(\omega - \omega_0)^2\phi_2(\omega_0) + \frac{1}{6}(\omega - \omega_0)^3\phi_3(\omega_0) + \mathcal{O}[(\omega - \omega_0)^4] \tag{1.54}$$

ϕ_0 is a *constant* phase, which manifests itself as a dephasing between the field carrier at ω_0 and its envelope, without distorting the pulse shape. The CEO phase ϕ_{CEO} mentioned in the previous section is a constant phase accumulated inside the laser cavity.

ϕ_1 is the *linear* phase, usually expressed in femtoseconds and defined as:

$$\phi_1(\omega) = \frac{d\varphi(\omega)}{d\omega} = \frac{2\pi\, L_{cav}}{\lambda} \left(\frac{dn_{med}(\omega)}{d\omega}\right) \tag{1.55}$$

$$\phi_1(\lambda) = \frac{\lambda\, L_{cav}}{c} \left(\frac{dn_{med}(\lambda)}{d\lambda}\right) \tag{1.56}$$

The linear phase results in a global time delay of the pulse, i.e. fluctuations of the laser repetition rate.

ϕ_2 is the *chirp* expressed in femtosecond squared. This phase evolves quadratically with frequency and impacts the phase velocity (defined in eq. 1.43) of the comb teeth. Depending on its sign, the instantaneous frequency, defined as the evolution in time of the carrier frequency $\omega_0(t)$, increases (up-chirp) or decreases (down-chirp) with time. Both lead to longer pulses ($\Delta\tau_{chirped} \geqslant \Delta\tau$). From [Weiner 09], the spectral/temporal chirp is defined as:

$$\phi_2(\omega) = \frac{d^2\varphi(\omega)}{d\omega^2} = \frac{d^2k(\omega)}{d\omega} L_{cav} = \frac{\omega}{c} \left(\frac{d^2n(\omega)}{d\omega^2}\right) L_{cav} \tag{1.57}$$

$$\phi_2(\lambda) = \frac{\lambda^3\, L_{cav}}{2\pi c^2} \left(\frac{d^2n(\lambda)}{d\lambda^2}\right) \tag{1.58}$$

As quadratic phase is acquired through propagation in dispersive media, it can be compensated with materials adding negative group velocity dispersion, e.g. prisms or spatial light modulators (SLM). The maximal compensation corresponds to no chirp, for which the pulses are Fourier limited.
N.B.: Chirp can also be angular/spatial: frequency components are emitted at a different angle, resulting in a frequency-dependent optical path. If the divergence is corrected with a converging lens (e.g.), the beam becomes collimated and frequency components propagate approximately parallel to each other. The chirp is then referred to as *spatial* chirp.

Another term of the spectral phase is *cubic* phase ϕ_3, on which we will not extend on. It results in the apparition of repulses of lower intensity following the main pulse [Weiner 11, Thiel 15].

1.4.2 Description of a Noisy Frequency Comb

The noise in an optical frequency comb (OFC) originates notably from mechanical and thermal cavity drifts, spontaneous emission or pump intensity noise [Haus 93]. It is

distributed on few parameters being the fluctuation of the pulse amplitude $\delta\mathcal{E}$, the central frequency $\delta\omega$, the arrival time $\delta\tau_e$ and the fluctuation of the carrier-envelope offset (CEO) phase $\delta\tau_{CEO}$. Compared to equation 1.49, the field of the noisy frequency comb reads [De 19]:

$$E_{comb}(t) = \left(\mathcal{E}(1+\delta\mathcal{E})\ \mathrm{f}(t-\delta\tau_e)\, e^{-i(\omega_0-\delta\omega)(t-\delta\tau_{CEO})}\right) * \left(\sum_n \delta(t-n\tau_r)\right) \tag{1.59}$$

$$= \sum_n \mathcal{E}(1+\delta\mathcal{E})\ \mathrm{f}(t-n\tau_r-\delta\tau_e)\, e^{-i(\omega_0-\delta\omega)(t-n\tau_r-\delta\tau_{CEO})} \tag{1.60}$$

To access the different noise parameters, the OFC can be described with a modal approach and the electric field can be decomposed into its different noise sources. With this approach, the first mode corresponds to the noiseless OFC and the high-order modes are the noise components. Thus, it is possible to map the noise modes to a basis, whose elements are normalized solutions of the Maxwell's equation [Thiel 15, Schmeissner 14]. In this work, we are interested in the modal decomposition of quantum noise of the field, i.e. squeezing (see section 2.3), in nonlinear optical processes pumped by an optical frequency comb. We will see that the Hermite-Gaussian basis presented in section 1.2 (fig. 1.3) will play a major role in the modal description of the generated quantum states.

1.4.3 Pulse Energy and Power

Light power P and energy W are defined as:

$$P(t) = \int_S d^2r\, |\mathbf{E}(r,t)|^2 \tag{1.61}$$

$$W = \int_\tau dt\, P(t) \tag{1.62}$$

The pulsed regime allows the emission of high-intensity light in a short period of time. This is the peak power P_{peak}. When a photo-sensor is placed in front of the light beam, the displayed value corresponds to an average light power P_{avg} over the integration time of the detector. However, light is emitted preferentially during over the fraction $\frac{\delta\tau}{\tau_r}$ of the repetition rate:

$$P_{avg} \sim P_{peak}\left(\frac{\delta\tau}{\tau_r}\right) + \varepsilon\left(\frac{\tau_r-\delta\tau}{\tau_r}\right) \tag{1.63}$$

Where $\varepsilon \sim 0$ corresponds to residual light power emitted over the fraction $\frac{\tau_r - \delta\tau}{\tau_r}$ and can be neglected. By considering Gaussian pulses, the expression of P_{avg} becomes:

$$P_{avg} = \sqrt{2\pi}\, P_{peak} \times \delta\tau \times f_r \tag{1.64}$$

$$= \frac{\sqrt{\pi}}{2\sqrt{\ln(2)}}\, P_{peak} \times \Delta\tau \times f_r \tag{1.65}$$

$$\sim P_{peak} \times \Delta\tau \times f_r \tag{1.66}$$

Where the pulse duration $\Delta\tau = 2\,\delta\tau\sqrt{2\ln(2)}$ is a full width at half maximum (FWHM).

Chapter 2

Description of Multimode Squeezed Light

Contents

2.1 Electric Field Operator 23
2.2 Description of Light in the Phase Space 25
2.2.1 Coherent State 26
2.2.2 The Wave Function of Gaussian States 27
2.2.3 The Wigner Function 28
2.3 Representation of Squeezed Light 29
2.3.1 Single-mode Squeezing 30
2.3.2 Two-Mode Squeezed States 32
2.3.3 Multimode Squeezing 33
2.3.4 Description of Correlations with Covariance Matrices 34
2.3.5 Schmidt Decomposition 35
2.3.6 Bloch-Messiah Decomposition 37
2.3.7 Relation between Schmidt and Squeezed Modes 38

2.1 Electric Field Operator

In the quantum regime, light is better described by the statistics of number of photons impinging on a detector. We can then describe the light field in the Fock basis [Grynberg 10, Loudon 00], i.e. quantum states with a fixed number of photons, which represent the allowed and discrete excited levels of a quantized harmonic oscillator (fig. 2.1). The last is associated with each mode of the electromagnetic field and the transition between the energy levels involves the addition or the subtraction of a photon of energy $\hbar\omega$ from the field, with ω being the angular frequency of the photon. These

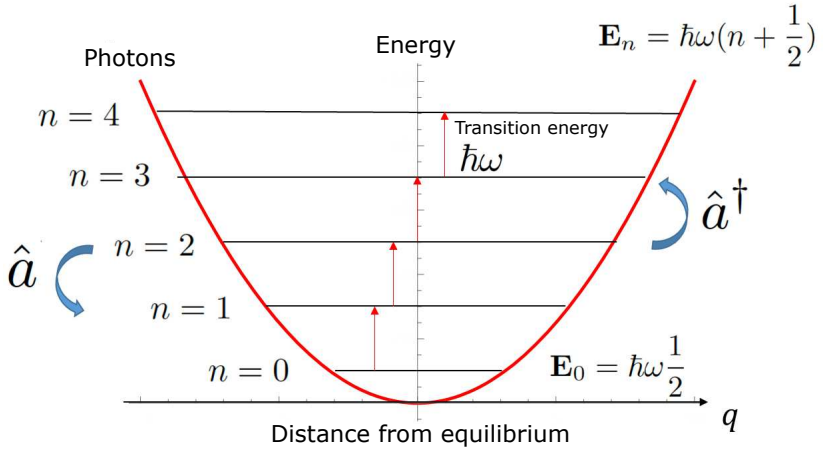

Figure 2.1 – Quantum harmonic oscillator.

operations are described by creation and annihilation quantum operators, $\hat{a}^\dagger$ and $\hat{a}$ respectively, linked by the commutation relation $[\hat{a}, \hat{a}^\dagger] = \hat{a}\hat{a}^\dagger - \hat{a}^\dagger\hat{a} = 1$. Likewise, a set of mode operators $\{\hat{a}_m, \hat{a}_m^\dagger\}$ are associated to each mode of a multimode field respecting the commutation relations $[\hat{a}_m, \hat{a}_{m'}^\dagger] = \delta_{m,m'}$ and $[\hat{a}_m, \hat{a}_{m'}] = 0$. Thus, the energy in the field is defined by:

$$\hat{H} = \sum_m \hbar\omega_m \left(\hat{a}_m^\dagger \hat{a}_m + \frac{1}{2}\right) \tag{2.1}$$

Where $\hat{N}_m = \hat{a}_m^\dagger \hat{a}_m$ is the photon-number operator of one mode. The vacuum state, defined by a mean-photon number $\langle \hat{N} \rangle = 0$, is the fundamental state of the quantum harmonic oscillator with the energy $\frac{\hbar\omega}{2}$ associated with what are called vacuum fluctuations. The photon numbers are discrete variables representing the quantum state but it is possible to use another description of quantum states based on the amplitude and phase quadratures. They are called continuous variables and are particularly useful to describe field fluctuations. In the case of a monomode field, the quadrature operators $\hat{q}$ and $\hat{p}$ (which we write without an index m), are linked by the commutation relation:

$$[\hat{q}, \hat{p}] = 2i \tag{2.2}$$

and are defined by the linear combination of $\hat{a}$ and $\hat{a}^\dagger$ such as:

$$\hat{q} = \hat{a} + \hat{a}^\dagger \tag{2.3}$$

$$\hat{p} = i\left(\hat{a}^\dagger - \hat{a}\right) \tag{2.4}$$

They are the rescaled adimensional form of the position and momentum variables of a harmonic oscillator, according to the convention used in this manuscript. In this convention, the Heisenberg inequality reads:

$$\Delta q \Delta p \geqslant 1 \tag{2.5}$$

where Δ describes the standard deviation of the quadratures. It is the square-root of the variance written Δ^2. In the multimode case, the electric fields reads:

$$\hat{\mathbf{E}}(\mathbf{r},t) = \hat{\mathbf{E}}^{(+)}(\mathbf{r},t) + \hat{\mathbf{E}}^{(-)}(\mathbf{r},t) \tag{2.6}$$

With

$$\hat{\mathbf{E}}^{(+)}(\mathbf{r},t) = \sum_m \mathcal{E}_m \, \mathbf{f}_m(\mathbf{r},t) \, \hat{a}_m \, e^{-i(\omega_m t - \vec{k}\cdot\vec{r})} \tag{2.7}$$

$$= \sum_m \frac{\mathcal{E}_m}{2} \, \mathbf{f}_m(\mathbf{r},t) \, \left(\hat{q}_m + i\hat{p}_m\right) \, e^{-i(\omega_m t - \vec{k}\cdot\vec{r})} \tag{2.8}$$

Where $\mathcal{E}_m$ reads:

$$\mathcal{E}_m = \sqrt{\frac{\hbar\omega_m}{2\epsilon_0 V}} \tag{2.9}$$

The bold notation denotes vectors and $\hat{\mathbf{E}}^{(+)}$ and $\hat{\mathbf{E}}^{(-)}$ are hermitian conjugate. In the following section we will present the continuous-variables (CV) description of quantum states of light that is the most appropriate to describe the states generated in our setup.

2.2 Description of Light in the Phase Space

The state of a quantum system can be described by a state vector, denoted $|\psi\rangle$ or a more general representation, the density matrix $\hat{\rho}$ defined, for a pure state, by:

$$\hat{\rho} = |\psi\rangle\langle\psi| \tag{2.10}$$

And for a mixed state:

$$\hat{\rho} = \sum_k p_k \, \hat{\rho}_k \tag{2.11}$$

$$= \sum_k p_k \, |\psi_k\rangle\langle\psi_k| \tag{2.12}$$

It is the statistical mixture of pure states $|\psi_k\rangle$ where p_k is the probability for the system to be in the state $|\psi_k\rangle$ and $|\psi_k\rangle\langle\psi_k|$ is an outer-product written in bra-ket notation [Fano 57, Nielsen 00]. The state purity $P = \mathrm{tr}(\hat{\rho}^2)$ can be used to distinguish pure states characterized by $P = 1$, from the mixed states for which $P < 1$ [Leonhardt 97]. Quantum states of light can be also represented in a plane by their complex amplitude and in particular by the statistics of their components, the quadratures q and p, constituting the abscissa and ordinate of the phase space. The electromagnetic modes excited by the annihilation operator $\hat{a}$ experience amplitude fluctuations, i.e. quadrature fluctuations, which cannot be reduced to zero according to the Heisenberg inequality. It is possible to associate eigenstates to the quadratures $\hat{q}$ and $\hat{p}$, called quadrature states $|q\rangle$ and $|p\rangle$ [Leonhardt 97] such that $\hat{q}|q\rangle = q|q\rangle$ and $\hat{p}|p\rangle = p|p\rangle$. Both states are related to each other by Fourier transform but do not describe experimentally accessible states. However, they are used to define quadrature wavefunctions $\psi(q) = \langle q|\psi\rangle$ and $\psi(p) = \langle p|\psi\rangle$, which are probability amplitudes of a state $|\psi\rangle$ [Leonhardt 97]. Depending on the system under consideration, several representations can be used like quasiprobability distributions. In this section, after recalling the expression of the wave functions for coherent light, we will present the Wigner function, one of the quasiprobability distributions used to represent coherent and squeezed states of light.

2.2.1 Coherent State

The monomode coherent state is defined as the eigenstate of the annihilation operator $\hat{a}$ with the eigenvalue $\alpha \in \mathbb{C}$, such that $\hat{a}|\alpha\rangle = \alpha|\alpha\rangle$. It corresponds to the light emitted by a laser well above threshold and it is described as a flux of photons impinging on a detector with a Poissonian statistics. The state can represented in the phase space as in figure 2.2 where $q = \langle\hat{q}\rangle$ and $p = \langle\hat{p}\rangle$ are respectively proportional to the real and imaginary parts of the field. The diameter of the blue disks represents the standard deviation of the quadratures, which follow a Gaussian distribution.

$|\alpha| = \frac{1}{2}\sqrt{q^2 + p^2}$ is the amplitude of the state and θ its phase such that $\alpha = |\alpha|e^{i\theta}$. The vacuum is also a coherent state with $\alpha = 0$ and we use in this manuscript the standard deviation of its fluctuations as a reference [Bachor 04]. Indeed, according to equations 2.2 to 2.4

$$\Delta q_{|0\rangle} = \Delta p_{|0\rangle} = 1 \tag{2.13}$$

Which minimizes the Heisenberg inequality:

$$\Delta q \Delta p = 1 \tag{2.14}$$

Moreover, the coherent states $|\alpha\rangle$ are linked to the vacuum by a displacement operation such that:

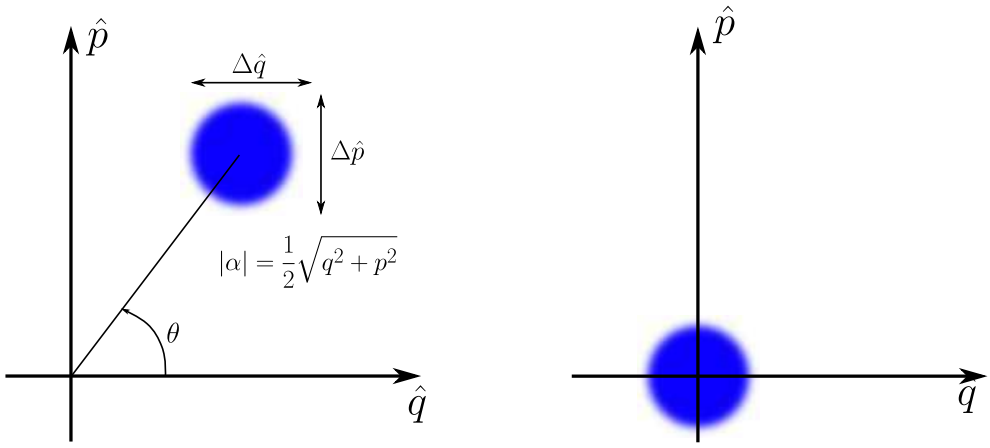

Figure 2.2 – Coherent state in the phase space.

$$|\alpha\rangle = \hat{D}(\alpha)\,|0\rangle \tag{2.15}$$

Where the displacement operator is defined as follows:

$$\hat{D}(\alpha) = e^{i(\alpha\hat{a}^\dagger - \alpha^*\hat{a})} \tag{2.16}$$

In the following sections, we will present the representations of other states and in particular the squeezed states of light.

2.2.2 The Wave Function of Gaussian States

The wave function of quantum states with Gaussian statistics in continuous variables is defined as [Lvovsky 14]:

$$\psi(q) = \frac{1}{\sqrt{2\pi}\Delta q} e^{-\frac{(q-\langle\hat{q}\rangle)^2}{2\Delta^2 q}} \tag{2.17}$$

$$\psi(p) = \frac{1}{\sqrt{2\pi}\Delta p} e^{-\frac{(p-\langle\hat{p}\rangle)^2}{2\Delta^2 p}} \tag{2.18}$$

where $\langle q\rangle$ and $\langle p\rangle$ denote the mean value of the quadrature. For a vacuum state, the mean amplitude $\langle\hat{a}\rangle = 0$ and mean quadratures $\langle q\rangle = \langle p\rangle = 0$. In this case, the equations 2.17 and 2.18 are simplified as such:

$$\psi_0(q) = \frac{1}{\sqrt{2\pi}} e^{-\frac{q^2}{2}} \tag{2.19}$$

$$\psi_0(p) = \frac{1}{\sqrt{2\pi}} e^{-\frac{p^2}{2}} \tag{2.20}$$

2.2.3 The Wigner Function

The Wigner function is a quasiprobability distribution defined to take into account that the quadratures $\hat{q}$ and $\hat{p}$ do not commute (equation 2.2) [Wigner 32]. It is one of the possible representations of light in continuous variables, which contrary to the classical joint probability distribution, can be negative [Leonhardt 97]. Hence the naming of quasi-probability distribution. It is defined as:

$$W(q,p) = \frac{1}{2\pi} \int dq' \langle q - q' | \, \hat{\rho} \, | q + q' \rangle e^{ipq'} \tag{2.21}$$

As for a probability distribution, W is normalized:

$$\int_{-\infty}^{+\infty} dq\, dp\, W(q,p) = 1 \tag{2.22}$$

And the probability to measure q and p is given by the reduced distributions, called marginal distributions defined as:

$$|\psi(q)|^2 = \langle q|\hat{\rho}|q\rangle = \int_{-\infty}^{+\infty} dp\, W(q,p) \tag{2.23}$$

$$|\psi(p)|^2 = \langle p|\hat{\rho}|p\rangle = \int_{-\infty}^{+\infty} dq\, W(q,p) \tag{2.24}$$

The Wigner function can be defined using the wave function 2.17, giving

$$W(q,p) = \frac{1}{2\pi} \int_{-\infty}^{+\infty} dq'\, \psi^*(q+q')\psi(q-q')\, e^{ipq'} \tag{2.25}$$

From which we deduce the Wigner function of a coherent state:

$$W_{|\alpha\rangle}(q,p) = \frac{1}{2\pi}\, e^{-\frac{(q-\langle\hat{q}\rangle)^2}{2} - \frac{(p-\langle\hat{p}\rangle)^2}{2}} \tag{2.26}$$

And in particular, the Wigner of the vacuum:

$$W_0(q,p) = \frac{1}{2\pi} e^{\frac{-q^2-p^2}{2}} \tag{2.27}$$

2.3 Representation of Squeezed Light

As mentioned in the previous section, the fluctuations of the quadratures are governed by the Heisenberg inequality. Nevertheless, in specific cases, the variance of the fluctuations of a quadrature can be reduced below that of the vacuum. This is *quantum squeezing*. This phenomenon goes along with the increase of the variance of the fluctuations of the orthogonal quadrature according to the Heisenberg inequality 2.5. Then, the representation of light in the phase space is rescaled, as shown on figure 2.3 with the Heisenberg limit $\Delta q \Delta p$ remaining unchanged.

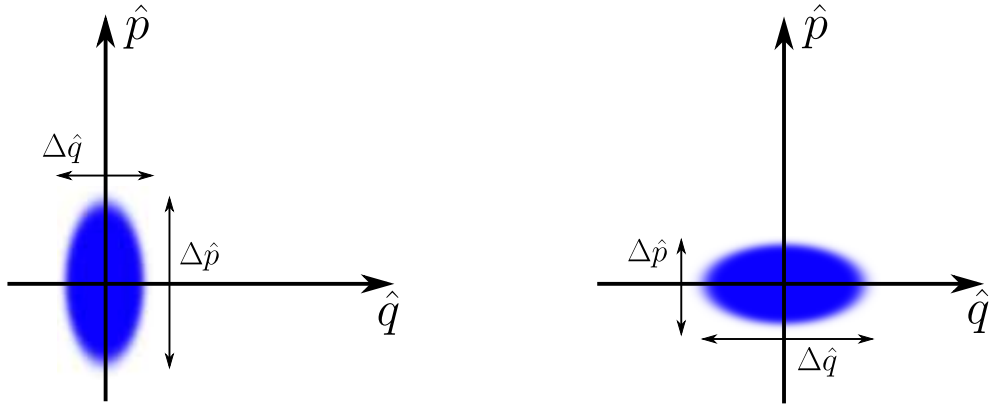

Figure 2.3 – Squeezed vacua in the phase space. The fluctuations of one quadrature are reduced, but they are increased for the conjugate quadrature according to the uncertainty principle.

Similarly to the previous sections, we can write the wave function:

$$\Psi_R(q) = \frac{R}{\sqrt{2\pi}} e^{-\frac{R^2\left(q-\langle q\rangle\right)^2}{2}} \tag{2.28}$$

$$\Psi_R(p) = \frac{1}{R\sqrt{2\pi}} e^{-\frac{\left(p-\langle p\rangle\right)^2}{2R^2}} \tag{2.29}$$

And the Wigner function:

$$W_0(q,p) = \frac{1}{2\pi} e^{-\frac{R^2\left(q-\langle q\rangle\right)^2}{2} - \frac{\left(p-\langle p\rangle\right)^2}{2R^2}} \tag{2.30}$$

Where the fluctuations of the amplitude quadrature $\hat{q}$ are reduced by the *squeezing factor* $R = e^r$, while the fluctuations of the phase quadrature $\hat{p}$ are increased by the same amount. From the previous equations, we can infer the expression of the quadrature variances:

$$\Delta^2 q = \frac{1}{R^2} = e^{-2r} \tag{2.31}$$

$$\Delta^2 p = R^2 = e^{2r} \tag{2.32}$$

And we can verify that the Heisenberg inequality is respected, because $\Delta q \Delta p = 1$. In the two following sections we will present the difference between the single-mode and two-mode squeezing.

2.3.1 Single-mode Squeezing

In this section, we consider the time evolution of the annihilation and creation operators through parametric down conversion. The parametric down conversion (PDC) is a non-linear process occuring when light of high intensity, the pump, is shined on a birefringent medium with $\chi^{(2)}$ susceptibility. One photon of the pump generates two photons called signal and idler, whose properties rely on energy and momentum conservation. Further details on this process will be given in the second part of this manuscript. The process can be mathematically described by a hamiltonian. In this section, let us consider a simplified single-mode hamiltonian for a degenerate type-I PDC, where signal and idler share the same polarization and are indistinguishable fields described with the annihilation operator $\hat{a}$. Also, we treat the pump as a classical field of amplitude α_p [Grynberg 10]:

$$\hat{H} \simeq \chi^{(2)} \alpha_p \left(\hat{a}^{\dagger 2} + \hat{a}^2\right) \tag{2.33}$$

$$\hat{H} \simeq g \left(\hat{a}^{\dagger 2} + \hat{a}^2\right) \tag{2.34}$$

Where g represents the gain of the nonlinear process. We can now write the time evolution of the bosonic operators $\hat{a}(t)$ and $\hat{a}^\dagger(t)$ and for simplicity we will use the notation $\hat{a} = \hat{a}(t)$:

$$i\hbar \frac{d\hat{a}}{dt} = [\hat{a}, \hat{H}] \tag{2.35}$$

$$i\hbar \frac{d\hat{a}^\dagger}{dt} = [\hat{a}^\dagger, \hat{H}] \tag{2.36}$$

We develop the expression of the hamiltonian and obtain the two following equations,

$$\frac{d\hat{a}}{dt} = -\frac{2ig}{\hbar}\,\hat{a}^\dagger \tag{2.37}$$

$$\frac{d\hat{a}^\dagger}{dt} = \frac{2ig}{\hbar}\,\hat{a} \tag{2.38}$$

We derive the equations 2.37 and 2.38 again:

$$\frac{d^2\hat{a}}{dt^2} = \frac{4g^2}{\hbar^2}\,\hat{a} \tag{2.39}$$

$$\frac{d^2\hat{a}^\dagger}{dt^2} = \frac{4g^2}{\hbar^2}\,\hat{a}^\dagger \tag{2.40}$$

The resolution of the second order equations gives the following solutions $\gamma = \pm\frac{2g}{\hbar}$. Taking the boundary conditions into account, we obtain the following operator functions $\hat{a}(t)$:

$$\hat{a}(t) = \frac{1}{2}\,[\hat{a}(0) + \hat{a}^\dagger(0)]e^{\gamma t} + \frac{1}{2}\,[\hat{a}(0) - \hat{a}^\dagger(0)]e^{-\gamma t} \tag{2.41}$$

We set the quantity $r = \gamma t$ as the *squeezing parameter*, we rearrange the previous expressions and obtain the *Bogoliubov transformations* of the input operators of the PDC:

$$\hat{a} = \hat{a}(0)\cosh(r) - \hat{a}^\dagger(0)\sinh(r) \tag{2.42}$$

$$\hat{a}^\dagger = \hat{a}^\dagger(0)\cosh(r) - \hat{a}(0)\sinh(r) \tag{2.43}$$

Where we removed the interaction time t, which is fixed by the length of the nonlinear crystal. The Bogoliubov transformations preserve the commutation relations, as illustrated in the following calculation.

$$[\hat{a}, \hat{a}^\dagger] = (\cosh^2(r) - \sinh^2(r))\,[\hat{a}(0), \hat{a}^\dagger(0)] \tag{2.44}$$

$$= 1 \tag{2.45}$$

The mean photon number $\langle\hat{N}\rangle$ in one mode can be inferred from the previous calculation:

$$\langle \hat{N} \rangle = \sinh^2(r) \tag{2.46}$$
$$= \frac{1}{4}\left(e^{2r} + \frac{1}{e^{2r}} - 2\right) \tag{2.47}$$

As well as the evolution of the position and momentum operators:

$$\hat{q} = \hat{a} + \hat{a}^\dagger = \hat{q}(0)\, e^{-r} \tag{2.48}$$
$$\hat{p} = i\left(\hat{a}^\dagger - \hat{a}\right) = \hat{p}(0)\, e^{r} \tag{2.49}$$

As well as the evolution of their variance:

$$\Delta^2\hat{q}(t) = \Delta^2\hat{q}(0)\, e^{-2r} \tag{2.50}$$
$$\Delta^2\hat{p}(t) = \Delta^2\hat{p}(0)\, e^{2r} \tag{2.51}$$

The parametric down conversion conserves the product of variances but affects the noise distribution in the state. As can be seen in the equations 2.50, 2.51, the noise of the $\hat{q}+$ quadrature is reduced by a factor e^{2r} while the noise of the $\hat{p}$ quadrature is increased by the same amount. In general, this reasoning applies to any orthogonal quadratures $\hat{q}_\theta$ and $\hat{q}_{\theta+\frac{\pi}{2}}$, where $\hat{q}_\theta = \hat{q}\cos(\theta) + \hat{p}\sin(\theta)$ is the general field quadrature, defined such that when $\theta = 0$, $\hat{q}_0 = \hat{q}$ and when $\theta = \frac{\pi}{2}$, $\hat{q}_{\frac{\pi}{2}} = \hat{p}$.

2.3.2 Two-Mode Squeezed States

The two-mode squeezed state (TMSS) is an entangled state [Lvovsky 14]. It is the result of the combination of two single-mode squeezed states (SMSS), one squeezed along q and the other squeezed along p, on a balanced beam splitter (BS) [Lvovsky 14]. This basis change is described mathematically by a beamsplitter operator B, such that:

$$B = \frac{1}{\sqrt{2}}\begin{pmatrix} 1 & 1 \\ -1 & 1 \end{pmatrix} \tag{2.52}$$

When, two SMSS of quadratures $\hat{q}_{a,b}$ and $\hat{p}_{a,b}$ are sent to the BS inputs the beams are partially transmitted and reflected and the quadratures $\hat{Q}_\pm$ and $\hat{P}_\pm$ of the output state read:

$$\begin{pmatrix} \hat{Q}_- \\ \hat{Q}_+ \end{pmatrix} = \frac{1}{\sqrt{2}}\begin{pmatrix} 1 & -1 \\ 1 & 1 \end{pmatrix}\begin{pmatrix} \hat{q}_a \\ \hat{q}_b \end{pmatrix} \tag{2.53}$$

$$\begin{pmatrix} \hat{P}_- \\ \hat{P}_+ \end{pmatrix} = \frac{1}{\sqrt{2}} \begin{pmatrix} 1 & -1 \\ 1 & 1 \end{pmatrix} \begin{pmatrix} \hat{p}_a \\ \hat{p}_b \end{pmatrix} \tag{2.54}$$

We can develop the previous equations to obtain the expression of the output quadratures with respect to the mode quadratures:

$$\hat{Q}_\pm = \frac{1}{\sqrt{2}} \left(\hat{q}_a \pm \hat{q}_b\right) \tag{2.55}$$

$$\hat{P}_\pm = \frac{1}{\sqrt{2}} \left(\hat{p}_a \pm \hat{p}_b\right) \tag{2.56}$$

The output state is a two-mode squeezed state. Thus, we have the following equations for $\hat{Q}_+$ and $\hat{P}_-$:

$$\Delta^2 \hat{Q}_+ = \Delta^2(\hat{q}_a + \hat{q}_b) = e^{-2r} \tag{2.57}$$

$$\Delta^2 \hat{P}_- = \Delta^2(\hat{p}_a - \hat{p}_b) = e^{-2r} \tag{2.58}$$

Which corresponds to the squeezing of a two-mode state, i.e. a bipartite entangled state [Einstein 35], which can also be generated from a PDC in a non-degenerate configuration (see chapter 6). When $r \to \infty$, $\Delta^2(q_a + q_b) \to 0$ and $\Delta^2(p_a - p_b) \to 0$ such that $q_a = -q_b$ and $p_a = p_b$. In the following section, we will present the multimode squeezed states (MMSS) corresponding to a collection of m independently single-mode squeezed states, with $m \geq 2$.

2.3.3 Multimode Squeezing

In the multimode case, the output electric field is expressed as defined in chapter 1 as the linear combination of modal electric fields $\mathbf{E}_m(\mathbf{r}, t)$. The squeezing of each mode occurs according to the same process and is described by a Bogoliubov transformation. Depending on the configurations, the modes can either share a same squeezing parameter r or display different levels of squeezing. In the second case, a parameter r_m is attached to each mode and the quadratures read similarly to the previous section:

$$\hat{q}_m(t) = \hat{q}_m(0)\, e^{r_m} \tag{2.59}$$

$$\hat{p}_m(t) = \hat{p}_m(0)\, e^{-r_m} \tag{2.60}$$

It follows the expressions of the variance:

$$\Delta^2 \hat{q}_m(t) = \Delta^2 \hat{q}_m(0)\, e^{2\,r_m} \tag{2.61}$$
$$\Delta^2 \hat{p}_m(t) = \Delta^2 \hat{p}_m(0)\, e^{-2\,r_m} \tag{2.62}$$

Experimentally, the measurement of multimode squeezed states requires to be able to separate the modes experimentally and to be able to access the modal squeezing parameters. The techniques involved in such experiment can be found in chapters 4, 6 and 5.

2.3.4 Description of Correlations with Covariance Matrices

2.3.4.1 Covariance in the Classical Domain

Correlations in a Multimode Electric Field As light propagates, the classical electric field experiences amplitude and phase fluctuations, which can be modeled by the laws of probability. In general, the field can be associated to a continuous random variable E and the modes of the field to the variables $\{\mathrm{E}_m\}$ (chapter 1), which evolution can be described with a probability density function [Ash 08, Billingsley 95]. In particular, their mean and variance can be calculated with the first and second moments of the probability distribution. The variance $\mathrm{Var}(\mathrm{E}_m) = \mathrm{V}_m$ describes the fluctuations of the field and corresponds to the expectation of the squared deviation of a field E_m from its mean $\langle \mathrm{E}_m \rangle$. It is defined as [Mood 01]:

$$\mathrm{V}_m(\mathrm{E}_m) = \langle [\mathrm{E}_m - \langle \mathrm{E}_m \rangle]^2 \rangle \tag{2.63}$$
$$= \langle \mathrm{E}_m^2 \rangle - \langle \mathrm{E}_m \rangle^2 \tag{2.64}$$

Correlations between modes E_m and E_n of the field can be revealed by calculating their covariance $\mathrm{Cov}(E_m, E_n) = \mathrm{V}_{mn}$ [Opatrný 02].

$$\mathrm{Cov}(\mathrm{E}_m, \mathrm{E}_n) = \langle\, [\mathrm{E}_m - \langle \mathrm{E}_m \rangle]\, [\mathrm{E}_n - \langle \mathrm{E}_n \rangle]\, \rangle \tag{2.65}$$
$$= \langle \mathrm{E}_m \mathrm{E}_n \rangle - \langle \mathrm{E}_m \rangle \langle \mathrm{E}_n \rangle \tag{2.66}$$

The correlation $\mathrm{Corr}(\mathrm{E}_m,\mathrm{E}_n)$ is a dimensionless coefficient obtained by dividing the covariance with the standard deviation $\sigma_m = \sqrt{V_m}$. It expresses the mutual influence of the variables.

$$\mathrm{Corr}(\mathrm{E}_m, \mathrm{E}_n) = \frac{\mathrm{Cov}(\mathrm{E}_m, \mathrm{E}_n)}{\sigma_m\, \sigma_n} \tag{2.67}$$

The existence of correlations between field modes strongly relies on the presence of fluctuations. In particular, even in absence of mean field, $\langle \mathrm{E} \rangle = 0$, the fluctuations alone

can generate correlations. In the remaining of the manuscript, we will refer equally to covariance and correlations.

Correlations between Field Quadratures The electric field can be described in terms of its quadratures corresponding to the real and imaginary parts of the field in the complex plane. Thus, any fluctuations of the field corresponds to fluctuations of the quadratures, which can be described with the equations defined in the previous section.

2.3.4.2 Correlations in the Quantum Domain

In the quantum domain, the electric field is a linear combination of complex modes with quadratures $\hat{q}_m$ and $\hat{p}_m$ (chapter 2). The variance of the measured quadratures describe their fluctuations and can be labeled $\Delta^2 q_m$ or V_m^q for the q quadrature and similar for p. The notation $\mathrm{V}_m^q = \langle \hat{q}_m^2 \rangle$ can be used in the particular case of vacuum where $\langle \hat{q}_m \rangle = 0$. The covariance V_{mn} between modes can be represented in a matrix. Let us define a quadrature vector $\hat{\mathbf{Q}}^{\mathbf{T}} = [\hat{\mathbf{q}}_{\mathbf{1}}, ..., \hat{\mathbf{q}}_{\mathbf{m}}, \hat{\mathbf{p}}_{\mathbf{1}}, ..., \hat{\mathbf{p}}_{\mathbf{m}}]$ containing $2N$ elements such that the covariance matrix $\mathbf{V} = \frac{1}{2} \langle \hat{\mathbf{Q}} \hat{\mathbf{Q}}^{\mathbf{T}} \rangle^{\mathbf{T}}$. It is a $2N \times 2N$ real and positive semi-definite matrix composed of four blocks.

$$\mathbf{V} = \begin{bmatrix} \mathbf{V}^{\mathbf{q}} & \mathbf{V}^{\mathbf{qp}} \\ \left(\mathbf{V}^{\mathbf{qp}}\right)^T & \mathbf{V}^{\mathbf{p}} \end{bmatrix} \tag{2.68}$$

Where the diagonal elements of each block $\mathbf{V}^{\mathbf{j}}$ of the matrix are the quadratures variances while the off-diagonal elements are the covariances between $\hat{q}$ quadratures, $\hat{p}$ quadratures and between $\hat{q}$ and $\hat{p}$. The expression of the covariance in the quantum case is symmetric for quadratures. For $\hat{q}_m$ and $\hat{q}_n$, it reads:

$$\mathrm{V}_{mn}^q = \frac{\langle (\hat{q}_m - \langle \hat{q}_m \rangle)(\hat{q}_n - \langle \hat{q}_n \rangle) \rangle + \langle (\hat{q}_n - \langle \hat{q}_n \rangle)(\hat{q}_m - \langle \hat{q}_m \rangle) \rangle}{2} \tag{2.69}$$

$$= \frac{1}{2} \langle \{\hat{q}_m, \hat{q}_n\} \rangle - \langle \hat{q}_m \rangle \langle \hat{q}_n \rangle \tag{2.70}$$

Where $\{\hat{q}_m, \hat{q}_n\} = \hat{q}_m \hat{q}_n + \hat{q}_n \hat{q}_m$ is the anticommutator of $\hat{q}_m$ and $\hat{q}_n$. Similar expressions can be written for the elements of $\mathbf{V}^{\mathbf{p}}$ and $\mathbf{V}^{\mathbf{qp}}$.

2.3.5 Schmidt Decomposition

In chapter 3, we will derive the hamiltonian of the PDC process in the non-degenerate condition, i.e. when the signal and idler channels are distinguishable, as:

$$\hat{H}_{int} = \mathcal{K} \int d\omega_s d\omega_i \, \Phi(\omega_s, \omega_i) \, \hat{a}_s^\dagger \, \hat{a}_i^\dagger + h.c. \tag{2.71}$$

Where $\mathcal{K}$ is a constant defined in equation 3.72. We can simplify this expression via a Schmidt decomposition. The Schmidt decomposition was introduced in 1957 by Hugh Everett to describe the decomposition of a bipartite quantum system [Everett 57]. In particular, for parametric down conversion (PDC), it is used to decompose the joint spectral amplitude (JSA) $\Phi(\omega_s, \omega_i)$, which contains the correlations between the generated photons (see chapter 3). In the general form, the Schmidt decomposition involves two sets of basis functions $\{g_k\}$ and $\{h_k\}$ sharing pairwise correlations [Brecht 14, Roman-Rodriguez 20]:

$$\Phi(\omega_s, \omega_i) = \sum_k \lambda_k \, g_k(\omega_s) \, h_k(\omega_i) \tag{2.72}$$

Where the Schmidt coefficients λ_k are real, non-negative and respect the normalization condition $\sum_k \lambda_k^2 = 1$. Then, we can define *broadband* operators corresponding to the signal and idler photons of the PDC:

$$\hat{c}_k^\dagger = \int d\omega_s \, g_k(\omega_s) \, \hat{a}_s^\dagger \tag{2.73}$$

$$\hat{d}_k^\dagger = \int d\omega_i \, h_k(\omega_i) \, \hat{a}_i^\dagger \tag{2.74}$$

And the hamiltonian can be written as:

$$\hat{H}_{int} = \mathcal{K} \sum_k \lambda_k \, \hat{c}_k^\dagger \, \hat{d}_k^\dagger \, + \, h.c. \tag{2.75}$$

This is the hamiltonian associated to the generation of a two-mode-squeezed state. The functions g_k and h_k are defined as the Schmidt mode functions of the signal and idler photons respectively and the squared Schmidt coefficient λ_k^2 corresponds to the probability to generate a particular pair k of biphoton state. We will see that in our case, g_k and h_k can be approximated by Hermite-Gaussian functions (section 1.2.2). The Schmidt decomposition gives an additional parameter K, called the Schmidt number or cooperativity [Christ 11, Brecht 14], given by:

$$\mathrm{K} = \frac{1}{\sum_j \lambda_j^4} \tag{2.76}$$

which corresponds to the number of entangled modes generated by the PDC. The hamiltonian above indicates that in the Schmidt mode basis, the generated state is a collection of TMSS, one for each pair of Schmidt modes.

2.3.6 Bloch-Messiah Decomposition

The Schmidt decomposition is useful to give a compact description of the parametric process in the non-degenerate case as a collection of two-mode-squeezed states (TMSS). Moreover, we saw in section 2.3.2, that a beamsplitter allows to perform a basis change from two squeezed states to an entangled state and vice versa. Thus, it is possible to express the states generated by the PDC as a set of squeezed states. This is called the Bloch-Messiah (BM) decomposition [Braunstein 05] and we will see in section 2.3.7 that it is linked to the Schmidt decomposition by a beamsplitter transformation. We discretize $\Phi(\omega_{s\ell}, \omega_{im})$ of equation 2.71 so we obtain a discretized hamiltonian such that:

$$\hat{H}_{int} = \sum_{\ell,m} \Phi(\omega_{s\ell}, \omega_{im})\, \hat{a}^\dagger_\ell \hat{a}^\dagger_m \; + \; h.c. \tag{2.77}$$

We can write $\hat{\mathbf{Q}}^T = [\hat{q}_1, ..., \hat{q}_m, \hat{p}_1, ..., \hat{p}_m]$ the quadratures operators associated with the annihilation and creation operators at different frequencies as it was done in the single mode case in the equations 2.48 and 2.49. The transformation of the quadratures can be written in a compact form as $\hat{\mathbf{Q}}_{\mathbf{out}} = \mathbf{S}\, \hat{\mathbf{Q}}_{\mathbf{in}}$, where $\mathbf{S}$ is a symplectic matrix, which conserves the commutation relations [Fabre 20]. $\mathbf{S}$ can be decomposed with a Bloch-Messiah reduction as:

$$\mathbf{S} = \mathbf{R_1}\, \mathbf{\Delta^{sq}}\, \mathbf{R_2^\dagger} \tag{2.78}$$

Where $\mathbf{R_1}$ and $\mathbf{R_2}$ are orthogonal matrices describing a basis change, i.e. linear optics transformations and $\mathbf{\Delta^{sq}}$ is a squeezing matrix. It is diagonal and defined as $\mathbf{\Delta^{sq}} = \{\mathbf{e}^{\mathrm{r}_1}, \mathbf{e}^{\mathrm{r}_2}, ...\mathbf{e}^{-\mathrm{r}_1}, \mathbf{e}^{-\mathrm{r}_2}...\}$.

If the input modes $\mathbf{Q_{in}}$ are in the vacuum state, then $\mathbf{R_2}$ can be ignored and $\mathbf{R_1}$ defines the basis change between the basis of the Schmidt modes and the squeezed-modes basis. This basis change allows to write the equation 2.77 in a diagonal form:

$$\hat{H}_{int} = \sum_i g_i\, (\hat{s}^\dagger_i)^2 \; + \; h.c. \tag{2.79}$$

Where $\{\hat{s}^\dagger_i\}$ are the creation operators of the squeezed modes and $\{g_i\}$ are the squeezing eigenvalues defined as $g_i = \dfrac{\hbar}{2\,t}\, r_i$, with t the interaction time. As in section 2.3.1, we can remove the interaction time, which is fixed by the length of the nonlinear crystal. We define the vectors $\hat{\mathbf{s}} = [\hat{s}_1, ..., \hat{s}_m, \hat{s}^\dagger_1, ..., \hat{s}^\dagger_m]^T$ for the operators associated to the squeezed modes and $\hat{\mathbf{a}} = [\hat{a}_1, ..., \hat{a}_m, \hat{a}^\dagger_1, ..., \hat{a}^\dagger_m]^T$ for the operators associated to plane waves. They are linked by:

$$\hat{\mathbf{s}}^\dagger = U \hat{\mathbf{a}}^\dagger \tag{2.80}$$

U can be defined as: $U = X + iY$ where X and Y come from the block form of the matrix $\mathbf{R_1}$ defined as:

$$\mathbf{R}_1 = \begin{pmatrix} X & Y \\ -Y & X \end{pmatrix} \tag{2.81}$$

The matrix U also gives the squeezed modes $S_k(\omega)$ defined as a combination of plane-wave components:

$$S_k(\omega) = \sum_i U_{ki}\, g_i(\omega) \tag{2.82}$$

The covariance matrix 2.68 is related to the symplectic matrix $\mathbf{S}$ by

$$\mathbf{V} = \frac{1}{2}\,\mathbf{S}\mathbf{S}^T \tag{2.83}$$

And in the basis of the annihilation operators $\hat{s}$, it is diagonal and reads:

$$\mathbf{V} = \frac{1}{2}\,(\mathbf{\Delta^{sq}})^2 \tag{2.84}$$

2.3.7 Relation between Schmidt and Squeezed Modes

To find the relation between the Schmidt and Bloch-Messiah decompositions we compare the equations 2.75 and 2.79. We have the following identity [Horoshko 19]:

$$\exp\left[r_k\left(\hat{c}_k^\dagger \hat{d}_k^\dagger\right) + h.c.\right] = \exp\left[\frac{r_k}{2}\left(\hat{s}_{k+}^\dagger\right)^2 + h.c.\right] \times \exp\left[\frac{r_k}{2}\left(\hat{s}_{k-}^\dagger\right)^2 + h.c.\right] \tag{2.85}$$

When,

$$\hat{s}_{k\pm}^\dagger = \frac{\hat{c}_k^\dagger \pm \hat{d}_k^\dagger}{\sqrt{2}} \tag{2.86}$$

If $g_i = \dfrac{\lambda_i}{2}$, we can write equation 2.79 by appliying the basis change defined in equation 2.86 to the equation 2.75 [Patera 09, Patera 12]. This corresponds to a beam splitter operation. Moreover, the squeezed modes S_k can be derived from the Schmidt modes as follows:

$$S_{k,\pm}(\omega) = \frac{1}{\sqrt{2}}\,(g_k(\omega) \pm h_k(\omega)) \tag{2.87}$$

Finally, the squeezing parameters are linked to the Schmidt coefficients by:

$$r_i = \lambda_i \frac{t}{\hbar} \tag{2.88}$$

It is possible to include the integration time t and the $\hbar$ constant in the definition of the Schmidt coefficients, such that:

$$r_i = \lambda_i \tag{2.89}$$

Part II

Generation and Characterization of Ultrafast Multimode Squeezed Light

Chapter 3

Spontaneous Parametric Down Conversion of Ultrafast Light

Contents

3.1 Birefringence . . . 44
3.2 Index Ellipsoid . . . 45
3.3 Sellmeier's Equations . . . 46
3.3.1 Influence of the Temperature . . . 48
3.4 Polarization in a Nonlinear Medium . . . 49
3.4.1 Electric Susceptibility . . . 49
3.4.2 Kleinman Symmetry . . . 51
3.5 Building the Parametric Process . . . 52
3.5.1 Coupled-Wave Equations . . . 54
3.5.2 Interaction Hamiltonian . . . 57
3.5.3 PDC Phase-Matchings . . . 59

Spontaneous parametric down conversion (SPDC) is a nonlinear process occurring in birefringent media featuring a significant second-order susceptibility $\chi^{(2)}$, such as Beta-Barium Borate (BBO), Bismuth Borate (BiBO), Potassium titanyl phosphate (KTP) or Lithium Niobate (LN) [Klyshko 69, Harris 67]. This process converts a photon of energy $\hbar\omega_p$ from an intense pump beam into two photons called signal and idler of lower energy $\hbar\omega_s$ and $\hbar\omega_i$ respectively, according to energy conservation $\hbar\omega_p = \hbar\omega_s + \hbar\omega_i$. The generation of the biphoton also respects momentum conservation, referred to as phase-matching (PM) $\vec{k}_p = \vec{k}_s + \vec{k}_i$. SPDC is a popular nonlinear process used to generate single photons [Mosley 07], pairs of entangled photons [Hong 86] or in our case quadrature-squeezed light. In this chapter, we will present the tools necessary to design an experiment of generation of multimode squeezed states of light, starting with the study of the nonlinear media we used in our experiment, i.e. the BBO and the KTP (section 3.1 to 3.3). Then, we will describe the evolution of the light field inside

a nonlinear medium as well as the evolution of the amplitudes of the fields involved in the PDC process, i.e. the pump, signal and idler (section 3.5.1). Afterward, we will use the quantum-optics formalism to describe the same process and write the Hamiltonian associated to it (section 3.5.2). Finally, in section 3.5.3, we will focus on the different types of phase-matching and their influence on the down-converted light.

3.1 Birefringence

In chapter 1, we wrote the expression of the electric field 1.1. Let us first consider a monomode field, which we recall the expression:

$$\mathbf{E}(\vec{r},t) = A(\vec{r},t)\,\vec{\epsilon}\,e^{-i(\omega_0 t - \vec{k}\cdot\vec{r})} + c.c. \tag{3.1}$$

Where $\vec{\epsilon}$ indicates the direction of the field polarization, *c.c.* denotes the complex conjugate and $A(\vec{r},t)$ is the amplitude of the field. Light propagation is impacted by the properties of the medium. Isotropic media are characterized by a unique refractive index $n(\lambda)$ depending on the wavelength of the light. The light path inside the medium involves refraction and absorption due to this index. On the contrary, birefringent materials are anisotropic, i.e. their refractive index $n(\lambda)$ experienced by the light in the medium depends on its polarization. We distinguish uniaxial and biaxial crystals. Uniaxial crystals are characterized by a main axis called the *optical axis* $\vec{k} = o\vec{a}$. Light polarized along the optical axis experiences a wavelength-dependent refractive index $n_e(\lambda)$ called the *extraordinary* index. Light polarized along a direction orthogonal to the optical axis experiences a refractive index $n_o(\lambda)$ called the *ordinary* index because no birefringent phenomenon occurs. The birefringence is defined as [Bragg 53]:

$$b(\lambda) = n_e(\lambda) - n_o(\lambda) \tag{3.2}$$

which can be either positive or negative. One consequence of birefringence is double refraction of light, when light energy is distributed between two polarizations components, one part traveling along the ordinary direction and the other along the extraordinary one [Boyd 08]. Biaxial crystals have two optical axes and are characterized by three refractive indices n_x, n_y and n_z corresponding to the three principal axes of the crystal. They are referred to as *fast* and *slow* indices, the smallest being the fastest as light travels faster in low-index materials such as air. Parametric down conversion is often performed in bulk crystals such as BBO, KTP or LN [Vitelli 13, Harder 13, Christ 09]. In the experiment described in chapter 6, we used a bulk BBO crystal, which is negative uniaxial, to generate two-mode squeezed states of light in a non-collinear configuration. The design of this experiment involved the study of BBO properties, in particular the evolution of the refractive index with the direction of propagation of the pump beam.

This can be done using an index ellipsoid discussed in the next section. We also studied the properties of the KTP, which is a biaxial material, for the development of a waveguide-based PDC experiment.

3.2 Index Ellipsoid

The index ellipsoid (fig. 3.1) describes the dependence between the polarization and the refractive index $n(\lambda)$ experienced by the light. In the case of an uniaxial crystal described in section 3.1, according to its polarization, the light propagates in a medium of refractive index $n(\lambda, \theta)$, which is a function of n_e and n_o. The corresponding index ellipsoid reads:

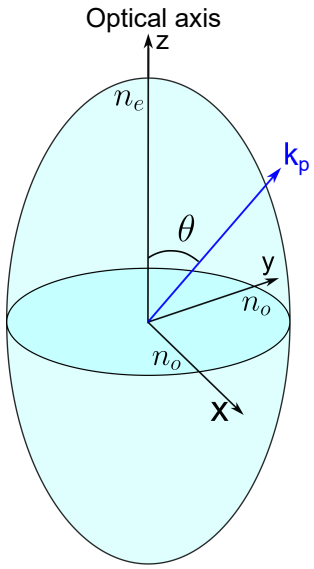

Figure 3.1 – Schematic of the index ellipsoid of an uniaxial crystal.

$$\frac{n_x^2 + n_y^2}{n_o^2} + \frac{n_z^2}{n_e^2} = 1 \tag{3.3}$$

Where n_x and n_y are the projections on the axis of length n_o of the ellipsoid and n_z the projection on the axis of length n_e. For a given wavelength λ_0, let us consider a light beam propagating with an angle θ with respect to the optical axis as illustrated in the figure 3.1. For example, when $\theta = \frac{\pi}{2}$, the beam propagates along the x direction and the corresponding ellipse is in the plane (y, z) orthogonal to the direction of propagation. In the general case, the equation of the ellipse reads:

$$\frac{n^2(\theta)\,\cos^2(\theta)}{n_o^2} + \frac{n^2(\theta)\,\sin^2(\theta)}{n_e^2} = 1 \tag{3.4}$$

from which the expression of $n(\theta)$ can be inferred:

$$\frac{1}{n(\theta)^2} = \frac{\cos(\theta)^2}{n_o^2} + \frac{\sin(\theta)^2}{n_e^2} \tag{3.5}$$

Considering the central wavelength $\lambda_0 = 795$ nm of our laser and the phase-matching of the PDC, this angle is $\theta = 29.62°$ in BBO.

In biaxial crystals, the index ellipsoid reads:

$$\frac{x^2}{n_x^2} + \frac{y^2}{n_y^2} + \frac{z^2}{n_z^2} = 1 \tag{3.6}$$

Where the refractive indices, as well as those of the BBO, can be calculated with the Sellmeier's equations. This will be the subject of the following section.

3.3 Sellmeier's Equations

The Sellmeier's equations are empirical relations between wavelength and the index of refraction of a medium [Sellmeier 72]. In the most general form, they are defined as:

$$n^2(\lambda) = 1 + \sum_i \frac{A_i\,\lambda^2}{\lambda^2 - B_i^2} \tag{3.7}$$

Where $\{A_i\}$ and $\{B_i\}$ are the Sellmeier coefficients, usually expressed in μm and obtained experimentally. Therefore, the function $n(\lambda)$ is an approximation of the evolution of the refractive index and its expression differs depending on the material under consideration. For the BBO, we used the coefficients measured at 20°C from [Eimerl 87]:

$$n_o^2(\lambda) = 2.7405 + \frac{0.0184}{\lambda^2 - 0.0179} - 0.0155\lambda^2 \tag{3.8}$$

$$n_e^2(\lambda) = 2.3730 + \frac{0.0128}{\lambda^2 - 0.0156} - 0.0044\lambda^2 \tag{3.9}$$

These refractive indices are valid for wavelengths between 212.8 nm and 1064 nm. For the KTP, we used the equations from [Kato 02]:

$$n_x^2 = 3.29100 + \frac{0.04140}{\lambda^2 - 0.03978} + \frac{9.35522}{\lambda^2 - 31.45571} \tag{3.10}$$

$$n_y^2 = 3.45018 + \frac{0.04341}{\lambda^2 - 0.04597} + \frac{16.98825}{\lambda^2 - 39.43799} \tag{3.11}$$

$$n_z^2 = 4.59423 + \frac{0.06206}{\lambda^2 - 0.04763} + \frac{110.80672}{\lambda^2 - 86.12171} \tag{3.12}$$

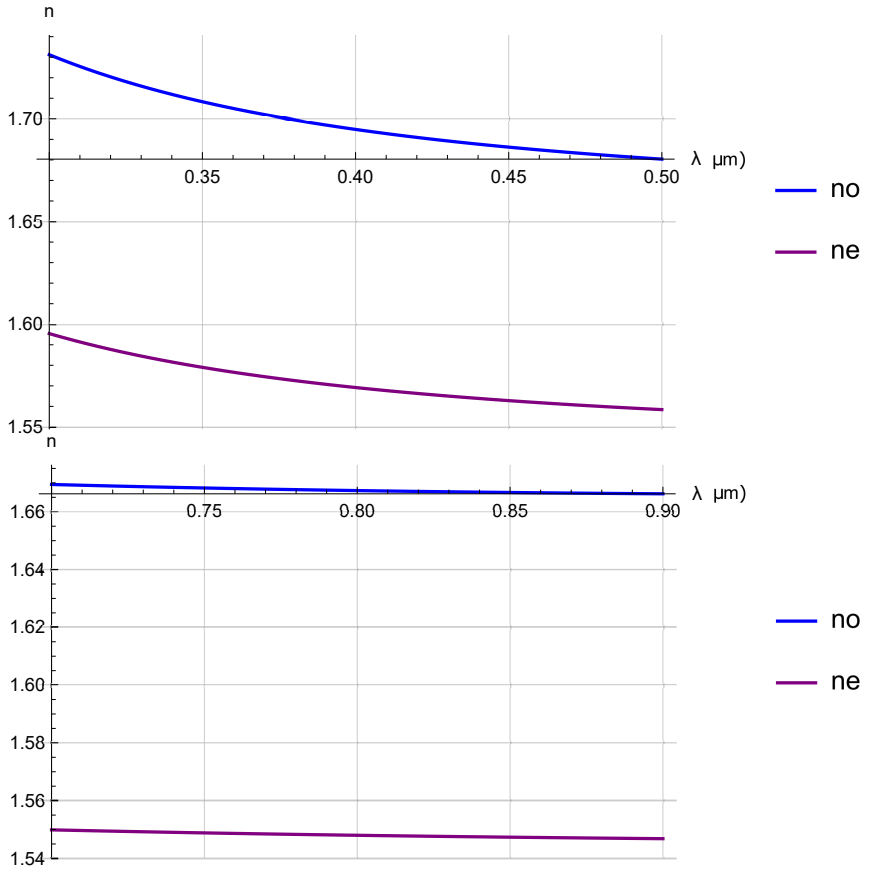

Figure 3.2 – Evolution of the refractive indices in BBO according to the wavelength. Top: for the pump light of a PDC process; Bottom: for the signal light.

Where the coefficients were also measured at 20°C. These refractive indices are valid for wavelengths between 430 nm and 3.54 μm. The figures 3.2 and 3.3 show the indices of the BBO and the KTP around two different wavelengths, the one of our laser at 795 nm and its second harmonic at 397.5 nm.

We plotted the refractive indices over a 200-nm range and we see that depending on the wavelength range, the evolution of $n(\lambda)$ is not the same on the two plots as well as the discrepancy between the indices. In addition, the material properties can vary with the temperature, a parameter not taken into consideration in equations 3.8 to 3.12. In the next section, we will consider the influence of temperature variation on the refractive index.

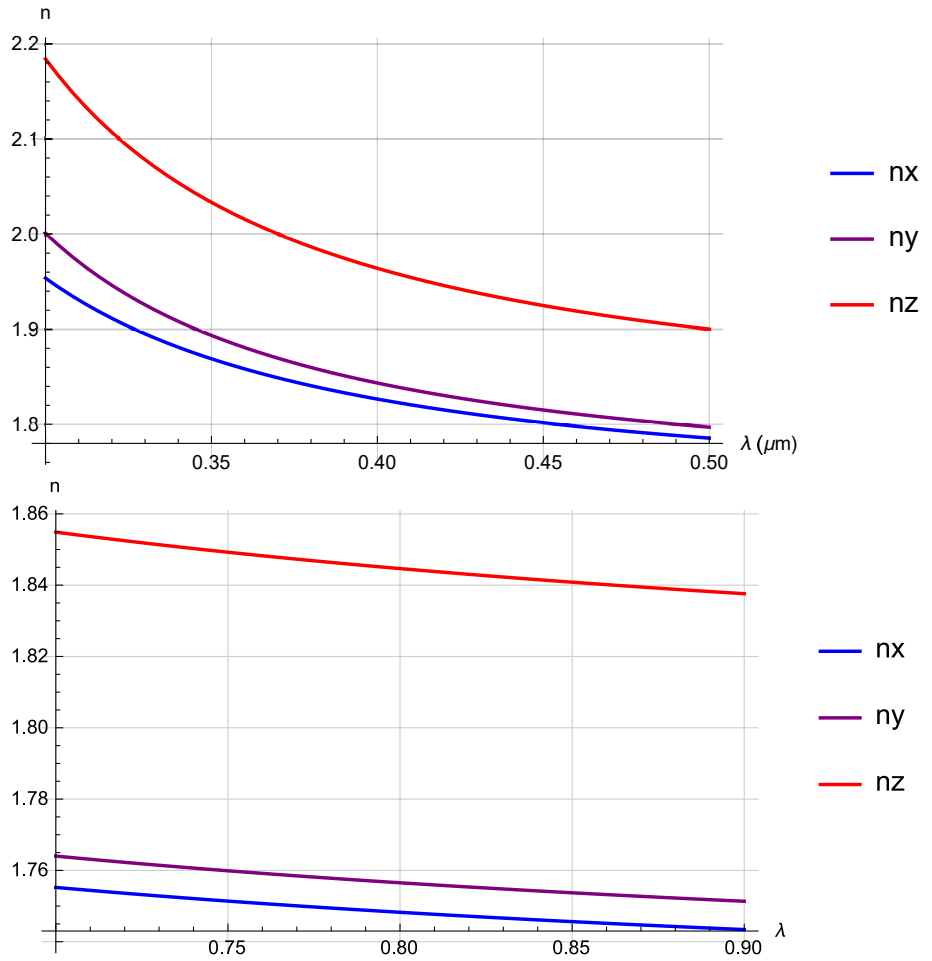

Figure 3.3 – Evolution of the refractive indices in KTP according to the wavelength. Top: for the pump light of a PDC process; Bottom: for the signal light.

3.3.1 Influence of the Temperature

The influence of the temperature on the refractive index is estimated experimentally at several temperatures between 20°C and 80°C. For the BBO, the obtained values are called thermo-optic coefficients. They are similar in the [400,1014] nm range, so the authors of [Eimerl 87] worked with the following averaged values:

$$\frac{dn_o}{dT} = -16.6 \times 10^{-6}\ (^\circ\mathrm{C})^{-1} \tag{3.13}$$

$$\frac{dn_e}{dT} = -9.3 \times 10^{-6}\ (^\circ\mathrm{C})^{-1} \tag{3.14}$$

For the KTP, we used the thermo-optic dispersion formulas from [Kato 02]:

$$\frac{\partial n_x}{\partial T} = \left(\frac{0.1717}{\lambda^3} - \frac{0.5353}{\lambda^2} + \frac{0.8416}{\lambda} - 0.1627\right) \times 10^{-5} \tag{3.15}$$

$$\frac{\partial n_y}{\partial T} = \left(\frac{0.1997}{\lambda^3} - \frac{0.4063}{\lambda^2} + \frac{0.5154}{\lambda} + 0.5425\right) \times 10^{-5} \tag{3.16}$$

$$\frac{\partial n_z}{\partial T} = \left(\frac{0.9221}{\lambda^3} - \frac{2.9220}{\lambda^2} + \frac{3.6677}{\lambda} - 0.1897\right) \times 10^{-5} \tag{3.17}$$

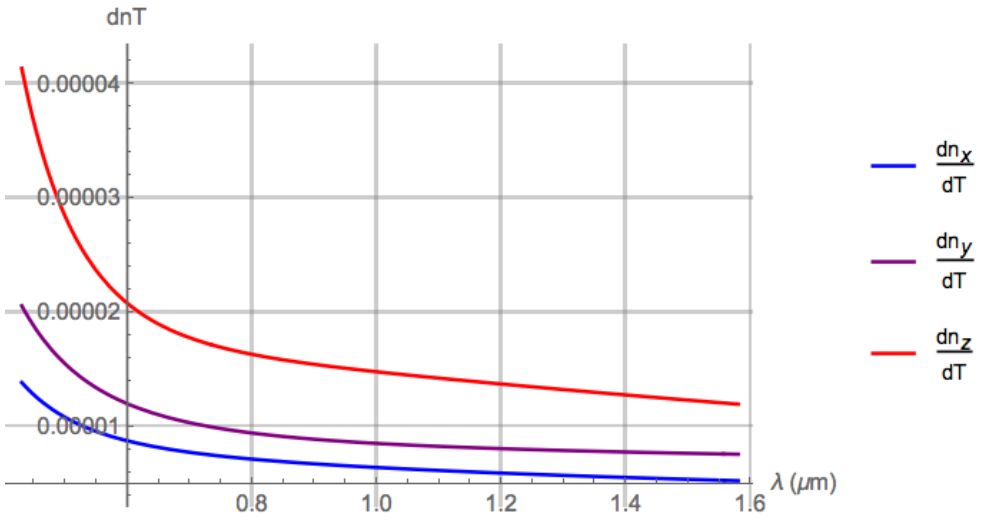

Figure 3.4 – Thermo-optic dispersion in potassium titanyl phosphate (KTP).

We can see from the equations 3.13 and 3.14 and from the plots of figure 3.4, that the thermo-optic coefficients are very small. Thus, it is possible to add the influence of the temperature to the evolution of the refractive indices in the form of a first-order perturbation, such that the refractive index function $n(\lambda, T)$ reads:

$$n_i(\lambda, T) = n_i(\lambda) + (T - T_0)\frac{\partial n_i}{\partial T}(\lambda, T_0), \quad i \in \{x, y, z\} \tag{3.18}$$

Where $T_0 = 20°\text{C}$ is the reference temperature.

3.4 Polarization in a Nonlinear Medium

3.4.1 Electric Susceptibility

Let us introduce the electric displacement $\mathbf{D}$:

$$\mathbf{D}(\omega) = \epsilon_0 \mathbf{E}(\omega) + \mathbf{P}(\omega) \tag{3.19}$$

Where bold notations designate vector quantities and $\epsilon_0 = 8.854 \times 10^{-12}$ F.m^{-1} is the vacuum permittivity. $\mathbf{P}(\omega)$ is the electric polarization defined as the density of electric dipole moments in a material in the presence of an electric field. In linear media, the vectors $\mathbf{E}$, $\mathbf{P}$ and $\mathbf{D}$ are parallel. We have:

$$\mathbf{P}(\omega) = \epsilon_0 \, \chi^{(1)}(\omega) \, \mathbf{E}(\omega) \tag{3.20}$$

where $\chi(\omega)$ is the electric susceptibility. It may take complex values and it is frequency dependent. It is related to the permittivity of the medium ϵ_r, i.e. its refractive index $\epsilon_r(\omega) = n^2(\omega)$:

$$\epsilon_r(\omega) = n^2(\omega) = 1 + \mathrm{Re}[\chi^{(1)}(\omega)] \tag{3.21}$$

Giving another expression of the electric displacement field:

$$\mathbf{D}(\omega) = \epsilon_0 \, \epsilon_r \, \mathbf{E}(\omega) \tag{3.22}$$

In nonlinear media, the electric field is not always parallel to the polarization but the electric displacement remains parallel to the polarization and orthogonal to the direction of propagation of the light. The polarization evolves as a power function of the electric field. In most cases, nonlinear interactions involve fields with frequencies much lower than the resonance frequency of the medium. Consequently, the nonlinear susceptibility is mostly independent of frequency and in particular, it is approximately constant over the spectrum of the input light. The Taylor expansion of the polarization reveals the combination of a linear component $\mathrm{P}^{(L)}$, defined in equation 3.20 and a nonlinear part $\mathrm{P}^{(NL)}$ comprising higher-order susceptibilities:

$$\mathbf{P}(\omega) = \mathbf{P}^{(L)}(\omega) + \mathbf{P}^{(NL)}(\omega) \tag{3.23}$$

With,

$$\mathbf{P}^{(NL)}(\omega) = \epsilon_0 \chi^{(2)}(\omega) \mathbf{E}^2(\omega) + \epsilon_0 \chi^{(3)}(\omega) \mathbf{E}^3(\omega) + ... \tag{3.24}$$

Where $\chi^{(2)}(\omega)$ is a second-order tensor and $\chi^{(3)}(\omega)$ is a third-order tensor, with $\chi^{(3)} \ll \chi^{(2)} \ll \chi^{(1)}$. The nonlinear polarization is added to the electric displacement field, modifying the equation 3.22 as follows:

$$\mathbf{D}(\omega) = \epsilon_0 \, \epsilon_r \, \mathbf{E}(\omega) \; + \; \mathbf{P}^{(NL)}(\omega) \tag{3.25}$$

Nonlinear processes occur in centrosymmetric or non-centrosymmetric media. The first ones possess a center of symmetry inversion. When an electric field is applied to

the medium, its atomic structure feels a polarization to which it responds by a restoring force. The associated potential energy presents the symmetry $\mathrm{U}(x) = \mathrm{U}(-x)$, with x being the electron displacement in the atom. In these materials, the lowest-order nonlinearity is $\chi^{(3)}$ ($\chi^{(2)} = 0$). Four-wave mixing (FWM) processes occur preferably in centrosymmetric media [Owyoung 71]. In non-centrosymmetric media, the potential energy is not symmetric and contains even and odds powers of the displacement. Therefore, susceptibilities of all orders are present, with $\chi^{(2)}$ being the strongest. These materials support three-wave mixing processes such as parametric down conversion (PDC), second-harmonic generation (SHG) or difference-frequency generation (DFG) [Boyd 08], which are the processes we are interested in.

3.4.2 Kleinman Symmetry

In the previous section, we mentioned that nonlinear processes involve frequencies much lower than the resonance of the media. For that reason, we can consider that the susceptibility does not depend on the frequency. For a nonlinear process involving the interaction of three waves, such as second-harmonic generation (SHG) or parametric down conversion (PDC), the components of the second-order susceptibility are labeled $\chi^{(2)}_{ijk}$, where i, j and k refer to the polarization of the pump, the signal and the idler respectively. Therefore, i, j and k can be x, y or z. Moreover, $\chi^{(2)}$ displays symmetries because of which the susceptibility remains unchanged when the indices i, j and k, especially the two last ones, are permuted. We also place ourselves in the case of a lossless medium, i.e. when there is no exchange of energy between the interacting fields and the medium, so the components of the nonlinear susceptibility are real. The permutation of the last two indices allows to use a contracted notation of the $\chi^{(2)}$ elements according to the following table:

$$\begin{array}{cccccccc} jk: & 11 & 22 & 33 & 23,32 & 31,13 & 12,21 \\ \ell: & 1 & 2 & 3 & 4 & 5 & 6 \end{array} \tag{3.26}$$

And to introduce the nonlinear coefficient $d_{i\ell}$ defined by:

$$d_{i\ell} = \frac{1}{2}\,\chi^{(2)}_{ijk} \tag{3.27}$$

Where i still refers to the pump polarization and ℓ is a function of the indices j and k. The nonlinear coefficients for a nonlinear material can be gathered in a matrix d as presented below for the BBO:

$$d_{BBO} = \begin{bmatrix} 0 & 0 & 0 & 0 & d_{15} & d_{16} \\ d_{21} & d_{22} & 0 & d_{24} & 0 & 0 \\ d_{31} & d_{32} & d_{33} & 0 & 0 & 0 \end{bmatrix} \tag{3.28}$$

$$= \begin{bmatrix} 0 & 0 & 0 & 0 & 0.08 & 2.2 \\ 2.2 & -2.2 & 0 & 0.08 & 0 & 0 \\ 0.08 & 0.08 & d_{33} & 0 & 0 & 0 \end{bmatrix} \tag{3.29}$$

Where each coefficient, expressed in pm/V corresponds to a different phase-matching. For example, the type-I phase-matching, with a pump vertically polarized and signal and idler horizontally polarized, corresponds to the coefficient $d_{21} = 2.2$ pm/V. This matrix was given in [Eckardt 90], in which the coefficient d_{33} had not be estimated. For the KTP, the matrix on the nonlinear coefficients reads [Pack 04, Brecht 14]:

$$d_{KTP} = \begin{bmatrix} 0 & 0 & 0 & 0 & d_{15} & 0 \\ 0 & 0 & 0 & d_{24} & 0 & 0 \\ d_{31} & d_{32} & d_{33} & 0 & 0 & 0 \end{bmatrix} \tag{3.30}$$

$$= \begin{bmatrix} 0 & 0 & 0 & 0 & 1.95 & 0 \\ 0 & 0 & 0 & 3.9 & 0 & 0 \\ 1.95 & 3.9 & 15.3 & 0 & 0 & 0 \end{bmatrix} \tag{3.31}$$

We notice that the strongest interaction is achieved for $d_{i\ell} = d_{33} = 15.3$ pm/V. It corresponds to a type-0 phase-matching, where pump, signal and idler beams share the same polarization, along the z direction. This phase-matching cannot be achieved in a bulk birefringent material and is only encountered when quasi-phase-matching, described in section 3.5.3.3, is performed.

3.5 Building the Parametric Process

Let us describe the evolution of the electric field in a nonlinear medium. From now on, we will replace the polarization vector $\vec{\epsilon}$ by the indices i, j and k from section 3.4.2 in the equation 3.1. The electric field can also be defined as the Fourier transform of a field $E(\mathbf{r}, \omega)$:

$$E(\mathbf{r}, t) = \int \frac{d\omega}{\sqrt{2\pi}} E(\mathbf{r}, \omega) e^{i\omega t} + c.c. \tag{3.32}$$

$$= \int \frac{d\omega}{\sqrt{2\pi}} A(\omega) e^{i\omega t + i\mathbf{k}\cdot\mathbf{r}} + c.c. \tag{3.33}$$

If we consider three fields, pump E_i, signal E_j and idler E_k, where i, j and k denote their directions in the Cartesian frame, the nonlinear polarization associated to their interaction reads:

$$P_i(\omega) = \epsilon_0 \int d\omega_m \, \chi^{(2)}_{ijk} \, E_j(\omega_m) \, E_k(\omega - \omega_m) \tag{3.34}$$

$$= 2\,\epsilon_0 \int d\omega_m \, d_{i\ell} \, E_j(\omega_m) \, E_k(\omega - \omega_m) \tag{3.35}$$

where $\chi^{(2)}_{ijk}$ is the nonlinear susceptibility linked to the nonlinear coefficient $d_{i\ell}$ by the equation 3.27, with ℓ being a contracted notation of the indices j, k. Finally, ω, ω_m and $\omega_n = \omega - \omega_m$ are the angular frequencies involved in the nonlinear process defined according to the energy conservation $\omega = \omega_p = \omega_m + \omega_n$.

Let us now consider the different processes, which can occur in the nonlinear medium, e.g. the KTP, according to the polarization of the pump. We use the Kleinman matrix d_{KTP} (eq. 3.31) for the KTP. We write the derivatives $\delta P_j(\omega)$ for a set of frequencies ω_p, ω_m, $\omega_n = \omega - \omega_m$:

$$\begin{bmatrix} \delta P_x(\omega_m,\omega_n) \\ \delta P_y(\omega_m,\omega_n) \\ \delta P_z(\omega_m,\omega_n) \end{bmatrix} = 4 \begin{bmatrix} 0 & 0 & 0 & 0 & d_{15} & 0 \\ 0 & 0 & 0 & d_{24} & 0 & 0 \\ d_{31} & d_{32} & d_{33} & 0 & 0 & 0 \end{bmatrix} \begin{bmatrix} E_x(\omega_m)E_x(\omega_n) \\ E_y(\omega_m)E_y(\omega_n) \\ E_z(\omega_m)E_z(\omega_n) \\ E_y(\omega_m)E_z(\omega_n) + E_y(\omega_n)E_z(\omega_m) \\ E_x(\omega_m)E_z(\omega_n) + E_x(\omega_n)E_z(\omega_m) \\ E_x(\omega_m)E_y(\omega_n) + E_x(\omega_n)E_y(\omega_m) \end{bmatrix} \tag{3.36}$$

Which we develop to get:

$$\delta P_x(\omega_m,\omega_n) = 4\,d_{15}\,\{E_x(\omega_m)E_z(\omega_n) + E_x(\omega_n)E_z(\omega_m)\} \tag{3.37}$$

$$\delta P_y(\omega_m,\omega_n) = 4\,d_{24}\,\{E_y(\omega_m)E_z(\omega_n) + E_y(\omega_n)E_z(\omega_m)\} \tag{3.38}$$

$$\delta P_z(\omega_m,\omega_n) = 4\,\{d_{31}\,E_x(\omega_m)E_x(\omega_n) + d_{32}\,E_y(\omega_m)E_y(\omega_n) + d_{33}\,E_z(\omega_m)E_z(\omega_n)\} \tag{3.39}$$

When the pump is polarized along the x or y direction, it means that it experiences the refractive indices n_x or n_y of the KTP crystal. The signal and idler photons are generated with orthogonal polarization: this is called type-II phase-matching. On the contrary, when the pump polarization is aligned with the z direction, it experiences the n_z index of the KTP and the generated signal and idler share the same polarization.

In the latter case, we can distinguish two configurations: the type-I phase-matching, when the signal/idler polarization is orthogonal to the one of the pump and the type-0 phase-matching, when all three waves share the same polarization. All phase-matching configurations are associated to a nonlinear coefficient $d_{i\ell}$ (section 3.4.2). Thus, we can write the equations 3.37 to 3.39 in a general form as follows:

$$P_i(\omega) = \epsilon_0 \int d\omega_m \sum_{j,k} \chi^{(2)}_{ijk}\, E_j(\omega_m)\, E_k(\omega - \omega_m) \tag{3.40}$$

$$= 2\,\epsilon_0 \int d\omega_m \sum_{j,k} d_{ijk}\, E_j(\omega_m)\, E_k(\omega - \omega_m) \tag{3.41}$$

3.5.1 Coupled-Wave Equations

3.5.1.1 Monomode Case

The propagation of light is described by the wave equation (1.32). In a nonlinear medium, considering the relation 3.25 between the electric displacement $\mathbf{D}$, the electric field $\mathbf{E}$ and the polarization $\mathbf{P}$, the wave equation reads:

$$\nabla^2\mathbf{E}(\mathbf{r},t) - \frac{\epsilon_r}{c^2}\frac{\partial^2}{\partial t^2}\mathbf{E}(\mathbf{r},t) = \frac{1}{\epsilon_0 c^2}\frac{\partial^2}{\partial t^2}\mathbf{P}^{(NL)}(\mathbf{r},t) \tag{3.42}$$

To simplify the derivation, we will use the notation $\mathbf{P}$ from now on to designate the nonlinear polarization. We derive equation 3.42 and simplify the temporal factor to obtain,

$$\nabla^2\mathbf{E}(\mathbf{r}) + \frac{\epsilon_r\,\omega_s^2}{c^2}\,\mathbf{E}(\mathbf{r}) = -\frac{\omega_s^2}{\epsilon_0 c^2}\,\mathbf{P}(\mathbf{r}) \tag{3.43}$$

We consider a propagation along the x direction. In this case, the nonlinear polarization can be along the y or the z direction. In particular, for the PDC in KTP, we are interested in a pump field polarized along z because it is associated to the highest nonlinear coefficient d_{33} (see equation 3.39).

In this section, we write the monomode field as follows:

$$E_j(x,t) = E_j(x)e^{-i\omega_s t} \tag{3.44}$$

$$E_j(x) = A_j(x)\,e^{ik_s x} \tag{3.45}$$

With $A_j(x)$ the amplitude of the field. As a result, the polarization reads:

$$P_j(x,t) = P_j(x)\, e^{-i\omega_s t} \tag{3.46}$$

$$P_j(x) = 4\, d_{i\ell}\, A_i(x) A_k(x)^*\, e^{i(k_p - k_i)x} \tag{3.47}$$

We stress that in this section, we use the index i to denote the polarization of the pump field $A_i(x)$ and to designate the idler wavevector k_i. We replace $P_j(x)$ and $E_j(x)$ by their expressions in equation 3.43 and obtain the general expression of the coupled-wave equations for the PDC process. Details about this calculation can be found in [Boyd 08].

$$\frac{dA_j(x)}{dx} = \frac{2i\,\omega_s\, d_{i\ell}}{n(\omega_s)c}\, A_i(x) A_k(x)^*\, e^{i\Delta k x} \tag{3.48}$$

$$\frac{dA_k(x)}{dx} = \frac{2i\,\omega_i\, d_{i\ell}}{n(\omega_i)c}\, A_i(x) A_j(x)^*\, e^{i\Delta k x} \tag{3.49}$$

Where $\Delta k = k_p - k_i - k_j$ and $(\omega_s,\, \omega_i)$ are the angular frequencies of the signal and idler. In the low-gain regime, the PDC process occurs rarely and few down-converted photons are produced. Thus, the pump intensity does not vary much and can be considered undepleted $A_i(x) \sim A_i$. We introduce the quantity κ, called the coupling constant, corresponding to the gain per unit distance of the nonlinear process. It is defined as:

$$\kappa^2 = \frac{4\, d_{i\ell}^2\, \omega_s \omega_i}{n(\omega_s)\, n(\omega_i)\, c^2}\, |A_i|^2 \tag{3.50}$$

The nonlinear coefficient $d_{i\ell}$ should be replaced according to the chosen phase-matching as well as the refractive index. For example, for a type-I PDC in a BBO crystal, $d_{i\ell} = d_{21}$ and the refractive index experienced by the signal and idler beams is $n_o(\omega)$ (section 3.1). For a PDC in KTP, $d_{i\ell} = d_{24}$ in type II and $d_{i\ell} = d_{33}$ in type-0 phase-matching while the couple of refractive indices is $(n_y(\omega_s), n_z(\omega_i))$ in type II configuration and $(n_z(\omega_s), n_z(\omega_i))$ in type 0.

The general solutions of the coupled equations 3.48 and 3.49 are the classical version of the Bogoliubov equations (chapter 2):

$$A_j(x) = C \sinh(\kappa x) \;+\; D \cosh(\kappa x) \tag{3.51}$$

In our experiment, we use parametric down conversion to produce squeezed states of light (chapters 2 and 6). In the section 2.3.1, we introduced a squeezing parameter r, which can also be defined as $r = \kappa \ell_c$, where ℓ_c is the crystal length.

3.5.1.2 Multimode Case

The parametric beams can be multimode either spatially or spectrally. In the latter case, for example, the coupled-wave equations 3.48 and 3.49 are modified as follows [Gatti 15]:

$$\frac{dA_s(\omega_s,x)}{dx} = \frac{2i\,\omega_s\,d_{i\ell}}{n(\omega_s)c}\int d\omega_i\,A_p(\omega_s+\omega_i)\,A_i^*(\omega_i)\,e^{i\Delta kx} \tag{3.52}$$

$$\frac{dA_i(\omega_i,x)}{dx} = \frac{2i\,\omega_i\,d_{i\ell}}{n(\omega_i)c}\int d\omega_s\,A_p(\omega_s+\omega_i)\,A_s^*(\omega_s)\,e^{i\Delta kx} \tag{3.53}$$

where the energy conservation $\hbar\omega_p = \hbar\omega_s + \hbar\omega_i$ sets the frequencies in the previous equation. The solutions of these equations are found by integrating 3.52 and 3.53 along the length ℓ_c of the nonlinear crystal. To simplify the derivation we can set the position $x = 0$ at the center of the nonlinear crystal:

$$\int_{-\frac{\ell_c}{2}}^{\frac{\ell_c}{2}} dx\,\frac{dA_s(\omega_s,x)}{dx} = A_s(\omega_s,\frac{\ell_c}{2}) - A_s(\omega_s,-\frac{\ell_c}{2}) \tag{3.54}$$

Where $A_s(\omega_s,-\frac{\ell_c}{2})$ denotes the down-converted beam at the input of the crystal. While this term is important in stimulated PDC configurations, it is null for spontaneous PDC, which is the case of our experiments. Thus, at the crystal output, the amplitude of the signal and idler beams read:

$$A_s(\omega_s,\frac{\ell_c}{2}) = A_s(\omega_s,-\frac{\ell_c}{2}) + \frac{2i\,\omega_s\,d_{i\ell}}{n(\omega_s)c}\int_{-\frac{\ell_c}{2}}^{\frac{\ell_c}{2}} dx\,e^{i\Delta kx}\int d\omega_i\,A_p(\omega_s+\omega_i)\,A_i^*(\omega_i) \tag{3.55}$$

$$A_i(\omega_i,\frac{\ell_c}{2}) = A_i(\omega_i,-\frac{\ell_c}{2}) + \frac{2i\,\omega_i\,d_{i\ell}}{n(\omega_i)c}\int_{-\frac{\ell_c}{2}}^{\frac{\ell_c}{2}} dx\,e^{i\Delta kx}\int d\omega_s\,A_p(\omega_s+\omega_i)\,A_s^*(\omega_s) \tag{3.56}$$

Then,

$$A_s(\omega_s,\frac{\ell_c}{2}) = A_s(\omega_s,-\frac{\ell_c}{2}) + \frac{2i\,\omega_s\,d_{i\ell}}{n(\omega_s)c}\int d\omega_i\,\mathrm{sinc}\left(\frac{\Delta k\ell_c}{2}\right)A_p(\omega_s+\omega_i)\,A_i^*(\omega_i) \tag{3.57}$$

$$A_i(\omega_i,\frac{\ell_c}{2}) = A_i(\omega_i,-\frac{\ell_c}{2}) + \frac{2i\,\omega_i\,d_{i\ell}}{n(\omega_i)c}\int d\omega_s\,\mathrm{sinc}\left(\frac{\Delta k\ell_c}{2}\right)A_p(\omega_s+\omega_i)\,A_s^*(\omega_s) \tag{3.58}$$

We denote:

$$\Phi(\omega_s,\omega_i) = A_p(\omega_s+\omega_i)\,\mathrm{sinc}\left(\frac{\Delta k\ell_c}{2}\right) \tag{3.59}$$

which is the joint spectral amplitude (JSA). As we will see in the next section, its square modulus, called the joint spectral intensity (JSI), corresponds to the probability to generate a biphoton state at the frequencies (ω_s, ω_i). We include the JSA in the previous equations and we find:

$$A_s(\omega_s, \frac{\ell_c}{2}) = A_s(\omega_s, -\frac{\ell_c}{2}) + \frac{2i\,\omega_s\,d_{i\ell}}{n(\omega_s)c} \int d\omega_i\,\Phi(\omega_s, \omega_i)\,A_i^*(\omega_i) \tag{3.60}$$

$$A_i(\omega_i, \frac{\ell_c}{2}) = A_i(\omega_i, -\frac{\ell_c}{2}) + \frac{2i\,\omega_i\,d_{i\ell}}{n(\omega_i)c} \int d\omega_s\,\Phi(\omega_s, \omega_i)\,A_s^*(\omega_i) \tag{3.61}$$

The same development can be done for a quantum field. In this case, the field amplitude $A(\mathbf{r}, t)$ would be replaced by the annihilation operator $\hat{a}$.

3.5.2 Interaction Hamiltonian

In the quantum domain, parametric down conversion is a source of twin photons correlated according to energy and momentum conservation. It is often used as a source of entangled photon pairs, EPR states [Einstein 35] or heralded single photons [Mosley 07]. Let us consider the general hamiltonian $\hat{H}$ defined as:

$$\hat{H}(t) = \hat{H}_0 + \hat{H}_{int}(t) \tag{3.62}$$

$\hat{H}$ is a hermitian operator, meaning that its eigenvalues are real. $\hat{H}_0$ is the free radiation hamiltonian defined in eq. 2.1 and $\hat{H}_{int}$ is the time-dependent part of the hamiltonian due to the interaction between light and a material, in our case a nonlinear crystal. It is defined by [Ou 07, La Volpe 19, Horoshko 19]:

$$\hat{H}_{int}(t) = \frac{1}{4\pi} \int d^3r\,\hat{P} \cdot \hat{E}(\mathbf{r}, t) \tag{3.63}$$

where the notation $\hat{E}$ denotes the operator for the pump field and $\hat{P}$ denotes the operator for the nonlinear polarization induced by the light in the crystal. We consider the parametric down conversion process, assuming that all other nonlinear processes have a low probability compared to that of the PDC, for which it is phase-matched (see section 3.5.3). In this case, we only keep the terms associated to the PDC and we have:

$$\hat{P}_i(\mathbf{r}, t) = \epsilon_0 \sum_{j,k} \chi^{(2)}(\omega_s, \omega_i)\,\hat{E}_j^{(-)}(\mathbf{r}, t)\,\hat{E}_k^{(-)}(\mathbf{r}, t) + h.c. \tag{3.64}$$

Where $\sum_{j,k}$ is the sum over the combinations of polarizations and $\hat{E}(\mathbf{r}, t) = \hat{E}^{(+)}(\mathbf{r}, t) + \hat{E}^{(-)}(\mathbf{r}, t)$. The polarization operator can also be defined as the Fourier transform of a

polarization operator $\hat{P}_i(\mathbf{r},\omega_p)$, which expression is given by the equation 3.40 where the classical electric fields are replaced by quantum operators. Thus,

$$\hat{P}_i(\mathbf{r},t) = \int \frac{d\omega_p}{\sqrt{2\pi}}\,\hat{P}_i(\mathbf{r},\omega_p)\,e^{i\omega_p t} \tag{3.65}$$

$$= \frac{\epsilon_0}{\sqrt{2\pi}}\int d\omega_p\,d\omega_s \sum_{j,k}\chi^{(2)}(\omega_s,\omega_p-\omega_s)\hat{E}_j^{(-)}(\mathbf{r},\omega_s)\,\hat{E}_k^{(-)}(\mathbf{r},\omega_p-\omega_s)\,e^{i\omega_p t} \;+\; h.c. \tag{3.66}$$

where ω_p and ω_s denote the frequency of the pump and signal fields respectively. We recall the Fourier transforms of equation 3.32 to 3.33:

$$\hat{E}^{(-)}(\mathbf{r},t) = \int \frac{d\omega}{\sqrt{2\pi}}\,\hat{E}^{(-)}(\mathbf{r},\omega)e^{i\omega t} \tag{3.67}$$

$$= \int \frac{d\omega}{\sqrt{2\pi}}\,\hat{a}^\dagger(\omega)e^{i\omega t - i\mathbf{k}\cdot\mathbf{r}} \tag{3.68}$$

For a given set of frequencies ω_p, ω_s, $\omega_p-\omega_s$ and a given combination of polarizations i,j,k, the equation 3.66 has now four terms.

$$\hat{P}_i(\mathbf{r},t) = \frac{\epsilon_0\,\mathcal{E}^2}{2\pi\sqrt{2\pi}}\int d\omega_p\,d\omega_s \sum_{j,k}\chi^{(2)}(\omega_s,\omega_p-\omega_s)\,\hat{a}_j^\dagger(\omega_s)\,\hat{a}_k^\dagger(\omega_p-\omega_s)\;e^{i\omega_p t}\,e^{-i\left(\mathbf{k}_s+\mathbf{k}_{k(\omega_p-\omega_s)}\right)\cdot\mathbf{r}} + h.c. \tag{3.69}$$

where $\mathcal{E}\in\mathbb{R}$ and $\hat{a}_{j,k}^\dagger$ denotes the creation operators of the signal and idler photons at the frequencies ω_s and $\omega_i=\omega_p-\omega_s$. From now on we replace $\omega_p-\omega_s$ by ω_i in the previous equation and we compute $\hat{P}_i\hat{E}_i(\mathbf{r},t)$:

$$\hat{P}_i\hat{E}_i(\mathbf{r},t) = \frac{\epsilon_0\,\mathcal{E}^2}{4\pi^2}\int d\omega_s d\omega_i \sum_{j,k}\chi^{(2)}(\omega_s,\omega_i)\,\hat{a}_j^\dagger(\omega_s)\,\hat{a}_k^\dagger(\omega_i)\;\hat{a}_i(\omega_p)\,e^{-i\Delta\mathbf{k}\cdot\mathbf{r}} \;+\; h.c. \tag{3.70}$$

where again we kept the terms associated to the PDC and $\Delta\mathbf{k}\cdot\mathbf{r}=\mathbf{k}_p-\mathbf{k}_s-\mathbf{k}_i$ is the phase mismatch. In practice, the intensity of the pump beam is a lot bigger than the one of the down-converted beams. In this case, we consider the pump as a classical field and we replace the annihilation operator of the pump $\hat{a}_i(\omega_p)$ by its mean value $\alpha_p(\omega_p)$ which is the one of a coherent state. Finally, we integrate the previous equation over the length of the nonlinear crystal ℓ_c and obtain the following hamiltonian:

$$\hat{H}_{int} = \frac{\epsilon_0 \mathcal{E}^2 \alpha_p(\omega_p)}{16\pi^3} \int d\omega_s d\omega_i \sum_{j,k} \chi^{(2)}(\omega_s, \omega_i)\, \hat{a}_j^\dagger(\omega_s)\, \hat{a}_k^\dagger(\omega_i)\ \mathrm{sinc}\left(\frac{\Delta k \ell_c}{2}\right) + h.c. \quad (3.71)$$

$$= \frac{\epsilon_0 \mathcal{E}^2 \chi^{(2)}}{16\pi^3} \int d\omega_s d\omega_i \sum_{j,k} \Phi(\omega_s, \omega_i)\, \hat{a}_j^\dagger(\omega_s)\, \hat{a}_k^\dagger(\omega_i) + h.c. \quad (3.72)$$

Where, the nonlinear susceptibility is considered constant $\chi^{(2)}(\omega_s, \omega_i) \sim \chi^{(2)}$ because it slowy varies with frequency (section 3.4.1) and:

$$\Phi(\omega_s, \omega_i) = \alpha_p(\omega_p)\ \mathrm{sinc}\left(\frac{\Delta k \ell_c}{2}\right) \quad (3.73)$$

We retrieve the joint spectral amplitude (JSA) from equation 3.59. We can see in figure 3.5, that the highest probability for biphoton generation can be obtained when $\frac{\Delta k \ell_c}{2}$ is close to zero and especially when $\Delta k \sim 0$. In bulk crystals like BBO, this configuration can be approached via critical phase-matching (section 3.5.3.1) by slightly changing the index of refraction $n(\theta)$ perceived by the pump beam (section 3.2).

Finally, we use the singular-value decomposition defined in section 2.3.6 and express the Hamiltonian in the basis of squeezed modes:

$$\hat{H}_{int} = \frac{\epsilon_0 \mathcal{E}^2 \chi^{(2)}}{16\pi^3} \sum_j \Lambda_j\, (\hat{s_j^\dagger})^2 + h.c. \quad (3.74)$$

Where Λ_j is a matrix containing squeezing eigenvalues and $\{\hat{s_j^\dagger}\}$ are the bosonic operators associated to the squeezed modes. In the following sections, we will focus on the phase-matching and its influence on the down-converted light.

3.5.3 PDC Phase-Matchings

For three-wave mixing processes, we defined the phase mismatch Δk as:

$$\Delta k = k_p(\omega_p) - k_s(\omega_m) - k_i(\omega_n) \quad (3.75)$$

$$\Delta k = n_i(\omega_p)\frac{\omega_p}{c} - n_j(\omega_s)\frac{\omega_s}{c} - n_k(\omega_i)\frac{\omega_i}{c} \quad (3.76)$$

Where, c is the speed of light in vacuum, $n_{i,j,k}$ are the refractive indices in the nonlinear medium depending on the polarization of the field and $\omega_{p,s,i}$ are the angular frequencies of the pump, signal and idler. In the previous section, we introduced the joint spectral amplitude $\Phi(\omega_s, \omega_i)$ (eq. 3.73), whose square modulus corresponds to the probability to generate a biphoton state at the frequencies (ω_s, ω_i). This probability is the highest when the phase mismatch is close to zero, $\Delta k \sim 0$. We distinguish three types of phase-matching according to the polarization of the fields:

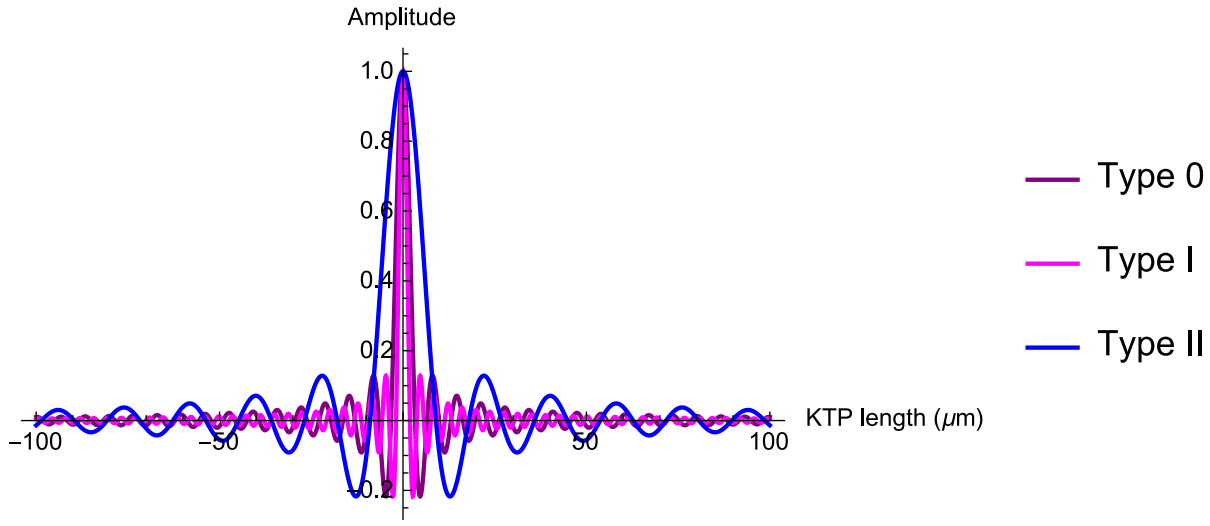

Figure 3.5 – Joint Spectral Amplitude for different phase-matchings in KTP.

The type I Signal and idler share the same polarization, which is perpendicular to the one of the pump.

The type II Signal and idler have orthogonal polarizations, with the pump sharing the polarization of one of the down-converted beams as presented in equations 3.37 and 3.38.

The type 0 Pump, signal and idler share the same polarization. This configuration cannot be achieved with critical phase-matching (see below). The nonlinear crystal needs to be manufactured so as to compensate the phase mismatch. This corresponds to *Quasi-Phase-Matching* (section 3.5.3.3). In KTP, this phase-matching can only be achieved with a pump polarization along the z direction (section 3.4.2)

3.5.3.1 Critical Phase-Matching

Contrary to the frequency-matching, which is fixed by the energy conservation, the phase-matching often needs adjustments. In uniaxial bulk crystals (section 3.1), the phase-matching requires to control the angle between the optical axis of the crystal and the polarization of the pump. This is called *critical phase-matching*. It allows to determine the refractive index $n(\theta)$ 3.5 involved in the process.

3.5.3.2 Non-Collinear Phase-Matching

Additional phase-matching configurations can be found with non-collinear down-converted beams. In the latter case, signal and idler are not parallel to the pump direction, their

angle can be used to adjust the phase-matching conditions. We define α_s and α_i, the angles between the direction of propagation of the pump and the direction of propagation of the signal and idler respectively. In this configuration, the phase-matching reads:

$$k_e(\omega_p, \theta) = k_o(\omega_s)\cos(\alpha_s) + k_o(\omega_i)\cos(\alpha_i) \tag{3.77}$$
$$k_o(\omega_s)\sin(\alpha_s) = k_o(\omega_i)\sin(\alpha_i) \tag{3.78}$$

Where θ is the critical angle, i.e. the angle between the crystal optical axis and the direction of the pump (section 3.2). We emphasize the fact that the non-degenerate case leads to different PM angles α according to 3.78. In bulk uniaxial crystals like BBO, the refractive index experienced by the down-converted beams is n_o while the pump experiences an index depending on its orientation with respect to the crystal axis $n_e(\theta)$. This is recalled in equation 3.77 where we substitute k_p, k_s and k_i by $k_e(\theta)$, k_o and k_o respectively. However, degenerate non-collinear phase-matching can also be achieved. This is the configuration we chose for our experiment with BBO (chapter 6)[La Volpe 19]. In this case, signal and idler are emitted apart from the pump direction with the same angle, which is smaller than in the non-degenerate case [Ou 07]. In our experiment with BBO, this angle was $\alpha = 1.8°$.

3.5.3.3 Quasi-Phase Matching

Sometimes, the phase mismatch is to big to be compensated with critical phase-matching. Below, we give examples of phase-mismatchs in KTP, at $\lambda_{pump} = 397.5$ nm and $\lambda_{signal,idler} = 795$ nm, for the type 0 (d_{33}), type I (d_{32}) and type II (d_{24}) configurations:

$$\Delta k_{d_{33}} = n_z(\omega_p)\frac{\omega_p}{c} - n_z(\omega_s)\frac{\omega_s}{c} - n_z(\omega_i)\frac{\omega_i}{c} = 1.92\,\mu m^{-1} \tag{3.79}$$
$$\Delta k_{d_{32}} = n_z(\omega_p)\frac{\omega_p}{c} - n_y(\omega_s)\frac{\omega_s}{c} - n_y(\omega_i)\frac{\omega_i}{c} = 3.32\,\mu m^{-1} \tag{3.80}$$
$$\Delta k_{d_{24}} = n_y(\omega_p)\frac{\omega_p}{c} - n_y(\omega_s)\frac{\omega_s}{c} - n_z(\omega_i)\frac{\omega_i}{c} = 0.7\,\mu m^{-1} \tag{3.81}$$

In these cases, the probability to generate a biphoton at (ω_s, ω_i) is very low. Also, when light propagates inside the crystal, the JSA is even more reduced with the propagation distance. *Quasi-Phase-Matching* aims at preventing the reduction of the JSA inside the nonlinear medium. The most common technique is periodic poling, which consists in a periodic inversion of the nonlinearity in the birefringent material [Risk 96]. This is modeled by modulating the $\chi^{(2)}$ tensor with a periodic sign-flip function g such that $\chi^{(2)} = g(x) \times \chi^{(2)}$ with $g(x) = \text{sgn}\left[\sin\left(\frac{2\pi x}{\Lambda}\right)\right]$ [Armstrong 62], [Franken 63]. The flip funtion is also defined by its Fourier series:

$$g(x) = \sum_{\substack{\pm p=2n+1 \\ n\in\mathbb{N}}} \frac{1}{p}\, e^{ip\,k_\Lambda x} \tag{3.82}$$

Where x is the direction of propagation, $k_\Lambda = \frac{2\pi}{\Lambda}$ and $p \in \mathbb{N}^*$ is called the phase-matching order. Each domain is of width Λ, determined so as to compensate the phase-mismatch and is specific to the chosen configuration 0, I or II. According to equation 3.82, several poling periods are available for a same phase mismatch 3.76. However, the first order is often preferred, because smaller periods are more difficult to manufacture and the nonlinearity evolves in $\frac{1}{p}$. When the modulated $\chi^{(2)}$ is added to the interaction hamiltonian, the phase-mismatch gains an additional term:

$$\Delta k_{i\ell,\ m} = n_i(\omega_p)\frac{\omega_p}{c} - n_j(\omega_s)\frac{\omega_s}{c} - n_k(\omega_i)\frac{\omega_i}{c} - p\frac{2\pi}{\Lambda_{i\ell}} \tag{3.83}$$

The type-0 and type-II KTP crystals used in our experiment are periodically poled with a poling period $\Lambda_0 = 3.19\,\mu$m and $\Lambda_{II} = 8.39\,\mu$m respectively.

3.5.3.4 Phase-Matching of SPDC in a Rectangular Waveguide

As discussed in 1.3, the bi-dimensional confinement of light in a rectangular waveguide limits the wavelengths, which can be coupled in it. The waves of the parametric processes propagate along the same direction inside the waveguide and the spatial constraints are added to the phase mismatch:

$$\Delta k = k_p - k_s - k_i - p\frac{2\pi}{\Lambda_{i\ell}} - n\frac{2\pi}{\lambda_{ny}} - m\frac{2\pi}{\lambda_{mz}} \tag{3.84}$$

$$= n_i(\omega_p)\frac{\omega_p}{c} - n_j(\omega_s)\frac{\omega_s}{c} - n_k(\omega_i)\frac{\omega_i}{c} - p\frac{2\pi}{\Lambda_{i\ell}} - n\frac{2\pi}{\lambda_{ny}} - m\frac{2\pi}{\lambda_{mz}} \tag{3.85}$$

Where m and n refer to the coupled-mode number.

Chapter 4

Ultrafast Pulse Shaping for Mode Selectivity

Contents

4.1 Zero-dispersion Line . . . 64
4.2 Focal Length and Reflecting Telescope . . . 65
4.3 Spatial Light Modulator . . . 66
4.4 Blazed Grating . . . 66
4.4.1 Choose a Blazed Grating . . . 67
4.5 Shaping Performances . . . 68
4.6 Useful Phase Masks for Multimode Squeezing . . . 69
4.6.1 Masks for Homodyne Detection . . . 71
4.6.2 Correction of Dispersion . . . 71

Femtosecond lasers, developed at the end of the nineties [Hänsch 06, Fortier 19, Amy-Klein 10], are of great interest for the shape and duration of the ultrashort pulses they emit. They are used in various fields of research including spectroscopy [Shim 09], imaging [Silberberg 09] and optical communication [Marin-Palomo 17]. Most of these experiments rely on pulse shaping. Amplitude modulation can be performed with a grating. Indeed, a grating diffracts light in various orders of diffraction, so if we collect only the 0^{th} order, its amplitude depends on the periodic structure of the grating. Then, if we can modulate the number of grooves per mm of the grating, e.g. with a spatial light modulator, we can modulate the amplitude of the 0^{th} order. Phase modulation implies to be able to modulate the refractive index $n(\lambda)$ of the medium in which light propagates. We can use birefringent materials, Acousto-Optic Modulators (AOM) or Electro-Optic Modulators (EOM) as well as Spatial Light Modulators (SLM). Phase masks that can imprint arbitrary amplitude and spectral shapes can be displayed on a SLM screen. Pulse shaping is an essential tool for mode-selective homodyne detection as it allows to unveil the multimode character of the quantum states we produce via

PDC.

4.1 Zero-dispersion Line

A folded pulse-shaper setup is a 4f line (fig. 4.1), also called *zero-dispersion line* [Monmayrant 10, Weiner 11] composed of three major elements: a blazed grating, a lens (a cylindrical mirror in our case) and a SLM. In a zero-dispersion line, the distance between the optical elements is rigorously f, the focal length of the cylindrical mirror. The incoming light is diffracted by the blazed grating (see section 4.4), collimated by the cylindrical mirror and reaches the SLM placed at the Fourier plane. If a mirror is placed in the Fourier plane instead of the SLM, this setup is dispersion free, meaning that the incoming and outgoing pulses are identical [Froehly 83]. The light shaped by the SLM is reflected back to the cylindrical mirror with a small vertical angle, before being focused back on the grating. That way, incoming and outcoming beams can be separated. When we work with ultrafast light, the spectrum is wide and very sensitive to dispersion. Thus, the folded configuration, using cylindrical mirrors instead of lenses and reflective grating, allows to avoid unwanted dispersion in the shaped pulses. The

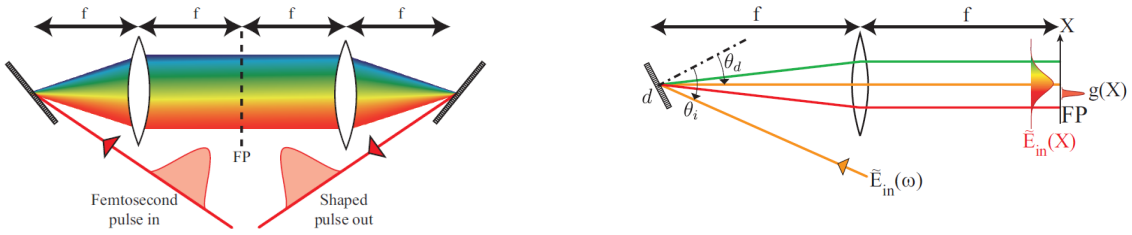

Figure 4.1 – Schematic of a zero-dispersion line or 4f line. Left: unfolded configuration. Right: folded configuration where the lens is replaced by a cylindrical mirror in our case. Pulse shaping occurs in the Fourier plane [Monmayrant 10].

spectral resolution depends on the g-parameter, i.e. the number of grooves per mm, of the diffraction grating (section 4.4.1) and the spatial resolution relies on the coverage of the SLM screen, i.e. the beam waist at the Fourier plane. The waist size of a monochromatic beam should in fact be compatible with the pixels size on the SLM. I took care of the design of the pulse shaper setup of our experiment. The chosen parameters for our configuration are $f = 25$ cm and $g = 600$ gr/mm. In the following, we will comment on the different components of the pulse shaper.

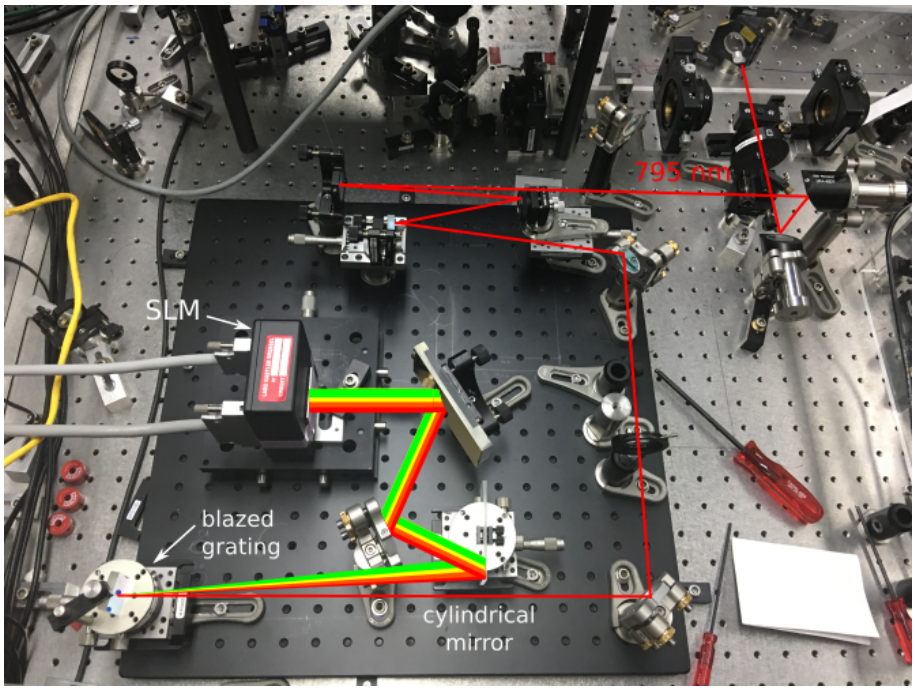

Figure 4.2 – Picture of the pulse shaper setup. The reflecting telescope is visible at the top of the image.

4.2 Focal Length and Reflecting Telescope

The focal length f has been chosen as short as possible such that the beam waist in the focal plane matches the size of the SLM screen. A short f implies a smaller optical setup, which is not easy to align, we chose f = 25 cm as a good compromise. The waist can be further reduced by increasing the beam waist before the cylindrical mirror so we expanded the size of the laser beam with a reflecting telescope (fig. 4.2). It is composed of three curved mirrors of radius of curvature R_1 = -800 mm, R_2 = -1000 mm and R_3 = 750 mm. Distances between the mirrors were finely adjusted and angles of incidence kept close to 0°, so as to limit the ellipticity in the beam shape and obtain a collimated TEM_{00} beam. In our case, the distance between the first and the second curved mirrors was 16 cm and the second and third curved mirrors were placed 12 cm apart. We measured the beam waist with a video camera connected to a LabVIEW program. In this configuration, the beam waist was expanded from 1.34 mm to 2.62 mm.

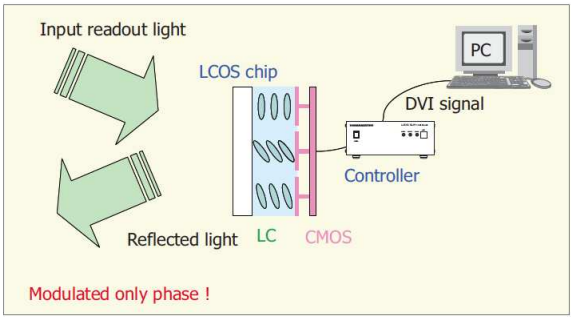

Figure 4.3 – Schematic of the LCOS-SLM X10468.

4.3 Spatial Light Modulator

The spatial light modulator (SLM) is based on liquid crystals. We used a LCOS-SLM X10468 (Liquid Crystal On Silicon) from Hamamatsu (fig. 4.3), in which liquid crystals lie between a covering glass and a dielectric mirror, in such a way that when no phase modulation is sent, the SLM operates like a plane mirror. Liquid crystals behave as a birefringent material 3.1, whose refractive-index difference between the ordinary and extraordinary axes $\Delta n = n_e - n_o$ 3.2 can be modulated with a voltage V. Therefore, the dephasing (between 0 and 2π) applied to a light field writes [Engström 13]:

$$\phi(\lambda, V) = \frac{4\pi\ \Delta n(\lambda, V)\ e}{\lambda} \tag{4.1}$$

Where e is the thickness of the liquid-crystals chip, c the speed of light in vacuum and λ is the wavelength of the incoming light. Because the SLM is reflective, the beam is dephased twice, hence the factor 4 in 4.1 instead of 2. Behind the dielectric mirror, lies a 792×600 pixel matrix allowing to locally apply voltage in the liquid crystals. The SLM can be interfaced with a computer that generates phase masks. The phase values of the computer-generated masks are converted into 8-bit values between 0 and 255 and the masks are sent to the SLM. In section 4.6, we will present some useful phase masks for our experiment.

4.4 Blazed Grating

Blazed gratings are diffraction gratings designed to achieve maximum diffraction at an angle θ_B called the *blazed angle*. Thus, most of the optical power is concentrated in a given diffraction order, usually the first one. Blazed gratings are based on the Littrow configuration [Popov 90, Zorabedian 95, Loewen 90], in which the angle of incidence of light α is identical to the angle of diffraction β. For a reflection grating, this means that the diffracted beam is reflected back into the first order of diffraction only and in

the direction of the incident beam (the blue beam in figure 4.4). The beams are then perpendicular to the sawtooth step and parallel to its normal. If the angle of incidence is slightly different than the blazed angle, the angle of departure of the light is slightly different than the blazed angle as well, but most of the light power is still concentrated in a given diffraction order. This corresponds to a *near Littrow configuration*. We choose to work in this configuration so as to be able to separate the incoming beam and the first order. The blazed angle θ_B can be calculated with the grating equation in the Littrow configuration and is wavelength dependent (see section 4.4.1).

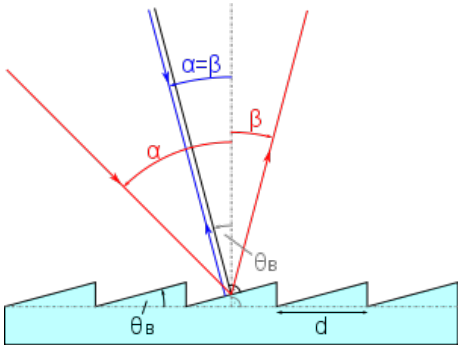

Figure 4.4 – Littrow configuration. θ_B is the blazed angle, α and β are respectively the angle of incidence and the angle of diffraction, d is the spacing between the sawtooth steps.

4.4.1 Choose a Blazed Grating

To determine the number of grooves per millimeter g needed in the pulse-shaping setup, we start from equations 4.2 to 4.4. For a reflection grating, the grating equation reads:

$$\sin(\theta_{out}) - \sin(\theta_{in}) = m\,\lambda_d\,g \;\; ; \;\; (m = 1) \tag{4.2}$$

where, θ_{in} and θ_{out} are the angle of incidence of the beam on the grating and the angle of departure respectively. In a reflection grating, the incoming and outgoing beams propagate on either sides of the sawtooth normal. Therefore, in a blazed configuration, $\theta_{in} = \theta_B$ and $\theta_{out} = -\theta_B$ and equation 4.2 becomes:

$$\sin(\theta_B) = \frac{m\,\lambda_d\,g}{2} \tag{4.3}$$

where λ_d is called the design wavelength of the grating and corresponds to the wavelength for which the blaze condition is achieved. After the grating, the beam size after the grating Δl is given by:

$$\Delta l = f \times \tan\left(\frac{\Delta\theta_{out}}{2}\right) \tag{4.4}$$

where $f = 25$ cm is the focal length of the cylindrical mirror and $\Delta\theta_{out}$ represents the angles over which the angle of departure varies.

The blaze condition is achieved for the design wavelength only, so when we work with multimode light, the other wavelengths are diffracted with an angle $\theta_{out}(\lambda)$ given by the grating equation. In this case, the grating equation reads:

$$\sin\left(\theta_B + \frac{\Delta\theta_{out}}{2}\right) + \sin\left(\theta_B - \frac{\Delta\theta_{out}}{2}\right) = \Delta\lambda\, g \tag{4.5}$$

in which $\Delta\lambda$ denotes the spectrum. Then, by replacing θ_B and $\Delta\theta_{out}$ by their expression, we can deduce an equation for g:

$$g = \frac{2}{\Delta\lambda} \sin\left[\arctan\left(\frac{\Delta l}{f}\right)\right] \times \cos\left[\arcsin\left(\frac{\lambda_d\, g}{2}\right)\right] \tag{4.6}$$

Which can be resolved graphically. From the graphical resolution of this equation (fig. 4.5) we obtained $g = 600$ gr/mm and $\theta_B = 13°$ at 800 nm for the blazed angle.

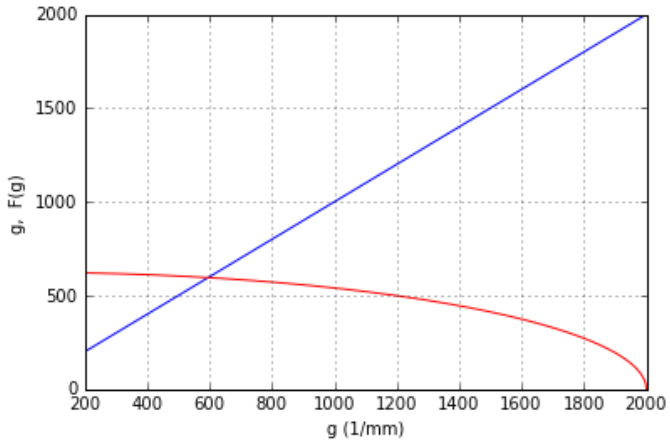

Figure 4.5 – Graphical resolution of equation 4.6. The red curve is the equation 4.6 and the blue curve is $f(g) = g$. In our configuration, g = 600 gr/mm.

4.5 Shaping Performances

On the SLM screen, the performances of the pulse shaper depend on how well the incoming beam spreads on the screen. Horizontally, the beam is spread spectrally and

covers the SLM screen area. The size Δx_k of a light spot at a given wavelength λ_k is defined by [Danailov 89, Monmayrant 10]:

$$\Delta x_k = 2\ln(2) \times \frac{\cos(\theta_{in})\ f\lambda_k}{\cos(\theta_{out})\ \pi\Delta x_{in}} \tag{4.7}$$

In our configuration, $\theta_{in} = \theta_B{+}3 = 16°$ and $\theta_{out} = \theta_B{-}3 = 10°$. $\Delta x_{in} = w_{in}\sqrt{2\ln(2)}$ is the full width at half maximum (FWHM) of the incoming beam, which depends on the beam waist w_{in}. In our case, the width on the SLM screen of a light spot at $\lambda_{k=0} = 795$ nm is $\Delta x_{k=0} = 27.7$ μm. The size of one SLM pixel being 20 μm, Δx_0 is slightly less than the size of two pixels. Vertically, the coverage ratio allows better spatial shaping of the beam and a better modulation of its amplitude. Thus, the initial size of the beam is an important parameter for the shaping efficiency. The frequency resolution is given by:

$$\delta\omega = \frac{\Delta x_0}{\alpha} \tag{4.8}$$

where α is a coefficient set by the geometry 4f line. It is defined in [Monmayrant 10] as:

$$\alpha = \frac{\lambda_0^2\, fg}{2\pi c\ \cos(\theta_{out})} \tag{4.9}$$

In our case, the spectrum of a light spot at $\lambda_0 = 795$ nm is $\delta\omega = 5.42 \times 10^{11}$ Hz, which corresponds to approximately 3479 teeth of our frequency comb. This resolution corresponds approximately to 0.13 nm per pixel. Finally, let us consider the distribution of the light spots at different wavelengths in the Fourier plane. Thanks to α, the relation between the frequency ω_k and the position x_k of the spot can be determined:

$$x_k = \alpha\,\omega_k \tag{4.10}$$

The figure 4.6 gives an example of the spacing between two light spots.

4.6 Useful Phase Masks for Multimode Squeezing

The phase masks are images of size 800×600 pixels coded on a computer and displayed on the SLM screen. The phase masks presented in this section were coded in LabVIEW, but they can be coded in Python as well. The SLM is handled as a second screen by the computer so any image can be displayed on it as long as its size is 800×600. Arbitrary phase and amplitude modulations can be applied to the light. Our masks all shared the same basis, i.e. a sawtooth grating as depicted on fig. 4.7, which diffracts the light preferentially in the first order and is used for efficient amplitude modulation

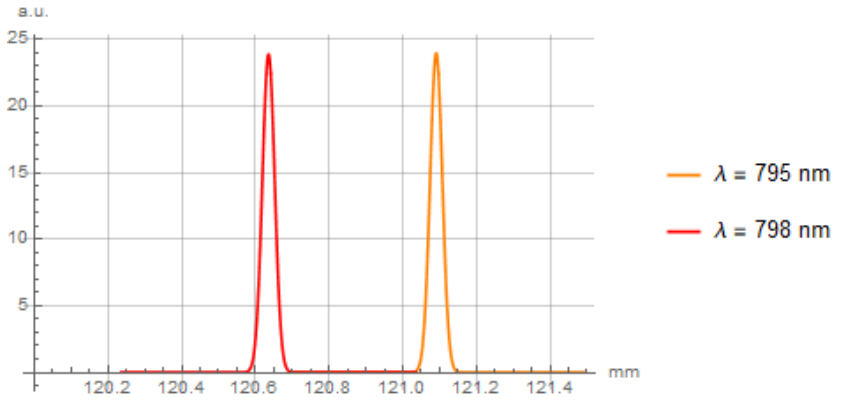

Figure 4.6 – Separation of the light spots centered at $\lambda_0 = 795$ nm and at $\lambda_1 = 798$ nm.

and to separate the incoming beam from the shaped one. Indeed, the shaped beam is diffracted at a slight vertical angle above the incoming beam. The separation angle between the two beams is tuned with the sawtooth period, i.e. the number of grooves per mm defined in section 4.4.1. Also, by shifting the sawtooth grating vertically, we can implement phase shifts to the beam.

Horizontally, we shape the light spectrum by multiplying the grating with a function corresponding to the desired spectrum. We use it to perform mode-selective homodyne detection (see below).

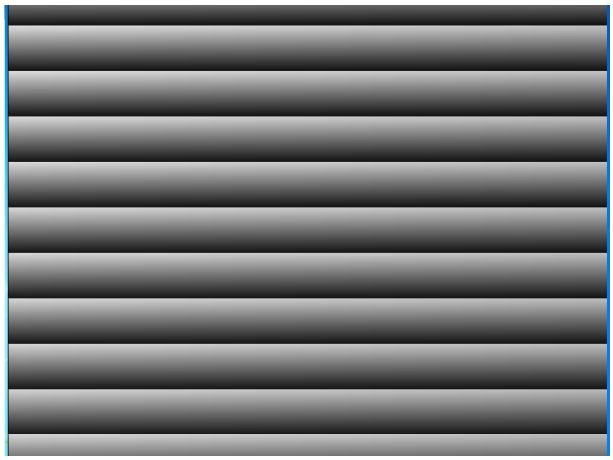

Figure 4.7 – SLM allows displaying phase masks of arbitrary shapes. Here we show a sawtooth grating.

4.6.1 Masks for Homodyne Detection

In homodyne detection, which is the subject of chapter 5, the interference between the signal and a reference called local oscillator (LO) allows to measure the quadratures of the signal by scanning the phase of the LO [Schumaker 84]. In the spectral domain, shaping the LO spectrum allows to measure parameters associated to a specific spectral mode. In particular, the measurement of a multimode squeezed state gives access to the level of squeezing per mode and allows to unveil the squeezing distribution between the modes. As mentioned in previous chapters 1.2.2 and 2.3.5, the basis of squeezed modes can be approached by the Hermite-Gaussian (HG) basis, so the latter was included in our phase masks. The figures 4.8 and 4.9 show the phase masks of the first four spectral modes of the HG basis superposed with a sawtooth grating. The vertical shifts in the sawtooth gratings of the modes HG_1 to HG_3 correspond to phase shifts. The light spectrum after the pulse shaper is measured with a spectrometer from Avantes. The measured spectra are in good agreement with the parameters of the phase masks, i.e. central wavelength and spectrum. Nevertheless, we can see an asymmetry in the measured spectra compared to the phase masks when the spectrum chosen for the shaped mode is close to the spectrum of the incoming light, i.e. before the pulse shaper. This effect is further increased if the chosen central wavelength differs from the central wavelength of the incoming light. We show this effect in the modes HG_1 to HG_3 from figures 4.8 and 4.9.

4.6.2 Correction of Dispersion

Despite all precautions, it can be necessary to implement additional corrections of dispersion within a phase mask in order to compensate for the dispersion accumulated by the light during its propagation in free space. The figure 4.10 shows a temporal-chirp-compensation mask on the left. It is done by multiplying the mask of the HG_0 mode with a quadratic function. On the right of the figure 4.10 we implement a wavelength-dependent phase shift to the sawtooth grating to compensate for angular chirp. Additionally, Hamamatsu provided us with a correction pattern (fig. 4.11), which helps correcting the physical imperfections of the device when it is displayed on the SLM screen.

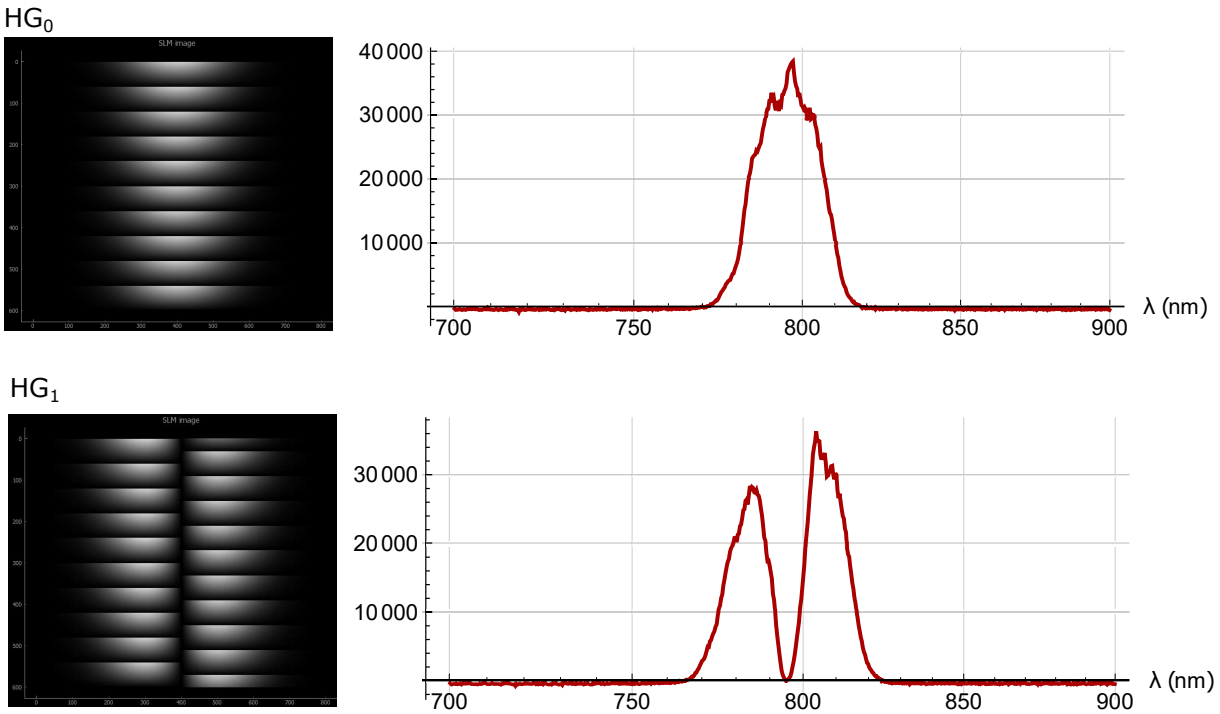

Figure 4.8 – Left: Phase masks used in homodyne detection to measure squeezing in spectral modes HG_0 and HG_1 with a sawtooth grating superposed to it. Right: associated mode spectrum measured with a spectrometer

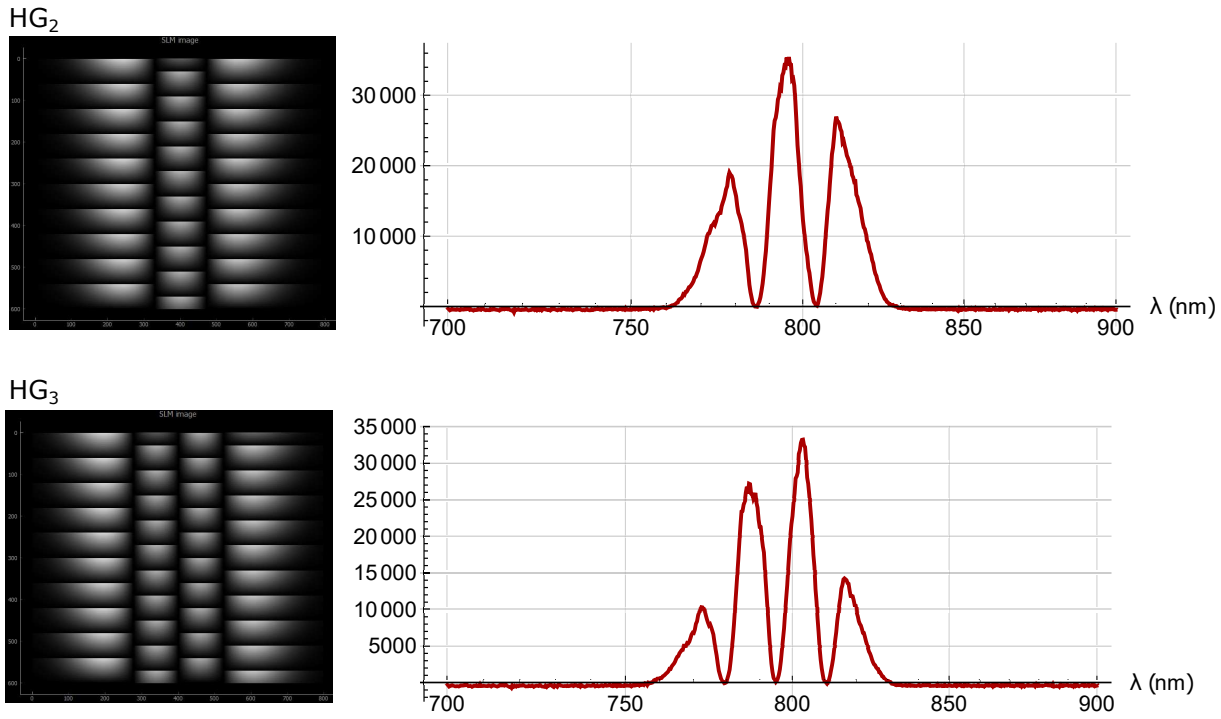

Figure 4.9 – Left: Phase masks used in homodyne detection to measure squeezing in spectral modes HG_2 and HG_3 with a sawtooth grating superposed to it. Right: associated mode spectrum measured with a spectrometer

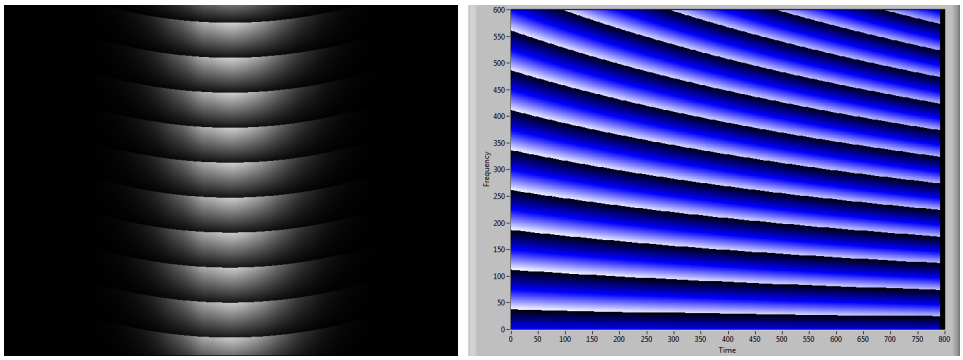

Figure 4.10 – Phase masks used for dispersion compensation. Left: spectral-chirp correction on a HG_0 mode; right: angular-chirp compensation.

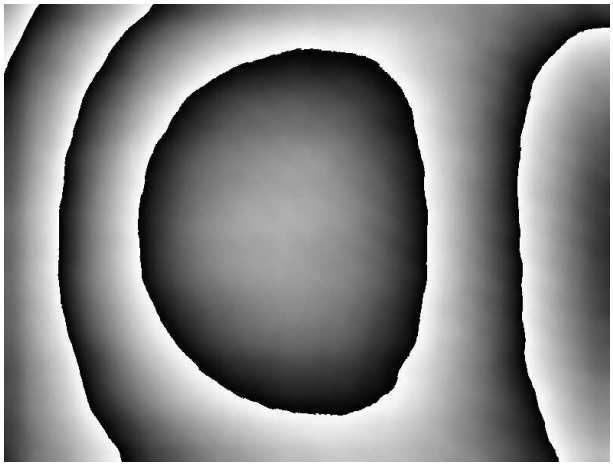

Figure 4.11 – Phase masks used for dispersion compensation. Left: spectral chirp correction on a HG_0 mode; right: Correction pattern provided by Hamamatsu.

Chapter 5

Principle of Homodyne Detection for Ultrafast Light

Contents

5.1 Homodyne Signal 75
5.2 Noise and Losses in Homodyne detection 77
5.2.1 Non-Ideal Photodetection 77
5.2.2 Electronic Noise 80
5.2.3 Mode-Matching Losses 81
5.3 Detector Performances 82
5.3.1 Shot-Noise Clearance 82
5.3.2 Common-Mode Rejection Ratio 83
5.4 Noisy Squeezing Levels 83
5.5 Examples of Homodyne Detections in the Multimode Regime 85
5.5.1 Mode-Selective Homodyne Detection 85
5.5.2 Multipixel Homodyne Detection 85

5.1 Homodyne Signal

Homodyne detection is a measurement technique based on the interference between a beam of interest, the signal, and a reference beam called Local Oscillator (LO), usually derived from the same laser source. In two-port homodyne [Schumaker 84, Yuen 83], light is mixed at a balanced (50/50) and lossless beam splitter. The outgoing beams are then sent to two photodiodes (PD) (see fig. 5.1). At the beamsplitter outputs (eq. 2.52), we have the operators $\hat{a}_1$ and $\hat{a}_2$:

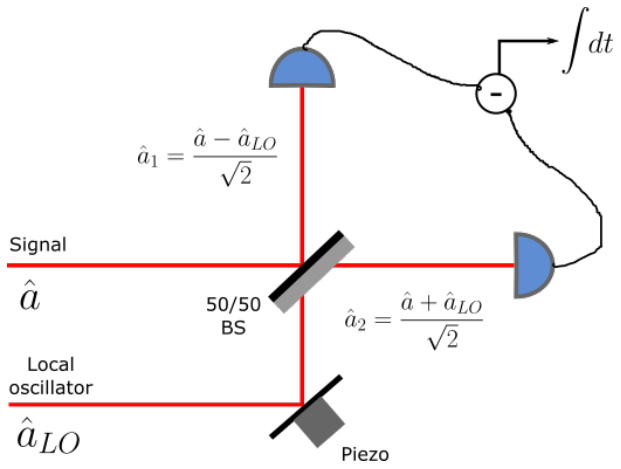

Figure 5.1 – Basic schematics of a homodyne setup.

$$\hat{a}_1 = t\hat{a} - r\hat{a}_{LO} = \frac{1}{\sqrt{2}}(\hat{a} - \hat{a}_{LO}) \tag{5.1}$$

$$\hat{a}_2 = r\hat{a} + t\hat{a}_{LO} = \frac{1}{\sqrt{2}}(\hat{a} + \hat{a}_{LO}) \tag{5.2}$$

Where $\hat{a}$ and $\hat{a}_{LO}$ are the annihilation operators for the signal and the LO field respectively. The number of photons $\hat{N}_j = \hat{a}_j^\dagger \hat{a}_j$ (section 2.1) can be derived:

$$\hat{N}_1 = \frac{1}{2}(|\hat{a}_{LO}|^2 + |\hat{a}|^2 - \hat{a}_{LO}^\dagger \hat{a} - \hat{a}^\dagger \hat{a}_{LO}) \tag{5.3}$$

$$\hat{N}_2 = \frac{1}{2}(|\hat{a}_{LO}|^2 + |\hat{a}|^2 + \hat{a}_{LO}^\dagger \hat{a} + \hat{a}^\dagger \hat{a}_{LO}) \tag{5.4}$$

In this section, we use the notation $|\hat{a}|^2$ to denote the photon numbers $\hat{a}^\dagger \hat{a}$ to lighten the notation.

Each photodiode generates a photocurrent i_j, which is proportional to the flux of photons. Its magnitude depends on the photodiode photosensitivity S given in A/W.

$$i_j = S_j \times P_{LO} \tag{5.5}$$

Where $j = 1, 2$ denotes a photodiode and P_{LO} is the LO power on one photodiode. We assume the photosensitive area of the PD to be larger than the size of the beam. After the detector, the photocurrents generated by each photodiode are subtracted giving a signal proportional to $\langle \hat{N}_2 - \hat{N}_1 \rangle$, where the subtraction of the photon number reads:

$$\hat{N}_{21} = \hat{N}_2 - \hat{N}_1 \tag{5.6}$$
$$= \hat{a}_{LO}^{\dagger}\hat{a} + \hat{a}^{\dagger}\hat{a}_{LO} \tag{5.7}$$

Additionally, in the hypothesis that $\langle \hat{a}_{LO}^{\dagger}\hat{a}_{LO} \rangle \gg \langle \hat{a}^{\dagger}\hat{a} \rangle$ and that the fluctuations of the LO are negligible with respect to the mean field, we replace the bosonic operators of the local oscillator with their mean value $\langle \hat{a}_{LO} \rangle = \alpha_{LO}$ with $\alpha_{LO} \in \mathbb{R}$ being the field amplitude. Therefore, $\hat{N}_{21}$ writes:

$$\hat{N}_{21} = \alpha_{LO} \left(\hat{a}e^{-i\theta} + \hat{a}^{\dagger}e^{i\theta} \right) \tag{5.8}$$

$$\hat{N}_{21} = \alpha_{LO}\, \hat{q}_{\theta} \tag{5.9}$$

where $\hat{q}_{\theta} = \hat{a}e^{-i\theta} + \hat{a}^{\dagger}e^{i\theta} = \hat{q}\cos(\theta) + \hat{p}\sin(\theta)$ is the general field quadrature. The angle θ describes the phase shift in respect to the quadratures $\hat{q}$ and $\hat{p}$ in the phase space. It is defined such that when $\theta = 0$, $\hat{q}_0 = \hat{q}$ and when $\theta = \frac{\pi}{2}$, $\hat{q}_{\frac{\pi}{2}} = \hat{p}$. Thus, by scanning the phase of the local oscillator, one can access states quadratures and derived quantities, such as the mean and the variance, and measure quadrature squeezing:

$$\langle \hat{N}_{21} \rangle = \langle \alpha_{LO} \left(\hat{a}e^{-i\theta} + \hat{a}^{\dagger}e^{i\theta} \right) \rangle = \alpha_{LO} \langle \hat{q}_{\theta} \rangle \tag{5.10}$$
$$\Delta^2 \hat{N}_{21} = \langle \hat{N}_{21}^2 \rangle - \langle \hat{N}_{21} \rangle^2 \tag{5.11}$$
$$\Delta^2 \hat{N}_{21} = \alpha_{LO}^2\, \Delta^2 \hat{q}_{\theta} \tag{5.12}$$

In practice, the retrieved homodyne signal $\mathcal{N}_{21}^{\tau}$ corresponds to the subtraction of the photocurrents i_j generated by each detector integrated over the time response of the detector [Cooper 13, Raymer 95]:

$$\mathcal{N}_{21}^{\tau} = \int_0^{\tau} dt \, \left(\hat{i}_2 - \hat{i}_1 \right) \tag{5.13}$$

Where τ is the response time of the detector. If we want to measure a signal corresponding to the time of a single pulse, the integration time should be shorter than the time between consecutive pulses.

5.2 Noise and Losses in Homodyne detection

5.2.1 Non-Ideal Photodetection

The subtraction of the photocurrents allows to cancel the classical noise of the LO if the balanced-detection setup is properly aligned. But let us consider the case of a non-ideal homodyne detection. The simplest derivation consists in modeling a non-ideal

photodetection by a leaking beam splitter (BS) of transmission η placed on the signal path ($\hat{a}$ in fig. 5.1) before the beamsplitter of the homodyne [Leonhardt 97]. One port of the leaking BS receives the signal field and the other one receives vacuum $\hat{a}_0$ such that:

$$\hat{a}' = \sqrt{\eta}\,\hat{a} + \sqrt{1-\eta}\,\hat{a}_0 \tag{5.14}$$

We adapt the homodyne operators defined in equations 5.1 and 5.2 using the equation 5.14 and we compute the photon numbers:

$$\hat{N}'_1 = \frac{1}{2}(|\hat{a}_{LO}|^2 + |\hat{a}'|^2 - \hat{a}^\dagger_{LO}\hat{a}' - \hat{a}'^\dagger\hat{a}_{LO}) \tag{5.15}$$

$$\hat{N}'_2 = \frac{1}{2}(|\hat{a}_{LO}|^2 + |\hat{a}'|^2 + \hat{a}^\dagger_{LO}\hat{a}' + \hat{a}'^\dagger\hat{a}_{LO}) \tag{5.16}$$

We replace $\hat{a}'$ by its expression and make the hypothesis that $\langle\hat{a}^\dagger_{LO}\hat{a}_{LO}\rangle \gg \langle\hat{a}^\dagger\hat{a}\rangle$ to replace $\hat{a}_{LO}$ with its mean α_{LO}. We obtain the following photon-number subtraction:

$$\hat{N}'_{21} = \alpha_{LO}\sqrt{\eta}\,\left(\hat{a}e^{-i\theta} + \hat{a}^\dagger e^{i\theta}\right) + \alpha_{LO}\sqrt{1-\eta}\left(\hat{a}_0\,e^{-i\theta} + \hat{a}^\dagger_0\,e^{i\theta}\right) \tag{5.17}$$

$$= \alpha_{LO}\left(\sqrt{\eta}\,\hat{q}_\theta + \sqrt{1-\eta}\,\hat{q}_{0,\theta}\right) \tag{5.18}$$

The vacuum is a state of mean $\langle\hat{q}_{0,\theta}\rangle = 0$ and variance $\Delta^2\hat{q}_{0,\theta} = 1$ (eq. 2.13) for all values of θ. We find the same equation as in 5.9 with an added term that takes into account the vacuum contribution. When the quantum efficiency is large, i.e. $\eta > 90\%$, the added vacuum noise can be neglected.

This derivation does not take into account the fact that the photodiodes are not identical. In a more complete description, we can model the losses by two leaking BS placed before each photodiode ($\hat{a}_1$ and $\hat{a}_2$ in fig. 5.1). In this case, we have:

$$\hat{a'}_1 = \sqrt{\eta_1}\,\hat{a}_1 + \sqrt{1-\eta_1}\,\hat{a}_{v1} \tag{5.19}$$

$$\hat{a'}_2 = \sqrt{\eta_2}\,\hat{a}_2 + \sqrt{1-\eta_2}\,\hat{a}_{v2} \tag{5.20}$$

$$\tag{5.21}$$

where $\hat{a}_{v1}$ and $\hat{a}_{v2}$ are the annihilation operators of the vacuum interfering with the signals impinging on the photodiodes. $\eta_1 \neq \eta_2$ indicates that the losses at the PD are not necessarily the same and the operators $\hat{a'}_1$ and $\hat{a'}_2$ are defined in order to conserve the commutation relations. We compute the photon numbers:

$$\hat{N'}_1 = \eta_1 \hat{N}_1 + (1-\eta_1)\,|\hat{a}_{v1}|^2 + \sqrt{\frac{\eta_1(1-\eta_1)}{2}}\left[\left(\hat{a}^\dagger - \hat{a}^\dagger_{LO}\right)\hat{a}_{v1} + \hat{a}^\dagger_{v1}\,(\hat{a}-\hat{a}_{LO})\right] \tag{5.22}$$

$$\hat{N'}_2 = \eta_2 \hat{N}_2 + (1-\eta_2)\,|\hat{a}_{v2}|^2 + \sqrt{\frac{\eta_2(1-\eta_2)}{2}}\left[\left(\hat{a}^\dagger + \hat{a}^\dagger_{LO}\right)\hat{a}_{v2} + \hat{a}^\dagger_{v2}\,(\hat{a}+\hat{a}_{LO})\right] \tag{5.23}$$

and the photon-number subtraction:

$$\begin{aligned}\hat{N'}_{21} = \eta_2\hat{N}_2 - \eta_1\hat{N}_1 + (1-\eta_2)|\hat{a}_{v2}|^2 - (1-\eta_1)|\hat{a}_{v1}|^2 + \\ \sqrt{\frac{\eta_2(1-\eta_2)}{2}}\left[\left(\hat{a}^\dagger + \hat{a}^\dagger_{LO}\right)\hat{a}_{v2} + \hat{a}^\dagger_{v2}\,(\hat{a}+\hat{a}_{LO})\right] - \\ \sqrt{\frac{\eta_1(1-\eta_1)}{2}}\left[\left(\hat{a}^\dagger - \hat{a}^\dagger_{LO}\right)\hat{a}_{v1} - \hat{a}^\dagger_{v1}\,(\hat{a}-\hat{a}_{LO})\right]\end{aligned} \tag{5.24}$$

We can see that in this case, the signal is not simply the sum of the contributions of the vacuum and the signal of interest. But, here also, the contribution of the vacuum noise can be neglected when the quantum efficiency is large, i.e. $\eta > 90\%$. In general, $\eta_1 \simeq \eta_2$ and we retrieve the equation 5.17.

The overall detection efficiency depends not only on the photodiode efficiency but also on the electronic noise of the detector as well as the quality of the interference between the beams before the photodiodes, such that:

$$\eta = \eta_{mod} \times \eta^2_{PD} \times \eta_{elec} \tag{5.25}$$

Where η_{mod}, which we will define in section 5.2.3, depends on the visibility of the interference between the signal of interest and the LO. η_{PD} is the photodiode efficiency corresponding to the efficiency of the photon-to-electron conversion. It depends on the photosensitivity S of the photodiode by the following equation:

$$\eta_{PD}(\omega) = S_{PD} \times \frac{\hbar\omega}{e} \tag{5.26}$$

Where $\hbar = 1.054\times10^{-34}$ J.s is the reduced Planck constant and $e = 1.602\times10^{-19}\,C$ is the elementary charge. The photodiode efficiency also depends on the angular frequency ω of the incoming light and is limited by the photodiode material. Silicon (Si) gives the best performances around 800 nm.

Finally, we need to take into account the electronic noise of the detector. In [Appel 07], it is shown that the effect of the electronic noise on the detector performances is equivalent to that of optical losses. Thus, it can be associated to an efficiency and reads [Kumar 12]:

$$\eta_{elec} = 1 - \frac{\sigma_{en}^2}{\sigma_o^2} \tag{5.27}$$

Where σ_{en}^2 is the variance of the measured electronic noise and σ_o^2 is the variance of the output signal. In the next section, we will describe the major contributions to the electronic noise in our detector.

5.2.2 Electronic Noise

The electronic noise (EN) is the accumulation of the noise generated by the electrical components of the circuit and perturbations from the detector environment. A direct consequence of EN is to reduce the signal-to-noise ratio of the circuit and so reduce the efficiency η_{elec}. In this section, we will focus on the two main sources of noise in our homoyne circuit, being the thermal noise and the noise of operational amplifiers.

Thermal noise Also called Johnson-Nyquist noise, it depends on the intrinsic impedance of an electrical component and results from the thermal agitation of charge carriers. Resistors are the main source of thermal noise in an electronic circuit. The thermal voltage Δv and current Δi noises are defined by:

$$\Delta v = \sqrt{4\, k_B T\, R} \tag{5.28}$$

$$\Delta i = \sqrt{\frac{4\, k_B T}{R}} \tag{5.29}$$

Where $k_B = 1.3806 \times 10^{-23}$ J.K^{-1} is the Boltzmann constant, R is the resistance and T is the temperature in Kelvin. The voltage noise is usually expressed in nV/$\sqrt{\text{Hz}}$ and the current noise in nA/$\sqrt{\text{Hz}}$. As an example, considering the resistance values in our circuits and a 200-MHz bandwidth, the thermal voltage is comprised between 1 and 6 nV/$\sqrt{\text{Hz}}$ and the current noise between 2 and 3 pA/$\sqrt{\text{Hz}}$. To consider the thermal noise over a given bandwidth Δf, we multiply equations 5.28 and 5.29 by $\sqrt{\Delta f}$.

Noise of an Operational Amplifier Balanced homodyne detectors use operational amplifiers (op-amp) to perform a current-to-voltage conversion of the subtracted photocurrent. The noise of the op-amp comes from the noise of the elements constituting the op-amp, such as transistors, as well as the impedances of the amplifier's inputs, which contrary to the ideal case are not infinite and can display a discrepancy. We worked with three models of amplifiers: the OPA847, OPA855 and LMH6624. The homodyne measurements presented in the chapter 6 were performed with a low-bandwidth detector using a LMH6624 amplifier. Subsequently, we used the op-amps OPA847 and

OPA855 from Texas Instrument in the development of higher-bandwidth detectors. This will be the subject of the chapter 7. We give here the noise parameters of these amplifiers:

	LMH6624	OPA847	OPA855
Δv	0.92 nV/$\sqrt{\text{Hz}}$	0.85 nV/$\sqrt{\text{Hz}}$	0.98 nV/$\sqrt{\text{Hz}}$
Δi	2.3 pA/$\sqrt{\text{Hz}}$	2.5 pA/$\sqrt{\text{Hz}}$	2.3 pA/$\sqrt{\text{Hz}}$

Thus, if we compare the thermal noise calculated in the previous paragraph to the noise of the operational amplifiers, we see that the thermal voltage noise is larger than the voltage noise of the op-amps, but the current noises are of the same order of magnitude.

5.2.3 Mode-Matching Losses

In section 2.3.7, we introduced the mode functions $S(\mathbf{r},\omega)$ and the annihilation operators $\hat{s}$ associated to the squeezed states. In this basis, the monomode electric field reads:

$$\hat{E}^{(+)}_{sq}(\mathbf{r},\omega) = \mathcal{E}\, S(\mathbf{r},\omega)\, \hat{s}\, e^{i\mathbf{k}\cdot\mathbf{r}} \tag{5.30}$$

Where $\mathcal{E} \in \mathbb{R}$ is defined by eq. 2.9. In homodyne detection, low interferometric visibility is another source of losses, which can be modeled by a leaking beamsplitter of transmission η_{mod} placed on the signal phase ($\hat{a}$ in fig. 5.1). It is commonly referred to as mode matching losses and depends on the overlap between the signal mode $S(\mathbf{r},\omega)$ and the mode of the LO. We write $g_{LO}(\mathbf{r},\omega)$ the mode function of the LO and we define an overlap coefficient O [La Volpe 19, Aichele 02]:

$$O = \int d\mathbf{r}\, d\omega\, g_{LO}(\mathbf{r},\omega)\, S^*(\mathbf{r},\omega) \tag{5.31}$$

The quantity O is the measure of the mode matching and it is equal to the quantum efficiency η_{mod} (eq. 5.25), see for instance [Aichele 02, Grosshans 01a]. It corresponds to the square of the visibility of the interferences between the two fields. In this case, the homodyne signal $\hat{N}_{21}$ is given by the equation 5.18 with $\eta = \eta_{mod} = O$.

Unbalanced Beamsplitter We consider the equations 5.1 and 5.2 with an unbalanced homodyne BS, i.e. $r \neq t$ with $r < t$ and $rt < \frac{1}{2}$ in the case where there are no other losses, i.e. $\eta = 1$. The subtracted photon-numbers reads:

$$\hat{N}_{21} = 2rt\left(\hat{a}^{\dagger}\hat{a}_{LO} + \hat{a}^{\dagger}_{LO}\hat{a}\right) + \left(t^2 - r^2\right)\left(|\hat{a}_{LO}|^2 - |\hat{a}|^2\right) \tag{5.32}$$

As $\langle \hat{a}^{\dagger}_{LO}\hat{a}_{LO}\rangle \gg \langle \hat{a}^{\dagger}\hat{a}\rangle$, the subraction can leave a parasitic term if the homodyne beamsplitter is misaligned. Especially, when we work with pulsed light, this term can be very high at the laser repetition rate and saturate the detector.

5.3 Detector Performances

5.3.1 Shot-Noise Clearance

When we characterize a detector with a spectrum analyzer, we first look at the signal when no light is shined on the photodiodes. In this case, the signal is the electronic noise σ^2_{en} corresponding to the noise of the electronic components constituting the detector and the noise of the detection device, in our case a spectrum analyzer or an oscilloscope. Then, we illuminate the photodiodes with the local oscillator. In this case, we measure an output signal σ^2_o corresponding to the sum of the shot noise of the local oscillator σ^2_{SN} and the electronic noise such that $\sigma^2_o = \sigma^2_{SN} + \sigma^2_{en}$. To assess the electronic performances of the homodyne detection, we evaluate the fraction of the electronic noise in the output signal. Usually, it is done by computing the ratio between the variance of the output signal σ^2_o and the variance of the electronic noise σ^2_{en}. This quantity is called the *shot-noise clearance* (SNC) and is defined as [Raffaelli 18, Kumar 12]:

$$SNC = \frac{\sigma^2_o}{\sigma^2_{en}} \tag{5.33}$$

In the previous sections, we mentioned that the electronic noise could be modeled as an additional loss channel of efficiency η_{elec} (section 5.2.1). From the equation 5.27, we can write the following relation between the shot-noise clearance of the detector and the electronic efficiency:

$$\eta_{elec} = 1 - \frac{1}{SNC} \tag{5.34}$$

In practice, we measure the power spectrum of the signal and of the noise with a spectrum analyzer and we define the subtraction of the measured signals as a shot-noise clearance in dB:

$$SNC_{dB} = 10 \times \mathrm{Log}_{10}\left(SNC\right) \tag{5.35}$$

The SNC is a very important parameter of a homodyne detector. The higher it is, the better the measurement, as we can see from equation 5.34.

5.3.2 Common-Mode Rejection Ratio

In homodyne detection, the light detected by the photodiodes is converted into photocurrents which are then subtracted. This difference signal is the one we are interested in, it is proportional to the quadrature of the field we want to measure. To assess the quality of the subtraction, we shine light on each PD individually. We call the corresponding signal the common mode (CM). Then, we compare the CM with the signal we measure when both PDs are illuminated at the same time. The ratio between the two quantities is called the common-mode rejection ratio (CMRR):

$$\mathrm{CMRR} = \frac{\sigma_{CM}^2}{\sigma_d^2} \tag{5.36}$$

where σ_{CM} denotes the common mode signal and σ_d denotes the difference signal. In the pulsed regime, the laser source emits a train of pulses at the repetition rate f_{rep}. In the spectral domain, this means that the signal features a peak at f_{rep}. In this case, we need to reduce the light power on each PD in order not to saturate the electronic of the detector when we measure the signal from one PD. Often, in this configuration, the signal is very low at all frequencies except at the repetition rate, so we define the CMRR as the ratio between the common mode at f_{rep}, i.e. when one PD is illuminated, and the difference signal at the same frequency. In practice, we measure the power spectrum with a spectrum analyzer so we retrieve signals in dB scale. In this case, we define a CMRR_{dB} as:

$$\mathrm{CMRR}_{dB} = \left| 10\,\mathrm{Log}_{10}\left(\frac{\sigma_{CM}^2}{\sigma_{ref}^2}\right) - 10\,\mathrm{Log}_{10}\left(\frac{\sigma_d^2}{\sigma_{ref}^2}\right) \right| \tag{5.37}$$

where $P_{ref} = \frac{\sigma_{ref}^2}{R}$ is the reference electric power used by the spectrum analyzer to compute the gain and σ_{ref} is the inferred voltage. Its value depends on the measuring device scale (usually $P_{ref} = 1$ mW for a dBm scale and $R = 50\,\Omega$). In the pulse regime, a good CMRR should be in the order of 30 dB [Kumar 12].

5.4 Noisy Squeezing Levels

When we characterize a homodyne detector, we use the local oscillator only, so the mode-matching efficiency η_{mod} is not part of the total quantum efficiency η, i.e. $\eta_{mod} = 1$.

As we mentioned in section 5.3.1, we measure the SNC to assess the performances of the detector in term of η_{elec}. The figure 5.2 shows the relation between the efficiency

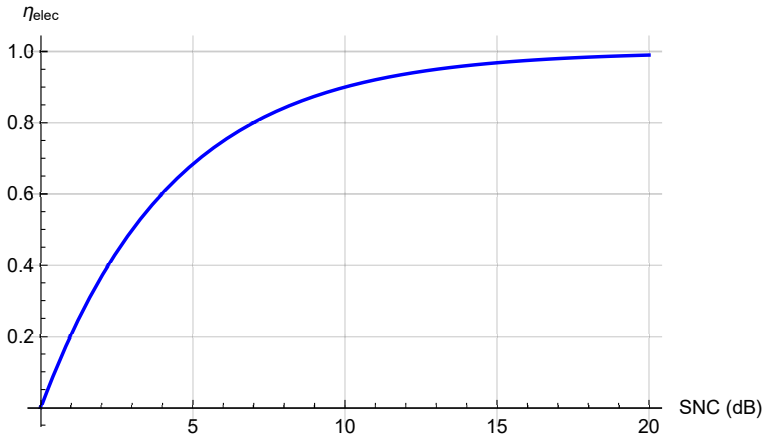

Figure 5.2 – Evolution of the detection efficiency η_{elec} with the clearance (SNC).

η_{elec} and the shot-noise clearance (SNC). We stress that even in the case where $\eta_{mod} = \eta_{PD} = 1$, it exists a minimum value of SNC_{dB} for which $\eta_{elec} > 90\%$.

In figure 5.3, we show the impact of the detector clearance on the measured squeezing. All curves reach a plateau at some point, indicating the minimum SNC required for good homodyne measurements according to the expected level of squeezing.

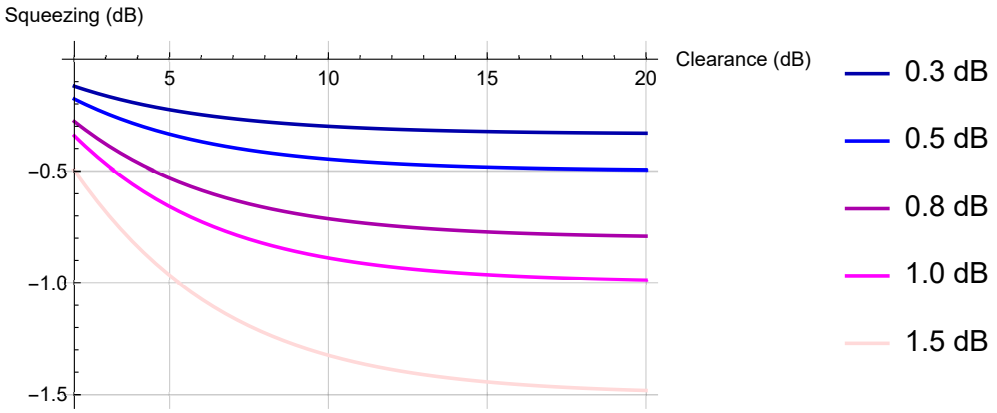

Figure 5.3 – Evolution of the measured squeezing levels with the SNC considering $\eta_{PD} = 1$ and $\eta_{mod} = 1$. Each curve corresponds to a different expected squeezing level.

5.5 Examples of Homodyne Detections in the Multimode Regime

5.5.1 Mode-Selective Homodyne Detection

The mode-selective homodyne detection allows to measure the quadratures of a selected mode of a multimode field by shaping the local oscillator. In chapter 6, we will present the generation of multimode squeezed states by parametric down conversion and use pulse shaping (presented in chapter 4) to shape the spectrum of the LO and measure different squeezed modes. In this case, the number of squeezed modes that we can measure is limited by the spectrum of the LO and the homodyne signal depends on the overlap of the squeezed field with the mode of the LO. As an example, we consider in this section the squeezed-mode basis introduced in section 2.3.7. In section 5.2.3, we wrote the monomode field. In the multimode case, we have:

$$\hat{E}^{(+)}_{sq}(\mathbf{r},\omega) = \mathcal{E} \sum_j S_j(\mathbf{r},\omega)\, \hat{s}_j\, e^{i\mathbf{k}\cdot\mathbf{r}} \tag{5.38}$$

Where $\hat{s}_j$ is the annihilation operator associated to the mode j and S_j is the mode function. We write $g_{LO}(\mathbf{r},\omega)$ the mode function of the LO as in section 5.2.3 and we use the overlap coefficient O_j (eq. 5.31) describing the interference between the local oscillator and the mode S_j as:

$$O_j = \int d\mathbf{r}\, d\omega\, g_{LO}(\mathbf{r},\omega)\, S_j^*(\mathbf{r},\omega) \tag{5.39}$$

If, e.g., the LO mode matches the mode S_1, the overlap with the other modes S_j of the basis is null and we measure the quadrature associated to this mode. But, if the LO mode function overlaps with several modes, then we would perform a homodyne measurement of a superposition of modes.

5.5.2 Multipixel Homodyne Detection

Multipixel homodyne detection was introduced in [Beck 00] for quantum state tomography in the spatial domain. It allows for the simultaneous measurement of modes of an electric field. This technique requires the different modes to be physically separated prior to the detection, hence it is not suitable for all mode basis. The modes are indeed separated in the case of, e.g., a diffraction grating when the targeted modes are the frequency modes. The measurement is then a spectrally-resolved homodyne detection.

This technique is interferometric and corresponds to several homodyne detections performed simultaneously. The signal light is combined with the local oscillator at a

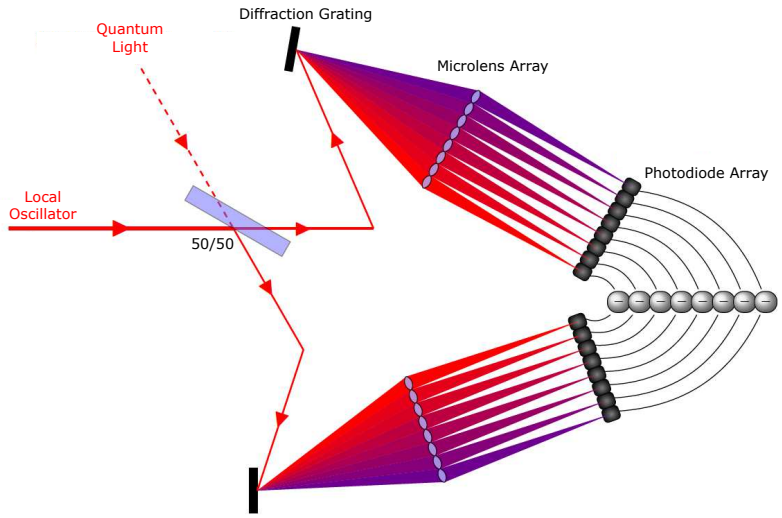

Figure 5.4 – Schematics of a multipixel detection [Dufour 18].

balanced beam splitter and the two interference beams are sent to a diffraction grating. The diffracted light corresponds to many homodyne signals separately focused on distinct photo-detectors thanks to an array of micro-lenses (fig. 5.4).

The overall homodyne signal is the collection of N measurements, with N corresponding to the number of photodectors of the multipixel homodyne detector. As the subraction of the photocurrents gives a signal proportional to the mode quadrature $\hat{q}_\theta$ (equation 5.9), a multipixel detection with N photo-detectors allows to measure $\frac{N}{2}$ quadratures at once.

Chapter 6

Experimental Realisation of Multimode Squeezed Vacua

Contents

6.1 Towards the Generation of Dual-Rail Cluster States 87
6.2 Laser Source 89
6.3 Bulk Non-Collinear Parametric Down Converter 89
6.3.1 Second Harmonic Generation 90
6.3.2 Type-I Parametric Down Conversion in Free Space 91
6.4 Guided Parametric Down Conversion 97
6.4.1 Numerical Analysis 98
6.4.2 Waveguide Chips 105
6.4.3 Waveguide Characterization 107
6.4.4 Reveal SPDC in PPKTP waveguides 108
6.4.5 Squeezing Measurements 109

6.1 Towards the Generation of Dual-Rail Cluster States

Optical cluster states [Briegel 01] are quantum networks, in which the nodes are different modes of the field in quantum states connected to each other by entanglement links according to a specific graphical pattern determining the shape of the cluster (fig. 6.2). They are at the basis of measurement-based quantum computation (MBQC) [Raussendorf 01, Raussendorf 03]. Such states have already been produced experimentally, in our group [Cai 17] and by several other groups in the world [Chen 14, Yokoyama 13]. Here, we are particularly interested in the scheme developed by the group of A. Furusawa that generated the largest cluster by using temporal modes [Yokoyama 13]. Figure 6.1 shows the experimental setup used to generate such dual-

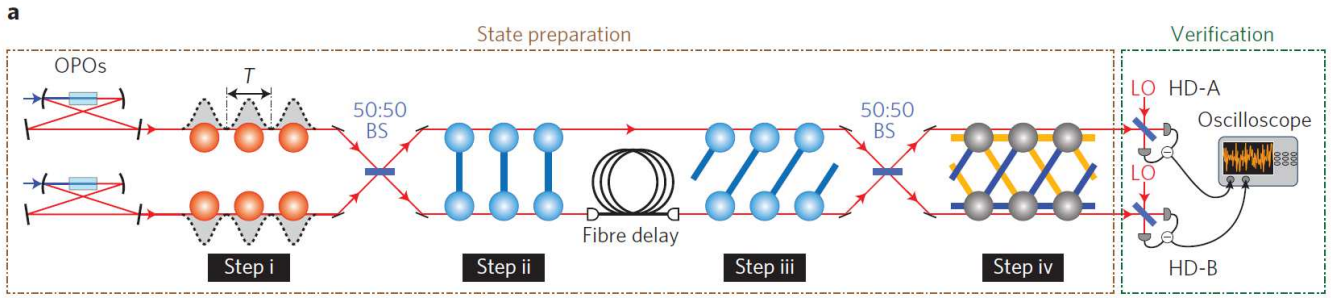

Figure 6.1 – Schematics of the experimental setup used in [Yokoyama 13] to generate dual-rail cluster states

rail cluster states. First, two OPO (Optical Parametric Oscillators) are pumped with a continuous-wave (CW) laser and generate two squeezed vacua. The squeezed beams are divided in time bins of duration T, corresponding to the lifetime of the OPO cavity, so that the time bins define independent squeezed states. The squeezed states are combined at a balanced beamsplitter (BS) to generate a series of EPR states separated by T (see sections 2.3.1 and 2.3.2). At this stage, the correlations between the nodes are represented by blue lines. To generate the dual-rail shape, an optical fiber is used to delay the time bins with respect to each other of a duration T. Afterwards, the beams are interfered on another 50/50 beamsplitter to create additional entanglement links (step iv). The output state, shown on figure 6.2, is measured by homodyne detection. It consists of more than 10^4 entangled time bins multiplexed in the time domain.

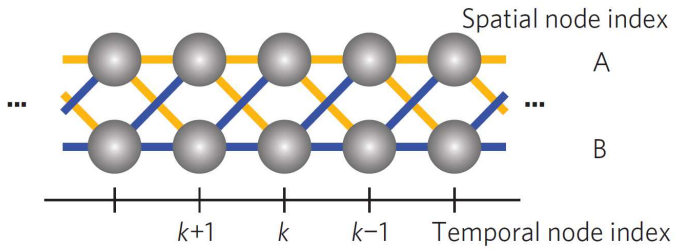

Figure 6.2 – Schematic of dual-rail cluster state [Yokoyama 13]. The nodes are the time bins and the lines represent entanglement links.

In the following sections, we will describe two different sources of multimode squeezed states of light. First, we will present the non-collinear and single-pass generation of entangle pulses via spontaneous parametric down conversion (SPDC) in a bulk nonlinear crystal (section 6.3). Then, we will present the development in parallel of two experiments of SPDC inside waveguides of PPKTP, in type 0 and type II configurations

(section 6.4). The general idea behind our schemes for future experiments is not only to reproduce the dual-rail cluster by using our pulses as time modes, but also to exploit larger sets of modes that correspond to the Hermite-Gaussian basis of our source.

6.2 Laser Source

Our light source is a Femtosource Synergy+ from Spectra-Physics. It is a femtosecond Titanium-Sapphire (Ti:Sa) laser delivering 25-fs pulses at a repetition rate $f_{rep} = 156$ MHz ($\tau_{rep} \simeq 6$ ns). In the spectral domain it corresponds to a spectrum of about 40 nm FWHM centered at 795 nm, the carrier wavelength. The laser cavity shown

Figure 6.3 – Captioned picture of the Synergy laser cavity.

in figure 6.3 is pumped with 5W of a horizontally polarized continuous-wave (CW) Finesse-Pure-CEP laser from Laser Quantum at 532 nm. At the cavity output, the light is horizontally polarized as well and the average IR power is about 0.9 W. Details about the cavity components, alignement and dispersion compensation can be found in [La Volpe 19].

6.3 Bulk Non-Collinear Parametric Down Converter

This setup was developed during the Ph.D. of L. La Volpe [La Volpe 19] and I have been involved in the design and the experiment. The IR beam is divided in two parts at the laser output. As shown in figure 6.4, one part (40 %) goes to an Ultrafast Pulse Shaper (see chapter 4) and is used as a reference while the rest (60%) is the pump for the experiment.

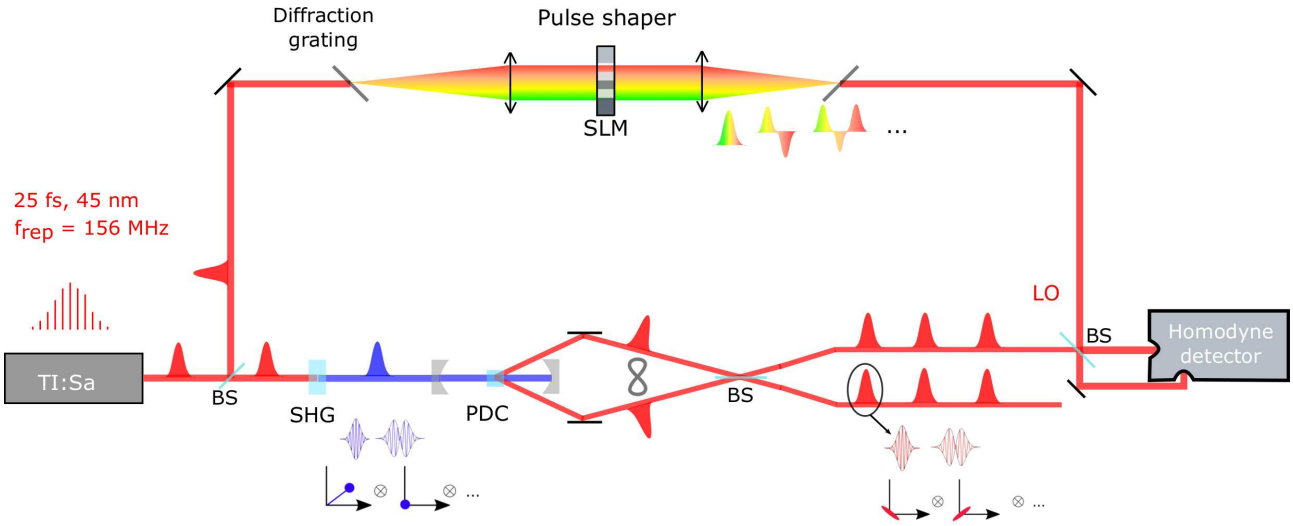

Figure 6.4 – Schematics of the PDC experiment in bulk BBO. At the output of a mode-locked Titanium Sapphire (Ti:Sa) laser centered at 795 nm the beam is separated in two parts. One part is the reference beam for the homodyne detection and the other part goes through the experiment. At each step, the corresponding states are displayed in the phase space. Homodyne detection is used for state characterization. BS: beam splitter; SHG: second harmonic generation; PDC: parametric down conversion; SLM: spatial light modulator; LO: local oscillator.

6.3.1 Second Harmonic Generation

The spectrum of the pump of the PDC is 1.9 nm FWHM centered at 397.5 nm. It is set by a second harmonic generation (SHG) process through a 1-mm long BiBO crystal (Bismuth Triborate) pumped with the 45-nm spectrum Ti:Sa laser. The positive biaxial crystal (section 3.1) is pumped by the horizontally-polarized IR laser. The phase-matching associated to this process is critical, depending on an angle θ between the beam polarization and the optical axis of the nonlinear medium (see section 3.5.3.1). Moreover, the incoming beam undergoes *spatial walk-off*. Indeed, when its polarization is parallel to the optical axis of the nonlinear crystal, the birefringence of the medium causes the intensity distribution, described by the Poynting vector $\vec{S}$, to drift away from the propagation direction $\vec{k}$ of an incoming beam. This is the spatial or birefringent walk-off (see chapter 3), described by an angle ρ between $\vec{S}$ and $\vec{k}$ [Gehr 98] and defined by:

$$\rho(\theta,\omega) = -\frac{1}{n(\theta,\omega)}\frac{\partial\, n(\theta,\omega)}{\partial\theta} \tag{6.1}$$

Where $n(\theta = 0,\omega) = n_e(\omega)$ is the extraordinary index 3.1. Even if, the spatial walk-off is usually of a few milliradians, the second-harmonic beam has an elliptical shape, which is compensated with a pair of anamorphic prisms.

6.3.2 Type-I Parametric Down Conversion in Free Space

The up-converted pulses are injected into a linear optical cavity with a bow-tie geometry to enhance the pump power and so the gain of the PDC process. In order to adjust the size of the beam at the cavity input, we use a telescope on its path. We built it with curved mirrors to avoid additional dispersion that can be caused by lenses. The cavity is composed of four mirrors including two curved mirrors $M1$ and $M2$ with radius $R = 200$ mm that have been chosen to reach a beam waist of 50 μm (see fig. 6.5) [La Volpe 19, Siegman 86]. The length of the optical cavity selects the spectral components that can resonate in it and, for pulsed light, it is linked to the repetition rate f_{rep} of the laser (see section 1.4). The cavity being linear, we tune its length such that the free spectral range is $FSR = \frac{c}{2\,L_{cav}} \simeq f_{rep}$, with c the speed of light in vacuum, giving $L_{cav} = 0.96$ m.

Inside the cavity, the light accumulates group delay dispersion ($GDD = 876\,fs^2$) in a round trip, which we compensate by placing off-the-shelf negatively chirped mirrors in the beam path. This way, we do not need to use additional optical elements, such as prisms, inside the cavity. We chose $M1$, $M2$ and M_{out} to be negatively chirped mirrors with a suitable compensation per reflection. The correction of the dispersion aims at maintaining Fourier-limited pulses inside the cavity.

The SPDC process occurs in a 2-mm long BBO crystal (β-Barium Borate) placed between $M1$ and $M2$, at the cavity waist. As mentioned in section 3.5.3.2, the phase-

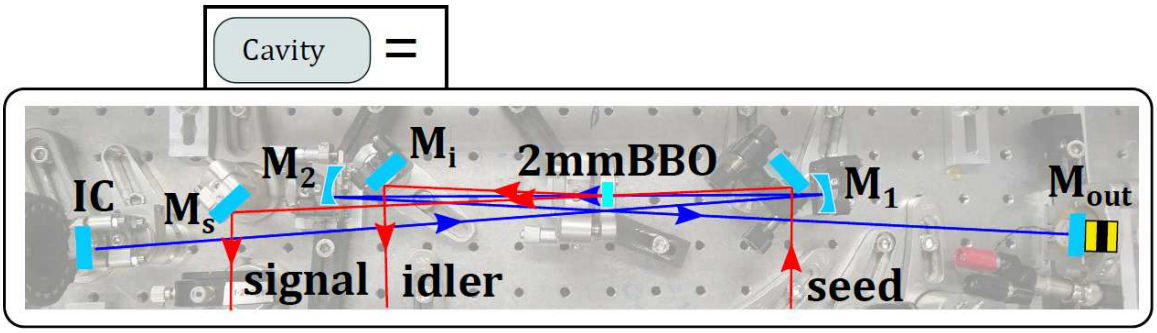

Figure 6.5 – Picture of the PDC cavity with superposed beam paths. The reflectivity R of the mirrors are: $R_{IC} = 98\,\%$ and $R_{M1} = R_{M2} = R_{out} = 99.9454\,\%$. A piezoelectric actuator is fixed on M_{out} [La Volpe 19].

matching is degenerate and non-collinear with an angle $\alpha = 1.8°$ between the direction of each down converted beam and the pump. In this configuration, the down converted light centered at 795 nm does not resonate in the cavity. Squeezed light (single or multimode) is usually generated in OPOs, where the generated light resonates into the cavity in order to increase the parametric gain. In such configurations the limited cavity

bandwidth usually prevents the generation of uncorrelated quantum states belonging to consecutive pulses. On the contrary, the single-pass non-collinear configuration of our setup allows for the generation of two-mode entangled states at the laser repetition rate. For that reason, we say that our setup generates a train of entangled pulses, one belonging to the signal channel and the other belonging to the idler channel. As shown in fig. 6.6 and 6.4, the signal and idler pulses are combined on a 50/50 beamsplitter to perform a basis change producing two single-mode squeezed vacua (SMSV, section 2.3.1). A delay line is inserted in the idler path to match the arrival time of the signal and idler pulses on the BS.

6.3.2.1 Role of the Seed Beam

A small fraction (7 %) of the laser light, the seed beam, is picked up before the SHG and it follows a distinct path to the PDC crystal. A delay line is installed on its path in order to synchronize the arrival time of the pump and seed pulses inside the nonlinear crystal, thus stimulating the single-pass PDC process. After the BBO, the seed follows the path of the signal beam and is used for alignment in the homodyne detection setup (see figure 6.6). For the measurements of squeezed light, the seed beam is blocked.

6.3.2.2 Spectrally-Multimode Squeezed States

To unveil the spectral multimode structure of the down-converted light, we spectrally shape the local oscillator (LO) beam in the homodyne detection with the pulse shaper (chapter 4). As shown in fig. 6.6, we combine the shaped LO with the squeezed vacuum on a balanced beamsplitter (BS) and send the interference light to a homodyne detector. The LO power is 10 mW at the BS corresponding to 5 mW on each homodyne photodiode. The homodyne signal from the detector is sent to a MXA spectrum analyzer from Agilent Technologies. The number of modes we can access is limited by the spectrum of the LO being 36 nm FMWH. If we consider the phase matching of the PDC and do a Schmidt decomposition as described in section 2.3.5, we find a Hermite-Gaussian basis with a first mode of width $\Delta\lambda = 15$ nm [La Volpe 19]. On figure 6.7, we show the overlap of the LO spectrum (in red) with the first and fifth HG modes. We see that the spectrum of the LO is wider than the spectrum of the first mode, indicating that it is possible to shape the LO spectrum to overlap with it. However, we cannot shape the spectrum of the fifth mode with our LO. Although the LO spectrum is wide enough, the spectral intensity of the LO at around 780 nm and 815 nm is too low compared to the level required to shape a HG_4 mode.

In the experiment, we measured quadrature squeezing in only four spectral modes, i.e. the modes HG_0 to HG_3. This is due to the low level of squeezing generated in our experiment that beyond the fourth mode is hidden by the noise of our homodyne detector (see sections 5.2 and 5.4). The measured quadrature variances are shown in

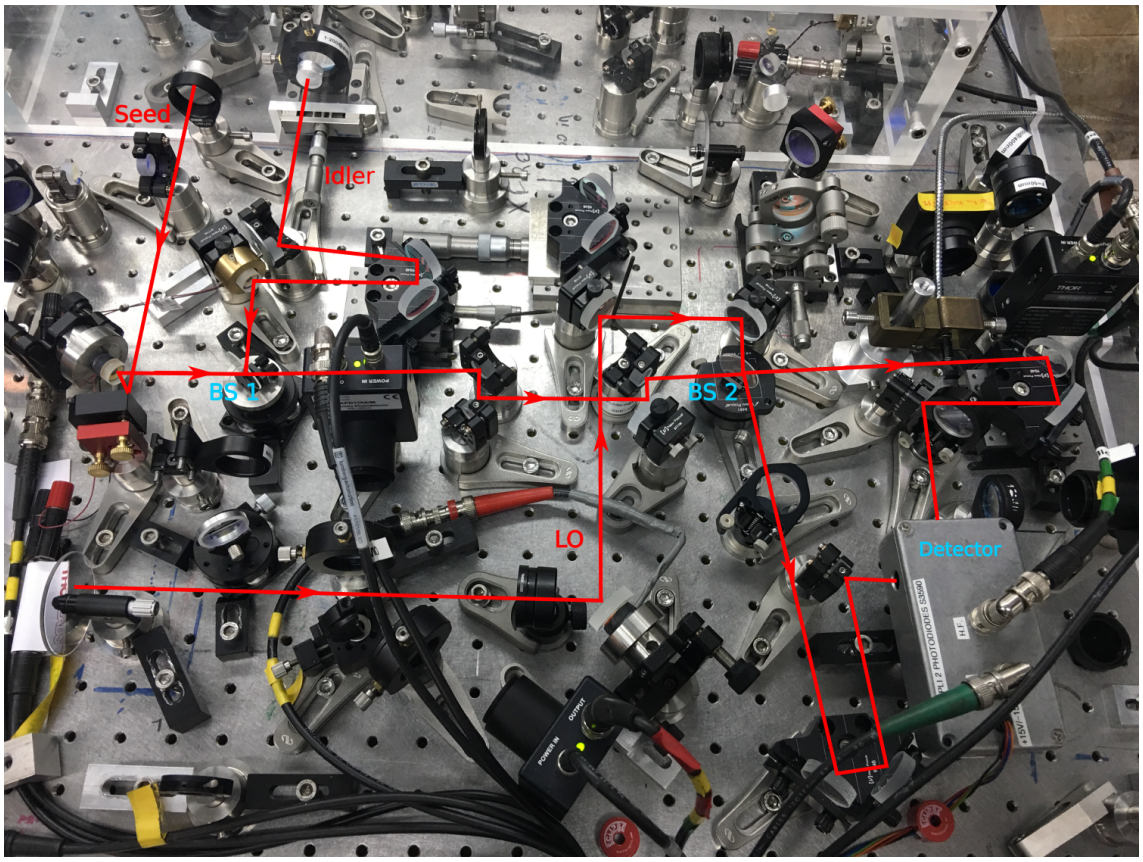

Figure 6.6 – Picture with a superposed scheme of the seed path from the PDC cavity to the Homodyne setup. BS1 is a 50/50 beam splitter used to perform the basis change to generate squeezed light. BS2 is the homodyne beam splitter. The squeezed light is interfered with the local oscillator. Detector: homodyne detector.

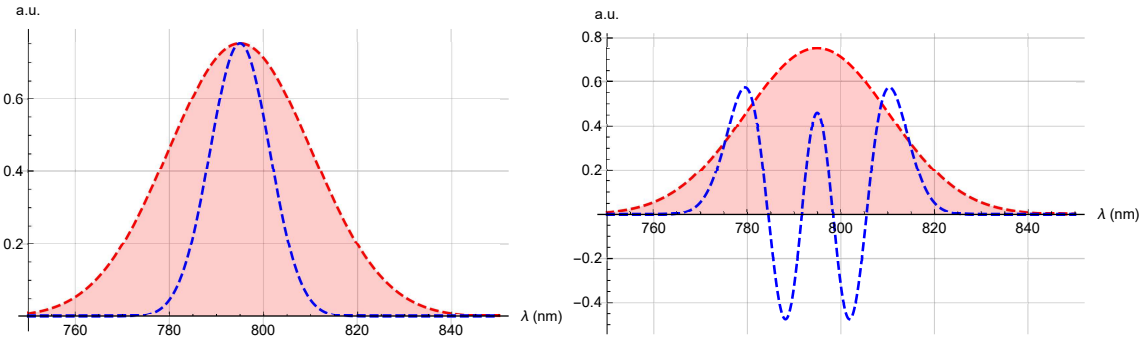

Figure 6.7 – Overlap of the LO spectrum (red curve) with the first and fifth HG modes (blue curve). Left: HG_0; right: HG_4.

figure 6.8. The blue curve indicates the shot-noise level corresponding to the noise of the vacuum state. The orange curve is the homodyne signal when the LO phase is scanned thanks to a piezoelectric actuator placed on the LO path. The amplitude of oscillations depends on the frequency of the ramp signal, here 300 mHz, on the piezo actuator. Each curve is the mean of five measurements traces, corresponding to 5000 data points. To perform these measurements, the pump cavity length is stabilized with a Pound-Drever-Hall lock so as to maximize the PDC emission (fig. 6.5). Details on cavity locking can be found in [Pinel 10, La Volpe 19]. The maximum squeezing is measured in the fundamental mode HG_0, where it is 0.31 dB and approximately the same anti-squeezing. This suggests that the amount of available squeezing is low not because of significant losses in the experiment but rather because we have a low parametric gain associated to the single-pass configuration of our experiment.

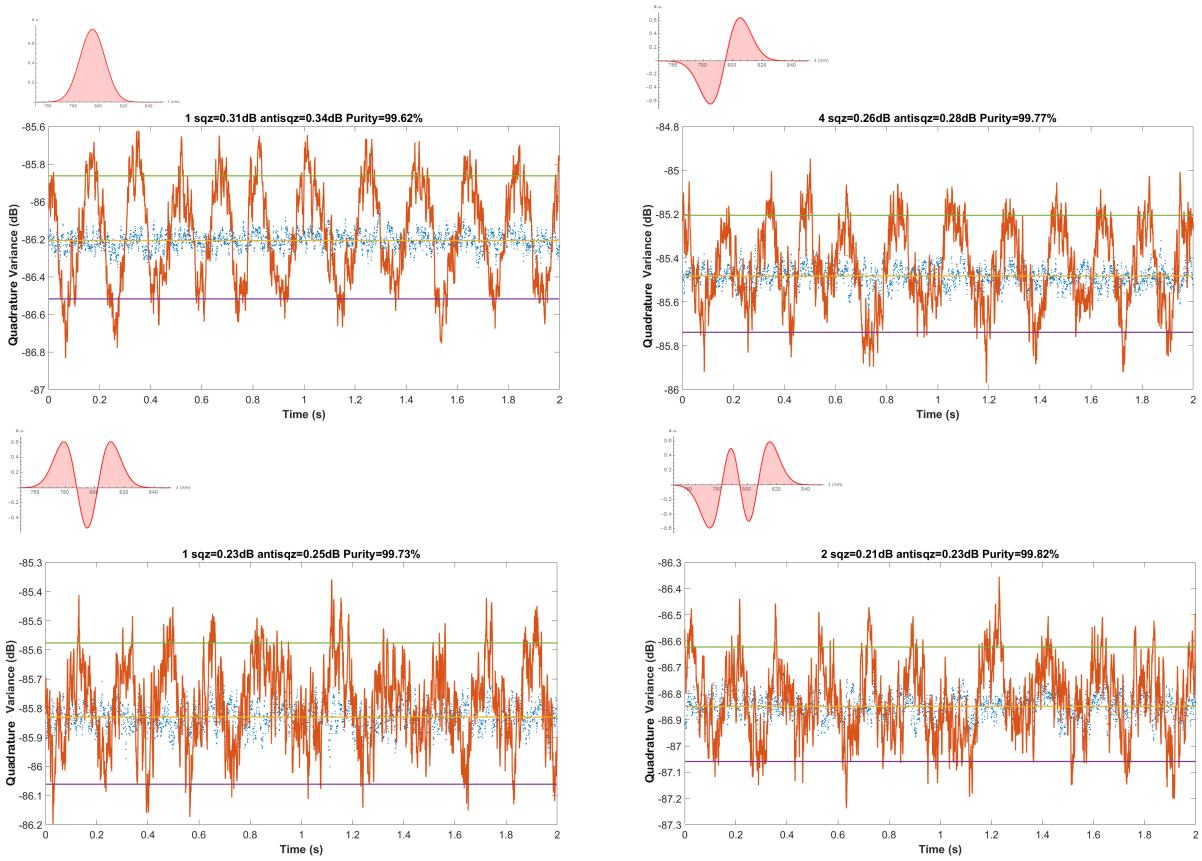

Figure 6.8 – Measurement of four squeezed modes. From top left to bottom right, HG_0, HG_1, HG_2 and HG_3. The blue curve is the shot-noise level, the orange curve is the homodyne signal recorded for 3 seconds while scanning the phase of the LO. The purple line indicates the mean level of squeezing and the green line indicates the mean antisqueezing level [La Volpe 20].

6.3.2.3 Spatio-Temporal Correlations

In the previous section, we presented the measurement of spectrally squeezed modes although the phase-matching of our experiment is non-collinear. In this case, the phase-matching function has spatial and spectral parameters and if we do a Schmidt decomposition as described in section 2.3.5, we obtain a new spatio-spectral Schmidt basis revealing that signal and idler have spectral and spatial correlations. Then, we do a Bloch-Messiah decomposition to calculate the squeezed modes and obtain a basis of spatio-spectral functions, whose first modes are shown on fig. 6.9. The details of this calculation can be found in the thesis of L. La Volpe [La Volpe 19]. The measurement

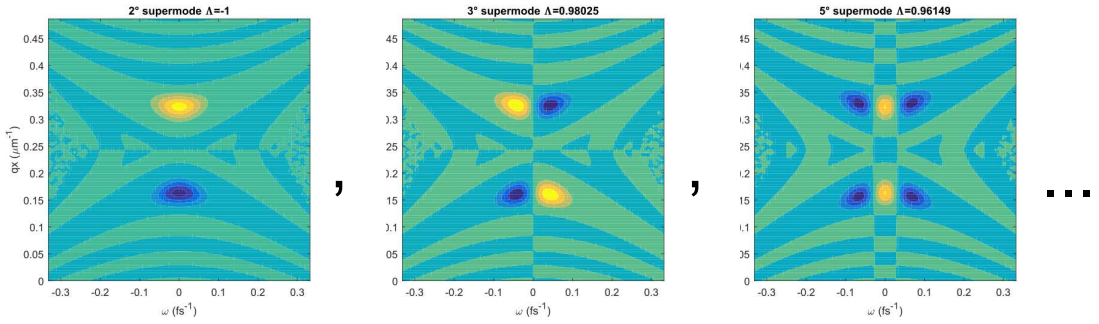

Figure 6.9 – Theoretical spatial-mode basis from the numerical simulation of the experiment [La Volpe 19]. The abscissa is the frequency ω in fs^{-1} and the ordinate is the wavenumber q_x in $\mu\mathrm{m}^{-1}$.

of such modes would require two shapers, one for the LO spectrum and another one for the spatial shape the LO. In the absence of a shaper for the spatial modes, we used a razor blade so as to approach the spatial shape of the first and second modes of fig. 6.9, while the spectrum was shaped with our pulse shaper. We considered a basis of four spatio-spectral modes (fig. 6.10) being distinct to the PDC eigenstates and made from the combination of the HG_0 and HG_1 spectra and two spatial modes, *top* and *bottom* beams. We performed homodyne measurements on these modes and constructed a covariance matrix (see chapter 2 eq. 2.68) to unveil quantum correlations (fig. 6.11 and 6.12).

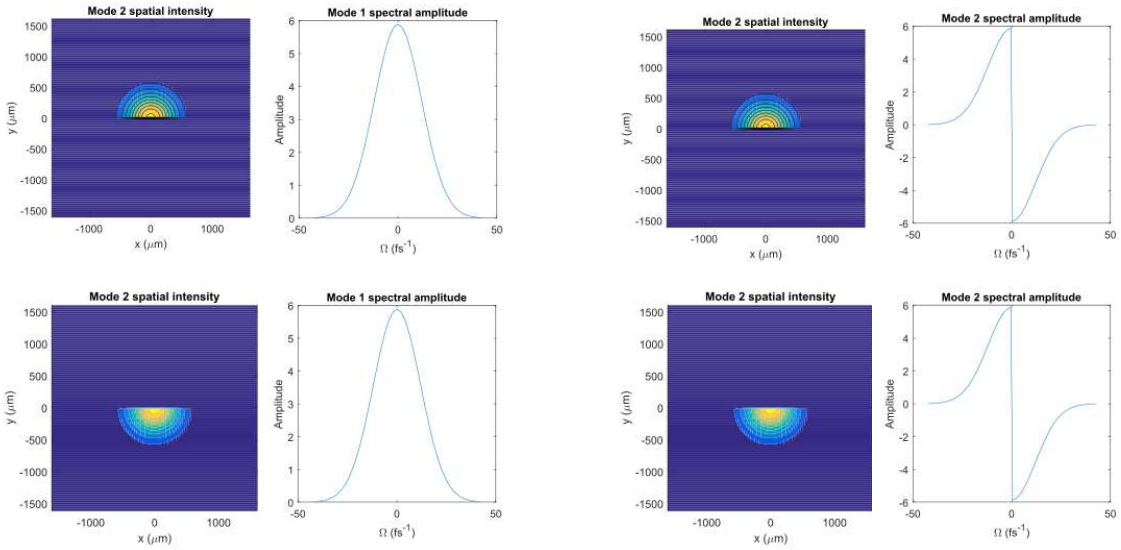

Figure 6.10 – Schematic of the spatio-spectral modes that we measured in our experiment. The abscissa and the ordinate of the spatial shapes is in μm. The abscissa of the associated spectral amplitude is the frequency in fs^{-1} and the ordinate is the amplitude in arbitrary units.

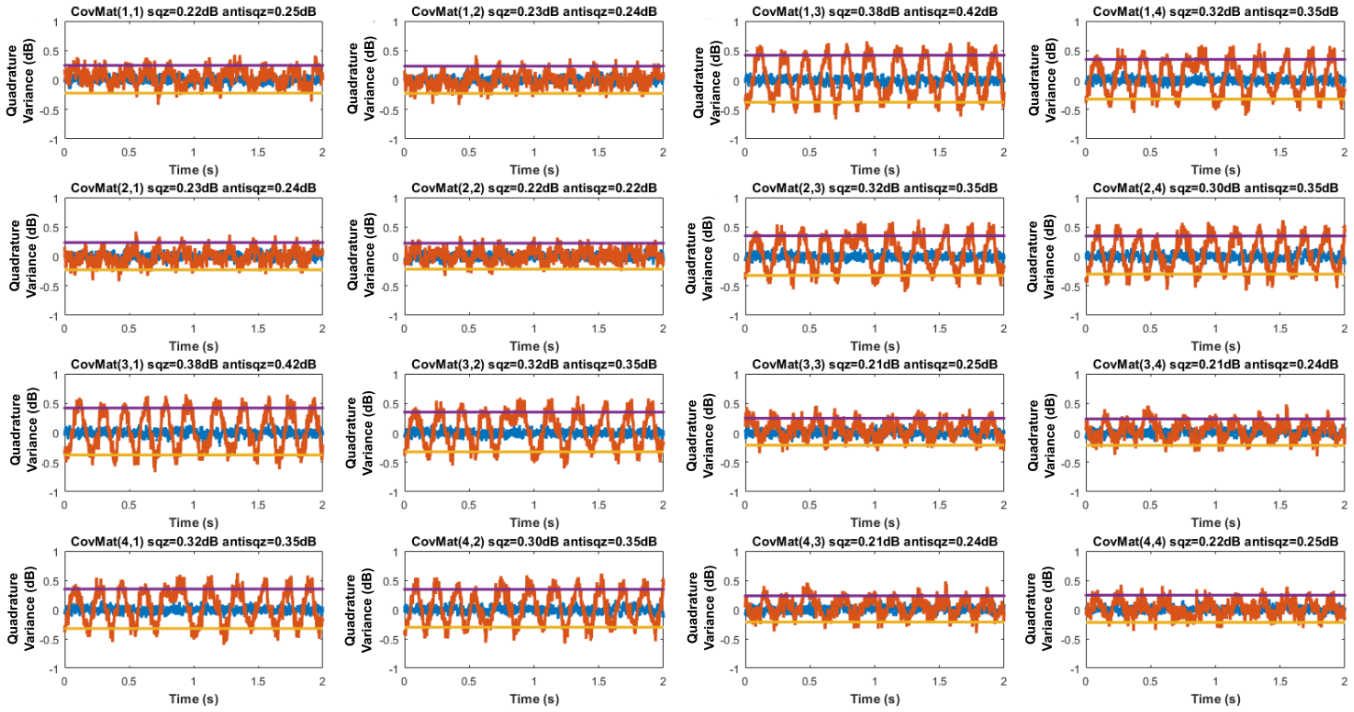

Figure 6.12 – Covariance measurements of the spatio-spectral mode basis. The abscissa is the time in s and the ordinate is the quadrature variance in dB. Each trace is the mean of five measurement traces corresponding to 5000 data points.

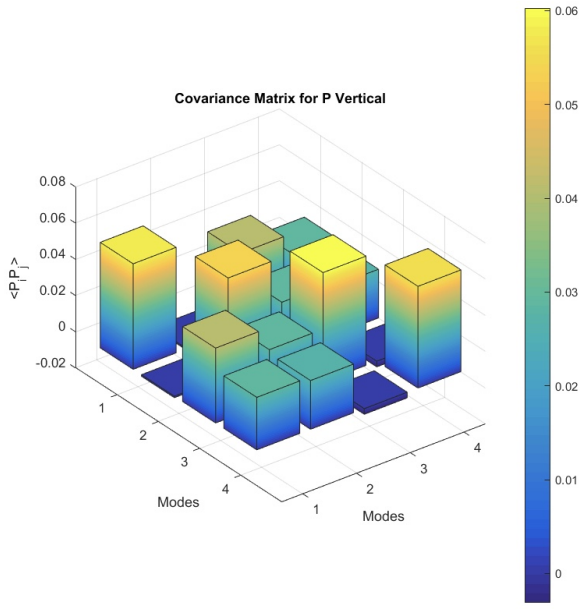

Figure 6.11 – Covariance matrix of the spatio-spectral mode basis.

Although the level of squeezing we measured is low (0.5 dB maximum), the results are promising, revealing the spatially and spectrally multimode structure of the down-converted light. Moreover, the non-zero off-diagonal terms of the covariance matrix (fig. 6.12) suggest the existence of bipartite quantum correlations between the spatio-spectral modes.

In the following section, we will present the development and implementation of parametric down conversion inside a waveguide of periodically-poled KTP.

6.4 Guided Parametric Down Conversion

Although the experiment presented in the last section allowed to generate multimode squeezed states of light at a high rate, the level of available squeezing is low so we can only measure few squeezed spectral modes. Moreover, the maximum level of squeezing measured is lower than that of an OPO experiment [Roslund 14]. Indeed, in the single-pass configuration, the down-converted light does not resonate inside a cavity reducing the gain of the PDC process in the BBO crystal. Additionally, because of the non-collinear phase-matching, the down-converted light is highly multimode in the spatial domain as well, reducing the squeezing per mode.

In order to increase the level of squeezing in our experiment, we chose to replace the bulk BBO crystal with a guided periodically poled KTP (Potassium Titanyl Phosphate). Amoung others, the gain of the PDC depends on the crystal nonlinearity and

the intensity of the pump (eq. 3.50). As presented in the section 3.4.2, for most phase-matching configurations the nonlinearity of the KTP is bigger than that of the BBO. Thus, we decided to develop in parallel two different setups with KTP crystals that explore the collinear type-0 and type-II phase matching configurations respectively. The setups are built on two separate breadboards so that they can be interchangeable and they can replace the BBO setup. While the cross-section of the BBO was 3×3 mm^2 with a pump waist of 50 μm in it, we work with waveguides of 4-μm width, corresponding to an increase of the pump intensity of a factor of 100 if the input pump power is kept the same.

In the type 0 configuration, the signal and idler pulses share the same polarization (section 3.5.3). The output state is a multimode squeezed state in the spectral domain. If we want to produce a train of entangled pulses with a structure similar to the [Yokoyama 13], we would use two type-0 PPKTP waveguides and combine the squeezed output states on a balanced beamsplitter as shown on figure 6.13.

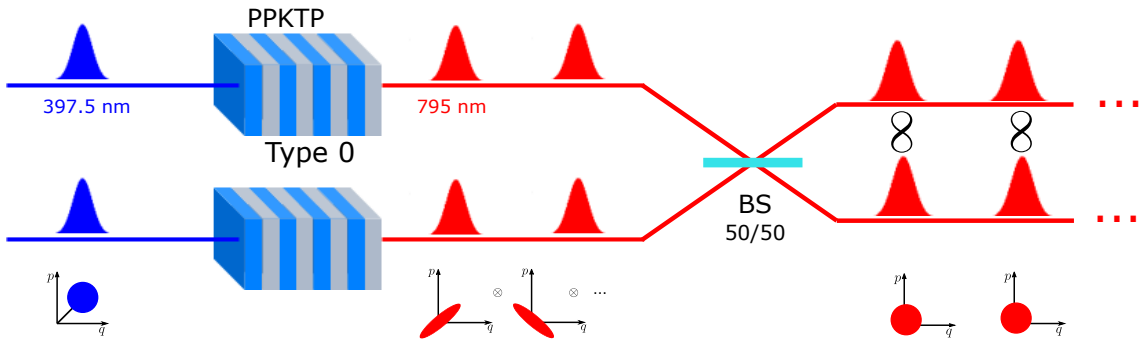

Figure 6.13 – Schematic of the setup for type-0 PDC.

The type-II phase-matching allows the compact and collinear generation of signal and idler beams in orthogonal polarizations. They can be separated with a polarizing beam splitter as shown on figure 6.14. In this configuration, the output state is already a train of entangled pulses, emitted at the repetition rate of our laser, similarly to our experiment with BBO. In practice, we consider using a Glan-Taylor polarizer for the beam separation, to achieve effective 50/50 separation and avoid to have a mixture of H polarized light inside the V polarized one. They are thinner and feature a higher damage threshold than the Glan-Thomson polarizer and the Wollaston prism.

6.4.1 Numerical Analysis

We use a code developed by our collaborators in Paberborn [Brecht 14] to design the waveguides for our experiments. In this section, we will review the parameters influencing the structure of the down-converted light.

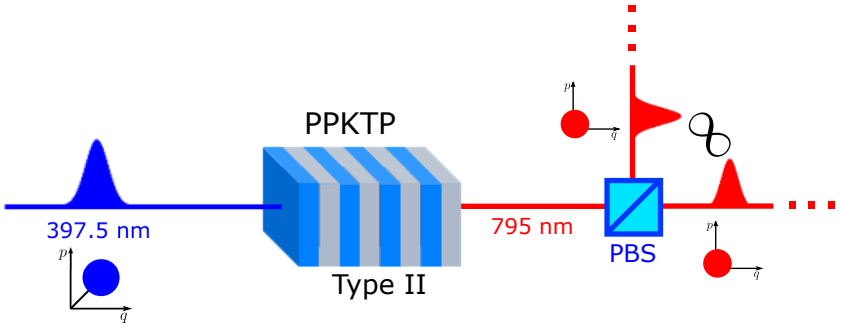

Figure 6.14 – Schematic of the setup for type-II PDC.

6.4.1.1 Differencies Between Type-0 and Type-II PDC

We do a Schmidt decomposition of the PDC process in KTP to determine the eigenmodes of the signal and the idler. We find a mode basis which we can approximate with Hermite-Gaussian functions and whose spectrum depends on the phase-matching. In figure 6.15, we show the first Schmidt modes of types 0 and II PDC. In type 0 phase-matching, signal and idler share the same polarization, they also share the same basis of Schmidt modes. We see in figure 6.15 that the spectrum of the first Schmidt modes perfectly overlap. On the contrary, in the type-II configuration, the spectra of the first modes of signal and idler are slightly different. The difference between their central frequency is $\Delta\lambda_0 = 2$ nm. Moreover, the idler mode is wider than the signal one, the difference between the two spectra is $\Delta\lambda = 3.5$ nm. Indeed, as signal and idler beams are generated in different polarizations in KTP, they experience different refractive indices (eq. 3.81) due to the birefringence of the KTP, which impacts the mode structure. Thus, their mode basis is intrinsically different. However, a possible solution to modify the mode spectrum is proposed in [Roman-Rodriguez 20].

Compared to the spectral modes of the BBO squeezed states, which first mode had a 15-nm spectral FWHM, the first modes from the waveguides would be narrower with $\Delta\lambda_{type0} \sim 9$ nm and $\Delta\lambda_{typeII} \sim 3$ nm. We compared the spectrum of the LO with the HG modes from the Schmidt decomposition for the type 0 and type II phase matchings. Considering the spectra $\Delta\lambda_{type0}$ and $\Delta\lambda_{typeII}$ of the first modes, the goal is to determine how many high-order HG modes we can shape with our local oscillator (section 5.5.1). This would give us an idea of the number of squeezed modes we could measure. In figure 6.16, we show the overlap of the local oscillator spectrum with one Hermite-Gaussian mode of the Schmidt decomposition, HG_{10}, in type 0 and II configurations. We can see that in type-II phase matching, the spectrum of the LO is much larger than that of HG_{10}, but this is not the case in type-0 phase matching, indicating that it is not possible to reproduce this mode with the spectrum of the LO.

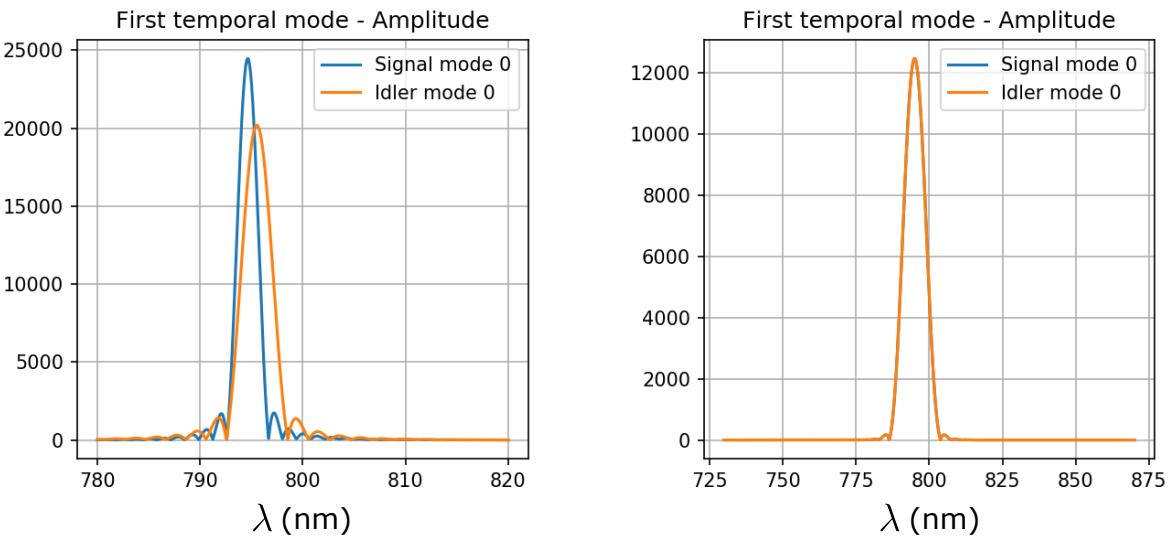

Figure 6.15 – Simulated first Schmidt modes. Left: Type-II phase-matching; Right: Type-0 phase-matching. The signal and idler spectra overlap.

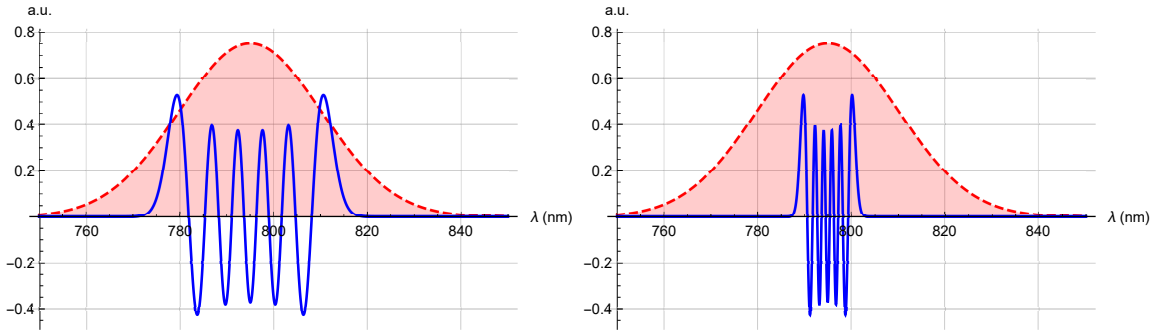

Figure 6.16 – Overlap between Hermite-Gaussian mode HG_{10} and the local oscillator (LO) spectrum. Left: type-0 phase-matching; Right: type-II phase-matching.

6.4.1.2 Waveguide Poling Length

Periodic poling consists in the periodic inversion of the nonlinearity of the birefringent medium. It is used to achieve quasi-phase matching and increase the gain of the PDC (see section 3.5.3.3). The poling length ℓ of a nonlinear crystal corresponds to the interaction length. When we increase ℓ, we increase the intensity of the parametric process [Boyd 08, Ou 07]. From the results of numerical simulations, this gives a larger Schmidt number K (section 2.3.5), i.e. the number of Schmidt modes, which here, we will assimilate to the squeezed ones (fig. 6.17). However, we observe the inverse evolution for the spectral width of the Schmidt modes. Indeed, when the interaction

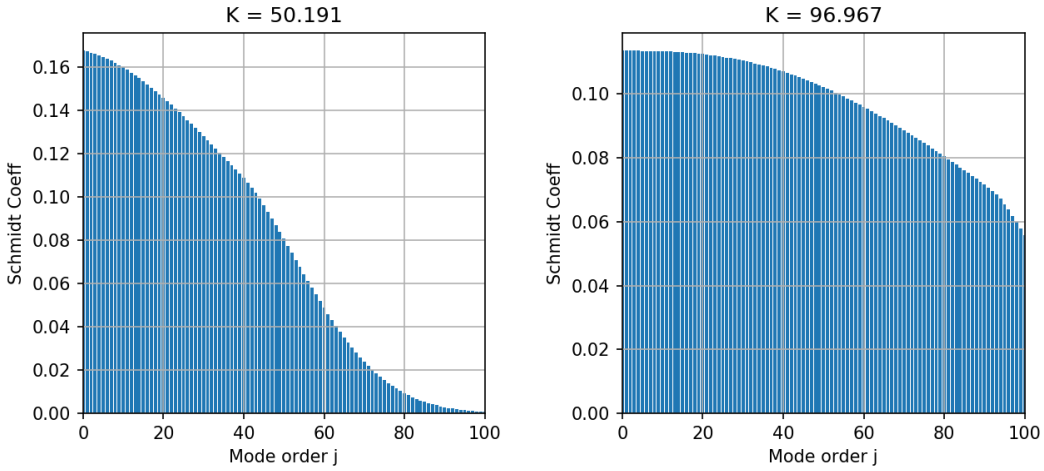

Figure 6.17 – Comparison of the Schmidt number K at two different interaction lengths ℓ in type-0 phase-matching. The spectrum of the pump is fixed to $\Delta\lambda = 1$ nm. Left: $\ell = 500$ μm; Right: $\ell = 1$ mm.

length is increased, the phase-matching function $\text{sinc}\left(\frac{\Delta k(\omega)\ell}{2}\right)$ becomes narrower. There are more modes but each one is spectrally narrower, as can be seen on figure 6.18, where only the first Schmidt modes are plotted for signal and idler in type-0 phase-matching. Although the interaction length contributes to increase the gain of the

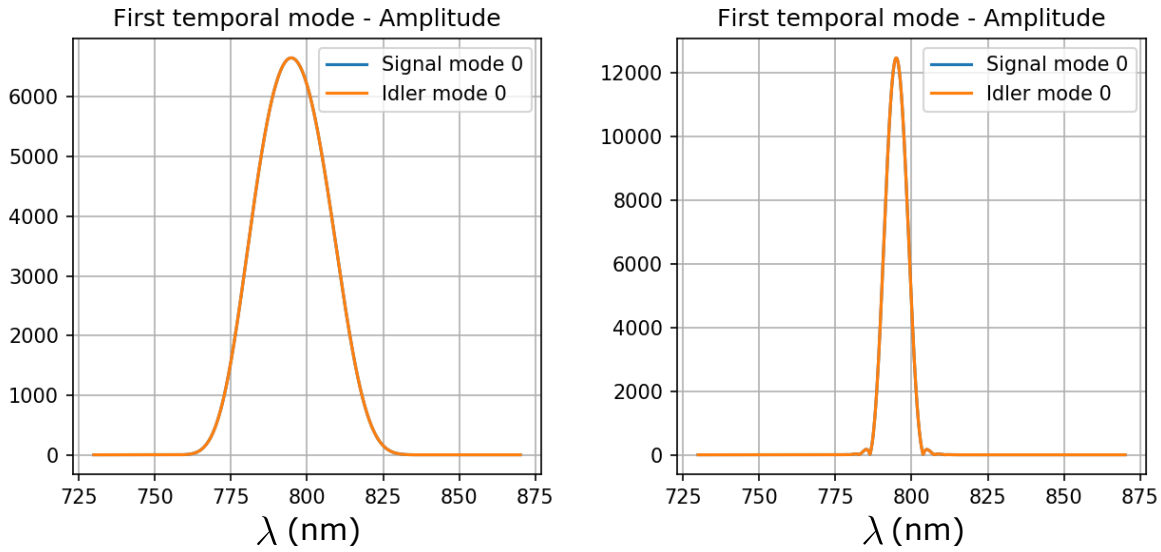

Figure 6.18 – Evolution with the interaction length of the spectral width of the first Schmidt modes. Left: $\ell = 500$ μm; Right: $\ell = 1$ mm.

parametric process (see section 3.5.1), the overall squeezing is distributed among a larger number of modes, which can lead to a lower squeezing level per mode. Therefore, we have to find a trade-off between the number of modes, linked to the level of squeezing per mode, and their spectral width, which fixes the number of modes we can measure by homodyne detection. In the simulations, the interaction length ℓ was varied from 500 μm to 3 mm with a fixed pump spectrum.

6.4.1.3 Pump Spectrum

When the pump is a frequency comb, its spectrum is wider than in the continuous wave regime and the range of pump frequencies experiencing parametric down conversion with the same phase-matching is increased (fig. 6.19). As a result, the down-converted light is also a frequency comb, which spectrum depends on the pump one. Thus, when the pump spectrum is increased, different frequency-matching are possible, according to the energy conservation, resulting in different multimode structure of squeezing (fig. 6.20). From the simulations, it appears that the spectral width of the generated modes evolves inversely to the pump spectrum. Experimentally, this means that we could tune the pump spectrum to slightly increase the number of modes that are accessible via homodyne detection. The reasoning is similar in type-II phase-matching, except

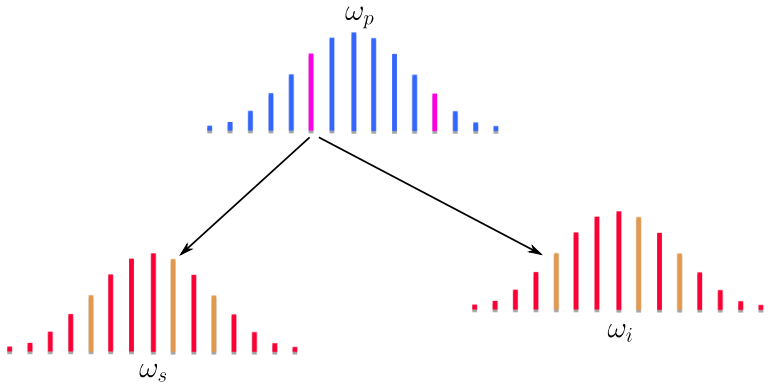

Figure 6.19 – Illustration of parametric down conversion with frequency combs. Each frequency component of the comb can undergo parametric down conversion. As a results the signal and idler beams are frequency combs.

the fact that because signal and idler modes are different (section 6.4.1.1), tuning the pump spectrum can also change their relative central frequency (fig. 6.20 bottom).

6.4.1.4 Influence of Temperature and Dispersion

The temperature has an influence on the inner structure of the nonlinear material. It slightly changes the poling length, modifying the phase-matching. In general, we

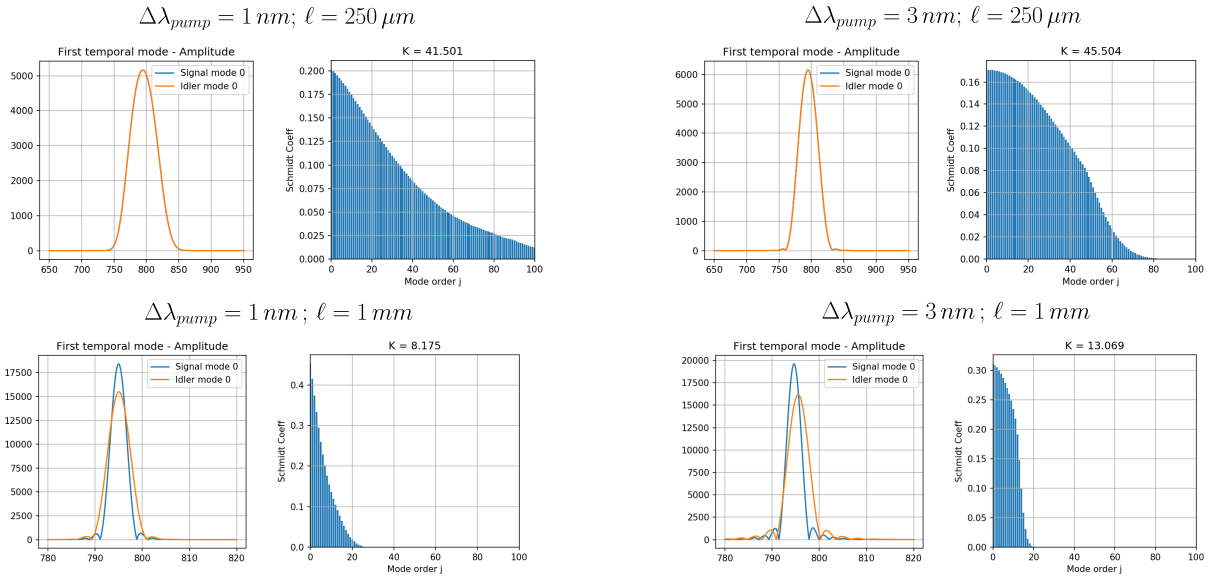

Figure 6.20 – Effect of the pump spectrum on the Schmidt decomposition. Top: Type 0; Bottom: Type II.

increase the temperature of the nonlinear crystal to reduce losses due to the *Blue-Light Induced InfraRed Absorption* (BLIIRA) and so increase the gain of the PDC.

BLIIRA Effect Crystals are characterized by the regular arrangement of elements at the nodes of a network. Potassium Titanyl Phosphate (KTP) is a ionic crystal of formula $KTIOPO_4$, i.e. composed of potassium, titanium, phosphate and oxygen ions. However, real crystals exhibit irregularities of various forms. These irregularities, also called impurities or defects, can be extended, which includes linear, planar and bulk defects or punctual. In the latter case, the volume occupied by the point defect is inferior to the lattice constant and is of the order of one or two atom radii. The most common point defects are the Schottky ones. They correspond to the vacancy of an element at a network node. As crystals are neutral in charge, the vacancies carry charges. In the case of an ionic crystal such as NaCl or KTP, vacancy always form in pairs, cationic and ionic vacancies, so that the overall charge of the crystal is conserved. Impurities are sparse and are found in every crystal. They form during crystal growth and their quantity can be adjusted at this stage. Additionally, they are associated to the crystal properties, notably higher electrical resistivity and reduced enthalpy [Laulhé 18, Fleury 83]. When the crystals are placed in particular environments, the vacancies can be filled with new elements being of the same species or not, modifying the crystal properties. In the case of colored centers [Schulman 62], a vacancy can be filled with a free electron. The absorption spectrum is modified and the crystal shows a specific color associated to the

nature of the color center.

In the case of KTP, depending on the ionic decomposition of the crystal, vacancies can be formed from Ti^{3+}/Ti^{4+}, O^{-}/O^{2-} and K^{+} ions. This corresponds to different types of traps for charge carriers. Additionally, the traps are associated to different energy levels, designated as shallow and deep traps. In particular, the occupancy rate of the shallow traps depends on thermal ionization, i.e. thermal agitation contributes to pull charge carriers off the more shallow traps, keeping them empty. When blue light is shined on a KTP crystal, it generates ionizations and contributes to fill in shallow traps in such a way that thermal ionization becomes insufficient to keep them empty. Filled-up traps are colored centers, which can interact with infrared (IR) photons. This phenomenon leads to BLIIRA characterized by a brutal increase of IR absorption, possibly up to crystal deterioration. The coefficient of IR absorption α_{IR} evolves with the blue-light intensity [Wang 17, Fleury 83]. Furthermore, for blue-light intensities below 1 kW/cm^2, the study of the influence of the absorption coefficient for the IR light presented in [Wang 17], reveals that it evolves quadratically with the pump power. The usual measurement protocols rely on the comparison of the IR-absorption coefficient with and without BLIIRA. They consist in measuring the increase of temperature of the crystal or to monitor the variation of the IR-light intensity exiting the crystal.

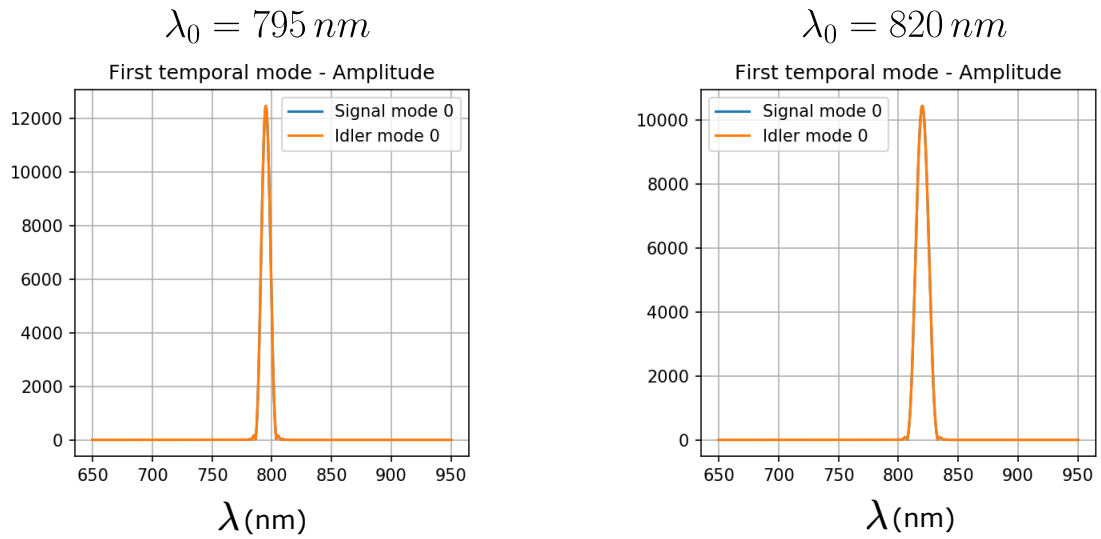

Figure 6.21 – Comparison of first Schmidt modes of type-0 PDC in PPKTP at central frequencies 795 nm and 820 nm, imposed by the spectrum of the pump.

To prevent the BLIIRA effect, one method is to increase the temperature of the nonlinear crystal, typically from 20°C to 90°C approximately, to promote thermal ionization and keep the shallow traps empty. Working with pulsed light is a way to limit

BLIIRA, as long as the pulse duration and the laser repetition rate remain inferior to the response time of the phenomenon. Another method is to increase the working wavelength of the IR above 800 nm, at which the phenomenon is reduced [Mabuchi 94]. However, this last option was not considered because we do not have such laser source. Moreover, the simulations show that the increase of the working wavelength, which we set by modifying the central wavelength of the pump, goes with a significant increase of the spectral width of the Schmidt modes (fig. 6.21), reducing the amount of squeezed modes measurable via LO-shaped homodyne detection 5.5.1. We work with KTP waveguides provided by AdvR (fig. 6.22). The company tested the waveguides for the SHG at different temperatures between 20°C and 90°C. However, they did not characterized the BLIIRA in them, so we do not have any information on this phenomenon and only experimental tests of the waveguides will give us information about its effect on our experiment.

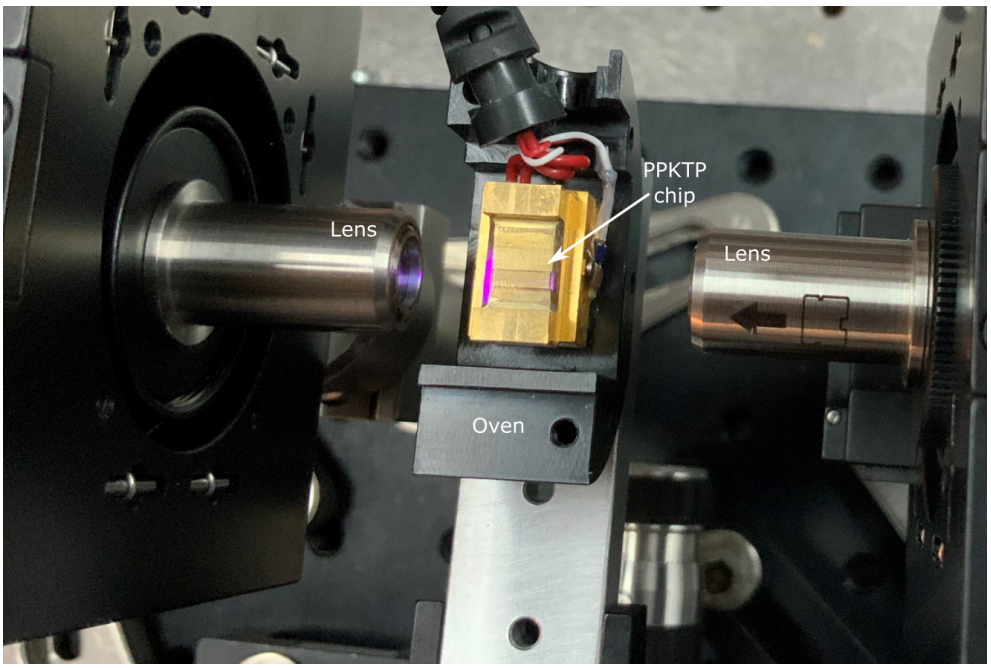

Figure 6.22 – Picture of the PPKTP waveguide chip on its mount.

6.4.2 Waveguide Chips

We performed numerical simulations of the PDC process to determine the poling period of KTP associated to each phase-matching, namely $\Lambda_0 = 3.19\,\mu m$ and $\Lambda_{II} = 8.39\,\mu m$, as well as the poling length or interaction length being $\ell_0 = 1\,mm$ and $\ell_{II} = 1.5\,mm$. However, for manufacturing reasons, the KTP crystals provided by AdvR Inc. could not

be shorter than 5 mm, the minimal length guaranteeing the quality of the crystal input and output facets. Therefore, the waveguides we use in our experiment are the one shown in fig. 6.23, with a periodically-poled portion ℓ of PPKTP, where the nonlinear process occurs and a portion of bulk KTP which is not phase-matched.

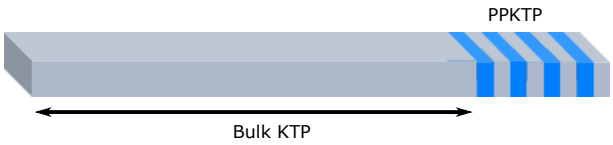

Figure 6.23 – Schematic of a chip of partially poled waveguides.

AdvR provided us with a 5-mm long and 1.5-mm wide chip containing 30 waveguides arranged in 5 groups of 6 waveguides of cross-section 2 μm, 3 μm and 4 μm - two of each size (fig. 6.24). All 30 waveguides have different performances, which need to be assessed before doing experiment.

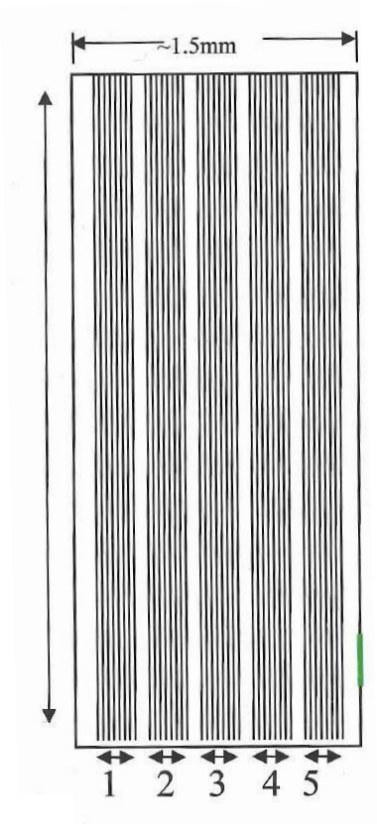

Figure 6.24 – Schematic of the waveguide chip provided by AdvR. Each group contains 6 waveguides of cross-section 2 μm, 3 μm and 4 μm.

6.4.3 Waveguide Characterization

The red beam at 795 nm is coupled inside each waveguide with a lens of focal $f = 11$ mm and a numerical aperture NA $= 0.2$. The numerical aperture NA describes the range of angles over which an optical device can collect or emit light. For a lens, it is defined as NA $= n \sin\theta$, where n is the refractive index of the medium in which light propagates and θ delimits a cone of acceptance of the emitted or collected light. θ is defined as $\theta = \frac{D}{2f}$, with D being the diameter of the lens and f the focal length. In our case, the NA is chosen to match the one of the waveguides ($\text{NA}_{wg} = 0.2$ from the datasheet) to focus the maximum light power at the waveguide input. On the contrary, the collimation lens at the waveguide output is chosen with a higher numerical aperture, NA $= 0.3$, to make sure to collect all the light from the waveguide. Because of the manufacturing process [Bierlein 87], it is difficult to produce two waveguides with the same performances. Thus, we couple light inside each waveguide of the chip to identify the ones featuring the best performances for our application. We measure the coupling efficiency of each waveguide and the output spectrum to verify that it is not changed by the guide. We also observe the shape of the output mode with a video camera.
The waveguides we designed with AdvR are monomode for the near infrared light, so the targeted output mode should resemble a fundamental TE mode (see section 1.3). Fig. 6.26 shows the distribution of intensity of a beam getting out of one of the best waveguides of the chip, where the coupling efficiency reaches 86 % (input light intensity compared to output light intensity). Fig. 6.25 is a picture of the setup we used to test the waveguide chips. For our experiment, we are interested in the 4-μm waveguides, which are the ones giving the best performances.
The lenses are installed on a XY-translation mount from Thorlabs and the mount itself is fixed on a one-axis translation stage to allow adjustments in the three directions of space. The chip is positioned on a metallic mount connected to an oven from Covesion which allows to control the temperature of the waveguides. The chip and oven are installed on an Elliot Martock XYZ flexure stage from Elliot Scientific. It is composed of a XYZ flexure stage on which an additional two-axes stage is mounted to allow orientation adjustments.

Additionally to the coupling efficiency measurement, we use a spectrometer AvaSpec-ULS3648 from Avantes to measure the input and output spectra of the IR beam. The curves are displayed on figure 6.27. The top curve represents the targeted spectrum which is similar to the one measured at the laser output. The bottom curve also represents an IR spectrum at the output of a waveguide. Its shape recalls an interference pattern and could indicate that several TE modes were coupled inside the waveguide. In a second time, we turn the polarization of the beam from the horizontal to vertical. For a vertically polarized input beam centered at 795 nm, second harmonic generation (SHG) takes place, producing a blue beam with a spectrum centered at 397.5 nm. We measure the spectrum of the light exiting each waveguide and identify those for which

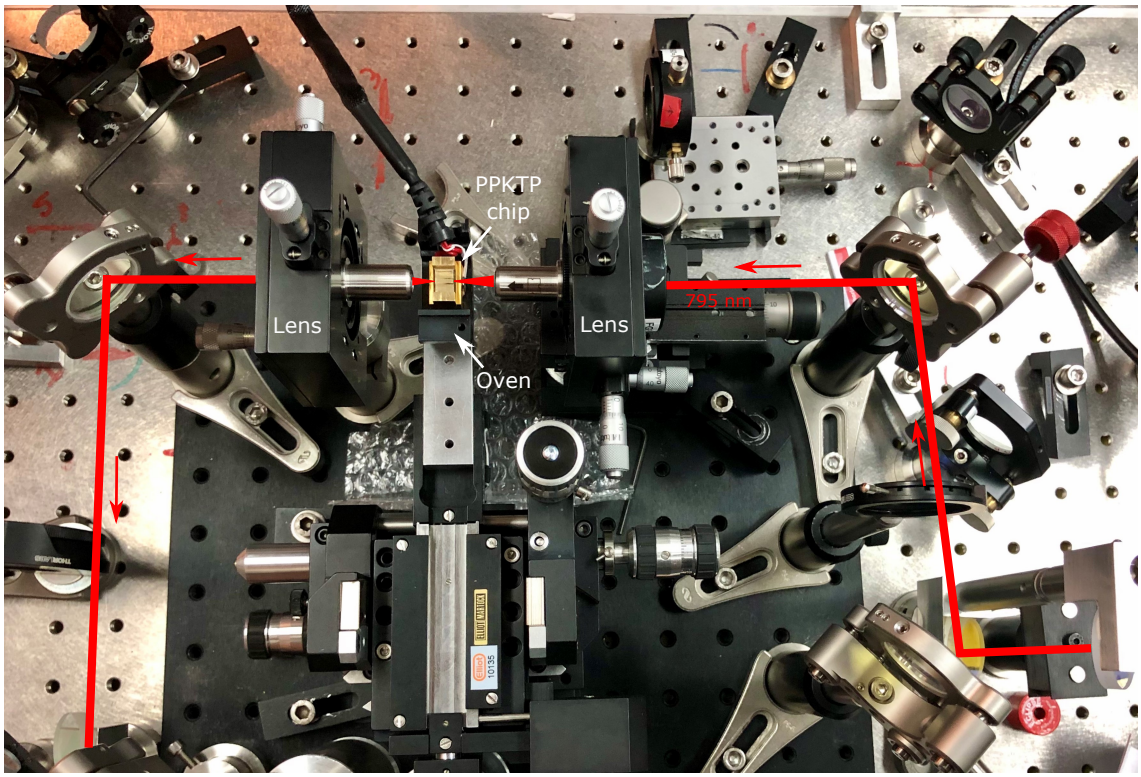

Figure 6.25 – Picture of the waveguide setup with superposed scheme of the red beam.

the output light spectrum has a sinc shape (the joint spectral intensity is defined in chapter 3), indicating that the proper process occurs (fig. 6.28).

For our experiment, we are interested in the reciprocal process, spontaneous parametric down conversion. To do so, the blue beam produced by SHG through our BiBO crystal 6.3.1 should be efficiently coupled in our chip. In practice, the coupling of our blue beam revealed to be very difficult with an efficiency around 15 %, much lower than that of the IR light. This is mainly due to the fact that at theses wavelengths, the waveguides are multimode and the coupling of higher-order modes is critical to the beam size and alignment, i.e. the angle of incidence of the beam on the waveguide input. On the one hand, this makes it difficult to transmit the entire spectrum through the guide and on the other hand, high-order modes do not contribute much to the down-conversion process [Christ 09]. On figure 6.29, a high-order TE blue mode at the output of one waveguide is displayed.

6.4.4 Reveal SPDC in PPKTP waveguides

To reveal the generation of down-converted photons inside the PPKTP waveguides, we used a COUNT-100C single-photon counter from Laser Components. We inject a

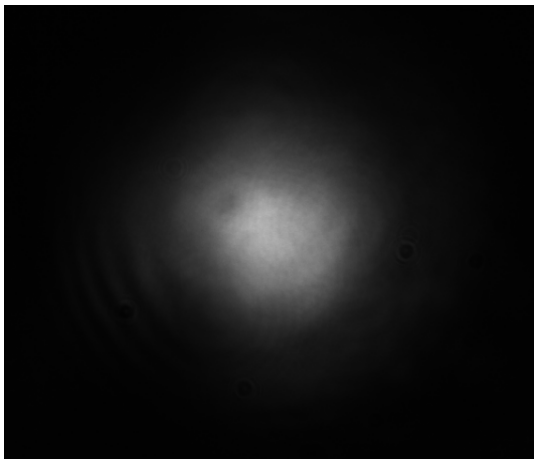

Figure 6.26 – Picture of the output mode from waveguide 1.6 of 4-μm cross-section.

vertically-polarized blue light centered at 397.5 nm inside a type-0 PPKTP waveguide. This is the pump beam for the SPDC process. At the waveguide output, the blue pump is transmitted through a dichroic mirror while the red light is reflected and sent to the single-photon counter whose efficiency is 80 % (fig. 6.30). Two additional density filters of transmission $T = 80\%$ are placed before the counter to filter out residual pump photons. Then we change the polarization of the blue light and measure the number of detected IR photons. When the pump is horizontally polarized, the number of detected photons is 3.5 in average in a time window of 2 μs for an input blue power of 9 mW, this is the reference signal where we take account for the dark counts (2.5 photons). Then, we change the polarization to vertical and measured 14.5 photons in average, which corresponds to an increase of 11 photons in the IR radiation. The measurements are done in a time window of 2 μs, which corresponds to approximately 300 pulses, according to the laser repetition rate. Thus, this measurement corresponds to an emission rate of 14.2 MHz, i.e. 0.091 photons per pulse, and corresponds to an estimation of 2.58 dB of squeezing per pulse calculated with the equation 2.46. These preliminary results would indicate that the generated level of squeezing should be larger than in the bulk configuration

6.4.5 Squeezing Measurements

We use the technique described in section 6.3.2.2 to unveil the spectrally multimode structure of the parametric light at the output of a type-0 waveguide of 4-μm cross-section. We combine the PDC signal with a 10 mW local oscillator (LO) at a 50/50 beam splitter. We scan the phase of the LO with a piezoelectric actuator and we set the frequency of the ramp signal to 300 mHz. To measure squeezing in different spectral modes, we shape the LO spectrum with the pulse shaper (see chapter 4 for details on

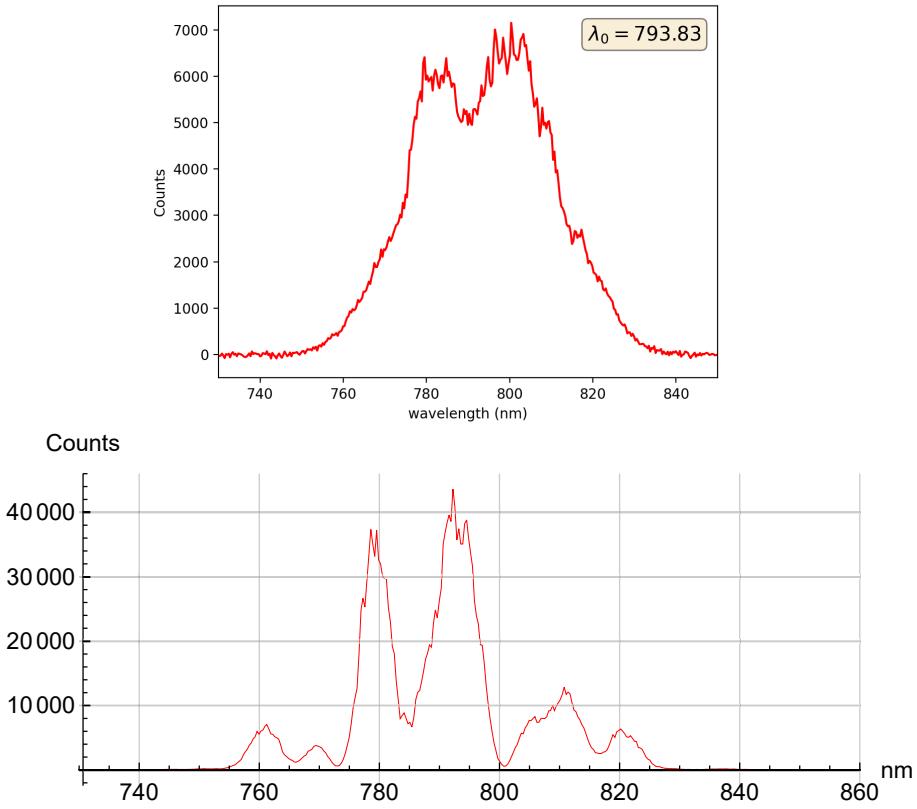

Figure 6.27 – Spectrum of the IR light at a waveguide output. Top: from a 4-μm waveguide; Bottom: from the same waveguide when more than one mode is coupled.

pulse shaping). We first set the spectrum of the Hermite-Gaussian to $\Delta\lambda = 15$ nm and we tune the spectrum and the central wavelength of the LO mode to optimize the squeezing measurement. In figure 6.31, we display the squeezing measurements of the modes HG_0, HG_1 and HG_2. On each graph, the green curve corresponds to the shot noise and the orange curve is the quadrature variance measured with a MXA spectrum analyzer with a resolution bandwidth (RBW) of 200 kHz and a video bandwidth (VBW) of 10 Hz. Data is acquired during one second, which corresponds to 1000 data points.

In the first two modes, i.e. HG_0 and HG_1, the levels of squeezing and anti-squeezing are similar, indicating a low level of loss in the experiment. In HG_0, the maximum measured squeezing is approximately 0.4 dB and in HG_1 it is 0.2 dB. We could measure squeezing in seven spectral modes, i.e. up to HG_6 where the squeezing level is 0.2 dB. It is more modes than in the experiment using a bulk BBO crystal which is very promising.

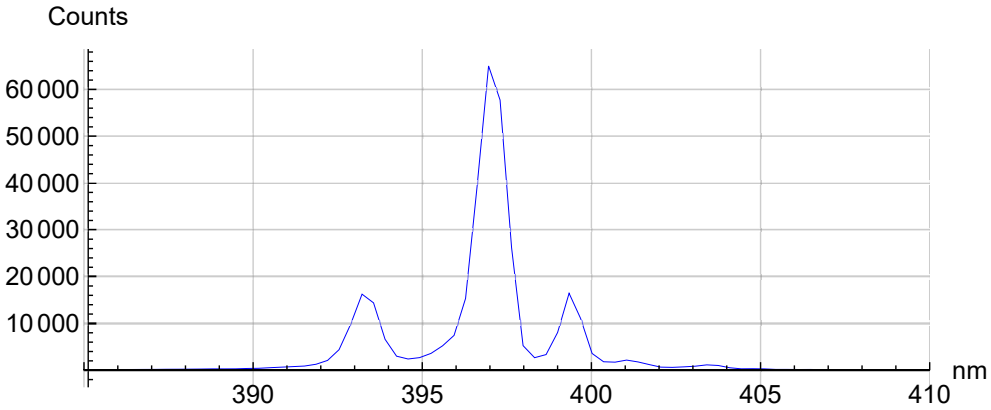

Figure 6.28 – SHG spectrum from a 3-μm waveguide

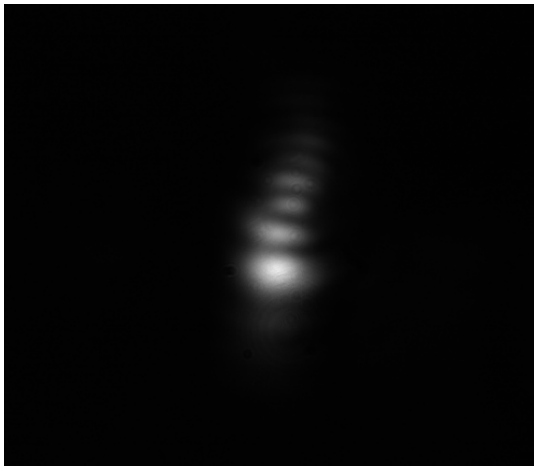

Figure 6.29 – Distribution of intensity of a high-order TE blue mode at the output of a 3-μm waveguide.

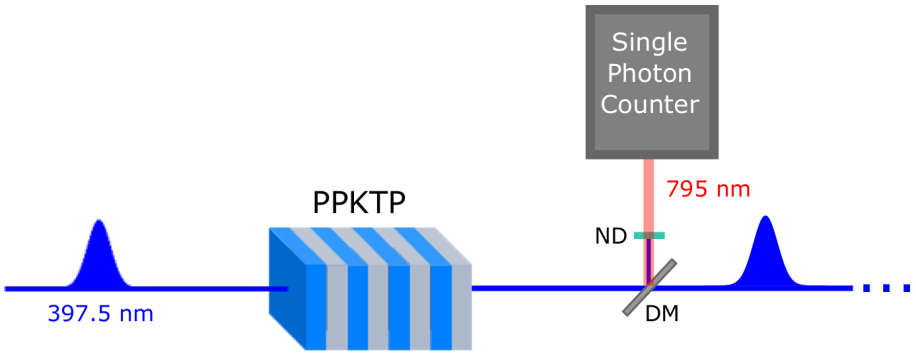

Figure 6.30 – Schematic of the setup used to reveal the SPDC process in the waveguides. ND: neutral density filter and DM: dichroic mirror.

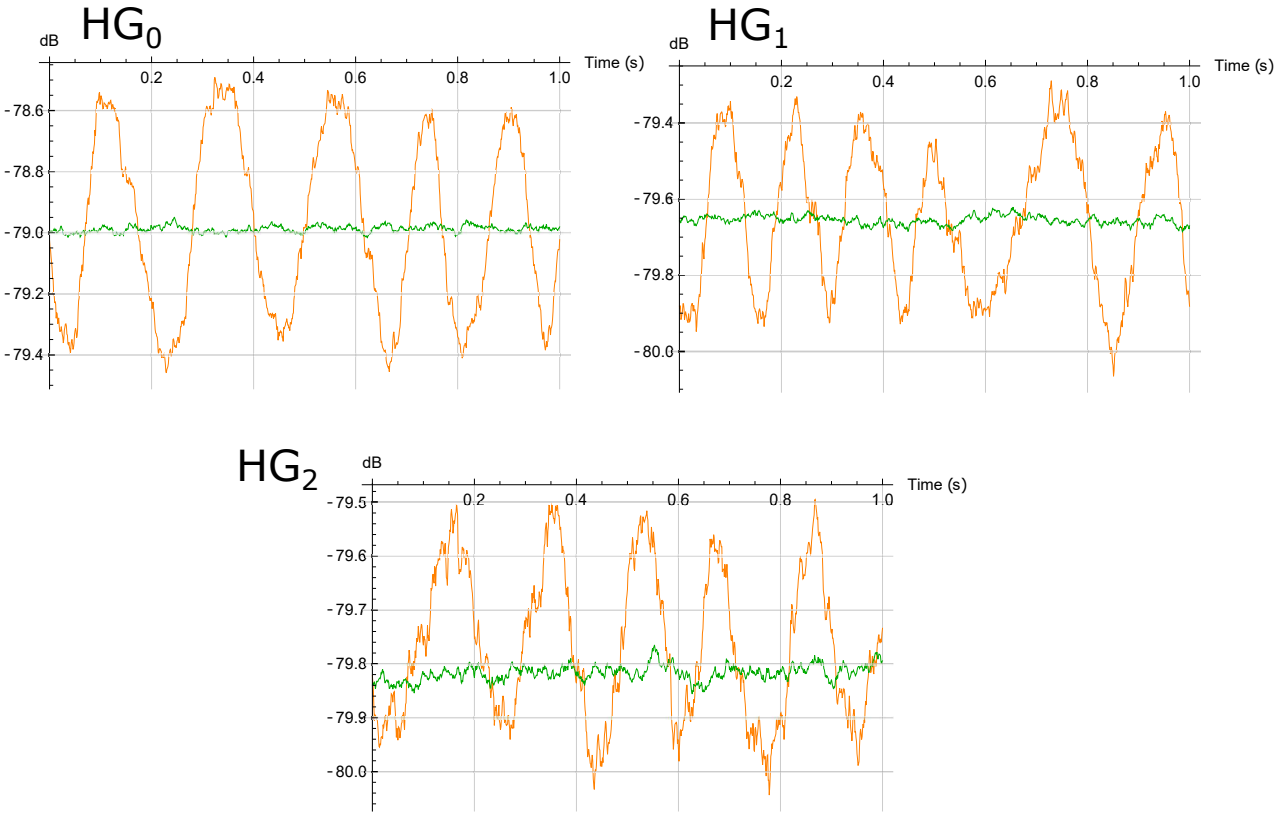

Figure 6.31 – Squeezing measurements in three spectral modes generated by type-0 parametric down conversion in a PPKTP waveguide. Green curve: shot noise; Orange curve: quadrature variance. Sweep time: 1 s; RBW: 200 kHz; VBW: 10 Hz.

Part III

Development of a Homodyne Detector for Light Characterization

Chapter 7

Development of Fast Homodyne Detection

Contents

7.1 Light Detection . . . 116
7.1.1 P-N junction . . . 116
7.1.2 PIN photodiode . . . 118
7.2 Transimpedance amplifier . . . 119
7.3 Voltage Amplification . . . 123
7.3.1 Separate DC and AC Signals . . . 124
7.3.2 Active High-Pass Filter . . . 124
7.4 Development of a Printed Circuit Board with EAGLE . . . 125
7.4.1 Multiple-layer Boards . . . 126
7.4.2 Choosing the Size of Electronic Components . . . 127
7.4.3 Characteristics of Conductive Tracks . . . 127
7.4.4 Vias: Role and Characteristics . . . 128
7.4.5 Filtering of the Power Supply . . . 129
7.5 Analysis of the Detector Response . . . 129
7.5.1 Noise Characterization with a Spectrum Analyzer . . . 129
7.5.2 Detector Analysis with a Network Analyzer . . . 131

A limited number of quantum optics groups in the world have developed their own fast homodyne detectors for pulsed-based experiments [Zavatta 02, Chi 11, Okubo 08, Haderka 09, Kumar 12, Cooper 13]. In our case, we have to design a large-bandwidth homodyne detector to be able to measure quadrature squeezing pulse-by-pulse, at a repetition of rate 156 MHz (see section 6.1), which goes beyond the bandwidth limit of all already implemented schemes, to the best of our knowledge. I have been working on the design and adaptation of fast homodyne circuits based on previous literature to build our homodyne detector. A homodyne detector is generally composed of a photocurrent-

subtraction stage followed by a current-to-voltage conversion (called transimpedance amplifier) and an additional signal-amplification stage (fig. 7.1). In this chapter, we will present the details of signal processing and the characteristics of the detector we focused on. The detector allows time and frequency analysis within a bandwidth set by the detector parameters. In general, good care is taken of the photodetection and transimpedance stages.

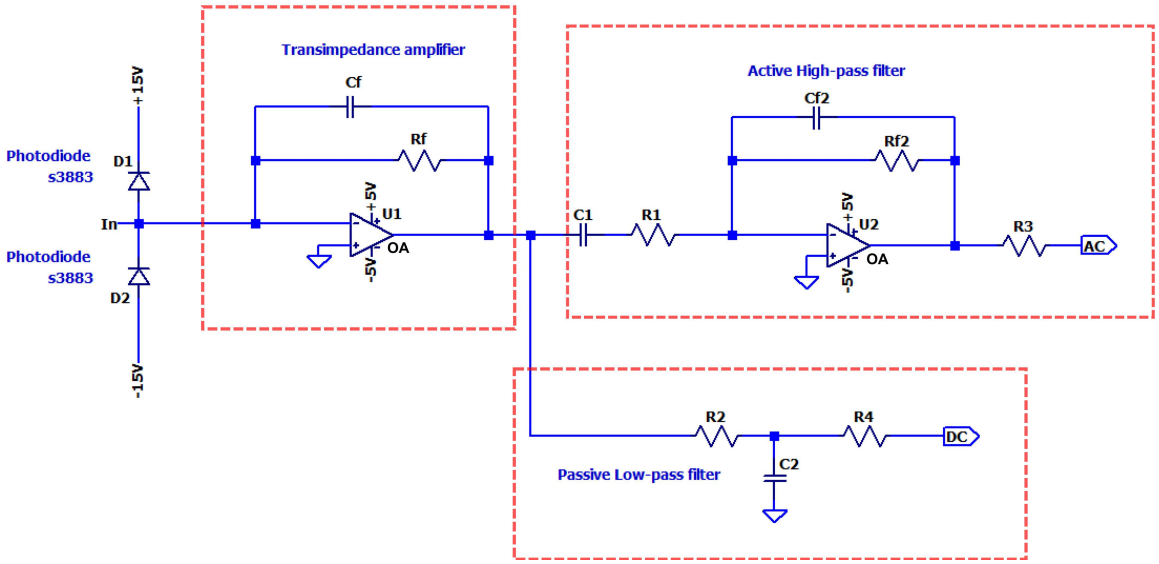

Figure 7.1 – Schematic of a dual-output homodyne circuit.

7.1 Light Detection

The signal light interferes with the local oscillator at a balanced beamsplitter and the output light is sent to two s3883 PIN photodiodes (see section 7.1.2) from Hamamatsu. Each photodiode generates a current with conversion efficiency η_{PD} (section 5.2.1). In this section, we will compare PN and PIN junctions to describe the functioning of photodiodes for homodyne detectors.

7.1.1 P-N junction

A PN junction is a semiconductor material at the interface between two regions of opposite doping, named P and N [Hook 01]. In the P-doped region, the charge carriers are holes in atoms such as boron or gallium, while in the N-doped region they are electrons in atoms such as arsenic or phosphorus. When the two regions are put in

contact, the charge carriers travel spontaneously towards the junction and electron-hole pairs recombine. This phenomenon creates, both in N and P regions, areas depleted in charge because of recombinations [Sah 57]. This region near the junction is called the *depletion zone*. Contrary to the N and P regions, which are electrically neutral, the depletion zone is composed of anions and cations, resulting from the charge-carrier movement from the P and N regions. As a consequence, a potential difference sets up on each side of the junction and generates a electric field E_d oriented from N to P. When important enough, this field blocks the movement of electrons towards the PN junction. Therefore, the depletion zone acts as an insulating region or a high electrical resistance, which value can be modulated by applying a voltage difference on each side of the material. We distinguish between two kinds of bias: the forward biasing and the reverse one.

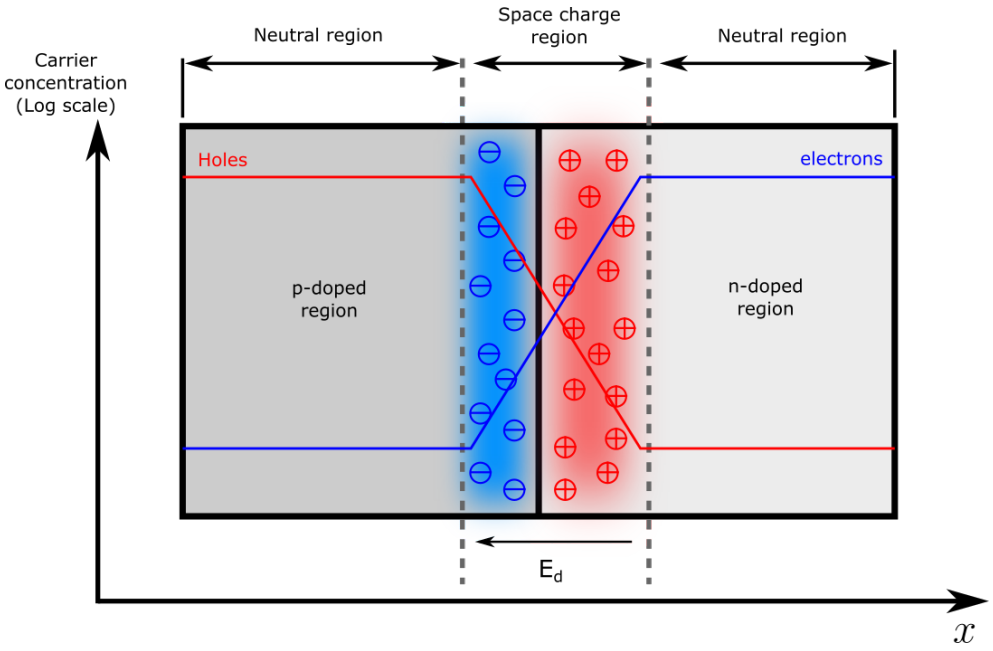

Figure 7.2 – Schematic of a PN junction

Forward biasing The PN junction is forward biased when the positive pole (cathode) of a voltage generator is connected to the P region and the negative pole (anode) to the N region. As a consequence, the movement charge carriers is encouraged towards the junction, which reduces the depletion zone and its associated resistance. In this configuration, the PN junction operates as a diode. When a voltage superior than a threshold is applied, $\Delta V \geq \Delta V_T$, a current can flow through the junction.

Reverse biasing In this case, the N zone is connected to the cathode, the P zone to the anode and the movement of charge carriers is encouraged away from the junction. As pair recombination still occurs, the depletion region is expanded and the associated resistance increases. In this configuration, electrical current hardly flows through the junction and the residual current is called *dark current*. however, a current can be generated if enough energy is brought to the depletion zone to create an electron-hole pair. This is the operating principle of a photodetection where the photon-absorption generates a current according to the photon energy [Weckler 67].

7.1.2 PIN photodiode

In the previous section, we saw that reversely-biased PN junctions can be used for photodetection. However, the functioning of most photodiodes is based on PIN junctions. In a P-I-N structure, there is an *intrinsic* I region between the N and P zones (fig. 7.3). This region is flooded with positive and negative charge carriers in equal concentration but superior to that of N and P. As the I zone contains an excess of charges, the movement of charge carriers from N and P is not blocked, thus allowing the creation of a wider depletion zone. In this case, the depletion zone is only within the intrinsic region and its width can be set arbitrarily. Thus, the PIN structure allows to reach higher photon-to-electron conversion efficiency. In our detectors, we used s3883 PIN photodiodes from Hamamatsu. We report their parameters in a table:

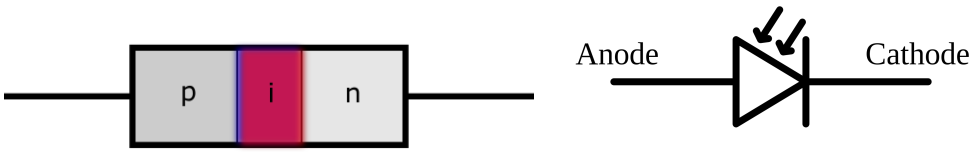

Figure 7.3 – Schematic of a PIN junction. Electronic symbol of a photodiode.

	Photosensitivity S	Terminal Capacitance C_{PD}	Cutoff Frequency
s3883	0.58 A/W	6 pF	300 MHz

The photodiodes s3883 feature a Watt-to-Ampere conversion coefficient of $S = 0.58$ A/W, which corresponds to a quantum efficiency $\eta_{PD} = 0.91$ at 795 nm. The bias voltage applied to their bounds allows to adjust their terminal capacitance (fig. 7.4).

Photocurrent subtraction To perform a current subtraction, the photodiodes are connected in series such that the current generated by each photodiode is of opposite sign (fig. 7.1). Thus, the current at their connection point is $i_{PD} = i_1 - i_2$ according to Kirchhoff's laws [Masalov 17].

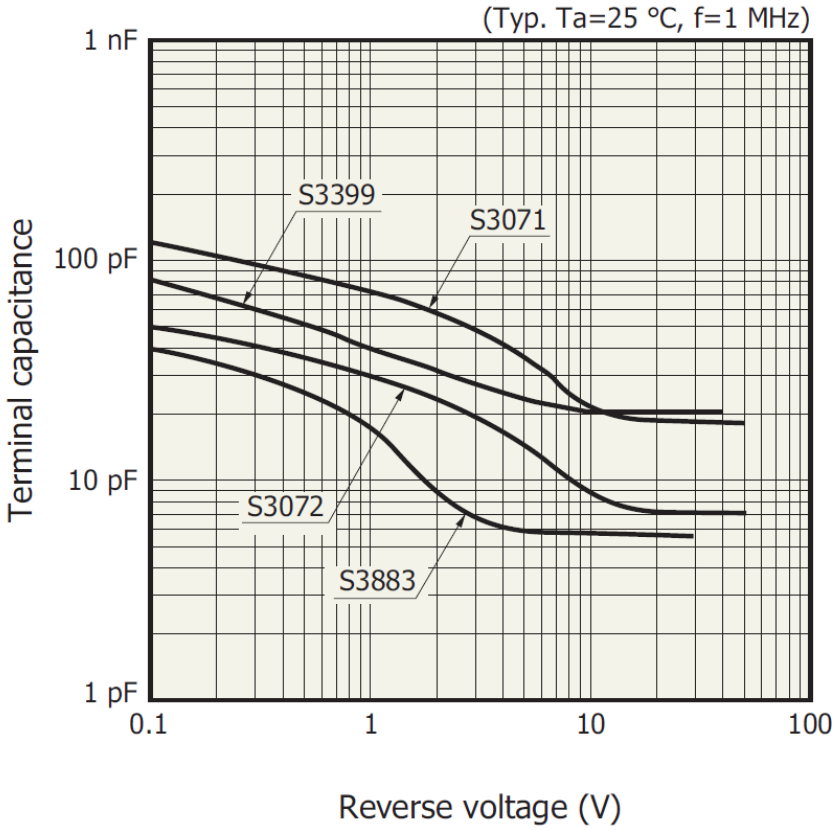

Figure 7.4 – Evolution of the s3883 PIN photodiode with the bias voltage. Curves from the Hamamatsu datasheet of the s3883 photodiode.

7.2 Transimpedance amplifier

A transimpedance amplifier (TIA) is an electrical circuit used to convert a current into a voltage with an adjustable gain. The functioning of a TIA relies on an operational amplifier (op-amp) as it is displayed in fig.7.5. The amplifier is characterized by a gain-bandwidth product GBP, which sets the limits of its performances and is provided in the datasheet of the device. The gain of the current-to-voltage conversion is set by a feedback resistor R_F, called the transimpedance gain, such that the output voltage V_{PD} reads:

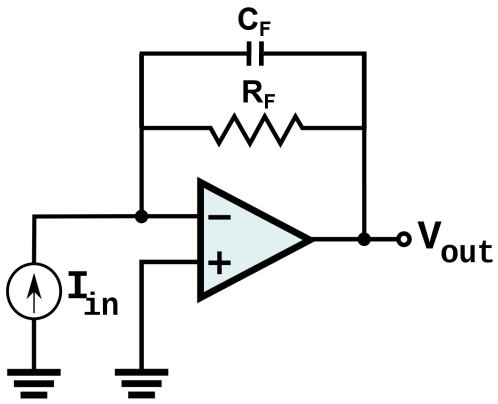

Figure 7.5 – Schematic of a transimpedance amplifer of gain R_F.

$$V_{PD} = R_F \times i_{PD} \tag{7.1}$$

Where, i_{PD} is the subtracted photocurrent. Moreover, the TIA gain is linked to the cutoff frequency of the circuit by the following relation:

$$f_{TIA} = \sqrt{\frac{GBP}{2\pi\, R_F\, (C_F + 2C_{PD} + C_{A1})}} \tag{7.2}$$

Where C_{PD} is the intrinsic capacitance of the photodiodes and C_{A1} the intrinsic capacitance of the operational amplifier, both indicated in the datasheet of the components. In practice, a feedback capacitor C_F is wired in parallel to R_F (fig. 7.5) and allows to flatten the gain curve of a Bode plot and can slightly increase the bandwidth of the circuit. On the figure 7.6, an example of Bode plot is presented. When the feedback capacitance C_F is too small, a peak can appear towards the highest frequencies of the Bode curve. This is a configuration in which the circuit could easily oscillate. On the contrary, if C_F is too big, the gain curve is damped and the bandwidth is reduced. Thus, the feedback capacitor is linked to the parameters of a TIA and can be estimated by [Masalov 17]:

$$C_F = \sqrt{\frac{2\,C_{PD} + C_{A1}}{\pi \times GBP \times R_F}} \tag{7.3}$$

To design a high-bandwidth detector, we need to take into account that the performance of the op-amp may not be the same at all frequencies. Therefore, the conditions of stability are not the same at low and high frequencies. While a feedback resistor R_F sets the TIA gain at low frequencies (eq. 7.1), at higher frequencies it depends on the noise gain such that [Ramus 09]:

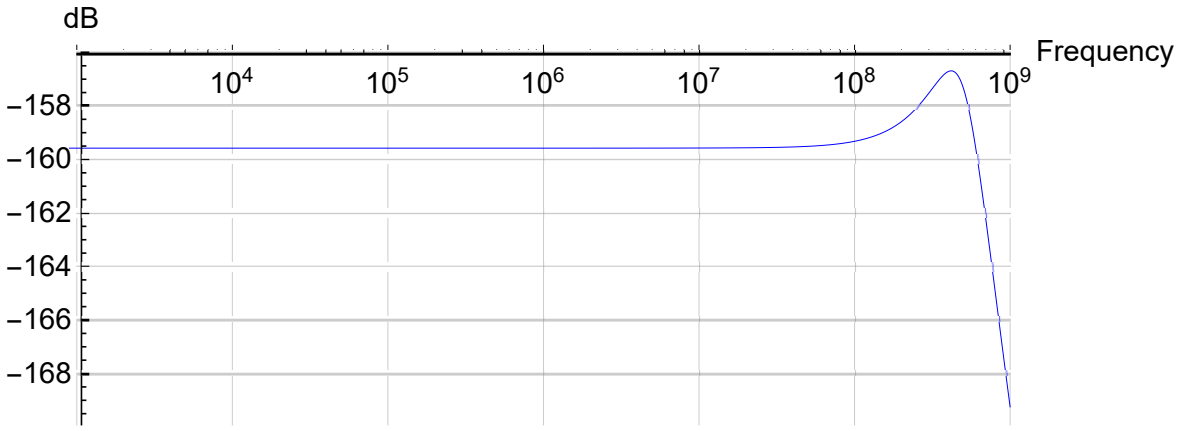

Figure 7.6 – SPICE simulation. Gain curve of a TIA when the feedback parameters are lower than the optimal values. The gain increase at higher frequencies indicates that the circuit may display parasitic oscillations.

$$V_{PD} = R_F\, G(f) \times i_{PD} \tag{7.4}$$

where,

$$G(f) = \frac{1}{1 + \dfrac{G_{NG}}{G_{OA}(f)}} \tag{7.5}$$

G_{NG} is the noise gain of the operational amplifier. Its value is fixed by the parameters of the TIA and is chosen such that $G_{NG} \geq G_{NG,min}$, with $G_{NG,min}$ being the minimum noise-gain value below which the op-amp is unstable (see paragraph 7.2 below). $G_{OA}(f)$ is the frequency-dependent gain of the operational amplifier (OA). It is a measure of the gain achieved when there is no feedback implemented in the circuit. It depends on the gain-bandwidth product (GBP) of the op-amp and is defined by [Ramus 09]:

$$G_{OA}(f) = \frac{GBP}{f + f_{max}} \tag{7.6}$$

where f_{max} is the maximum bandwidth achievable with an operational amplifier. It is defined by:

$$f_{max} = \frac{GBP}{G_{NG,min}} \tag{7.7}$$

Stability of Decompensated Op-Amps Regular operational amplifiers are designed to be stable for a noise gain $G_{NG,min} = 1$, which limits the maximum available

bandwidth of the transimpedance amplifier. Decompensated op-amps offer a larger gain-bandwidth product because they can be operated at minimum gains higher than 1 and specified in the datasheet of the device. They are more suited for large-bandwidth applications [Instruments 13]. The noise gain of the op-amp is defined by:

$$G_{NG} = 1 + \frac{R_F}{R_C} \tag{7.8}$$

Where R_C is a compensation resistor used to adjust the gain of a decompensated op-amp. In practice, R_C is placed in parallel to the feedback resistor R_F as shown in figure 7.7. In a homodyne circuit, the TIA follows the photocurrent-subtraction stage and corresponds to an infinite impedance. Thus, if no compensated resistor is used, the noise gain is very small ($G_{NG} \to 1$) and the circuit is unstable. At high frequencies, the noise gain depends on the capacitances of the transimpedance amplifier such that:

$$G_{NG,HF} = 1 + \frac{2C_{PD} + C_{A1}}{C_F} \tag{7.9}$$

Experimentally, unstable op-amps cause high oscillations at high frequencies ($f \geq$ 500 MHz), i.e. beyond our working frequency range. The oscillation acts as an offset in the electronic noise, which can be problematic especially if we need to measure signals of low amplitude. It is possible to damp this parasitic oscillation by increasing the transimpedance gain R_F, but it comes at a price of lowering the detector bandwidth.

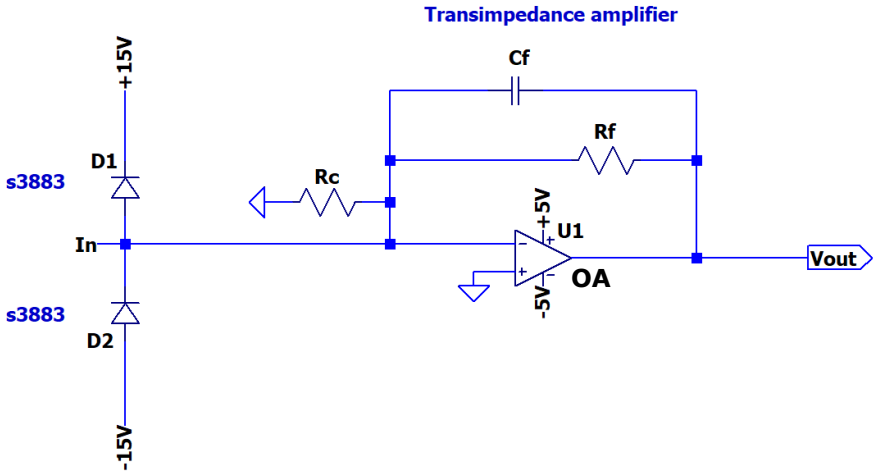

Figure 7.7 – Schematic of a transimpedance amplifier with a gain-adjusting resistor R_C.

We conclude this section with the table containing the parameters of the op-amps we considered in the development of our homodyne detector:

	OPA847	**OPA855**
Gain-Bandwidth Product (GBP)	3.9 GHz	8 GHz
Input Capacitance C_{A1}	3.7 pF	0.8 pF
Minimum Noise Gain ($G_{NG,min}$)	12 V/V	7 V/V
Maximum Bandwidth f_{max}	325 MHz	1.1 GHz

Considering the minimum noise gain of each op-amp, this corresponds to $f_{max} = 325$ MHz for the OPA847 op-amp and $f_{max} = 1.1$ GHz for the OPA855.

7.3 Voltage Amplification

If the signal of interest is low, voltage amplification can be performed with an operational amplifier wired in an inverting or non-inverting setup [Mancini 13, Malvino 98]. After the TIA, it allows to increase the signal level without reducing the bandwidth significantly. In our detectors, we chose an inverting setup (fig.7.8). Differential oper-

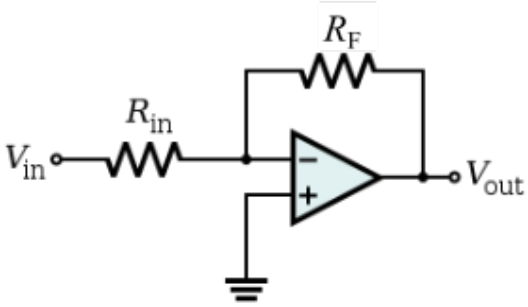

Figure 7.8 – Schematic of an inverting amplifier.

ational amplifiers are characterized by a high impedance ($R \to \infty$) on each input and ideally $V_+ - V_- = 0$. In this configuration, the voltage is amplified according to the following relation:

$$V_{out} = -\frac{R_F}{R_{in}} V_{in} \tag{7.10}$$

Where R_{in} and R_f are set to adjust the gain of the amplifier:

$$G_{inv} = \frac{R_F}{R_{in}} \tag{7.11}$$

7.3.1 Separate DC and AC Signals

We design a high-bandwidth detector to be able to measure quadrature squeezing at the repetition rate of our laser (156 MHz). While we use the DC signal to align the detector, the AC signal is much lower but contains the signal of interest. It needs to be amplified. To avoid saturating the detector, we can separate the DC and AC signals at the TIA output. This allows to amplify the AC signal separately. Thus, we retrieve the low-frequency signal with a low-pass filter (LPF) and the high-frequency part with a high-pass filter (HPF). We choose the lower cutoff frequency of the HPF such that we eliminate most of the noise at low frequencies while being able to discriminate the signal coming from different pulses at the AC output when we send pulsed light on the detector. In figure 7.9, we show a numerical simulation of the transformation of light pulses after a TIA and a HPF of lower cutoff frequency $f_0 = 8$ MHz. On the left, the initial pulses in arbitrary units and the output pulses on the right.

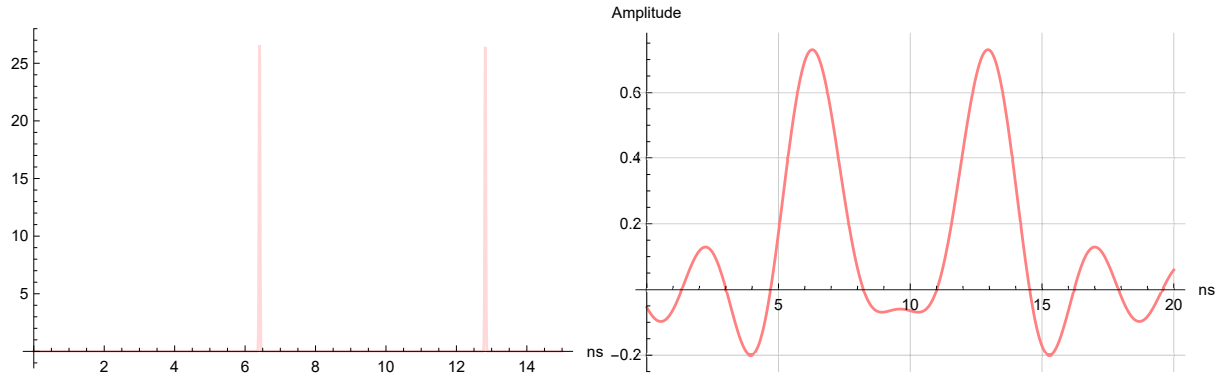

Figure 7.9 – Expected shape of the pulses at the AC output of the homodyne detector (right) compared to the incoming ones (left). Numerical simulations in arbitrary units.

It is possible to filter and amplify the AC signal simultaneously by designing an active high-pass filter with an operational amplifier 7.3.2.

7.3.2 Active High-Pass Filter

Passive high-pass filters (HPF), composed of a resistor R and a capacitor C in parallel, are used to filter out frequency components of a signal, which are inferior to a cutoff frequency f_0. The input-output relation of such circuit, i.e. the transfer function $H(\omega)$, reads:

$$H(\omega) = \frac{V_{out}}{V_{in}} = \frac{1}{1 + jRC\omega} \tag{7.12}$$

$$H(\omega) = \mathrm{Re}[H(\omega)] \; + \; j\,\mathrm{Im}[H(\omega)] \tag{7.13}$$

With,

$$\mathrm{Re}[H(\omega)] = \frac{1}{1 + R^2C^2\omega^2} \tag{7.14}$$

Where, the angular frequency ω and the cutoff frequency f_0 are defined by:

$$\omega = 2\pi\, f_0 \tag{7.15}$$

$$f_0 = \frac{1}{2\pi\, RC} \tag{7.16}$$

In an active high-pass filter, an operational amplifier is used to amplify the filtered signal as shown on figure 7.10. In this configuration, R_1 and C are the parameters of the HPF while R_2 is used to set the gain of the amplification. Thus, the transfer function reads:

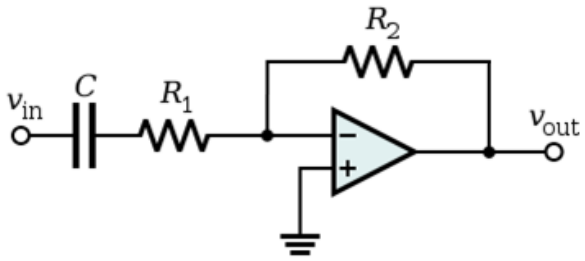

Figure 7.10 – Schematic of an active high-pass filter.

$$H(\omega) = -\frac{R_2}{R_1}\,\frac{1}{1 + jR_1C\omega} \tag{7.17}$$

$$\mathrm{Re}[H(\omega)] = -\frac{R_2}{R_1}\,\frac{1}{1 + R_1^2C^2\omega^2} \tag{7.18}$$

We use this setup in our detectors to separate and amplify the feeble high frequency part (AC) of the homodyne signal from the low-frequency part (DC). The figure 7.11 shows the active high-pass filter of one detector where we used an OPA855 amplifier and wired a feedback capacitor C_{21} to stabilize the circuit. The capacitors C_{12} to C_{17} are used to filter the power supply of the op-amp.

7.4 Development of a Printed Circuit Board with EAGLE

I developed our printed circuit boards (PCB) with Dr. Bérengère Argence and electronics engineers Loïc Garcia and Elie Gozlan at the Laboratoire Kastler Brossel (LKB).

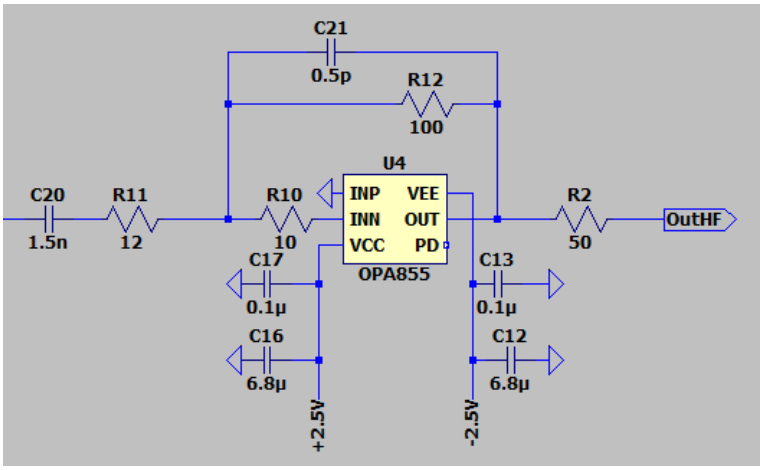

Figure 7.11 – Schematic of an inverting amplifier with a feedback capacitor. The capacitors C_{12}, C_{13}, C_{16} and C_{17} are used to filter out the noise from the power supply. This schematic is advised by the OPA855 manufacturer.

In the early stage of the project, we also collaborated a lot with Xavier Solinas from Laboratoire d'Optique et Biosciences (LOB), who helped us design our first operational circuit.

We worked with EAGLE which is a software dedicated to printed-circuit-board (PCB) design and developed by CadSoft Computer GmbH and Autodesk. It stands for *Easily Applicable Graphical Layout Editor*. An EAGLE program comprises a circuit-diagram editor associated to a simulator of PCB. Developing electronics at high frequencies is quite different than at low frequencies. One needs to adapt the routing of the circuit to the bandwidth of the signal to be processed. This includes adjusting the board thickness 7.4.1, the size and positioning of the electronic components 7.4.2 as well as the track dimensions 7.4.3. In this section, we will review these parameters.

7.4.1 Multiple-layer Boards

The main focus when developing a PCB is to protect the signal traveling inside from perturbations, i.e. to maintain the electromagnetic compatibility (EMC) of the circuit [Charoy 06]. The perturbations correspond to electromagnetic noise and consist essentially in modulations coming from an exterior source, i.e. outside of the board, or coming from neighboring conductive tracks, e.g. the ones carrying the power supply. To isolate the signal, one method is to divert critical tracks from the signal path on the PCB layout. This is done often in the design of 2-layer boards but it is possible to choose a 4-layer configuration and distribute the tracks between the layers [Shukla 09]. Typically, the top layer will be used for the signal path, the second layer would be the ground (GND) reference, and the third layer will be dedicated to the power-supply

tracks. The fourth layer would be an another layer for the signal or would be kept empty. This is defined as the stack-up of the PCB [Shukla 09]. The track thickness and their spacing can be adjusted as well to reduce radiations, crosstalks between tracks and improve the performances of the board. In our case, we started designing bi-layered PCBs and consider designing 4-layer circuits for future projects. Therefore, all the PCBs we will present in this chapter are bi-layered.

7.4.2 Choosing the Size of Electronic Components

Circuit optimization goes with the reduction of the electronic components. Each components brings a level of noise, which contributes to the overall electronic noise of the circuit. We use components of CMS dimensions 0603. This allows to bring the components closer and reduce the circuit size, thus reducing the length of the signal path. This is particularly relevant when working with RF signals and designing a bi-layered circuit. At these dimensions, the PCBs are soldered in an oven, which allows to produce circuits of reproducible quality but makes it more difficult to replace components on the board for tests.

7.4.3 Characteristics of Conductive Tracks

7.4.3.1 Track Length

The track length depends on the the signal path inside the circuit, including the number of transformation the signal will undergo. The signal travels inside conductive tracks, commonly in copper, in which dispersion and loss can occur through dissipation, heat and absorption. Therefore, good care should be taken to restrict the track length between electronic components to the minimum.

7.4.3.2 Track Width

The track width depends on the nature of the signal traveling in it. In particular, the width should be estimated considering the current, which will flow in the tracks in order to avoid signal loss and device deterioration due to heat dissipation. This is the case for power-supply tracks for example, which can carry high electric current. Therefore, the tracks carrying the power supply could be wider than those carrying the signal. On the contrary, the signals containing high-frequency components are very sensitive and can interact easily with the environment [Charoy 06]. Therefore, the conductive tracks carrying such signal are commonly narrower. The estimation of the track width consists in finding a trade-off between the reduction of material heating and low signal dissipation. In our case, we essentially apply voltage on our device so the current flowing in our circuits is low. Thus, we chose to set the same track size everywhere

on the board. Theoretically, the track width w can be determined with the following equation [IPC2221A 03]:

$$I_{max} = k \times A^{0.725} \times \Delta T^{0.44} \tag{7.19}$$

$$S = w \times t \tag{7.20}$$

Where I_{max} is the maximum current expected to flow inside the track, typically $I_{max} = 1$ A, S is the track cross-section in mils^2 (1 mil = 0.0254 mm) and is the product of the track thickness t and the track width w. $\Delta T = 100$°C is the temperature variation the track should be able to tolerate. Finally, the coefficient k has a different value depending on the position of the track in the PCB because the heat dissipation is different. $k = 0.048$ for an outer track and $k = 0.024$ for an inner track. Thus, for a surface track of typical thickness 35 μm, the track width on our PCB is $w = 0.3048$ mm. This is the width of the conductive tracks on our circuits.

7.4.3.3 Change of Direction

Change of direction on a PCB is associated with impedance discontinuities, which can cause the signal to be delayed or experience losses. Smoothing the outer right angle is already enough to limit loss, but it is often preferred to convert an angle at 90° into two consecutive angles at 45°. The best option is an arc-of-a-circle type of change of direction. As can be seen on the appendix D, all the changes of direction in our PCBs were smoothed, especially at the photocurrent-subtraction stage to limit signal loss.

7.4.4 Vias: Role and Characteristics

7.4.4.1 Via Spacing

Vias are metallic holes used to make vertical electrical connections between the layers of a PCB [IPC2226A 03]. Often, they allow to unify the ground reference on the PCB. By adjusting their size and density on a board, they can be used to isolate sensitive signal from noise sources. In principle, there are no limitations to the number of vias on a board. However, to estimate the spacing d between two vias, the most sensitive component of the signal should be taken as a reference, i.e. the highest-frequency component of the signal, similarly to a Faraday cage. Then, the maximum spacing is given by [Harmeling 17]:

$$d_{max} = \frac{\lambda_{HF}}{100} \tag{7.21}$$

Where λ_{HF} is the wavelength of the signal component of highest frequency. In our case, the spacing between vias is 6 mm maximum.

7.4.4.2 Via Size

Vias have an intrinsic capacitance and inductance which depend on its size. Thus, narrower vias feature lower capacitance while wider vias have lower inductance. However, the inductance increases with the length of a via. Therefore, the size of the vias need to be considered in the PCB design. It depends on the circuit parameters such that [Harmeling 17]:

$$\pi \times (R_0^2 - R_1^2) = T \times w \tag{7.22}$$

$$R_0 = R_1 + \alpha \tag{7.23}$$

Where, R_1 is the inner radius of the via, i.e. the drill size, R_0 is the outer radius and α is the width of the via annular ring. w is the width of a conductive track on the PCB and T is the board thickness setting the length of the via. In our design, the dimensions of the via are: $T = 1.55$ mm, $R_0 = 0.6096$ mm and $R_1 = 0.25$ mm.

7.4.5 Filtering of the Power Supply

In our detectors, we use capacitors to smooth the output of the power supplies in order to deliver a nearly constant voltage to the electronic components. The output signal of a power supply has a DC value, which is the desired voltage and an AC part called ripple voltage, of the order of 0.5 mWrms between 5 Hz and 1 MHz for a GPS-1830D power supply. Capacitors help reducing the amount of ripple in the voltage signal and their value depends on the amplitude and frequency of the ripple noise of the power supply [Mazda 89]. To perform efficient filtering, we use two capacitors in parallel and we place the highest capacitance right at the output of the supply. The lowest capacitance allows to get rid of residual noise. The same scheme is used for every supply in our circuits. Figure 7.12 shows an example of PCB using OPA847 operational amplifiers. The detailed schematics of our PCBs can be found in the appendix D. It is possible to combine the filter capacitors with resistors and inductors to improve the filtering, but it should be noted that they increase the overall impedance of the circuit and contribute to increase the thermal noise of the circuit (equation 5.28). The best solution is to work with power supplies with a low input noise.

7.5 Analysis of the Detector Response

7.5.1 Noise Characterization with a Spectrum Analyzer

The spectrum analyzer is used to display the noise spectrum of the detector. It allows to identify different sources of noise. When no light is shined on the detector, we observe

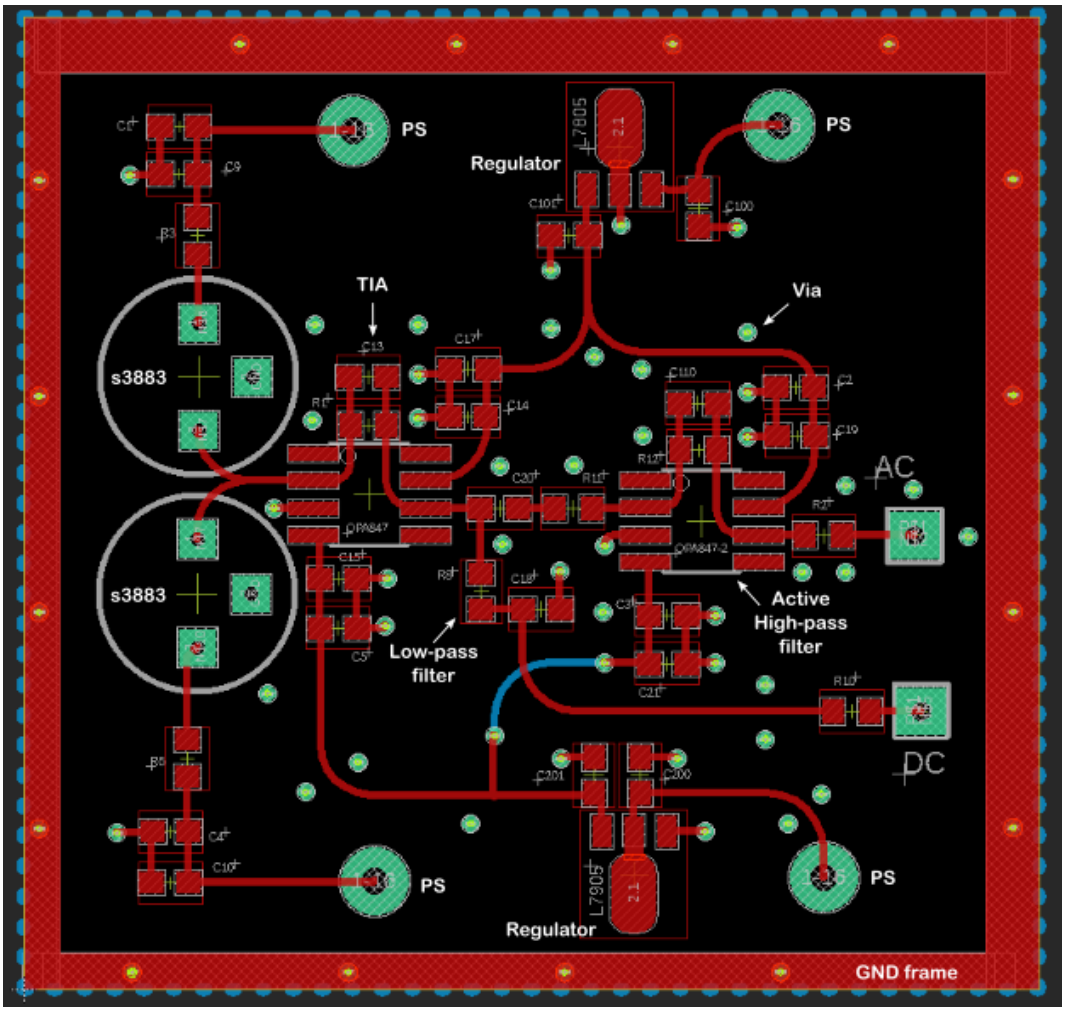

Figure 7.12 – Eagle board of the OPA847-based detector. PS: power suppliy; TIA: transimpedance amplifier; s3383 is the reference of the photodiodes we use; GND: ground.

the distribution of the electronic noise on a chosen frequency range. In particular, we can identify intense noise components, which cannot be noticed with an oscilloscope. When light is shined on the photodiodes, the trace on the spectrum analyzer corresponds to the total noise, i.e. the sum of the shot and electronic noise levels. Independently to any optical or quantum measurement, the shot noise displays the features of the incoming light. As we work with a femtosecond laser of 156-MHz repetition rate, we use the same source for the characterization of the detector. In this case, the shot noise displays an intense component at the repetition rate, which we use to determine the common mode rejection ratio (CMRR) of the detector (section 5.3.2). We also use a spectrum analyzer to measure the shot-noise clearance (SNC) of the detector (section 5.3.1). As the traces are power spectral densities, the SNC corresponds to the difference between the shot-noise level in dB and the electronic-noise level. In homodyne detection, the shot noise is measured to unveil quantum squeezing (section 2.3.1), thus the SNC indicates the highest level of squeezing which can be measured with the detector (see section 5.3.1). Additionally, the SNC helps determining the effective detector bandwidth, defined as the frequency range over which the SNC is above zero and the shot noise level is high enough to be detected. After the characterization with the spectrum analyzer, we look at the output signal in the time domain with an oscilloscope to verify that the pulses are 6 ns apart, i.e. 1/(156 MHz).

7.5.2 Detector Analysis with a Network Analyzer

A network analyzer can be used to measure the frequency response of an electronic circuit composed of passive components, amplifiers or filters among others. After setting the frequency range over which to make the analysis, the network analyzer sends a test signal through the electronic circuit and one can retrieve the S-parameter, i.e. the transfer function corresponding to the comparison of the input signal with the transmitted or reflected one. To characterize our detectors, we compared the input and the output of the circuit and observe the Bode plots, corresponding to the S_{21} parameter of forward transmission. In particular, we show in figure 7.13 the measured Bode plots of one of our detectors. We see that the Bode plot of the high-frequency part is higher than the one of the low-frequency part because we use an active high-pass filter to amplify the AC signal (section 7.3.2). The network analyzer also allowed us to unveil oscillatory behaviors, other parasitic noise sources and to determine the detector bandwidth at 3 dB from the maximum gain.

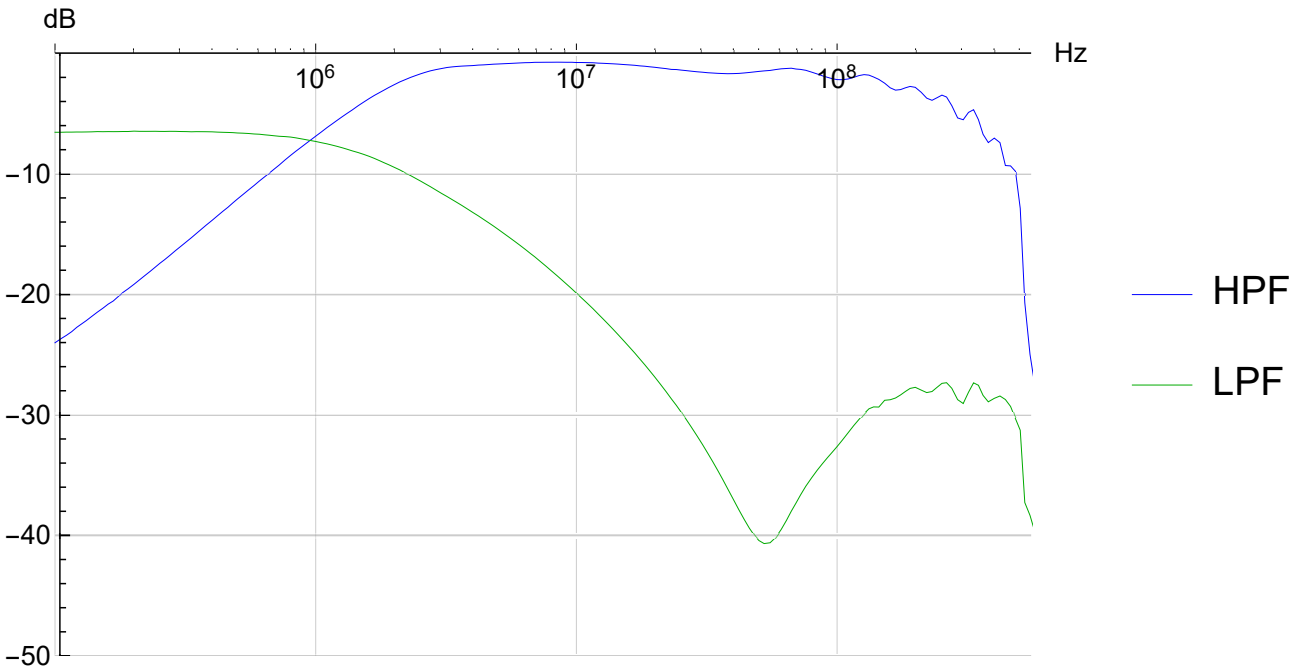

Figure 7.13 – Comparison of the output signal from the low and high-pass filters of a homodyne detector.

Chapter 8

Characterization of Homodyne Circuits

Contents

8.1 Circuit Layouts 134
8.1.1 Dual-Output Detector with OPA847 134
8.1.2 Dual-Output Detector with OPA855 135
8.2 Detector Characterization in CW Light 135
8.2.1 Evaluation of the Saturation Threshold in CW Light 137
8.2.2 Shot-Noise Renormalization 137
8.3 Detector Characterization with Pulsed Light 142
8.3.1 Measurement of the Common-Mode Rejection Ratio 142
8.3.2 Measurement of the Shot-Noise Clearance and Instabilities in the Pulsed Regime 143
8.3.3 Analysis in the Temporal Domain 144
8.3.4 Correction of the Amplifier Gain 146
8.3.5 Latest Results 150
8.3.6 Prospects 150

In this chapter, we describe and compare two kinds of detectors that we developed using different operational amplifiers, the OPA847 and the OPA855. We present tests that were done during the last period of the thesis and some questions remain that unanswered. We are still developing the detectors and the results that we present here are preliminary.

8.1 Circuit Layouts

8.1.1 Dual-Output Detector with OPA847

The simplified layout of the circuit is displayed on the figure 8.1. The detailled layout can be seen in appendix C. The photodetection is performed with two s3883 PIN photodiodes from Hamamatsu (see section 7.1.2). They are mounted such that the current between them is the subtraction of the photocurrents from each photodiode. The subtracted photocurrent is converted into a voltage by a transimpedance amplifier (section 7.2) based on an OPA847 operational amplifier, which feedback parameters were determined according to the targeted bandwidth and gain. In this section, we will present two TIA designs. The first one with the feedback parameter $R_F = 680\,\Omega$ and the second one with $R_F = 510\,\Omega$, which we tested to look at the influence of R_F on the detector bandwidth. We call these detectors OPA847-v1 and v2 respectively. In these first versions, the gain of the first amplifier was not corrected as described in section 7.2, so the transimpedance gain was given by the feedback resistance only and the value of the feedback capacity was calculated with the equation 7.3 and then adjusted experimentally. At the TIA output, the signal at low frequency is much higher than the AC signal, which is the one we are interested in, so we filter out the DC signal and we amplify the AC signal. The low-frequency part (DC) is filtered with a low-pass filter of cutoff frequency $f_{LF} = 1$ MHz and we use it to align the detectors. The high-frequency (AC) part is retrieved with an active high-pass filter (section 7.3.2) based on another OPA847. The lower cutoff frequency is $f_{HF} = 8$ MHz and it was chosen to filter most of the noise at low frequencies while allowing to discriminate the signal coming from different pulses at the AC output. In section 7.3.1, we presented the simulation on the influence of the lower cutoff frequency on the output signal. The pulses at the detector output would be wider but they should be still 6 ns apart, corresponding to the laser repetition rate (fig. 7.9). We adjusted the gain of the amplification to be above the noise threshold of the spectrum analyzer with which we characterized the detectors. In this configuration, the gain is 16.67 calculated with equation 7.11, where $R_F = R_{f2}$ and $R_{in} = R_1$. At this stage of the development, we expected that the feedback resistor and capacitance were sufficient parameters to set the gain of the TIA and to stabilize the op-amp. But as the high-pass filter used a voltage-voltage amplification, we used the formula 7.11 to set the stability gain.

Finally, to limit signal loss at the detector output, a 50Ω resistor is used for impedance matching and the signal is retrieved through a SMA connector, which is more suited to high-frequency signals. Finally, we used separate power supplies for the op-amps and the photodiodes in order to be able to adjust the bias voltage of the photodiodes without changing the supply of the op-amps, and the noise of the power supplies was filtered to protect the homodyne signal as presented in section 7.4.5.

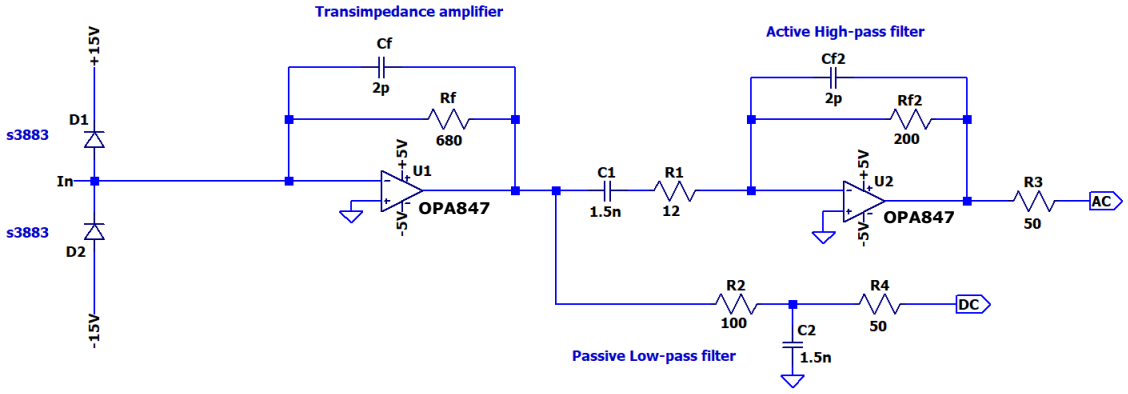

Figure 8.1 – Simplified schematics of the OPA847-based dual-output detector.

8.1.2 Dual-Output Detector with OPA855

The circuit layout for the OPA855-based detector is the same as the one used for OPA847-based detectors. We replace the op-amp with an OPA855 amplifier which features a higher gain-bandwidth product that the OPA847 amplifier, i.e. 8 GHz. The transimpedance gain is $R_F = 1$ kΩ and a feedback capacitance $C_F = 1$ pF is used to avoid parasitic oscillations (fig. 8.2). Similarly to the OPA847-based detector of fig. 8.1, the DC and AC parts of the output signal are separated with filters and the AC signal is amplified. The gain of the voltage amplification is 8 and is chosen so as to be superior to the minimum noise gain of the OPA855 (see section 7.3). The amplifiers are also smaller, which allows to build more compact circuits.

The figure 8.3 is a picture of one of our PCBs. The central part of the board corresponds to the TIA and the path of the AC signal. The goal is to reduce the path of the AC signal, which is the most sensitive, to a minimum. Thus, we soldered the photodiodes on the verso of the PCB in order to reduce the length of the tracks connecting the photodetection to the TIA. To protect the signal from perturbations (see section 7.4.4), the conductive tracks are surrounded by vias, which size and spacing was determined according the bandwidth of the AC signal (section 7.4.4).

8.2 Detector Characterization in CW Light

To evaluate the performance of a homodyne detector, the best method is to to use the same light source as the one used for the measurements. However, when working with a pulsed laser, the modulations from the repetition rate can saturate the detector.

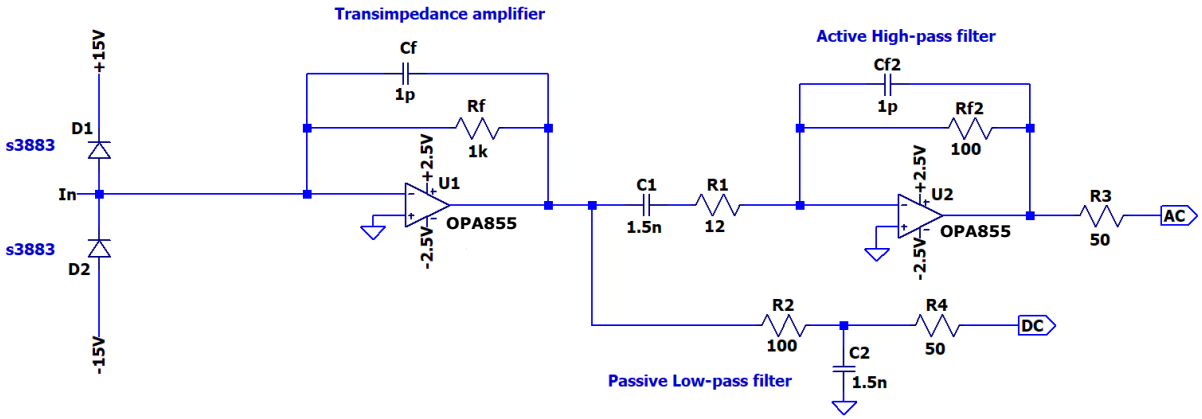

Figure 8.2 – Simplified schematics of the OPA855-based dual-output detector.

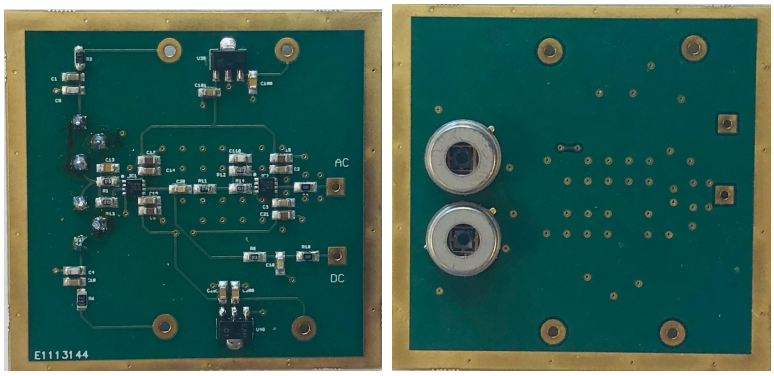

Figure 8.3 – Pictures of the printed circuit board of an OPA855-based detector.

Therefore, preliminary tests can be done in continuous-wave (CW) light in order to discriminate between possible general problems in the circuit and the potential saturation due to the pulsed regime. One option we considered is the use of our femtosecond laser without mode-locking. However, when such lasers are used in the continuous regime, the different modes oscillating in the laser cavity can transiently couple. This leads to a brief mode-locking which can saturate a detector. Therefore, it is important to use a stable CW source to evaluate the detector response to increasing light power.

8.2.1 Evaluation of the Saturation Threshold in CW Light

To test the homodyne detector in the continuous regime, we use a compact CW laser LDM785 from Thorlabs, centered at 785 nm and of 20 nm spectrum. The test setup is the same as the one used with pulsed light (fig. 8.4). The light is shined on a 50/50 beamsplitter (BS) and both BS outputs are focused on the detector photodiodes with a lens of focal length $f = 100$ mm. To evaluate the response of the detector and determine its saturation threshold, we gradually double the light power on each photodiode (PD) and record the corresponding shot noise (SN) trace from the spectrum analyzer. Thus, we recorded SN curves for incident light powers from 250 μW to 18 mW, i.e. half power on each PD (fig. 8.5).

8.2.2 Shot-Noise Renormalization

When the shot-noise clearance (SNC) is very low, the electronic noise (EN) has a strong influence on the shot-noise level and needs to be taken into account. Before calculating the clearance, the electronic-noise contribution should be retrieved from the shot-noise data. Considering the following notation:

$$G_{SN,dBm} = 10 \times \log\left(\frac{P_{SN}}{P_{ref}}\right) \tag{8.1}$$

$$G_{EN,dBm} = 10 \times \log\left(\frac{P_{EN}}{P_{ref}}\right) \tag{8.2}$$

We convert the data in linear scale and subtract the electronic noise contribution:

$$P'_{SN} = P_{SN} - P_{EN} = P_{ref}\left(10^{\frac{G_{SN,dBm}}{10}} - 10^{\frac{G_{EN,dBm}}{10}}\right) \tag{8.3}$$

To obtain the corrected data:

$$G'_{SN,dBm} = 10 \times \log\left(\frac{P'_{SN}}{P_{ref}}\right) \tag{8.4}$$

Where $P_{ref} = 1$ mW because the data were recorded in dBm with the spectrum analyzer. Then, the SNC is calculated again and plotted. In the following paragraphs we will present the results of the tests in CW light of the detectors OPA847-v1, OPA847-v2 and OPA855.

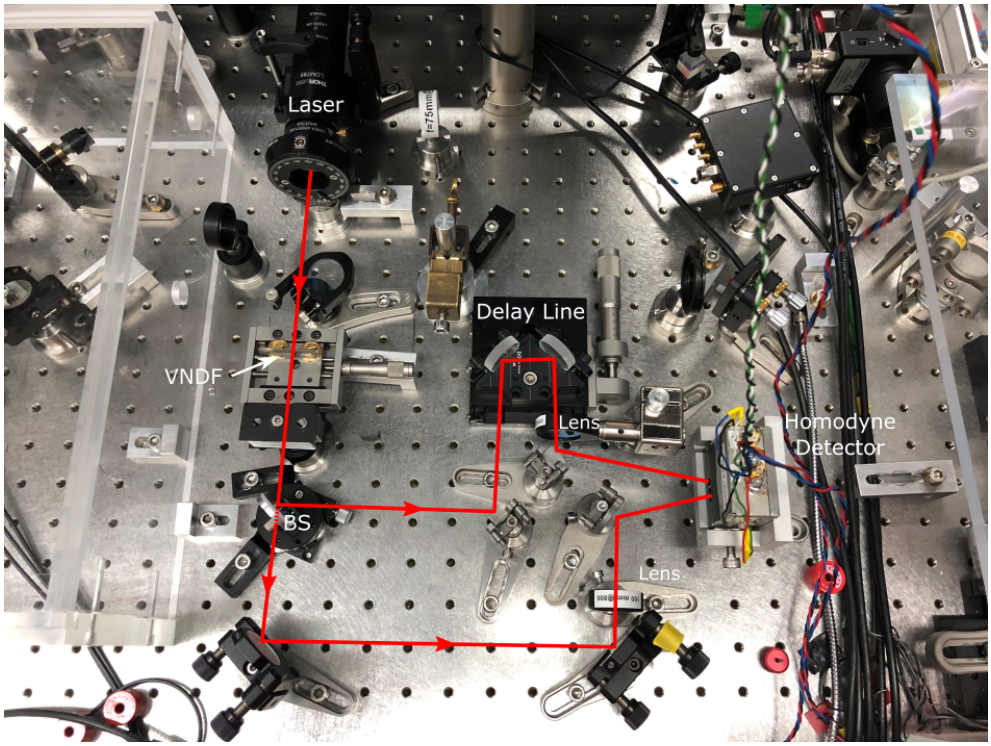

Figure 8.4 – Picture of the setup used to test the homodyne detectors with the superposed beam path. VNDF: variable neutral density filter.

Detector OPA847-v1 Let us consider the detector v1 with a transimpedance gain $R_F = 680\,\Omega$. We looked at the electronic noise (EN) and the shot-noise (SN) of the detector. We measured the traces with a MXA spectrum analyzer from Agilent Technologies with a resolution bandwidth (RBW) of 1.6 MHz and a video bandwidth (VBW) of 2.7 kHz. The results are shown on figure 8.5. From 1 mW to 16 mW, we double the light power each time. The first thing that we notice is that the SN evolves with the input light power but the clearance (SNC - section 5.3.1) is less than 5 dB at 16 mW.

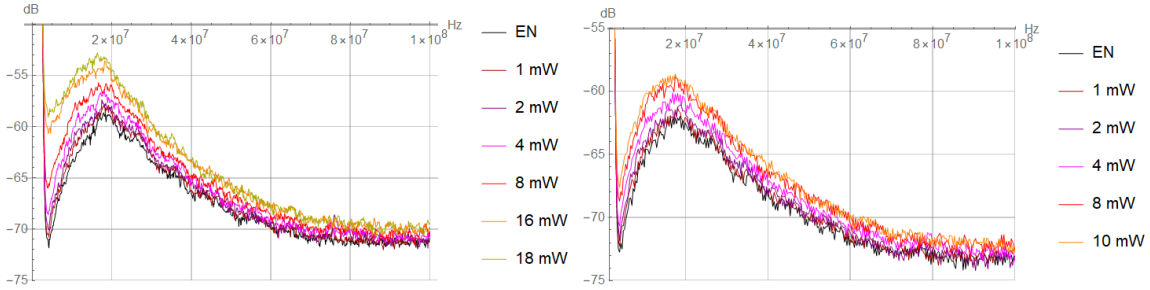

Figure 8.5 – Left: OPA847-v1, $R_F = 680\,\Omega$. Shot-noise curves measured in the CW regime from 1 mW to 18 mW. Right: OPA847-v2, $R_F = 510\,\Omega$. Shot-noise curves measured in the CW regime from 1 mW to 10 mW and on a 100-MHz frequency range. RBW = 1.6 MHz; VBW = 2.7 kHz.

The spacing should be 3 dB between two consecutive curves because $\Delta G = 10 \times \log\left(\frac{2\,P_{inc}}{P_{inc}}\right) = 3.01$ dB. As the clearance of the detector is low, we rescaled the shot-noise curves as presented above and plotted the spacing between the SN at 2 and 4 mW and the one between 8 and 16 mW. This is shown on figure 8.6 where the curves correspond to non-averaged data that we smoothed numerically. We see that on average the spacing between the shot-noise curves is 3 dB up to 60 MHz. We assume that the oscillations around this value could be partially due to the fact that the efficiency of the photocurrrent subtraction is not the same at all frequencies.

Let us consider the saturation of the detector. The maximum light power which we could use for our test was 18 mW, being the maximum power delivered by our CW laser. At this power, the shot noise is above the curve at 16 mW but the spacing with the latter rapidly decreases at frequencies above 40 MHz. It is difficult to say if the saturation threshold was reached at this point and it would require to perform tests at higher light power.

Finally, we looked at the bandwidth of this detector. In our case, we call bandwidth the frequency range over which we can distinguish the signal from the electronic noise. If we look at the curve at 16 mW in fig. 8.5, the shot-noise curve is above the electronic noise at 100 MHz but the clearance is very low ($\sim$ 3 dB). These results suggest that

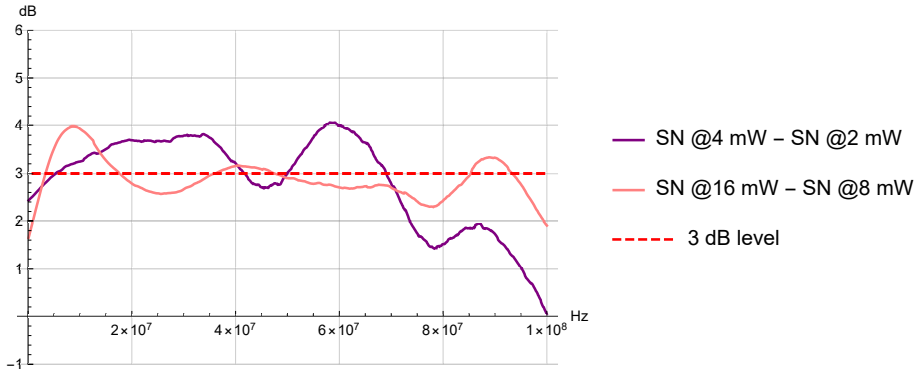

Figure 8.6 – OPA847-v1, $R_F = 680\,\Omega$. Shot-noise spacing between 2 and 4 mW and 8 and 16 mW. RBW = 1.6 MHz; VBW = 2.7 kHz.

the detector operates in a regime in which the transimpedance gain of the detector is too low. Increasing R_F would drastically reduce the bandwidth but increase the SNC (defined in section 5.3.1). As we want to measure quadrature squeezing at the repetition rate of our laser (156 MHz), we first chose to reduce the value of R_F to 510 Ω to see the effect it has on the detector bandwidth. This corresponds to the OPA847-v2 detector.

Detector OPA847-v2 We compare this detector to the previous one. We do not expect the functioning of the detector to be different, but test if we can retrieve the expected influence of R_F on the detector bandwidth. The circuit layout is the same as in figure 8.1, except for the transimpedance gain $R_F = 510\ \Omega$. We measured the electronic noise and the shot noise from 1 mW to 10 mW. The curves are shown on figure 8.5. As for the v1 detector, the SNC is very low and the signal does not increase much between 8 mW and 10 mW of input power, suggesting that the saturation has been reached. This observation is counter intuitive if we consider the definition of the output voltage of a TIA (eq. 7.1). For the same input light power, the output voltage of v2 is lower (fig. 8.7) so it should be possible to send more intense light on the detector before reaching the saturation, i.e. saturation should be higher than for the v1 detector.

If we compare the shot-noise measured at 4 mW with both versions of the detector, we see on fig. 8.7 that the signal is higher with the v1 detector than with the v2, which was expected according to equation 7.1. We make the same observation if we compare the electronic noise of the two detectors, the increase of R_F is associated to the increase of the thermal voltage noise (see section 5.2.2). As a result, the shot-noise clearance does not increase with the value of R_F.

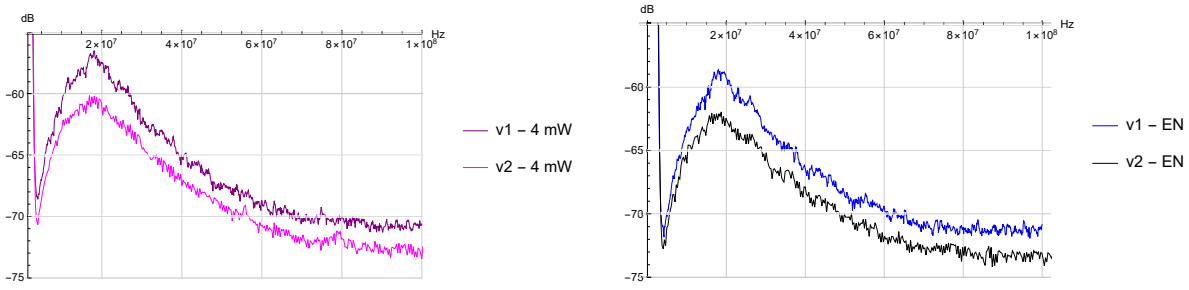

Figure 8.7 – Left: Shot-noise comparison at 4 mW of the OPA847-based detectors. Right: Comparison of the electronic noise (EN) of the OPA847-based detectors.

Also, the value of R_F does not seem to have an influence on the bandwidth of the detectors. This phenomenon is difficult to explain, but it could indicate that the detectors do not operate correctly when the transimpedance gain is that low. We will see in section 8.3 that this phenomenon is confirmed when we operate with pulsed light.

Detector OPA855 We test the OPA855-based detector with CW light and compare the results with the OPA847-based detectors. The results are displayed in fig. 8.8. In this regime, the SNC measured at 4 mW and 40 MHz is 6 dB and we can see that the detector seems to operate linearly up to 4 mW of total input power. The spacing between consecutive SN curves is reduced between 4 and 8 mW suggesting that the saturation was reached. In the following section, we will present the results of the same tests performed with our laser source.

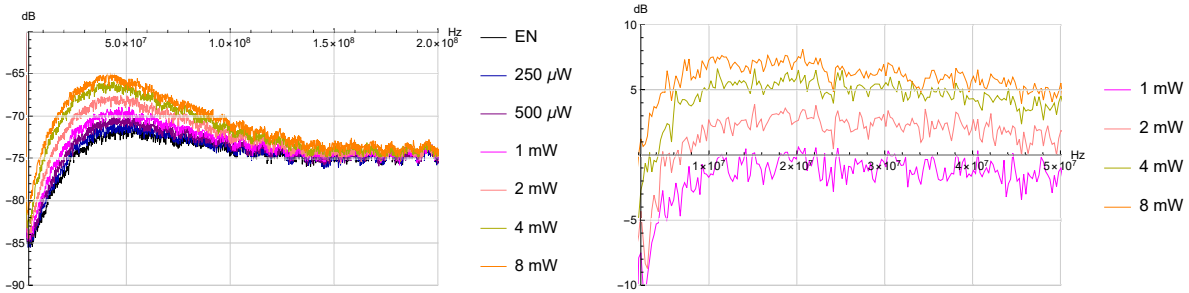

Figure 8.8 – Left: Shot noise curves of an OPA855-based detector in the CW regime. EN: electronic noise. RBW = 750 kHz; VBW = 750 Hz. Right: Shot-noise curves from 1 mW to 8 mW of the OPA855-based detector measured on a 50-MHz frequency range and corrected with the electronic noise. RBW = 820 kHz; VBW = 7.5 kHz.

8.3 Detector Characterization with Pulsed Light

8.3.1 Measurement of the Common-Mode Rejection Ratio

We use the same test setup and protocol as in the previous section to evaluate the response of the three detectors and their saturation. The signal of the femtosecond laser features an intense peak at its repetition rate, which we will call the common mode at 156 MHz. When one PD is illuminated, the measured common mode at 156 MHz is more intense than when both PDs are illuminated at the same time due to the subtraction of the photocurrents. The difference between the height of the two peaks is the common-mode rejection ratio (CMRR, see section 5.3.2) and should be as high as possible. Experimentally, to evaluate the CMRR we reduce the incident light power, such that the shot noise from one PD does not saturate the circuit. In practice, we can measure the CMRR at different incident powers from 10 μW to 200 μW (half on each photodiode). The CMRR should increase with the incident power, reach a maximum and decrease again when the SN from 1 PD saturates the detector. The highest rejection value is the CMRR of the detector. We measured similar values for the three detectors so we give as an example the results of the CMRR measurement of the OPA847-v1 detector. A typical measurement is shown in figure 8.9 where we superpose the shot-noise signal from one photodiode and the shot noise when both photodiodes are illuminated. At 75 μW, it is 40 dB indicating that the detector performs an efficient subtraction of the photocurrents.

Improve the CMRR with the PD Bias Voltage At each power, the common-mode rejection ratio can be improved by adjusting the bias voltage of the photodiodes (section 7.1.2). Indeed, the quality of the photosubtraction relies on the fact that the photodiodes are identical. In practice, this cannot be the case for manufacturing reasons. Thus, adjusting the bias voltage of each PD independently allows to modify their terminal capacitance so as to reduce the discrepancies in their performances (section 7.1.2, fig. 7.4).

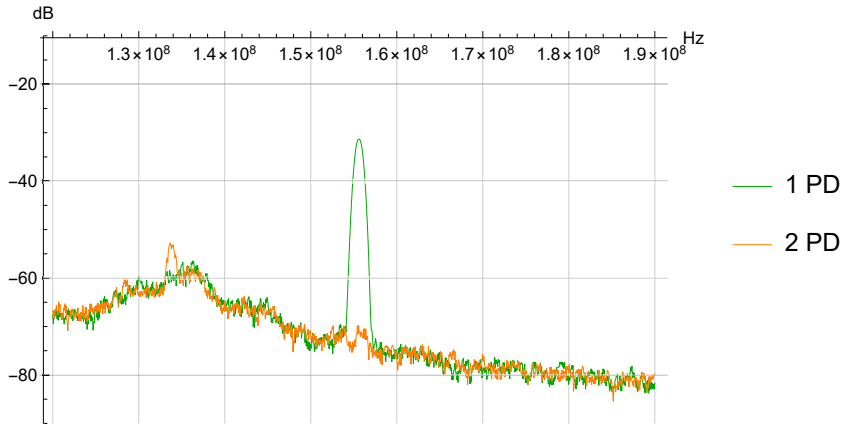

Figure 8.9 – CMRR of the OPA847-v1 detector, $R_F = 680\ \Omega$, measured at 75 μW. RBW = 820 kHz; VBW = 20 kHz.

8.3.2 Measurement of the Shot-Noise Clearance and Instabilities in the Pulsed Regime

OPA847-based Detectors In the pulsed regime, we measured the response of the detector at several input powers, from 250 μW, which was the lowest light power for which we could see some signal, to 8 mW, being the maximum power we could use in our test setup (fig. 8.4). Compared to the measurements in CW light, what was supposed to be the clearance was very high at 500 μW, i.e. around 30 dB, but the signal was very unstable (fig. 8.10, left). It displays small peaks arbitrarily distributed all along the 100-MHz measurement bandwidth, which could be caused by badly welded components on the PCB. We increased the input light progressively to reach the saturation threshold but we could never measure a signal which was proportional to the input power. For the v1 detector, the threshold was reached at around 4 mW, beyond which we could witness a drastic decrease of the shot-noise signal. We tried to do the same tests with the v2 detector, but it revealed to be very hard to align. Even at 250 μW of input power, the detector would saturate as can be seen in fig. 8.10, where the shot-noise curve is below the level of the electronic noise at some frequencies indicating that the detector is saturated.

Detector OPA855 We tested the OPA855-based detector in the same conditions and measured the curves of fig. 8.11. The electronic noise curve displays a small dip around 156 MHz caused by a notch filter. A notch filter is a filter that attenuates the signals within a specific frequency band. It is the opposite of a band-pass filter. We use it to reduce the amplitude of the common mode at 156 MHz. Because the filter is placed at the detector output, it does not affect the dynamic of the detector. Details on the functioning of notch filters can be found in the appendix B. The curves display less

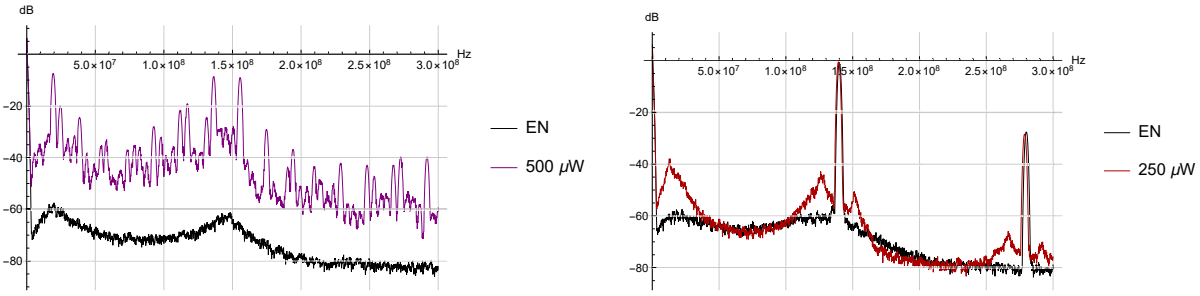

Figure 8.10 – Left: Shot noise measured in the pulsed regime at 500 μW of the detector OPA847-v1 with $R_F = 680\,\Omega$ (purple curve). The black curve is the electronic noise. Right: Comparison of the electronic noise of the detector OPA847-v2 (black curve) and the SN at 250 μW (red curve). RBW = 1.6 MHz; VBW = 33 kHz.

fluctuations than the OPA847-based detectors but the functioning of these detectors is similar with a large response at low input light power.

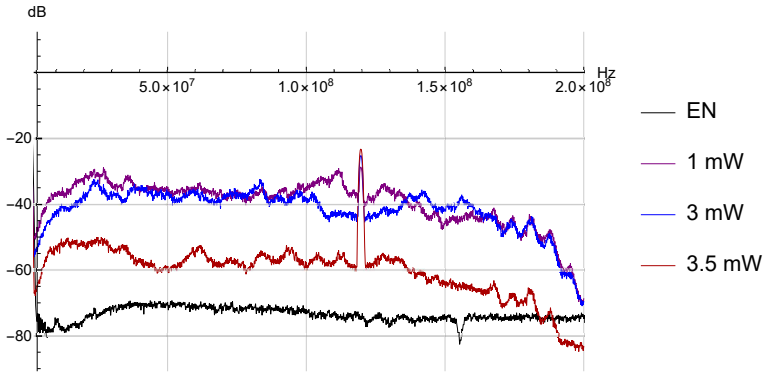

Figure 8.11 – Shot-noise curves of the OPA855-based detector measured in a pulsed regime. The black curve is the electronic noise (EN). A notch filter was placed at the detector output to reduce the height of the common mode at 156 MHz. RBW = 1.1 MHz; VBW = 7.5 kHz.

In order to understand why the performances of the detectors were different in CW and pulsed regime, we also analyzed the detectors in the temporal domain.

8.3.3 Analysis in the Temporal Domain

We looked at the shot noise of the detector on a 4-GHz-bandwidth Waverunner-8404M oscilloscope from Teledyne-Lecroy. The results are shown on figure 8.12.

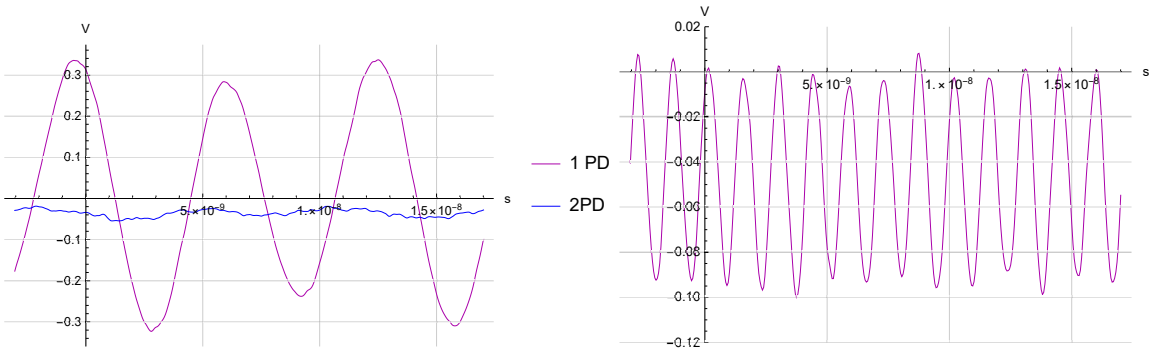

Figure 8.12 – Detector OPA847-v1. Left: Comparison of the SN measured with the oscilloscope when one PD is illuminated and when both are. The input power is 500 μW, i.e. half on each PD. Right: Electronic noise measured at the oscilloscope when no notch filter is used at the detector output.

We looked at the signal when one photodiode is illuminated and when both PD are illuminated. The signal of 1 PD in fig. 8.12 shows large oscillations at the laser repetition rate instead of an always positive signal (or negative depending on which PD we are looking at), which seems to indicate that we are in a saturated regime. Figure 8.12 shows the electronic noise measured with the oscilloscope. It displays large oscillations at around 700 MHz, which we also measured on the spectrum analyzer as a peak of high intensity (fig. 8.14). This peak could be an oscillation of the operational amplifier, which we did not detect before because it was at a frequency well beyond the bandwidth we were interested in (see appendix A). Finally, we compared the electronic noise with the shot noise when both PD are illuminated. For this measurement, we placed a low-pass filter (LPF) of cutoff frequency 250 MHz at the detector output. The LPF was used to smooth the measured curves, but it does not affect the dynamic of the detector. We obtained the curves of figure 8.13. We see that at 500 μW the amplitude of both signals is the same, meaning that the homodyne signal at this power is mostly electronic noise. This measurement tells us that the signal measured at the spectrum analyzer (fig. 8.10) does not correspond to a shot-noise clearance. We observed the same phenomenon with the OPA855-based detector, where the oscillation in the electronic noise was at 500 MHz.

Therefore, we investigated the origin of this oscillation and tried to get rid of it. So far, we assumed that the transimpedance gain of the detectors was low compared to [Masalov 17], but we did not consider the noise gain of the op-amp (eq. 7.8) because it was not mentioned in previous schemes. In the next section, we will present the modifications we did on our circuits to adjust the noise gain of the TIA amplifier and how it affected to output signal.

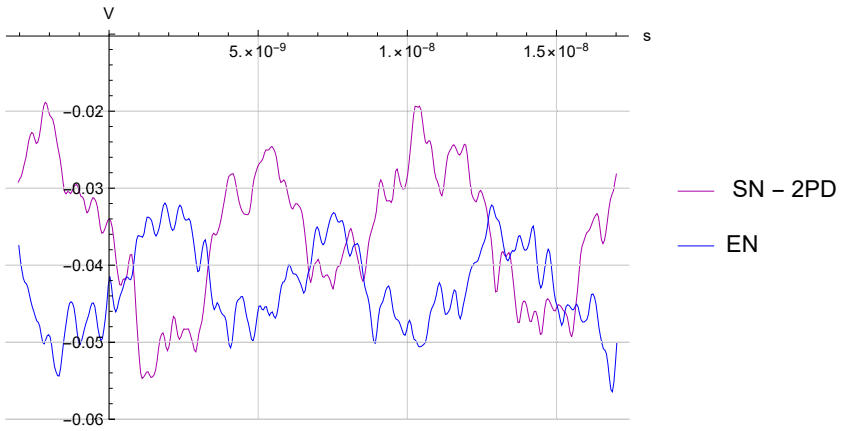

Figure 8.13 – Comparison of the homodyne signal at 500 μW and the electronic noise of the detector OPA847-v1. A low-pass filter was placed at the detector output to eliminate the oscillation at 700 MHz (fig. 8.14).

8.3.4 Correction of the Amplifier Gain

OPA847-based Detector To modify the noise gain of the transimpedance amplifier (TIA), we place a resistor R_C in parallel with the feedback resistor R_F as was presented in the previous chapter (see section 7.2, fig. 7.7). In this configuration, the TIA gain is $R_F = 2.2$ kΩ and the noise gain is $G_{NG} = 18$ V/V according to the definition given in equation 7.8 where we chose $R_C = 130$ Ω. We chose the noise gain to be above the minimum noise gain of the OPA847 amplifier, i.e. 12 V/V indicated in the datasheet of the device. The feedback capacitance C_F corresponds to the parasitic capacitance of the feedback resistor itself, which is estimated to 0.2 pF, i.e. close to the calculated value (eq. 7.3). First, we removed the second-amplification stage so as to be able to adjust each stage of the circuit independently. Because the gain of the TIA is low, we expect that the output signal would not be dominated by the DC signal. Thanks to this modification, we eliminated the peak at 700 MHz in the electronic noise (fig. 8.14).

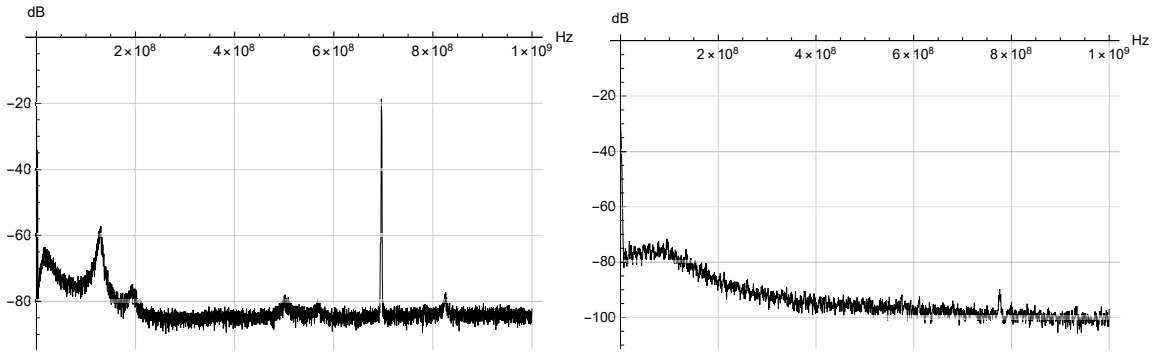

Figure 8.14 – Left: Electronic noise of the detector OPA847-v1 measured with the spectrum analyzer. RBW = 820 kHz; VBW = 20 kHz. Right: Electronic noise of the OPA847-based homodyne detector after adjustment of the noise gain. A residual peak is visible around 700 MHz. RBW = 3 MHz; VBW = 120 kHz.

We characterized the detector with pulsed light. We want to stress that the following results are preliminary and that the detector is still under test. We measured the output signal of the detector with the spectrum analyzer for several input powers. The results are shown on figure 8.15. We see that in comparison to fig. 8.10, the signal is

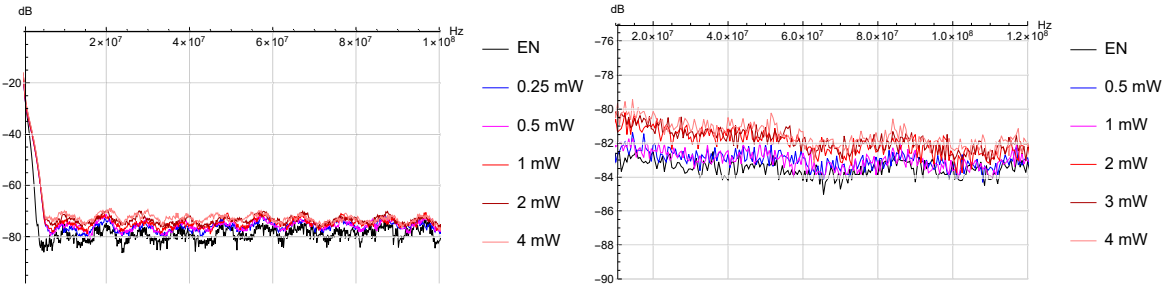

Figure 8.15 – Left: Shot-noise curves of the OPA847-based detector after adjustment of the noise gain. RBW = 3 MHz; VBW = 43 kHz; 100-MHz frequency range. Right: Shot noise of the OPA855-based detector after adjustment of the noise gain of the TIA amplifier. RBW = 3 MHz; VBW = 3 MHz; 120-MHz frequency range; average over 10^5 points.

very low, i.e. 5-6 dB at 4 mW but it evolves as it is supposed to do with the input power. Also, the common-mode rejection ratio is similar to what we previously measured, i.e. 44 dB at 50 μW and the SNC is above zero at least up to 100 MHz. For clarity, we chose to present the results in fig. 8.15 on a 100-MHz bandwidth, which does not include the common mode at the laser repetition rate, 156 MHz.

Then, we observed the output signal in the temporal domain. We compared the homodyne signal with the electronic noise (fig. 8.16) and we see that even though the homodyne signal is very low ($\sim$ 5 mW Vpp), it remains superior to the electronic noise

contrary to fig. 8.13.

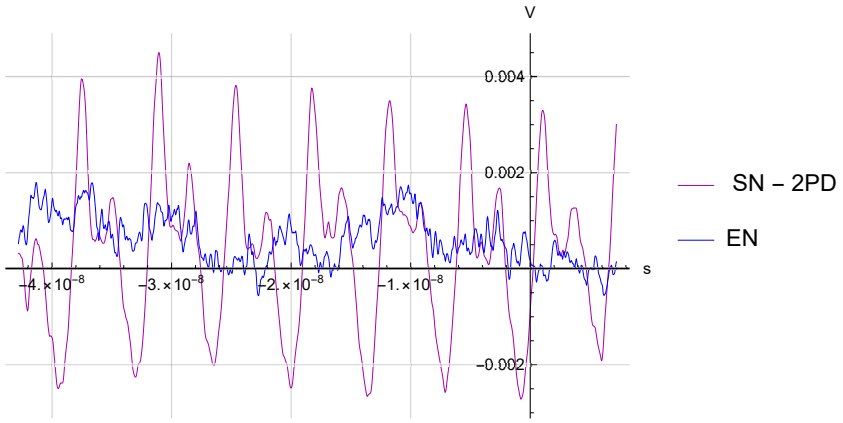

Figure 8.16 – OPA847-v1 detector. Superposition of the electronic noise and the homodyne signal at 310 μW total input power.

At this point, we need to increase the SNC of the detector if we want to do homodyne measurements. We have the option to increase the TIA gain, i.e. increase the output signal according to equation 7.1 and/or to decrease to level of the electronic noise by reducing the noise gain. At the same time, we need to take into account the evolution of the detector bandwidth. Indeed, for an OPA847 used with a noise gain of 12 V/V, the maximum bandwidth is 325 MHz, which will be even more reduced in case of a larger TIA gain according to the equations 7.7 and 7.2. For that reason, we considered using OPA855 operational amplifiers in our detectors, which features a gain-bandwidth product of 8 GHz (3.9 GHz for the OPA847, see section 7.2). In this case, the maximum available bandwidth with this op-amp is 1 GHz (eq. 7.7). As we are interested in doing homodyne measurement at the repetition rate of our laser, i.e. corresponding approximately to a 200-MHz bandwidth detector, we will be able to use high transimpedance gain R_F to increase the output signal.

OPA855-based Detector In order to adjust the noise gain of the first amplifier of the circuit, we placed a resistor $R_C = 65\,\Omega$ in parallel to the feedback resistor. In this configuration, the noise gain G_{NG} is 18 as in the OPA847-based detector and the transimpedance gain is $R_F = 1.1$ kΩ. Here also, the feedback capacitance corresponds to the parasitic capacitance of the feedback resistor (0.2 pF) and we removed the second-amplification stage.

We measured the shot noise for several input light powers and plotted the results (fig. 8.15). In this configuration, we see that the SNC is very low so we renormalized the shot-noise levels with the electronic noise to evaluate the response of the detector.

We obtained the curves of fig. 8.17, which correspond to averaged data measured at 50 MHz. The spacing between consecutive curves is the same, indicating that the shot noise evolves linearly with the incident power, but it is inferior to 3 dB, which we assume is another indication that the shot-noise level is very low compared to the electronic and that the TIA gain of the detector should be increased. Nevertheless, the CMRR = 55 dB at 300 μW which is very encouraging.

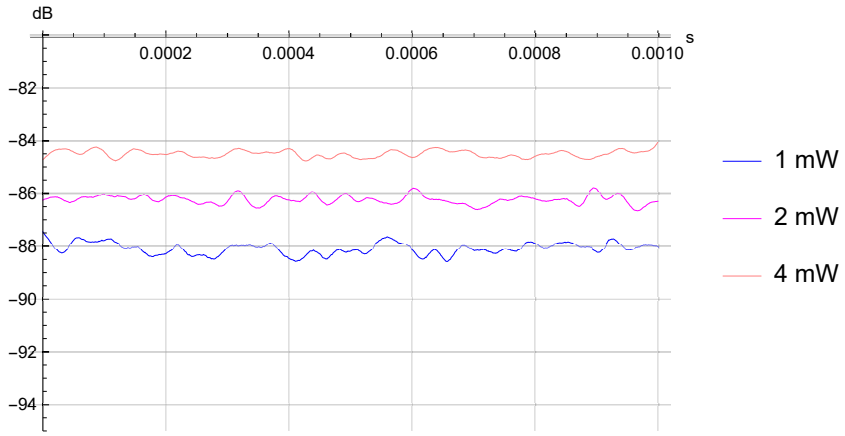

Figure 8.17 – Averaged shot-noise curves measured at 50 MHz and corrected from the electronic noise. RBW = 3 MHz; VBW = 3 MHz; average over 10^5 points.

The previous observations were confirmed by the detector analysis in the temporal domain. We looked at the output signal on the oscilloscope and compared the homodyne signal with the signal from one photodiode. The results are displayed on the figure 8.18.

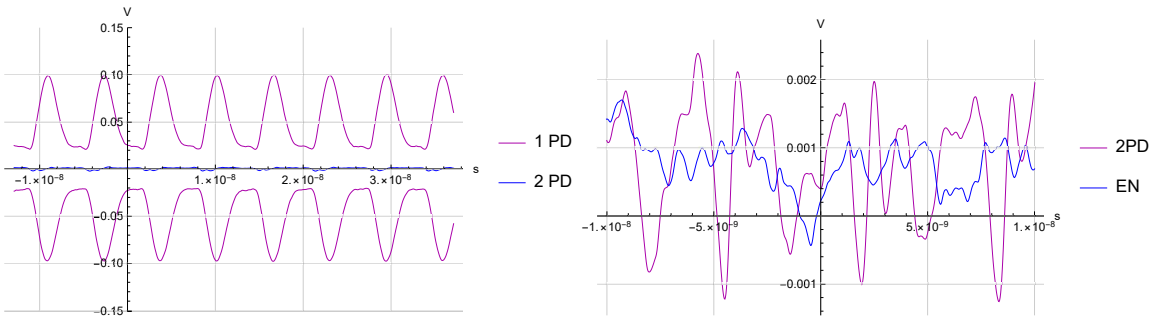

Figure 8.18 – Left: Comparison of the SN from each photodiode with the homodyne signal. OPA855-based detector after adjustment of the noise gain of the TIA amplifier. Right: Comparison of the homodyne signal with the electronic noise (EN).

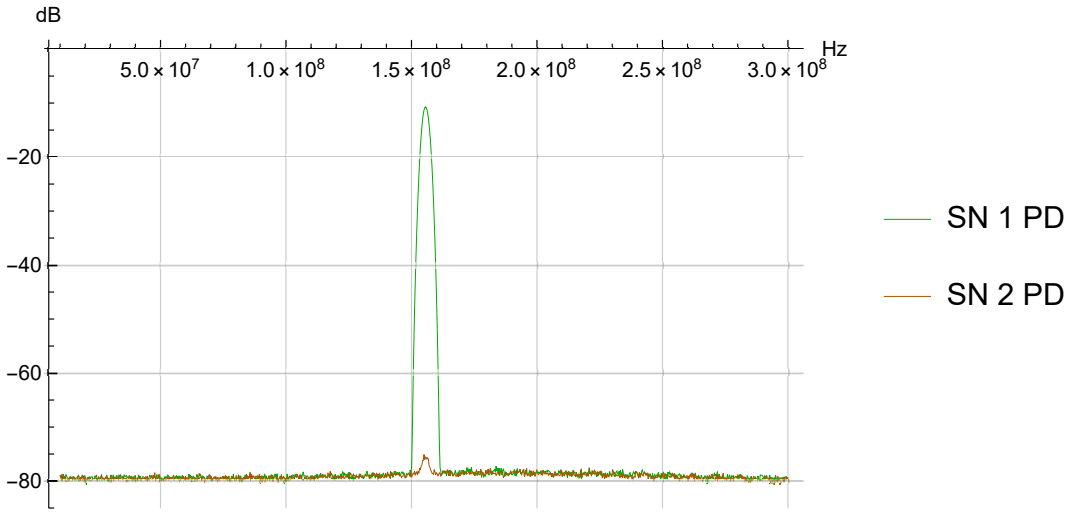

Figure 8.19 – CMRR measurement of the OPA855-based detector at 300 μW of input light power. The feedback resistor is $R_F = 2.1$ kΩ and the noise gain is $G_{GN} = 16.2$. CMRR = 64 dB. RBW = 2.7 MHz; VBW = 2.7 MHz.

8.3.5 Latest Results

We increased the transimpedance gain of the OPA855-based detector, $R_F = 2.1$ kΩ, and we set the noise gain of the circuit to $G_{NG} = 16.2$. We show the results in figures 8.19 and 8.20.

We measured a common-mode rejection ratio (CMRR) of 64 dB at 300 μW of input light power and the shot-noise clearance (SNC) with a spectrum analyzer. With 3 mW of input light power, i.e. 1.5 mW on each photodiode, SNC = 7 dB at 40 MHz and it is almost 5 dB at 100 MHz.

We can already use this detector to measure squeezing at 156 MHz from our waveguide-based experiment (see section 6.4), which is very promising.

8.3.6 Prospects

The preliminary results of the tests of the OPA855-based detector after correction of the amplifier gain are encouraging. Even if the signal is above the electronic noise at 100 MHz, it is low over the measurement bandwidth indicating that the TIA should be further increased. Nevertheless, compared to the version of the OPA855-based detector described is section 8.1.2, the signal we measure with the spectrum analyzer is consistent with what we measure with the oscilloscope and the common-mode rejection ratio is 64 dB at 300 μW.

In future developments, we will focus on this detector, starting with increasing the gain of the transimpedance amplifier while taking into account its evolution with the

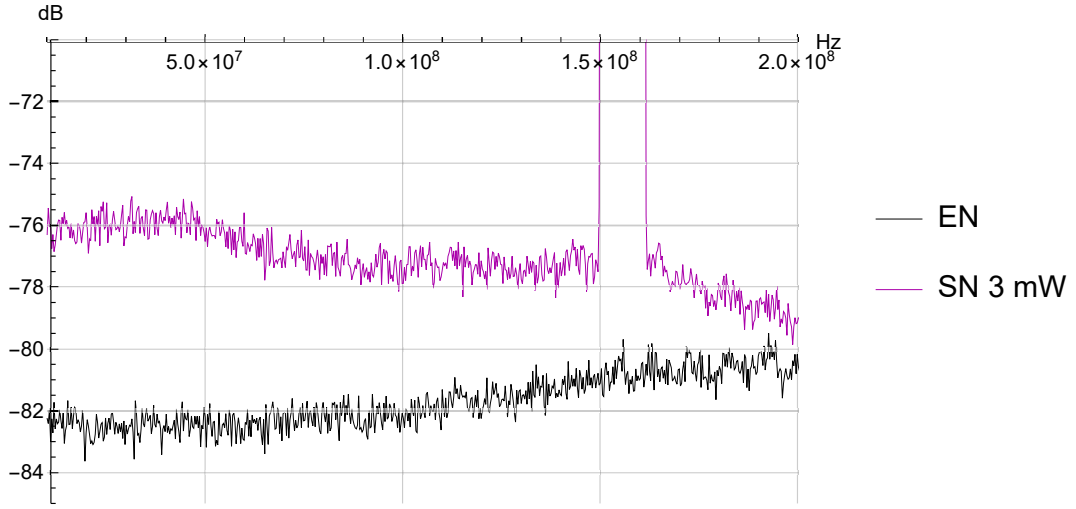

Figure 8.20 – OPA855-based detector with $R_F = 2.1$ kΩ and $G_{GN} = 16.2$. The black curve is the electronic noise (EN) and the purple curve is the shot noise (SN) at 3 mW of input light power, i.e. 1.5 mW on each photodiode. RBW = 2.7 MHz; VBW = 2.7 MHz.

feedback resistance R_F, as well as the evolution of the detector bandwidth (fig. 8.21). The goal is to evaluate the maximum SNC that we can have with this detector. In a second time, we want to reconnect the second-amplification stage and see if separating the AC and DC signal improves the performance of the detector. After these tests, we would try to measure quadrature squeezing in our PPKTP waveguide-based experiment (see section 6.4).

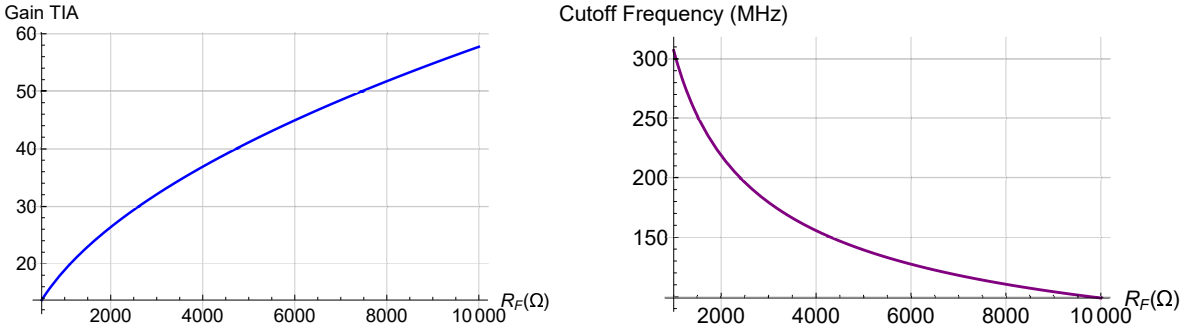

Figure 8.21 – Left: Evolution of the TIA gain with the feedback resistor R_F calculated with equation 7.9. Right: Evolution of the cutoff frequency f_{TIA} (eq. 7.2) with the R_F.

Conclusion

In this manuscript, we presented the generation of two-mode squeezed states of light via single-pass non-collinear parametric down conversion. We measured quadrature squeezing in four spectral modes using mode-selective homodyne detection and we unveiled non-classical correlations between spatio-spectral modes. The results of this work are published in [La Volpe 20]. This experiment, presented in chapter 6, was started during the Ph. D. of L. La Volpe [La Volpe 19]. When I joined the group, I worked on the design and implementation of the pulse shaper we used for the mode-selective homodyne detection. This is the subject of chapter 4.

The project was motivated by the work presented in [Yokoyama 13]. From the pairs of entangled pulses generated at a repetition rate of 156 MHz by our experiment, we wanted to produce dual-rail cluster states, in which the down-converted pulses would be the nodes and the links between them would be entanglement, according to the protocol described in chapter 6 and [Yokoyama 13]. In our configuration, the states generated by the PDC are highly multimode both spectrally and spatially. For that reason, the squeezing per mode that we measured was very low. As squeezing and entanglement are linked by a basis change which can be performed experimentally by a beam splitter (chapter 2), this corresponded to a low level of entanglement.

Thus, we decided to develop a PDC setup based on PPKTP waveguides. In chapter 6, we presented the numerical simulations that we did using the codes developed by our collaborators at Paderborn and the interactions we had with the company AdvR in order to design the waveguide chips for our experiment. We are developing in parallel two setups based on type-0 and type-II phase-matched waveguides, which would replace the BBO crystal and the pump cavity. Finally, we described the characterization of the waveguides and we presented the progress on our project, in particular the detection of PDC photons produced in a single-pass in a type-0 waveguide, which is encouraging.

In the meantime, we worked on the development of a large-bandwidth homodyne detector, based on the work done in [Cooper 13, Masalov 17, Zavatta 02], in order to perform pulse-by-pulse measurement, i.e. at a repetition rate of 156 MHz. In chapter 5, we recalled the theory of homodyne detection and presented the parameters we used to characterize the detectors. In chapter 7, we described the structure of the homodyne detectors as well as the development of printed circuit boards. Finally, in chapter 8,

we presented the preliminary results of the characterization of some of the detectors we built. The detectors that we presented have a bandwidth close to 100 MHz but their shot-noise clearance is not high enough yet to perform homodyne measurements.

Appendices

Appendix A

Parasitic Oscillations in Homodyne Detection

The two main sources of noise in our detector are the thermal noise (see chapter 5) and oscillation noise. The first one is a white noise and depends mainly on the temperature of the electronic components. The seconde one has at least two origins: it can be exterior to the circuit and be detected by it. In this case, we just need to identify the source of oscillation and turning it off. Otherwise, it can be generated by the circuit itself (fig. A.1). In high-frequency circuits, the size of the components and their nominal value are critical points, as well as the length and width of the conductive tracks.

A.1 Oscillations in RLC-like circuits

Oscillations can appear in any circuit composed of resistances R, capacitances C and inductances L. The frequency and amplitude of the oscillations depend on the values of R, C and L. This derivation aims at describing how a transimpedance amplifier (TIA) can constitute an oscillating circuit. The TIA can be modeled by a RLC circuit, which can be in series or in parallel (fig. A.2). It is composed of an inductance L, a capacitance C and total resistance $R_L = R + r$ where R corresponds to the value of a resistor and r to the intrinsic resistance of the coil, which we consider here to be ideal ($r = 0\ \Omega$). In this configuration, the RLC circuit is composed of the feedback capacitor C_F and resistor R_F of the TIA and the conductive track between the photodiodes and the operational amplifier is modeled by a coil with 1 spire. Its inductance reads:

$$L = \frac{\mu_0 N^2 S}{\ell} \tag{A.1}$$

where $\mu_0 = 4\pi \times 10^{-7}$ H.m^{-1} is the magnetic constant, ℓ is the length of the coil, i.e. the track length between the PDs and the transimpedance amplifier (TIA), S is the section of this coil and N is the number of spires, which we chose to be 1.

Figure A.1 – Screenshot of the shot-noise trace of an OPA855-based detector measured with a spectrum analyzer. The peak at 500 MHz corresponds to a resonance of the circuit. We can see its first harmonics at 1 GHz.

A.2 Temporal derivation

A TIA is used to convert a current - in our case a photocurrent - into a voltage U with a transimpedance gain R_F. The temporal evolution of U is described by the following differential equation:

$$LC\frac{d^2U(t)}{dt^2} + RC\frac{dU(t)}{t} + U(t) = 0 \tag{A.2}$$

from which we can determine ω_0, the frequency of the oscillations. The resolution of this equation gives: $\Delta = \frac{R^2}{L^2} - \frac{4}{LC}$. Because, we want to study the oscillations in this circuit, we consider the configuration in which $\Delta < 0$. In this case, the equations have two solutions from which we can infer an expression of $U(t)$:

$$U(t) = 2\,e^{-\frac{R}{2L}}\,\cos\left(\omega_0 t\right) \tag{A.3}$$

with $\omega_0 = \frac{1}{2}\sqrt{\frac{R^2}{L^2} - \frac{4}{LC}}$. The expression of $U(t)$ shows that oscillations are damped by R, meaning that with a sufficiently large value of R no oscillations should be witnessed. Moreover, when considering the reverse case where $R = 0\ \Omega$, ω_0 depends only on the capacitance and the inductance : $\omega_0 = \frac{1}{\sqrt{LC}}$.

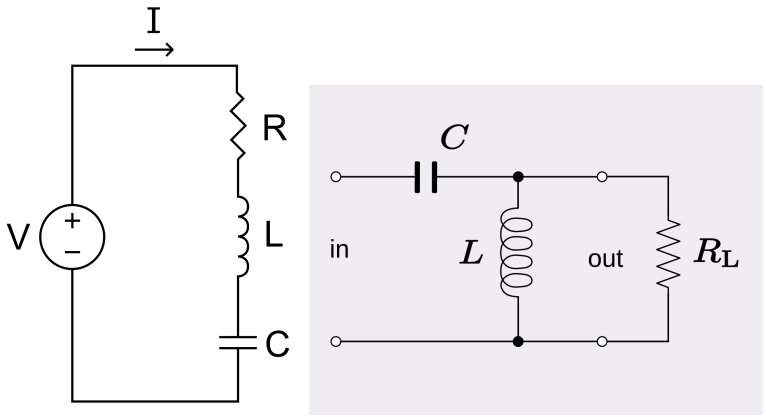

Figure A.2 – Schematics of RLC circuits in series (left) and in parallel (right).

In our case, the oscillation at 500 MHz was not caused by the TIA parameters. Its amplitude and frequency did not change when we changed the values of the feedback resistor R_F and capacitor C_F. We think that the oscillation could correspond to an intrinsic resonance of the OPA855 and we observed the same oscillation at 700 MHz in the OPA847-based detectors. To damp the oscillation, we used a compensation resistor R_C placed in parallel to R_F as descibed in section 7.2 of chapter 7.

Appendix B

Notch Filters

The RLC notch filter is a passive circuit composed of a resistance R mounted in parallel to a self (of inductance L) and a capacitance C (fig. B.1). It is the combination of a low-pass and a high-pass filter designed to filter out a specific frequency band, the *stop-band*, while leaving the other frequencies unaffected. It is the opposite of a pass-band filter, which is designed to filter out all frequencies outside of a specific range.

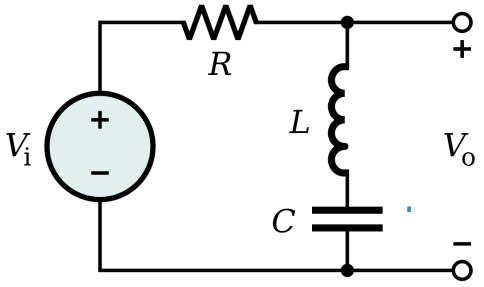

Figure B.1 – Schematic of a band-stop filter.

Transfer function The transfer function is the ratio between the output and input voltage of an electronic circuit. $H(s) = \frac{V_{out}(s)}{V_{in}(s)}$, where s is a variable, which here has the dimension of an angular frequency. It is defined as:

$$H(s) = \frac{s^2 + \omega_0^2}{s^2 + \Delta\omega\, s + \omega_0^2} \tag{B.1}$$

$$= \frac{s^2 + \frac{1}{LC}}{s^2 + \frac{R}{L}s + \frac{1}{LC}} \tag{B.2}$$

where we identify the central angular frequency ω_0:

$$\omega_0 = 2\pi f_0 = \frac{1}{\sqrt{LC}} \tag{B.3}$$

$$f_0 = \frac{1}{2\pi\sqrt{LC}} \tag{B.4}$$

f_0 is the central frequency of the stop band. We also define the bandwidth (FWHM):

$$\Delta\omega = 2\pi\Delta f = \frac{R}{L} \tag{B.5}$$

$$\Delta f = \frac{R}{2\pi L} \tag{B.6}$$

We see that while the inductance L is involved in the definition of both parameters, the resistance acts only on the dip width and the capacitance only on its position.

Quality Factor The transfer function can also be expressed with a quality factor Q, linking notably the center of the stop-band f_0 with its width Δf. The Q factor describes the resonance behavior. Therefore, for a notch filter, a narrow stop-band corresponds to a high quality factor (resonance).

$$H(s) = \frac{s^2 + \omega_0^2}{s^2 + \frac{\omega_0}{Q}s + \omega_0^2} \tag{B.7}$$

which gives several expressions involving the quality factor:

$$Q = \frac{f_0}{\Delta f} \tag{B.8}$$

$$\Delta f = \frac{1}{2\pi Q\sqrt{LC}} \tag{B.9}$$

Appendix C

Detailled LtSpice Schematics of Dual-Output Detectors

In this appendix, we focus on the elements of the circuits, which we did not mention in the chapter 7.

C.1 OPA847-based Homodyne Detector

Figure C.1 shows the detailled LtSpice schematics of the v1-OPA847 detector.

Photodetection The photodiodes (PD) are modeled by a current source in parallel to a capacitance, which value is the intrinsic capacitance of the chosen photodiode. It is possible to import data from a text file into the LTSpice schematics to define the waveform of the current source. It corresponds to the piecewise linear (PWL) parameter in fig. C.1. The capacitances C8, C9, C10 and C11 are used to filter the power supply of the PDs, as well as the resistors R4 and R5.

Transimpedance Amplifier We use an OPA847 operational amplfier (op-amp) for the current-to-voltage conversion of the photocurrents from the PD. Its gain-bandwidth product is 3.9 GHz and the minimum noise gain of the op-amp for stability is 12 V/V. The capacitances C1 to C4 are used to filter the power supply of the op-amp and their values are the one given in the datasheet of the component.

The feedback parameters of the transimpedance amplifier (TIA) are $R_F = 680\ \Omega$ and $C_F = 2$ pF. In this configuration, the cutoff frequency of the TIA is 250 MHz (fig. C.2).

High-Pass Filter We use another OPA847 to implement an active high-pass filter (HPF). This allows to retrieve and amplify the high-frequency components of the signal

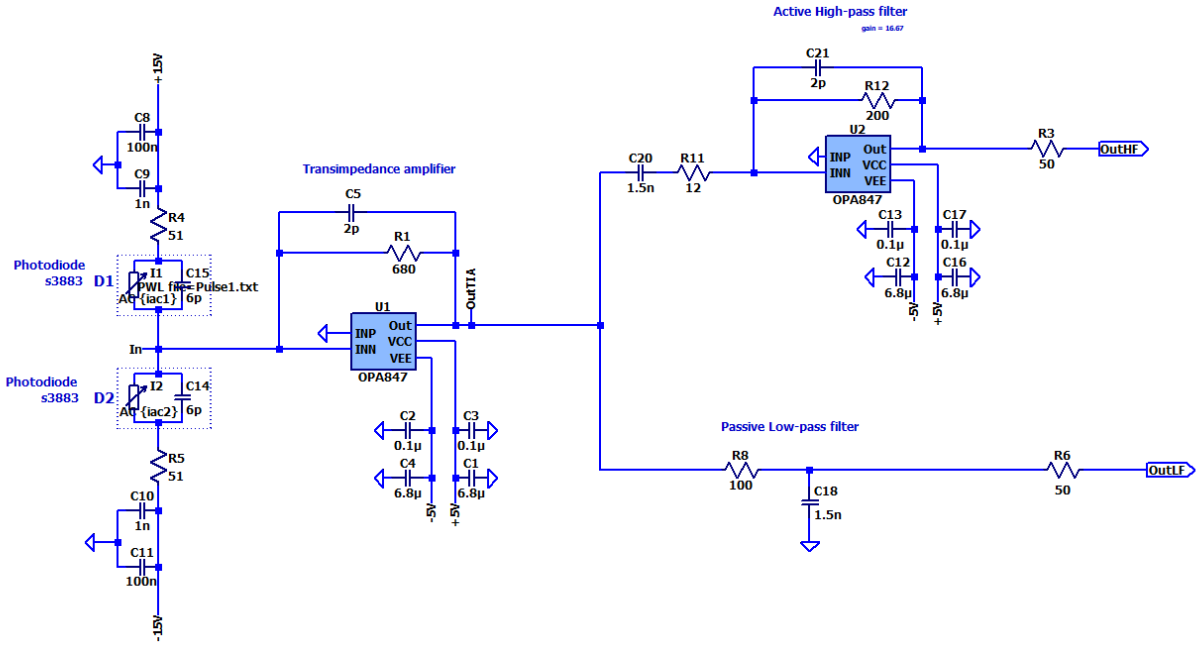

Figure C.1 – Spice schematics of the v1-OPA847 homodyne detector.

at the TIA output. The lower cutoff frequency of the HPF is fixed by R11 and C20 (f_c = 8 MHz), while the upper cutoff frequency is set by the TIA. The gain of the voltage amplification is fixed by R12 and R11 such that $G_{inv} = \frac{R12}{R11} = 16.67$. The corresponding Bode curve is displayed in figure C.2.

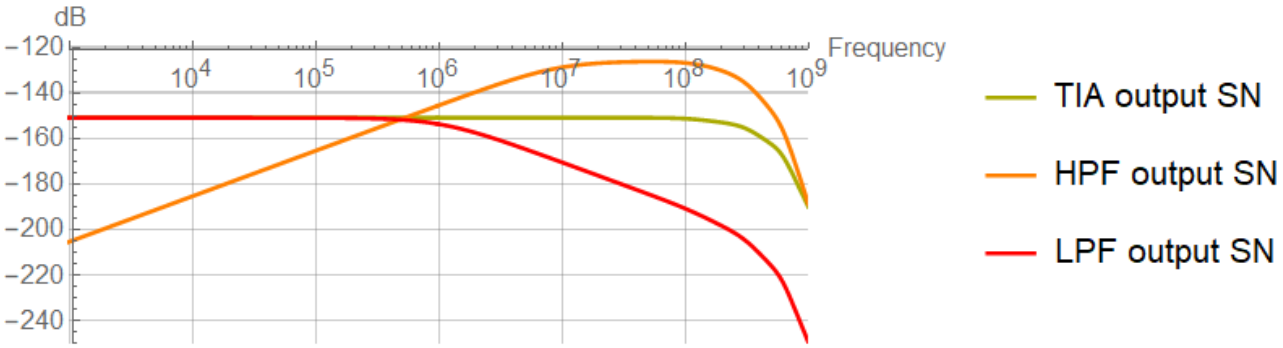

Figure C.2 – Bode curves of the OPA847-v1 detector.

Low-Pass Filter We retrieve the DC signal with a low-pass filter (LPF), which cutoff frequency is fixed by R8 and C18, f_{LPF} = 1 MHz. The corresponding Bode curve is displayed in figure C.2.

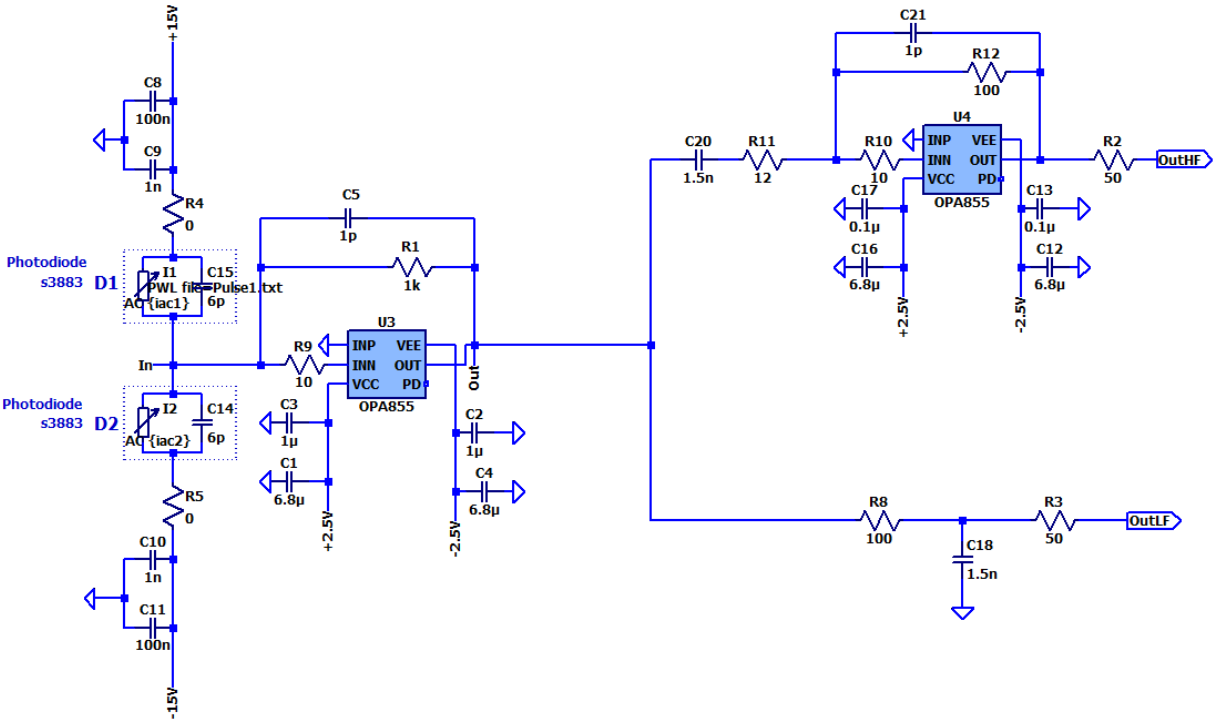

Figure C.3 – Spice schematics of the v1-OPA855 homodyne detector.

Finally, the resistors R3 and R6 are placed at the detector outputs for impedance matching (fig. C.1). Their value is set by the measurement device. For a spectrum analyzer or an oscilloscope R3 = R6 = 50 Ω.

C.2 OPA855-based Homodyne Detector

Figure C.3 shows the detailled LtSpice schematics of an OPA855 detector.

Photodetection The photodiodes (PD) are modeled by a current source in parallel to a capacitance, which value is the intrinsic capacitance of the chosen photodiode. The capacitances C8, C9, C10 and C11 are used to filter the power supply of the PDs. In this configuration, we fixed the values of R4 and R5 to zero because the noise of power supplies that we use is very low.

Transimpedance Amplifier The OPA847 op-amp has a gain-bandwidth product of 8 GHz and a minimum noise gain for stability is 7 V/V. The capacitances C1 to C4 are used to filter the power supply of the op-amp. The resistor R9 = 10 Ω is used to stabilize the op-amp. Its value is given in the datasheet of the OPA855.

The feedback parameters of the transimpedance amplifier (TIA) are $R_F = 1\ k\Omega$ and $C_F = 1$ pF. In this configuration, the cutoff frequency of the TIA is 220 MHz (fig. C.4).

High-Pass Filter We use another OPA855 op-amp to implement the HPF. The lower cutoff frequency is fixed by R11 and C20 ($f_c = 8$ MHz), while the upper cutoff frequency is set by the TIA. The gain of the voltage amplification is fixed by R12 and R11 such that $G_{inv} = \frac{R12}{R11} = 8.33$. The corresponding Bode curve is displayed in figure C.4.

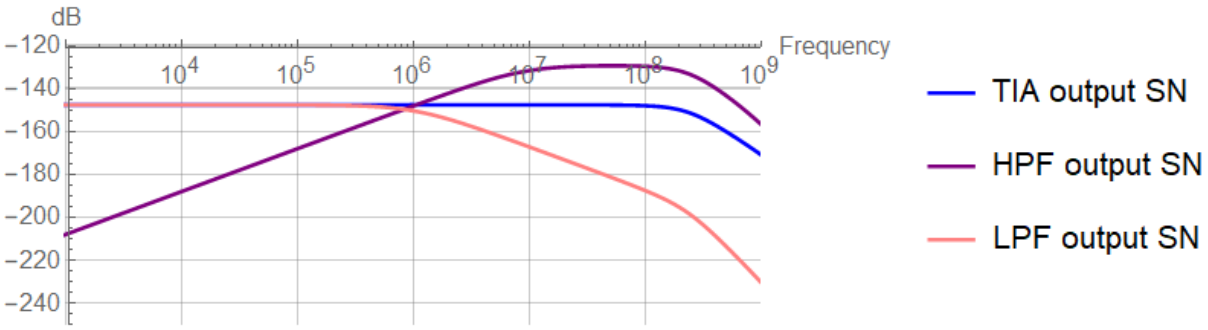

Figure C.4 – Bode curves of the OPA855 detector.

Low-Pass Filter The parameters of the LPF are the same as in the OPA847-based detector.

Finally, the resistors R2 and R3 are used at the detector outputs for impedance matching (fig. C.3).

Appendix D

Eagle Schematics of the Dual-Output Detectors

In this appendix, we show two examples of printed circuit boards (PCB) we designed with electronical workshop of the laboratory.

D.1 OPA847-based Homodyne Detectors

We use EAGLE (*Easily Applicabl Graphical Layout Editor*) to design the printed circuit boards (PCB) for our homodyne detectors. Figure D.1 is the PCB of a OPA847-based detector.

We can see that the circuit is very compact, the electronic components are placed very close to eachother and their size is 0603. The goal is to reduce the signal path in the circuit and avoid signal loss. In this case, it is easier and more precise to use an oven to weld the components on the board. However, the photodiodes (PD) s3883 from Hamamatsu are sensitive to heat, so they are welded by hand afterwards. The photodiodes are fixed on the opposite side of the PCB so as to be able to reduce the length of the track between the photocurrent subtraction stage and the transimpedance amplifier (TIA), which is the trickiest portion of the homodyne circuit. We can also see that the junction between the track from each PD is smooth (not at a right angle) to avoid signal loss. For the same reason, all the changes of direction on the PCB are smooth. The track width is $w = 0.3048$ mm everywhere on the PCB. It depends on the bandwidth of the signal traveling in it and on the electrical current flowing in the track.

Vias are metallic holes placed near conductive tracks to protect the signal from perturbations. Their size and spacing also depends on the signal flowing in the conductive tracks. Finally, we add a ground (GND) frame around the PCB. When we install a PCB inside a case, we weld it to the case to make sure that the GND plane is uniform.

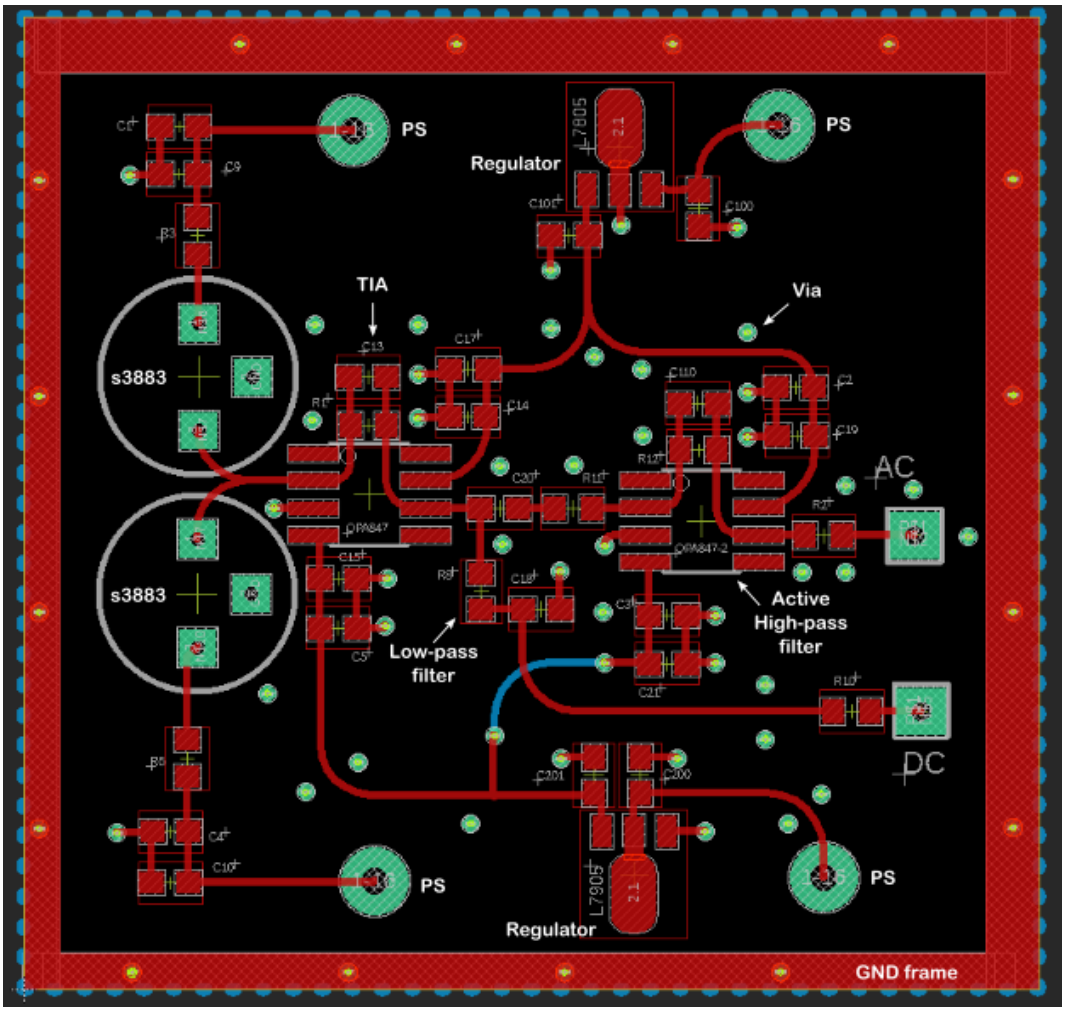

Figure D.1 – Eagle board of the OPA847-based detector (v1). PS: power suppliy; TIA: transimpedance amplifier; s3383 is the reference of the photodiodes we use; GND: ground.

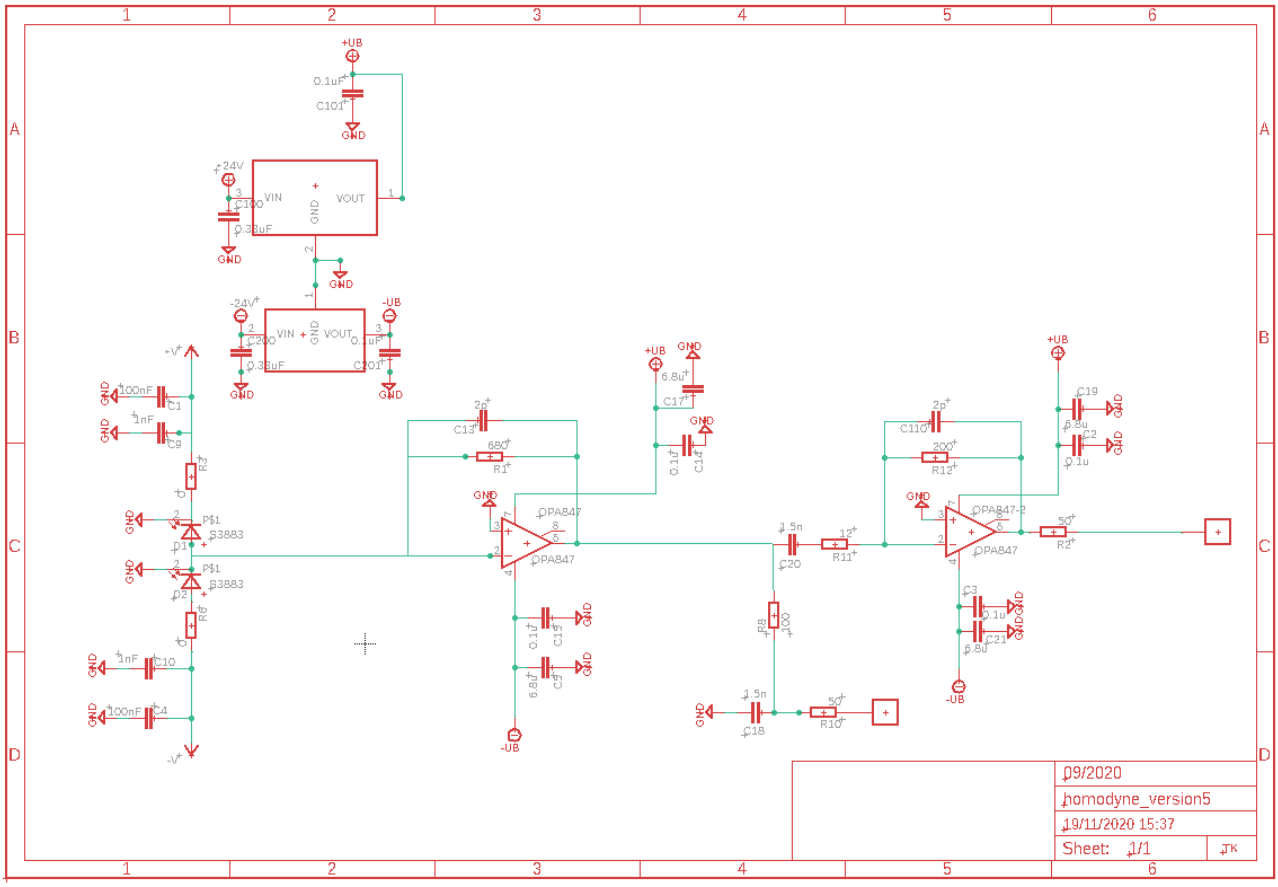

Figure D.2 – Eagle schematics of the OPA847-based detector (v1).

Figure D.2 is the associated electronical schematics. We use it to add components to the circuit and set their values.

D.2 OPA855-based Homodyne Detector

The routing the OPA855-based detectors is similar to the one of the OPA847-based detectors (fig. D.3). The electronic components are placed on one side of the PCB except the photodiodes s3883, which are placed on the opposite side of the PCB. As we can see in figure D.3, the OPA855 operational amplifiers are much smaller than the OPA847, which allows to design more compact circuits.

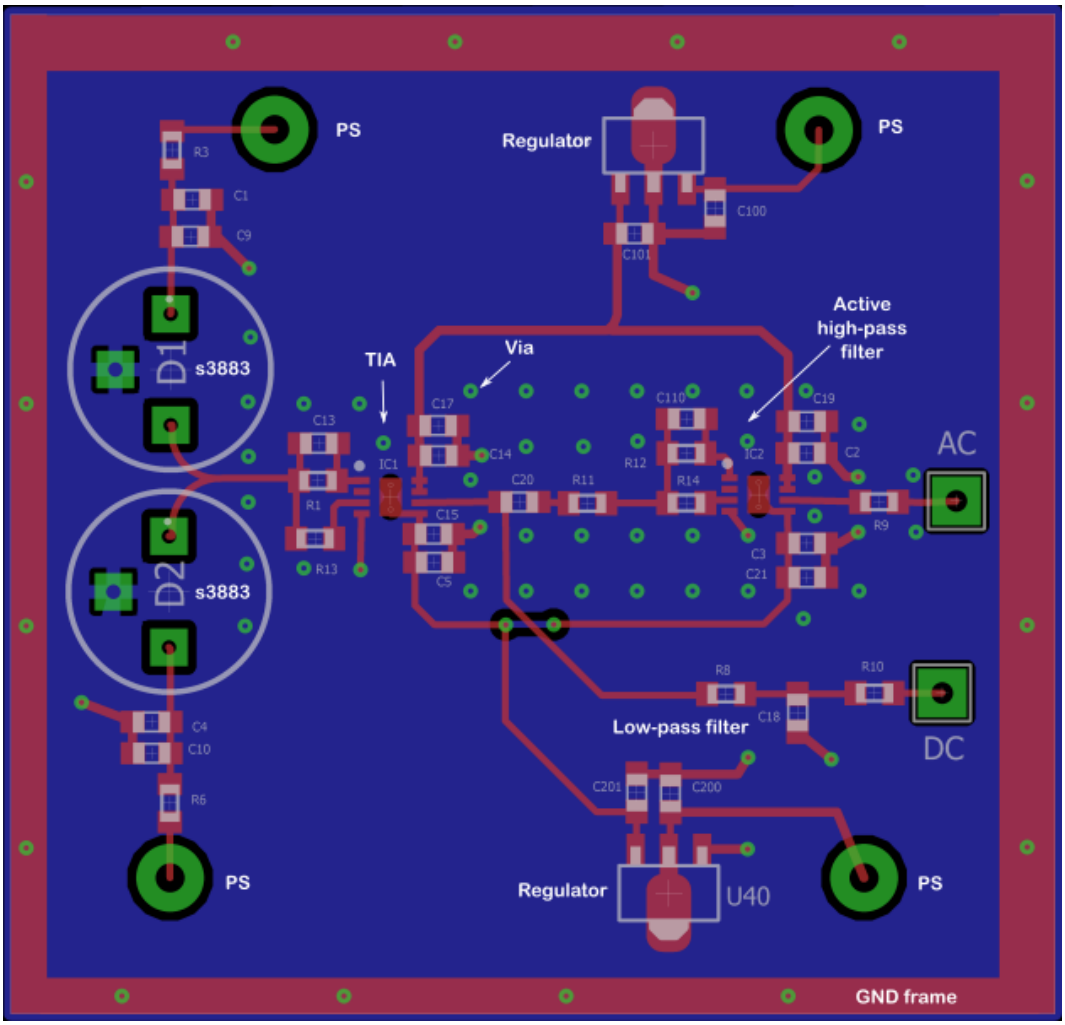

Figure D.3 – Eagle board of the OPA847-based detector (v1). PS: power suppliy; TIA: transimpedance amplifier; s3383 is the reference of the photodiodes we use; GND: ground.

Figure D.4 shows the electronic schematics associated to the board in figure D.3.

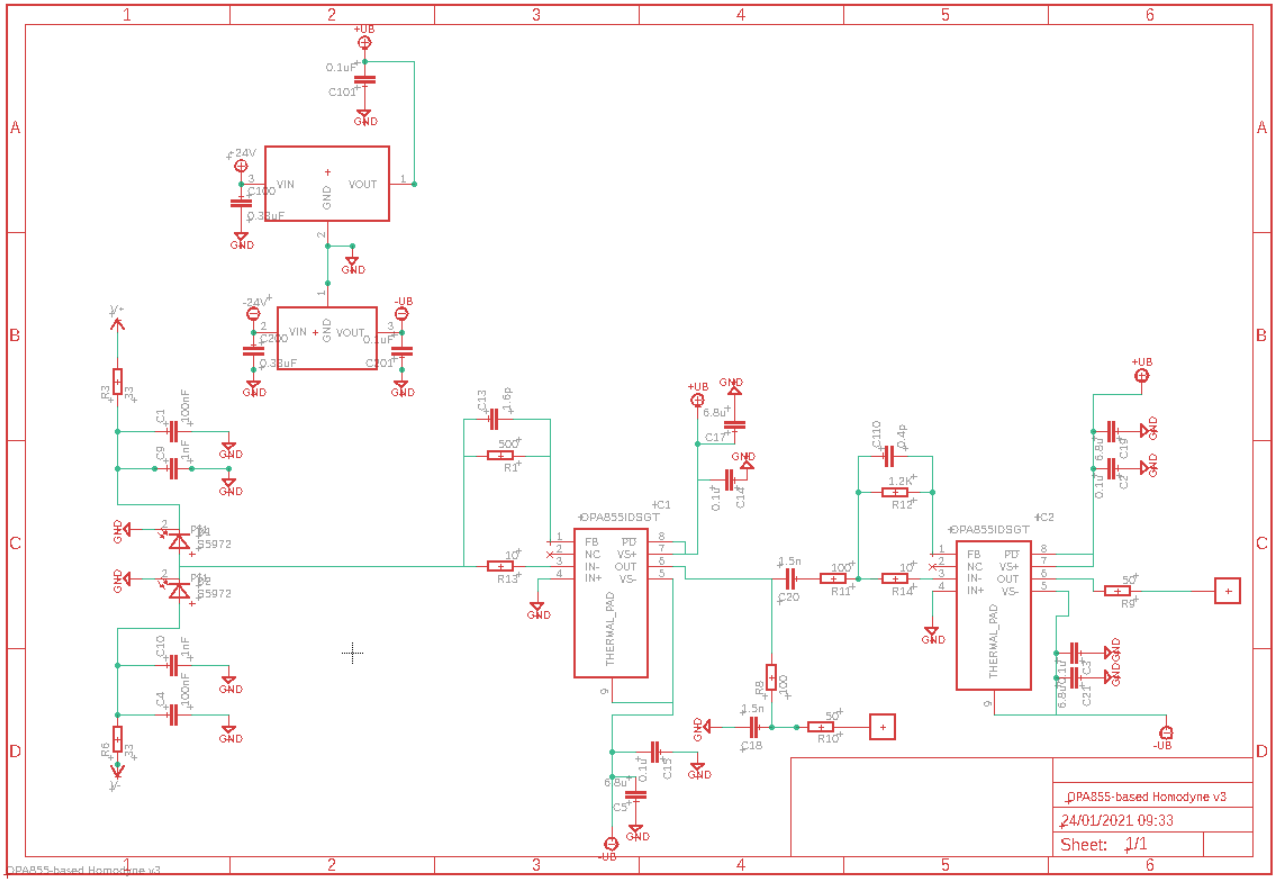

Figure D.4 – Eagle schematics of an OPA855-based detector.

Bibliography

[Aichele 02] T. Aichele, A. I. Lvovsky & S. Schiller. *Optical mode characterization of single photons prepared by means of conditional measurements on a biphoton state.* Eur. Phys. J. D, vol. 18, pages 237–245, 2002, (Cited on page 81.)

[Amy-Klein 10] A. Amy-Klein. *Des lasers à impulsions femtosecondes pour mesurer les fréquences.* Reflets Phys., no. 21, pages 42–45, 2010, (Cited on page 63.)

[Appel 07] J. Appel, D. Hoffman, E. Figueroa & A. I. Lvovsky. *Electronic noise in optical homodyne tomography.* Phys. Rev. A, vol. 75, no. 035802, 2007, (Cited on page 79.)

[Armstrong 62] J.A. Armstrong, N. Bloembergen, J. Ducuing & P. S. Pershan. *Interactions between Light Waves in a Nonlinear Dielectric.* Phys. Rev., vol. 127, no. 6, 1962, (Cited on page 61.)

[Arons 65] A. B. Arons & M. B. Peppard. *Einstein's proposal of the Photon concept - a Translation of the Annalen der Physik Paper of 1905.* Am. J. Phys., vol. 33, page 367, 1965, (Cited on page 1.)

[Ash 08] R. B. Ash. Basic probability theory. 2008. ISBN: 978-0-4864-6628-6. (Cited on page 34.)

[Bachor 04] H.-A. Bachor & T. C. Ralph. A guide to experiments in quantum optics - second edition. Wiley-VCH, 2004. ISBN: 978-3-5274-0393-6. (Cited on page 26.)

[Beck 00] M. Beck. *Quantum State Tomography with Array Detectors.* Phys. Rev. Lett., vol. 84, no. 25, pages 5748–5751, 2000, (Cited on page 85.)

[Bennett 84] C. H. Bennett & G. Brossard. *Quantum cryptography: Public key distribution and coin tossing.* Proceedings of IEEE International Conference on Computers, Systems and Signal Processing, vol. 175, page 8, 1984, (Cited on page 1.)

[Bierlein 87] J. D. Bierlein, A. Ferreti, L. H. Brixner & W. Y. Hsu. *Fabrication and characterization of optical waveguides in KTiOPO4.* Appl. Phys. Lett., vol. 50, no. 18, pages 1216–1218, 1987, (Cited on page 107.)

[Billingsley 95] P. Billingsley. Probability and measure, third edition. 1995. ISBN: 978-0-4718-0478-9. (Cited on page 34.)

[Boyd 08] R. W. Boyd. Nonlinear optics, third edition. Academic Press, 2008. ISBN: 978-0-12-369470-6. (Cited on pages 44, 51, 55, and 100.)

[Bragg 53] W. K. Bragg & A. B. Pippard. *The Form Birefringence of Macromolecules.* Acta Cryst., vol. 6, pages 865–867, 1953, (Cited on page 44.)

[Braunstein 98] S. L. Braunstein & H. J. Kimble. *Teleportation of Continuous Variables.* Phys. Rev. Lett., vol. 80, page 869, 1998, (Cited on page 2.)

[Braunstein 05] S. L. Braunstein. *Squeezing as an irreducible resource.* Phys. Rev. A, vol. 71, no. 5, page 055801, 2005, 2005. Online URL. (Cited on page 37.)

[Brecht 14] B. Brecht. *Engineering ulrafast quantum frequency conversion.* PhD thesis, University of Paderborn, 2014. (Cited on pages 36, 52, and 98.)

[Brecht 15] B. Brecht, D. V. Reddy, C. Silberhorn & M. G. Raymer. *Photon Temporal Modes: A Complete Framework for Quantum Information Science.* Phys. Rev. X, vol. 5, no. 041017, 2015, (Cited on page 17.)

[Briegel 01] H. J. Briegel & R. Raussendorf. *Persistent Entanglement in Arrays of Interacting Particles.* Phys. Rev. Lett, vol. 86, no. 5, 2001, (Cited on page 87.)

[Brosnan 79] S. Brosnan & R. Byer. *Optical parametric oscillator threshold and linewidth studies.* IEEE J. Quant. Elec., vol. 15, no. 6, pages 415–431, 1979, (Cited on page 2.)

[Burnham 70] D. C. Burnham & D. L. Weinberg. *Observation of simultaneity in parametric production of optical photon pairs.* Phys. Rev. Lett., vol. 25, no. 2, 1970, (Cited on page 1.)

[Byer 81] R. L. Byer, Y. K. Park, R. S. Feigelson & W. L. Kway. *Efficient second-harmonic generation of Nd:YAG laser radiation using warm phase-matching $LiNbO_3$.* Appl. Phys. Lett., vol. 39, pages 17–19, 1981, (Cited on page 2.)

[Cai 17] Y. Cai, J. Roslund, G. Ferrini, F. Arzani, X. Xu, C. Fabre & N. Treps. *Multimode entanglement in reconfigurable graph states using optical frequency combs.* Nat. Commun., vol. 8, no. 15645, 2017, (Cited on pages 2 and 87.)

[Caves 81] C. M. Caves. *Quantum-mechanical noise in an interferometer.* Phys. Rev. D, vol. 23, pages 1693–1708, 1981, (Cited on page 2.)

[Charoy 06] A. Charoy. Cem - parasites et perturbations des électroniques - tome 1 - sources, couplages, effets. Dunod, 2006. ISBN: 978-2-1005-0151-9. (Cited on pages 126 and 127.)

[Chen 87] C. Chen, X. Y. Fan, R. C. Eckardt & R. L. Byer. *Recent Developments in Barium Borate.* Proc. SPIE, vol. 0681, no. Laser and Nonlinear Optical Material, 1987, (Cited on page 2.)

[Chen 14] M. Chen, N. C. Menicucci & O. Pfister. *Experimental Realization of Multipartite Entanglement of 60 Modes of a Quantum Optical Frequency Comb.* Phys. Rev. Lett., vol. 112, no. 120505, 2014, (Cited on pages 2 and 87.)

[Chi 11] Y.-M. Chi, B. Qi, W. Zhu, L. Qian, H.-K. Lo, S. H. Youn, A. I. Lvovsky & L. Tian. *A balanced homodyne detector for high rate Gaussian-modulated coherent-state quantum key distribution.* New J. Phys., vol. 13, no. 013003, 2011, (Cited on page 115.)

[Christ 09] A. Christ, A. Eckstein, P. J. Mosley & C. Silberhorn. *Pure single photon generation by type-I PDC with backward-wave amplification.* Opt. Exp., vol. 17, no. 5, pages 3441–3446, 2009, (Cited on pages 44 and 108.)

[Christ 11] A. Christ, K. Laiho, A. Eckstein, K. N. Cassemiro & C. Silberhorn. *Probing multimode squeezing with correlation functions.* New J. Phys., vol. 13, no. 033027, 2011, (Cited on page 36.)

[Cooper 13] M. Cooper, C. Söller & B. J. Smith. *High-stability time-domain balanced homodyne detector for ultrafast optical pulse applications.* J. Mod. Opt., vol. 60, no. 8, pages 611–616, 2013, (Cited on pages 77, 115, and 153.)

[Danailov 89] M. B. Danailov & I. P. Christov. *Time-space shaping of light pulses by fourier optical processing.* J. Mod. Opt, vol. 36, pages 725–731, 1989, (Cited on page 69.)

[De 19] S. De, V. Thiel, J. Roslund, C. Fabre & N. Treps. *Modal analysis for noise characterization and propagation in a femtosecond oscillator.* Opt. Lett., vol. 44, no. 16, 2019, (Cited on page 21.)

[Dufour 18] A. Dufour. *Ingénierie d'états quantiques multimodes avec des impulsions femtosecondes.* PhD thesis, Sorbonne Université, 2018. (Cited on pages 17 and 86.)

[Eckardt 90] R. C. Eckardt, H. Masuda, Y. X. Fan & R. L. Byer. *Absolute and Relative Nonlinear Optical Coefficients of KDP, KD^*P, BaB_2O_4, $LiIO_3$, $MgO : LiNbO_3$ and KTP measured by Phase-Matched Second-Harmonic Generation.* IEEE Journal of Quantum Electronic, vol. 26, no. 5, 1990, (Cited on page 52.)

[Eimerl 87] D. Eimerl & et al. *Optical, mechanical and thermal properties of barium borate.* J. Appl. Phys., vol. 62, no. 5, (1987, (Cited on pages 46 and 48.)

[Einstein 05] A. Einstein. *Über einen die Erzeugung und Verwandlung des Lichtes betreffenden heuristichen Gesichtspunkt.* Annalen der Physik, vol. 322, pages 132–148, 1905, (Cited on page 1.)

[Einstein 16] A. Einstein. *Strahlungs-emission und -absorption nach der Quantentheorie.* Verhandlungen der Deutschen Physikalischen Gesellschaft, vol. 18, pages 318–323, 1916, (Cited on page 1.)

[Einstein 17] A. Einstein. *Zur Quantentheorie der Strahlung.* Physikalishe Zeitschrift, vol. 18, pages 121–128, 1917, (Cited on page 1.)

[Einstein 35] A. Einstein, B. Podolsky & N. Rosen. *Can Quantum-Mechanical Description of Physical Reality Be Considered Complete?* Phys. Rev., vol. 47, pages 777–780, 1935, (Cited on pages 1, 33, and 57.)

[Engström 13] D. Engström, M. Persson, J. Bengtsson & M. Goksör. *Calibration of spatial light modulators suffering from spatially varying*

phase response. Opt. Exp., vol. 21, no. 13, 2013, (Cited on page 66.)

[Esteban-Martin 09] A. Esteban-Martin, O. Kokabee, K. Moutzouris & M. Ebrahim-Zadeh. *High-harmonic-repetition-rate, 1 GHz femtosecond optical parametric oscillator pumped by a 76 MHz Ti:sapphire laser*. Opt. Lett., vol. 34, no. 4, pages 428–430, 2009, (Cited on page 2.)

[Everett 57] H. Everett. *"Relative State" Formulation of Quantum Mechanics*. Rev. Mod. Phys., vol. 29, no. 457, 1957, (Cited on page 36.)

[Fabre 20] C. Fabre & N. Treps. *Modes and states in quantum optics*. Rev. Mod. Phys., vol. 92, no. 3, 2020, (Cited on pages 9 and 37.)

[Fano 57] U. Fano. *Description of States in Quantum Mechanics by Density Matrix and Operator Techniques*. Rev. Mod. Phys., vol. 29, no. 74, 1957, (Cited on page 26.)

[Fleury 83] P. Fleury. *Les défauts ponctuels dans les cristaux*. Bulletin de l'union des physiciens, no. 658, 1983, (Cited on pages 103 and 104.)

[Fortier 19] T. Fortier & E. Baumann. *20 years of developments in optical frequency comb technology and applications*. Com. Phys., vol. 2, no. 153, 2019, (Cited on pages 17 and 63.)

[Franken 61] P. A. Franken, A. E. Hill, C. W. Peters & G. Weinreich. *Generation of Optical Harmonics*. Phys. Rev. Lett., vol. 7, no. 4, 1961, (Cited on page 1.)

[Franken 63] P.A. Franken & J. F. Ward. *Optical Harmonics and Nonlinear Phenomena*. Rev. Mod. Phys., vol. 35, no. 1, 1963, (Cited on page 61.)

[Froehly 83] C. Froehly, B. Colombeau & M. Vampouille. *Shaping and Analysis of Picosecond Light Pulses*. Prog. in. Opt., vol. 20, pages 65–153, 1983, (Cited on page 64.)

[Furusawa 98] A. Furusawa, J. L. Srenson, S. L. Braunstein, C. A. Fuchs, H. J. Kimble & E. S. Polzik. *Unconditional Quantum Teleportation*. Science, vol. 282, page 706, 1998, (Cited on page 2.)

[Gatti 15] A. Gatti, T. Corti & E. Brambilla. *Temporal Coherence and correlation of counterpropagating twin photons*. Phys. Rev. A, vol. 92, 2015, (Cited on page 56.)

[Gehr 98] R. J. Gehr, M. W. Kimmel & A. V. Smith. *Simultaneous spatial and temporal walk-off compensation in frequency-doubling femtosecond pulses in β-BaB_2O_4.* Opt. Lett., vol. 23, no. 16, pages 1298–1300, 1998, (Cited on page 90.)

[Gerke 16] S. Gerke, J. Sperling, W. Vogel, Y. Cai, J. Roslun, N. Treps & C. Fabre. *Multipartite Entanglement of a Two-Separable State.* Phys. Rev. Lett., vol. 117, no. 110502, 2016, (Cited on page 2.)

[Grosshans 01a] F. Grosshans & P. Grangier. *Effective quantum efficiency in the pulsed homodyne detection of a n-photon state.* Eur. Phys. J. D, vol. 14, pages 119–125, 2001, (Cited on page 81.)

[Grosshans 01b] F. Grosshans & P. Grangier. *Quantum cloning and teleportation criteria for continuous quantum variables.* Phys. Rev. A, vol. 64, no. 010301, 2001, (Cited on page 2.)

[Grynberg 10] G. Grynberg, A. Aspect & C. Fabre. Introduction to quantum optics: From the semi-classical approach to quantized light. Cambridge University Press, 2010. ISBN: 978-0-5215-5112-0. (Cited on pages 23 and 30.)

[Gu 09] M. Gu, C Weedbrook, N. C. Menicucci, T. C. Ralph & P. van Loock. *Quantum computing with continuous-variable clusters.* Phys. Rev. A, vol. 79, no. 6, page 062318, 2009, (Cited on page 2.)

[Haderka 09] O. Haderka, V. Michálek, V. Urbášek & M. Ježek. *Fast time-domain balanced homodyne detection of light.* Appl. Opt., vol. 48, no. 15, pages 2884–2889, 2009, (Cited on page 115.)

[Hänsch 06] T. W. Hänsch. *Nobel Lecture: Passion for precision.* Rev. Mod. Phys., vol. 78, no. 1297, 2006, (Cited on pages 16 and 63.)

[Harder 13] G. Harder, V. Ansari, B. Brecht, T. Dirmeier, C. Marcquart & C. Silberhorn. *An optimized photon pair source for quantum circuits.* Opt. Exp., vol. 21, no. 12, pages 13975–13985, 2013, (Cited on page 44.)

[Hargrove 64] L. E. Hargrove, R. L. Fork & M. A. Pollack. *Locking of He-Ne laser modes induced by synchronous intracavity modulation.* App. Phys. Lett., vol. 5, pages 4–5, 1964, (Cited on page 2.)

[Harmeling 17] P. Harmeling. *Étude et Réalisation de PCB.* Cours de l'Université de Liège, 2017, (Cited on pages 128 and 129.)

[Harris 67] S. E. Harris, M.K. Oshman & R. L. Byer. *Observation of Tunable Optical Parametric Fluorescence*. Phys. Rev Lett., vol. 18, pages 732–734, 1967, (Cited on page 43.)

[Haus 93] H. A. Haus. *Noise of Mode-Locked Lasers*. IEEE J. Quant. Elect., vol. 29, no. 3, 1993, (Cited on page 20.)

[Haus 20] H. A. Haus. *Mode-locking of lasers*. IEEE Journal of Selected Topics in Quantum Electronics, vol. 6, no. 6, 2020, (Cited on page 18.)

[Heidmann 87] A. Heidmann, R. J. Horowicz, S. Reynaud, E. Giacobino, C. Fabre & G. Camy. *Observation of Quantum Noise Reduction on Twin Laser Beams*. Phys. Rev. Lett., vol. 59, no. 22, pages 2555–2557, 1987, (Cited on page 1.)

[Hong 86] C. K. Hong & L. Mandel. *Experimental realization of a localized one-photon state*. Phys. Rev. Lett., vol. 56, no. 1, page 58, 1986, (Cited on pages 1 and 43.)

[Hook 01] J. R. Hook & H. E. Hall. Solid state physics. Wiley-Blackwell, 2001. ISBN: 978-0-4719-2805-8. (Cited on page 116.)

[Horodecki 09] R. Horodecki, P. Horodecki, M. Horodecki & K.Horodecki. *Quantum entanglement*. Rev. Mod. Phys., vol. 81, no. 2, pages 865–942, 2009, (Cited on page 1.)

[Horoshko 19] D. B. Horoshko, L. La Volpe, F. Arzani, N. Treps, C. Fabre & M. I. Kolobov. *Bloch-Messiah reduction for twin beams of light*. Phys. Rev. A, vol. 100, no. 1, 2019, (Cited on pages 38 and 57.)

[Instruments 13] Texas Instruments. *AN-1604 Decompensated Operational Amplifiers*. no. Application Report SNOA486B, 2013, (Cited on page 122.)

[IPC2221A 03] IPC2221A. *Generic Standard on Printed Board Design*. Association connecting electronics industries, 2003, (Cited on page 128.)

[IPC2226A 03] IPC2226A. *Sectional Design Standard for High Density Interconnect (HDI) Printed Boards*. Association connecting electronics industries, 2003, (Cited on page 128.)

[Karpiński 17] M. Karpiński, M. Jachura, L. J. Wright & B. J. Smith. *Bandwidth manipulation of quantum light by an electro-optic time lens*. Nat. Phot., vol. 11, pages 53–57, 2017, (Cited on page 17.)

[Kato 02] K. Kato & E. Takaoka. *Sellmeier and Thermo-Optics dispersion formula for KTP.* Appl. Opt., vol. 41, no. 24, 2002, (Cited on pages 46 and 48.)

[Klyshko 69] D. N. Klyshko. *Scattering of light in a medium with nonlinear polarizability.* Sov. Phys. JEPT, vol. 28, page 522, 1969, (Cited on page 43.)

[Kumar 12] R. Kumar, E. Barrios, A. MacRae, E. Cairns, E. H. Huntington & A. I. Lvovsky. *Versatile wideband balanced detector for quantum optical homodyne tomography.* Opt. Commun., vol. 285, no. 24, 2012, (Cited on pages 3, 79, 82, 83, and 115.)

[Kwiat 95] P. G. Kwiat, K. Mattle, H. Weinfurter, A. Zeilinger, A. V. Sergienko & Y. Shih. *New High-Intensity Source of Polarization-Entangled Photon Pairs.* Phys. Rev. Lett., vol. 75, no. 24, 1995, (Cited on page 1.)

[La Volpe 19] L. La Volpe. *Single-Pass Squeezing and Spatio-temporal Modes.* PhD thesis, Sorbonne Université, 2019. (Cited on pages 57, 61, 81, 89, 91, 92, 94, 95, and 153.)

[La Volpe 20] L. La Volpe, S. De, T. Kouadou, D. Horoshko, M. I. Kolobov, C. Fabre, V. Parigi & N. Treps. *Multimode single-pass spatio-temporal squeezing.* Opt. Exp., vol. 28, no. 8, pages 12385–12394, 2020, (Cited on pages 94 and 153.)

[Laulhé 18] C. Laulhé. *Chapitre IV - Les défauts dans les cristaux.* 2018, Cours de l'Université Paris Sud. (Cited on page 103.)

[Leonhardt 97] U. Leonhardt. Measuring the quantum state of light. Cambridge Studies in Modern Optics, 1997. ISBN: 978-0-5214-9730-5. (Cited on pages 26, 28, and 78.)

[Loewen 90] E. G. Loewen. Diffraction gratings and applications. Optical Engineering 58, 1990. ISBN: 978-1-3154-1484-9. (Cited on page 66.)

[Loudon 00] R. Loudon. The quantum theory of light. Oxford University Press, 2000. ISBN: 978-0-1915-8978-2. (Cited on page 23.)

[Louisell 61] W. H. Louisell, A. Yariv & A. E. Siegman. *Quantum Fluctuations and Noise in Parametric Processes.* Phys. Rev., vol. 124, no. 6, 1961, (Cited on page 1.)

[Luo 20] K.-H. Luo, V. Ansari, M. Massaro, M. Santandrea, C. Eigner, R. Ricken, H. Herrmann & C. Silberhorn. *Counter-propagating photon pair generation in a nonlinear waveguide.* Opt. Exp., vol. 28, no. 3, pages 3215–3225, 2020, (Cited on page 2.)

[Lvovsky 14] A. I. Lvovsky. *Squeezed light.* arXiv:1401.4118, 2014, (Cited on pages 27 and 32.)

[Mabuchi 94] H. Mabuchi, E. S. Polzik & H. J. Kimble. *Blue-light-induced infrared absorption in $KNbO_3$.* J. Opt. Soc. Am. B, vol. 11, no. 10, 1994, (Cited on page 105.)

[Maiman 60] T. H. Maiman. *Stimulated optical radiation in ruby.* Nature, vol. 187, pages 493–494, 1960, (Cited on page 1.)

[Malvino 98] A. P. Malvino & D. J. Bates. Electronic principles. McGraw-Hill Science, 1998. ISBN: 978-0-0280-2833-0. (Cited on page 123.)

[Mancini 13] R. Mancini. Op amps for everyone: Design reference. Newnes, 2013. ISBN: 978-0-7506-7844-5. (Cited on page 123.)

[Mandel 82] L. Mandel. *Squeezed States and Sub-Poissonian Photon Statistics.* Phys. Rev. Lett., vol. 49, no. 2, 1982, (Cited on page 3.)

[Marin-Palomo 17] P. Marin-Palomo & et al. *Microresonator-Based Solitons for Massively Parallel Coherent Optical Communications.* Nature, vol. 546, pages 274–279, 2017, (Cited on page 63.)

[Masalov 17] A. V. Masalov, A. Kuzhamuratov & A. I. Lvovsky. *Noise spectral in balanced optical detectors based on transimpedance amplifiers.* Rev. Sci. Instr., vol. 88, no. 113109, 2017, (Cited on pages 119, 120, 145, and 153.)

[Mazda 89] F.F. Mazda. Electronics engineer's reference book. Butterworth-Heinemann - 6th edition, 1989. ISBN: 978-1-4831-6106-8. (Cited on page 129.)

[Menicucci 06] N. C. Menicucci, P. van Loock, M. Gu, C. Weedbrook, T. C. Ralph & M. A. Nielsen. *Universal Quantum Computation with Continuous-Variable Cluster States.* Phys. Rev. Lett., vol. 97, no. 11, page 110501, 2006, (Cited on page 2.)

[Mondain 19] F. Mondain, T. Lunghi, A. Zavatta, E. Gouzien, F. Doutre, M. De Micheli, S. Tanzilli & V. D'Auria. *Chip-bazed squeezing*

at a telecom wavelength. Photon. Res., vol. 7, no. 7, pages A36–A39, 2019, (Cited on page 2.)

[Monmayrant 10] A. Monmayrant, S. Weber & B. Chatel. *A newcomer's guide to ultrafast pulse shaping and characterization.* J. Phys. B: At. Mol. Opt. Phys., vol. 43, no. 103001, 2010, (Cited on pages 64 and 69.)

[Mood 01] A. M. Mood, F. A. Graybill & D. C. Boes. Introduction to the theory of statistics. Tata McGraw-Hill, 2001. ISBN: 978-0-0704-2864-5. (Cited on page 34.)

[Mosley 07] P. J. Mosley. *Generation of Heralded Single Photons in Pure Quantum States.* PhD thesis, University of Oxford, 2007. (Cited on pages 43 and 57.)

[Nielsen 00] M. A. Nielsen & I. L. Chuang. Quantum computation and quantum information. Cambridge University Press, 2000. ISBN: 978-1-1070-0217-3. (Cited on pages 2 and 26.)

[Okubo 08] R. Okubo, M. Hirano, Y. Zhang & T. Hirano. *Pulse-resolved measurement of quadrature phase amplitudes of squeezed pulse trains at a repetition rate of 76 MHz.* Opt. Lett., vol. 33, no. 13, pages 1458–1460, 2008, (Cited on page 115.)

[Opatrný 02] T. Opatrný, N. Korolkova & G. Leuchs. *Mode structure and photon number correlations in squeezed quantum pulses.* Phys. Rev. A, vol. 66, no. 053813, 2002, (Cited on page 34.)

[Ou 07] Z.Y. Jeff Ou. Multi-photon quantum interference. Springer, (2007. ISBN: 978-0-387-25532-3. (Cited on pages 57, 61, and 100.)

[Owyoung 71] A. Owyoung. *The origins of nonlinear refractive indices of liquid and glasses.* PhD thesis, California Institute of Technology, 1971. (Cited on page 51.)

[Pack 04] M. V. Pack, D. J. Armstrong & A. V. Smith. *Measurement of the $\chi^{(2)}$ tensors of $KTiOPO_4$, $KTiOAsO_4$, $RbTiOPO_4$ and $RbTiOAsO_4$ crystals.* Appl. Opt., vol. 43, no. 16, pages 3319–3323, 2004, (Cited on page 52.)

[Patera 09] G. Patera. *Quantum properties of ultra-short pulses generated by SPOPOs: multi-mode squeezing and entanglement.* PhD thesis, Université Pierre et Marie Curie, 2009. (Cited on page 38.)

[Patera 12] G. Patera, C. Navarrete-Benlloch, G. J. de Valcárcel & C. Fabre. *Quantum coherent control of highly multipartite continuous-variable entangle states by tailoring parametric interactions.* Eur. Phys. J. D, vol. 66, page 241, 2012, (Cited on page 38.)

[Pinel 10] O. Pinel. *Optique quantique multimode avec des peignes de fréquence.* PhD thesis, Université Pierre et Marie Curie, 2010. (Cited on page 94.)

[Pinel 12] O. Pinel, P. Jian, R. Medeiros de Araùjo, J. Feng, B. Chalopin, C. Fabre & N. Treps. *Generation and Characterization of Multimode Quantum Frequency Combs.* Phys. Rev. Lett., vol. 108, no. 083601, 2012, (Cited on page 2.)

[Planck 00] M. Planck. *Ueber irreversible Strahlungsvorgänge.* Annalen der Physik, vol. 306, pages 69–122, 1900, (Cited on page 1.)

[Planck 01] M. Planck. *Ueber des Gesetz der Energieverteilung im Normalspectrum.* Annalen der Physik, vol. 309, page 553, 1901, (Cited on page 1.)

[Polycarpou 12] C. Polycarpou, K. N. Cassemiro, G. Venturi, A. Zavatta & M. Bellini. *Adaptive Detection of Arbitrarily Shaped Ultrashort Quantum Light States.* Phys. Rev. Lett., vol. 109, no. 053602, 2012, (Cited on page 17.)

[Popov 90] E. Popov, L. Tsonev & D. Maystre. *Gratings: general properties of the Littrow mounting and energy flow distribution.* J. Mod. Phys., vol. 37, page 367, 1990, (Cited on page 66.)

[Porta 89] A. La Porta, R. E. Slusher & B. Yurke. *Back-Action Evading Measurements of an Optical Field Using Parametric Down Conversion,.* Phys. Rev. Lett., vol. 62, page 28, 1989, (Cited on page 2.)

[Powers 93] P. E. Powers, R. J. Ellingson & W. S. Pelouch. *Recent advances of the Ti:sapphire-pumped high-repetition-rate femtosecond optical parametric oscillator.* J. Opt. Soc. Am. B, vol. 10, no. 11, 1993, (Cited on page 2.)

[Raffaelli 18] F. Raffaelli & et al. *A homodyne detector integrated onto a photonic chip for measuring quantum states and generating random numbers.* Quantum Sci. Technol., vol. 3, no. 025003, 2018, (Cited on page 82.)

[Ramus 09] X. Ramus. *Transimpedance Considerations for High-Speed Amplifiers*. Texas Instruments, no. Application Report SBOA122, 2009, (Cited on pages 120 and 121.)

[Raussendorf 01] R. Raussendorf & H. J. Briegel. *A One-Way Quantum Computer*. Phys. Rev. Lett., vol. 86, no. 22, 2001, (Cited on pages 2 and 87.)

[Raussendorf 03] R. Raussendorf, D. E. Browne & H. J. Briegel. *Measurement-based quantum computation on cluster states*. Phys. Rev. A, vol. 68, no. 022312, 2003, (Cited on pages 2 and 87.)

[Raymer 95] M. G. Raymer, J. Cooper, H. J. Carmichael, M. Beck & D. T. Smithey. *Ultrafast measurement of optical-field statistics by dc-balanced homodyne detection*. J. Opt. Soc. Am. B, vol. 12, no. 10, 1995, (Cited on page 77.)

[Risk 96] W. P. Risk & S. D. Lau. *Periodic Electric Field Poling of $KTiOPO_4$ using Chemical Patterning*. Appl. Phys. Lett, vol. 69, page 3999, 1996, (Cited on page 61.)

[Roman-Rodriguez 20] V. Roman-Rodriguez, B. Brecht, S. Kaali, C. Silberhorn, N. Treps, E. Diamanti & V. Parigi. *Continuous variable multimode quantum states via symmectric group velocity matching*. arXiv:2012.13629, 2020, (Cited on pages 16, 36, and 99.)

[Roslund 14] J. Roslund, R. Medeiros de Araùjo, S. Jiang, C. Fabre & N. Treps. Nat. Phot., vol. 8, pages 109–112, 2014, (Cited on pages 2, 17, and 97.)

[Sah 57] C. Sah, R. N. Noyce & W. Schokley. *Carrier Generation and Recombination in P-N Junctions and P-N Junction Characteristics*. Proceedings of IRE, vol. 45, no. 9, pages 1228–1243, 1957, (Cited on page 117.)

[Schmeissner 14] R. Schmeissner, J. Roslund, C. Fabre & N. Treps. *Spectral Noise Correlations of an Ultrafast Frequency Comb*. Phys. Rev. Lett., vol. 113, no. 263906, 2014, (Cited on page 21.)

[Schulman 62] J.H. Schulman & W.D. Compton. Color centers in solids. Pergamon Press, 1962. (Cited on page 103.)

[Schumaker 84] B. L. Schumaker. *Noise in homodyne detection*. Opt. Lett., vol. 9, no. 5, 1984, (Cited on pages 71 and 75.)

[Sellmeier 72] W. Sellmeier. *Ueber die durch die Aetherschwingungen erregten Mitschwingungen der Körpertheilchen un deren Rückwirkung auf die ersteren, besonders zur Erklärung der Dispersion und ihren Anomalien (II. Theil).* Annalen der Physik und Chemie, vol. 223, no. 11, pages 386–403, 1872, (Cited on page 46.)

[Serikawa 18] T. Serikawa & A. Furusawa. *500 MHz resonant photodetector for high-quantum-efficiency, low-noise homodyne measurement.* Rev. Sci. Instrum., vol. 89, no. 063120, 2018, (Cited on page 3.)

[Shim 09] S. H. Shim & M. T. Zanni. *How to turn your pump-probe instrument into a multidimensional spectrometer; 2D IR and VIS spectroscopies via pulse shaping.* Chem. Phys., vol. 11, pages 748–761, 2009, (Cited on page 63.)

[Shukla 09] V. Shukla. Signal integrity for pcb designers. Reference Designer - first edition, 2009. ISBN: 978-0-9821-3690-4. (Cited on pages 126 and 127.)

[Siegman 86] A. E. Siegman. Lasers. University Science Books, 1986. ISBN: 978-0-9357-0211-8. (Cited on pages 12 and 91.)

[Silberberg 09] Y. Silberberg. *Quantum coherent control for nonlinear spectroscopy and microscopy.* Annu. Rev. Phys. Chem., vol. 60, pages 277–292, 2009, (Cited on page 63.)

[Slusher 85] R. E. Slusher, L. W. Hollberg, B. Yurke & J. C. Mertz. *Observation of squeezed states generated by four-wave mixing in an optical cavity.* Phys. Rev. Lett., vol. 55, no. 22, 1985, (Cited on page 2.)

[Sorokin 00] E. Sorokin, G. Tempea & T. Brabec. *Meausurement of the root-mean-square width and the root-mean-square chirp in ultrafast optics.* J. Opt. Soc. Am. B, vol. 17, no. 1, pages 146–150, 2000, (Cited on page 18.)

[Spence 91] D. E. Spence, P. N. Kean & W. Sibbett. *60-fsec pulse generation from a self-mode-locked Ti:sapphire laser.* Opt. Lett., vol. 16, pages 42–44, 1991, (Cited on page 2.)

[Tanzilli 01] S. Tanzilli, H. De Riedmatten, W. Tittel, H. Zbinden, P. Baldi, M. De Micheli, D. B. Ostrowsky & N. Gisin. *Highly efficien photon-pair source using periodically poled lithium niobate*

waveguides. Elec. Lett., vol. 37, no. 1, pages 26–28, 2001, (Cited on page 2.)

[Thiel 15] V. Thiel. *Modal analysis of an ultrafast frequency comb: From classical to quantum spectra correlations*. PhD thesis, Sorbonne Université, 2015. (Cited on pages 20 and 21.)

[Udem 99] T. Udem, J. Reichert, R. Holzwarth & T. W. Hänsch. *Absolute Optical Frequency Measurement of the Cesium D_1 Line with a Mode-Locked Laser*. Phys. Rev. Lett., vol. 82, no. 3568, 1999, (Cited on pages 2 and 17.)

[Udem 02] T. Udem, E. Holzwarth & T. W. Hänsch. Nature, vol. 416, no. 6877, pages 233–237, 2002, (Cited on page 2.)

[Vahlbruch 16] H. Vahlbruch, M. Mehmet, K. Danzmann & R. Schnabel. *Detection of 15 dB Squeezed States of Light and their Application for the Absolute Calibration of Photoelectric Quantum Efficiency*. Phys. Rev. Lett., vol. 117, no. 110801, 2016, (Cited on page 2.)

[Vitelli 13] C. Vitelli, N. Spagnolo, L. Aparo, F. Sciarrino, E. Santamato & L. Marrucci. *Joining the quantum state of two photons into one*. Nat. Phot., vol. 7, pages 521–526, 2013, (Cited on page 44.)

[Wang 17] Y. Wang, W. Yang, Z. Li & Y. Zheng. *Determination of blue-light induced infrared absorption based on mode-matching efficiency in an optical parametric oscillator*. Scientif. Rep., vol. 7, no. 41405, 2017, (Cited on page 104.)

[Wasilewski 06] W. Wasilewski, A. I. Lvovsky, K. Banaszek & C. Radzewicz. *Pulsed squeezed light: Simultaneous squeezing of multiple modes*. Phys. Rev. A, vol. 73, no. 063819, 2006, (Cited on page 17.)

[Weckler 67] G. P. Weckler. *Operation of p-n junctions Photodetectors in a Photon Flux Integrating Mode*. IEEE J. Solid-State Circuits, vol. 2, no. 3, pages 65–73, 1967, (Cited on page 118.)

[Weiner 09] A. M. Weiner. Ultrafast optics. Wiley-Blackwell, 2009. ISBN: 978-0-4714-1539-8. (Cited on page 20.)

[Weiner 11] A. M. Weiner. *Ultrafast optical pulse shaping: A tutorial review*. Opt. Comm., vol. 284, pages 3669–3692, 2011, (Cited on pages 20 and 64.)

[Wigner 32] E. P. Wigner. *On the quantum correction for thermodynamic equilibrium.* Phys. Rev., vol. 40, no. 5, pages 749–759, 1932, (Cited on page 28.)

[Wu 87] L.-A. Wu, M. Xiao & H. J. Kimble. *Squeezed states of light from an optical parametric oscillator.* J. Opt. Soc. Am. B, vol. 4, no. 10, pages 1465–1475, 1987, (Cited on page 2.)

[Yokoyama 13] S. Yokoyama, R. Ukai, S. C. Armstrong, C. Sornphiphatphong, T. Kaji, S. Suzuki, J.-I. Yoshikawa, H. Yonezawa, N. C. Menicucci & A. Furusawa. *Ultra-large-scale continuous-variable cluster states multiplexed in the time domain.* Nat. Phot., vol. 7, pages 982–986, 2013, (Cited on pages 2, 3, 87, 88, 98, and 153.)

[Yuen 83] H. P. Yuen & V. W. S. Chan. *Noise in homodyne and heterodyne detection.* Opt. Lett., vol. 8, no. 3, 1983, (Cited on pages 3 and 75.)

[Yurke 85] B. Yurke. *Wideband photon counting and homodyne detection.* Phys. Rev. A, vol. 32, no. 1, 1985, (Cited on page 3.)

[Zavatta 02] A. Zavatta, M. Bellini, P. L. Ramazza, F. Marin & F. T. Arecchi. *Time-domain analysis of quantum states of light noise characterization and homodyne tomography.* J. Opt. Soc. Am. B, vol. 19, no. 5, 2002, (Cited on pages 3, 115, and 153.)

[Zel'Dovich 69] B. Y. Zel'Dovich & D. N. Klyshko. *Field statistics in parametric fluorescence.* ZhETF Pis ma Redaktsiiu, vol. 2, pages 69–72, 1969, (Cited on page 1.)

[Zorabedian 95] P. Zorabedian & F. J. Duarte. Tunable laser handbook - chapter 8 - tunable external-cavity semiconductor lasers. Academic Press, 1995. ISBN: 978-0-1222-2695-3. (Cited on page 66.)